DOCTORAL THESIS
in **Physical Sciences**

Wrocław
University
of Science
and Technology

Novel properties of exciton polaritons

Dąbrówka Biegańska

Supervisor: dr hab. eng. Marcin Syperek, Prof. WUST
Co-supervisor: dr hab. eng. Maciej Pieczarka

Wrocław
2024

Wrocław University of Science and Technology
Department of Experimental Physics
Department of Fundamental Problems of Technology
Wybrzeże Wyspiańskiego 27
50-370 Wrocław
Poland

Abstract

Exciton polaritons (polaritons herein) are mixed light-matter quasiparticles, emerging from the strong coupling between quantum-well (QW) excitons and cavity photons in a semiconductor optical microcavity. They are a quantum superposition of these two states, and as such they inherit their unique properties from both the excitonic and the photonic components. They are interacting bosons, with interactions inherited directly from the excitons, but they are also light-weight, fast and easily accessible in optical experiments, due to the photonic part. As bosons, they can form a macroscopically coherent state, such as a Bose-Einstein condensate.

Although they have been studied for more than twenty years, due to their complexity, their properties are still not fully understood and new research still emerges. They are often studied in novel contexts, in new novel platforms, or with potential for novel applications. Even some of their fundamental properties are still not fully unveiled and are subject to intensive research. This is why this thesis centers around novel properties of exciton polaritons, unexplored or unevidenced before. It focuses on several key parts: spin-dependent properties, fundamental interactions, topological and non-Hermitian properties, and dissipative effects.

The thesis studies solid-state semiconductor microcavities via optical experiments. It first centers around the experimental study of spin-dependent interactions of long-lived polaritons in a high-density condensate, where the polariton properties are governed by the polarization, optical anisotropy and the polarization-dependent interactions. It studies the condensate collective excitations, affected by a non-Abelian effective gauge field, which is formed by the polarization splittings. The thesis evidences the effective field with unique, monopole-like features and dispersion degeneracy points and directly measures the fundamental interaction constants. Then, using the same methods, it uncovers the topological and non-Hermitian properties of exciton polaritons, where not the interactions but the dissipation adds to the effective gauge field, with a high contribution of an optical anisotropy. It evidences paired exceptional points in momentum space of such a system and extracts a non-Hermitian topological invariant - serving as a first direct measurements of this feature. Then the influence of dissipation is studied further, resulting in an uncommon effect of level attraction. However, in order to do it, the excitonic properties of an AlGaAs platform need to be understood first. Based on experimental results, the thesis pinpoints three types of excitons - one direct and two momentum- and spatially-indirect - in the studied QW system, and explores their characteristics. The system understanding

is essential in unveiling the novel properties, when the coupling with photonic states is included. In a full polariton microcavity the thesis evidences an inverted, anomalous dispersion of a polariton state, inherently linked to a negative effective mass. It uncovers a basis of the effect, stemming from a dissipative coupling mediated via a coherent coupling to a dissipative mode. It pinpoints the dissipation to come from an indirect state characterized in another part of the thesis, and it presents a new method of anomalous dispersion curvature tuning. It is a first observation of an anomalous dispersion in an unstructured QW polariton system to date.

All the findings of the thesis have profound implications for further research and applications. They have been published or are under review in international peer-reviewed journals.

Streszczenie

Polarytony ekscytonowe (zwane dalej polarytonami) są kwaziczą̨stkami złożonymi ze światła i materii, powstającymi w wyniku silnego sprzężenia ekscytonów zlokalizowanych w studni kwantowej (QW) ze związanymi fotonami w półprzewodnikowej mikrownęce optycznej. Stanowią kwantową superpozycję tych dwóch stanów, a zatem dziedziczą swoje unikalne właściwości zarówno od składnika ekscytonowego, jak i fotonowego. Są oddziałującymi bozonami, przy czym ich oddziaływania są bezpośrednio dziedziczone od ekscytonów; jednocześnie są lekkie, szybkie i łatwo mierzalne w eksperymentach optycznych, dzięki składnikowi fotonowemu. Jako bozony mogą tworzyć makroskopowo koherentny stan, jakim jest kondensat Bosego-Einsteina.

Mimo, że polarytony są badane od ponad dwudziestu lat, ze względu na swoją złożoność ich właściwości wciąż nie są w pełni zrozumiane, co motywuje wciąż pojawiające się nowe badania. Są często badane w nowych kontekstach, w nowych platformach eksperymentalnych, lub z potencjałem do nowych zastosowań. Nawet niektóre ich fundamentalne właściwości nie zostały jeszcze w pełni odkryte i są przedmiotem intensywnych badań i dyskusji. Dlatego niniejsza praca skupia się właśnie na takich nowych właściwościach polarytonów ekscytonowych, dotąd niezbadanych lub nieudowodnionych. Koncentruje się na kilku kluczowych zagadnieniach: właściwościach zależnych od spinu, fundamentalnych oddziaływaniach, właściwościach topologicznych i niehermitowskich oraz efektach dyssypatywnych.

Praca bada półprzewodnikowe mikrownęki w ciele stałym za pomocą eksperymentów optycznych. W pierwszej kolejności skupia się na eksperymentalnym badaniu zależnych od spinu oddziaływań długożyjących polarytonów w kondensacie o wysokiej gęstości, w którym właściwości polarytonów są determinowane przez polaryzację, anizotropię optyczną i zależne od polaryzacji oddziaływania. Praca bada kolektywne wzbudzenia kondensatu, na które wpływa nieabelowe efektywne pole cechowania, tworzone przez rozszczepienia polaryzacji. Praca przedstawia to efektywne pole z unikalną strukturą przypominającą monopole magnetyczne oraz punktami degeneracji w dyspersji stanów, a także przedstawia bezpośredni pomiar fundamentalnych stałych oddziaływań. Następnie, wykorzystując te same metody, odkrywa właściwości topologiczne i niehermitowskie polarytonów ekscytonowych, dla których nie oddziaływania, lecz dyssypacja przyczynia się do struktury efektywnego pola cechowania, przy jednoczesnym dużym wkładzie anizotropii optycznej. Praca przedstawia sparowane punkty wyjątkowe w przestrzeni pędu takiego systemu i wyznacza niehermitowski niezmiennik topologiczny, co stanowi pierwsze bezpośrednie pomiary

tej cechy. Następnie badany jest dalej wpływ dyssypacji, który prowadzi jednak do nietypowego efektu przyciągania stanów kwantowych. Aby go wyjaśnić, należy najpierw zrozumieć właściwości ekscytonów w układzie materiałowym AlGaAs. Na podstawie wyników eksperymentalnych praca identyfikuje oraz charakteryzuje trzy typy ekscytonów – jeden prosty i dwa skośne w pędzie oraz w przestrzeni – w badanym systemie studni kwantowych. Zrozumienie tego układu jest kluczowe dla zrozumienia nowych właściwości, gdy uwzględnione jest sprzężenie ekscytonów ze stanami fotonowymi. W pełnej mikrownęce polarytonowej praca dokumentuje odwróconą, anomalną dyspersję stanu polarytonowego, nierozerwalnie związaną z ujemną masą efektywną. Wyjaśnia podstawy tego efektu, wynikające z dyssypatywnego sprzężenia, tworzonego przez koherentne sprzężenie ze stanem dyssypatywnym. Praca wskazuje, że dyssypacja pochodzi z jednego ze skośnych stanów, scharakteryzowanych we wcześniejszej części pracy, i prezentuje nową metodę zmiany i kontroli krzywizny anomalnej dyspersji. Jest to pierwsza obserwacja anomalnej dyspersji w niestrukturyzowanym systemie polarytonowym opartym o studnie kwantowe.

Wszystkie wyniki rozprawy mają ważne implikacje dla dalszych badań i zastosowań. Zostały one opublikowane lub są w trakcie recenzji w międzynarodowych czasopismach naukowych.

Acknowledgements

Finalizing this work was quite an adventure. There were bushfires, hail storms, sand storms, heatwaves, a worldwide pandemic, and a flood at the very end. Regardless, I would not be in the place I am today without many important people, to whom I would like to deeply thank and to whom I am eternally grateful.

First and foremost - I would like to thank my supervisor, Marcin Syperek. My adventure with experimental physics started back in 2014, at the very first year of my undergraduate studies when I met him, and I have kept working with him since then - he was my mentor throughout my whole journey. Most importantly - thank you for caring. Thank you for being the boss, who really cares about his people - for the person, and not only for their results. Thank you for the support, regardless of the circumstances, I have always felt I could count on your advice or help. Thank you for forgiving me my weaknesses (and standing my stubbornness ;)). Thank you for being a scientist at heart, but also for all the small-talk chats at work.

Of course, I also thank my second supervisor, Maciej Pieczarka, who was my research mentor throughout the PhD Studies. Thank you hugely as you played a crucially important role, intrinsic to my research since the beginning of my PhD. With all seriousness, thanks for teaching me a lot, for all the invaluable discussions and ideas, as well as for the new possibilities. Thank you for throwing me in at the deep end sometimes :)

I would not meet Marcin and Maciej without prof. Krzysztof Ryczko, who was the first one who saw a potential in me and who made me fall in love with physics - who knows if I would follow this path without the first-year course with him. I also need to mention mgr. Zbigniew Lis, owing to whom I understood how mathematical my brain is, and who made me believe I could follow a scientific path. Thank you to both of you!

I want to thank Charles Whittaker - my supervisor during an internship in Sheffield, Eliezer Estrecho and prof. Elena Ostrovskaya - my supervisors from Canberra, and Dario Ballarini with Riccardo Panico - my supervisors from Lecce. From all of you I learned so much, and every minute during my internships was worth hundreds of hours elsewhere.

Thank you to all the people who deeply cared for me, both at the University and outside of it.

Finally, I would like to greatly thank my dear family. My Mum, who is the most important person in my life, and my older Brother, who cannot even ever imagine

how important he is to me. Thank you for your support and for your presence, I would not be the person I am today without you.

I would like to dedicate this thesis to my Dad, even if he has no idea why. And to my Grandma - yes, it is finally finished, you can stop asking :)

Finally, thank You, Dear Reader - thank you for your time, attention, and your cognitive energy, which are the most valuable resources of all.

List of publications

Publications included in this thesis:

- **D. Biegańska**, M. Pieczarka, E. Estrecho, M. Steger, D.W. Snoke, K. West, L.N. Pfeiffer, M. Syperek, A.G. Truscott, and E.A. Ostrovskaya, "Collective Excitations of Exciton-Polariton Condensates in a Synthetic Gauge Field", *Physical Review Letters*, 127, 1853012021 (2021) - PART II,

- R. Su, E. Estrecho, **D. Biegańska**, Y. Huang, M. Wurdack, M. Pieczarka, A. G. Truscott, T. C.H. Liew, E. A. Ostrovskaya, Q. Xiong, "Direct measurement of a non-Hermitian topological invariant in a hybrid light-matter system", *Science Advances*, 7, eabj8905 (2021) - PART III,

- **D. Biegańska**, M. Pieczarka, K. Ryczko, M. Kubisa, S. Klembt, S. Höfling, C. Schneider, and M. Syperek, "Optical properties and dynamics of direct and spatially and momentum indirect excitons in AlGaAs/AlAs quantum wells", *second stage of review*, preprint at: *arXiv:*2404.01938 (2024) - PART IV,

- **D. Biegańska**, M. Pieczarka, C. Schneider, S. Höfling, S. Klembt, and M. Syperek, "Anomalous dispersion via dissipative coupling in a quantum well exciton-polariton microcavity", *in review*, preprint at: *arXiv:*2404.14116 (2024) - PART V.

Publications not included in this thesis:

- M. Pieczarka, M. Syperek, **D. Biegańska**, C. Gilfert, E. M. Pavelescu, J. P. Reithmaier, J. Misiewicz and G. Sęk, "Lateral carrier diffusion in InGaAs/-GaAs coupled quantum dot-quantum well system", *Applied Physics Letters*, 110, 221104 (2017),

- W. Rudno-Rudziński, **D. Biegańska**, J. Misiewicz, F. Lelarge, B. Rousseau and G. Sęk, "Carrier diffusion as a measure of carrier/exciton transfer rate in InAs/InGaAsP/InP hybrid quantum dot–quantum well structures emitting at telecom spectral range", *Applied Physics Letters*, 112, 51103 (2018),

- C. E. Whittaker, D. R. Gulevich, **D. Biegańska**, B. Royall, E. Clarke, M. S. Skolnick, I. A. Shelykh, and D. N. Krizhanovskii, "Optical and magnetic control

of orbital flat bands in a polariton Lieb lattice", *Physical Review A* 104, 063505 (2021),

- M. Pieczarka, **D. Biegańska**, C. Schneider, S. Höfling, S. Klembt, G. Sęk, and M. Syperek, "Crossover from exciton-polariton condensation to photon lasing in an optical trap", *Optics Express* 30, 17070-17079 (2022),

- J. Kutrowska-Girzycka, E. Zięba-Ostój, **D. Biegańska**, M. Florian, A. Steinhoff, E. Rogowicz, P. Mrowiński, K. Watanabe, T. Taniguchi, C. Gies, S. Tongay, C. Schneider and M. Syperek, "Exploring the effect of dielectric screening on neutral and charged-exciton properties in monolayer and bilayer $MoTe_2$", *Applied Physics Reviews* 9, 041410 (2022).

Preface

Since the first observation of exciton polaritons, there has been a growing interest in their studies, due to their fascinating properties and large application potential. These quasiparticles are often referred to as "part-light, part-matter" or even "interacting photons", what truthfully shows their complex and unique nature. Exciton polaritons arise from the strong coupling between photons and excitons and represent a quantum superposition of these two states. As complex bosons, they undergo a number of collective-coherence phenomena, such as Bose-Einstein condensation, parametric scattering, and superfluidity, what since the early days has sparked a huge interest in the field. As mixed particles, they inherit properties of both the excitons and the photons, merging the best of the two worlds, what makes them a superb experimental platform to study. Easy optical access to quantum observables such as phase, spin degree of freedom or momentum, combined with a low particle mass and with the possibility of high condensation temperatures, fuelled the research on those quasiparticles in many interest areas and topics.

However, despite years of research, there is still a need to understand some of the exciton polariton properties, with several milestone observations still ahead. With time, whole new fields have emerged, in which the use of polaritons can be beneficial or crucial, such as studies of analogue systems, complex non-Hermitian and topological phenomena, quantum computing, or neural networks with machine learning technologies. The properties of both the exciton polaritons and their condensates in these new contexts, new designs or in new material platforms still need to be studied.

This thesis focuses on several key aspects of the properties of exciton polaritons and their condensates. It explores novel characteristics, which have not been addressed before. Based on optical experiments, it dives into new features of polaritons, in novel contexts, crucial from a future research and applications point of view. In particular, it addresses:

- Polarization and fundamental properties of high density exciton-polariton condensates in the interaction-dominated Thomas-Fermi regime, related to their spin degree of freedom and with relation to the gauge-field emergence, unevidenced before,

- Fundamental study of polariton-polariton interaction strength, with spin resolution,

- Non-hermitian properties and the implications of the polariton's non-Hermiticity on the effective spin gauge filed, with crucial implications in topology,
- Dissipation role and the influence of a dissipative coupling on the polariton dispersion, including level attraction and an anomalous shape of the dispersion in an exciton-polariton microcavity,
- Crucial structure characteristics, necessary to achieve condensation and lasing in increased temperatures with the use of III-V based semiconductors.

The thesis is centred around AlGaAs-based semiconductor microcavities – a standard III-V semiconductor material platform, well known and studied since the very beginning of the polariton research. However, it re-discovers this material in the novel contexts. Dissipative coupling, non-hermiticity, gauge fields, topology, effective mass engineering for analogue systems, as well as the still-remaining holy grail of room temperature condensation in a III-V based system - all addressed in this thesis - are only a few examples of these contexts, remaining at the forefront of today's research. Moreover, recent years showed growing interest in the use of novel materials (like transition metal dichalcogenide monolayers or perovskites, among others) as an active medium in the exciton-polariton research, yet there is still a need for a deeper understanding of the well-known platform, which often proves to have a big advantage over the newer designs. III-V based systems are superb when compared to those emerging materials in reproducibility, ease of design and engineering, control during growth, in linewidths, quality and stability, to mention just a few – all crucially important in the novel phenomena studies or applications.

One part of the thesis differs from the others in the use of a novel material - a perovskite crystal - as an active medium, but the experimental methods are the same as in other parts. The studied phenomenon also importantly connects to the other parts, as it addresses the polarization, non-Hermitian, and fundamental polariton properties. The characteristics of the novel material increase the size of the effects studied.

The thesis first addresses an ultra-high quality microcavity with GaAs quantum wells, characterized by long polariton lifetimes, allowing for the study of fundamental properties of polariton condensates in a high density interaction-dominated Thomas-Fermi regime. It studies the polarization properties of collective (elementary) excitations of such a condensate, governed by their spinor properties. It serves as a first experimental observation of the fundamental excitations dispersion anisotropy, and measures the polariton-polariton interactions. It explores also the inherent gaugue field present in the system, studied by a direct measurement of the spin texture in an interacting spinor condensate.

Then the gauge field is studied in a perovskite crystal-based microcavity, with no polariton-polariton interactions, but with an important role of inherent polariton non-Hermiticity and with significant structural anisotropy. The study evidences the stark effect of polariton non-Hermiticity on topology. Importantly, it serves as the

first direct measurement of a non-Hermitian topological invariant in a hybrid light-matter system. It presents the effective gauge field with an imaginary component and looks at the topologically non-trivial, paired exceptional points in the effective spin field.

Then the thesis focus shifts to the AlGaAs-based microcavity, initially designed for room-temperature coupling and lasing. It carefully investigates another novel finding and a property, related to the inherent dissipation present in the structure and to the particle's negative effective mass. It shows and serves as the first experimental observation of the anomalous dispersion shape in an exciton-polariton microcavity with quantum well excitons as an active medium. Most importantly, it addresses the basis of this unexpected observation, with the dissipative coupling via a dissipative mode serving as the phenomenon's mechanism.

However, in order to offer this explanation, more basic properties of the structure need to be addressed first, with careful characterization of the underlying quantum well system. The thesis studies optical and temporal properties of the excitonic resonances present in the high Al-content AlGaAs quantum wells, discovering the presence of both a direct and two momentum- and space-indirect excitons. It characterizes all three species in a wide range of densities and temperatures, which is vital for the system's understanding under additional coupling with photons.

Finally, in order to report all these observations, the Results part is preceded by a conceptual Introduction, acquainting with the topic of exciton polaritons and their condensates. The Introduction focuses on several of the polariton's key properties - pivotal especially in the context of the results presented later. Each study in the Results section is additionally initiated with a specific introduction to the exact topic, with references to the fundamental facts stated in the Introduction and to the prior research in this field.

Hence, the thesis is structured as follows:

PART I - Introduction is a general introduction into the topic of exciton polaritons. It is divided into two main introductory chapters: first it addresses key properties of these quasiparticles in a single-particle (low density) limit in **Chapter 1**. It focuses on the properties important in the studies reported later in the Results parts. Then, **Chapter 2** focuses on the high-density properties of polaritons, introducing the topic of Bose-Einstein condensation and polaritonic condensation, similarly with implications in the Results parts. They are ended with an Outlook in **Chapter 3**. **Chapter 4** describes key Methods used, shared by all the Results.

Then, the thesis moves to the Results parts, divided into four main studies:

PART II - Collective excitations of exciton-polariton condensates in a synthetic gauge field addresses the fundamental properties of high-density exciton-polariton condensates, with the focus on the polarization, and investigates the topic of collective excitations of exciton-polariton condensates in a

synthetic gauge field. It explores the excitation spectrum anisotropy and the spin-anisotropy of polariton-polariton interactions.

PART III - Direct measurement of a non-Hermitian topological invariant in a hybrid light-matter system addresses the first experimental observation of the non-Hermitian invariant in an exciton-polariton system, implied by the dissipation and the optical anisotropy, which influence the effective gauge field, evidenced in polarization-resolved experiments. It uses a perovskite crystal as an active medium.

PART IV - Optical properties and dynamics of direct and spatially and momentum indirect excitons in AlGaAs/AlAs quantum wells serves as a crucial characterization of the AlGaAs/AlAs quantum well system, later used in Part V. It characterizes the direct and the momentum- and spatially-indirect excitons, exploring their temporal, temperature and density-dependent properties, uncovering the excitons' origin and studying their recombination dynamics. The results are essential in understanding the further results in the polariton microcavity, but also have important implications in potential applications.

PART V - Anomalous dispersion via dissipative coupling in a quantum well exciton-polariton microcavity describes an unexpected observation of an anomalous dispersion in a quantum-well polariton microcavity, linked to a negative effective mass. It addresses the influence of dissipation and explores the result of the aforementioned presence of indirect excitons on the polaritonic states.

The two first studies have been done in collaboration with the Polariton BEC Research Group at the Research School of Physics, the Australian National University, led by Prof. Elena Ostrovskaya. The experiments have been conducted during my research stay in Canberra during the first academic year of my Doctoral Studies, followed by the collaboration with the group. The rest of the presented experiments were performed at the Wrocław University of Science and Technology, the home institution, in a Nonlinear Quantum Photonics group led by Prof. Marcin Syperek at the Department of Experimental Physics.

Each of the Results parts is structured as follows: first, the exact topic is introduced in the **Introduction** section. Then the **Contributions** statement is made, directly stating my role in the reported studies, which are a collaborative work. They are followed by the **Results**, presenting published works. If necessary, the results are supported by **Supplementary Materials**. Each part is finished with a **Summary of the findings**.

The thesis is ended with a **Summary and Conclusion** of all the results.

This **Preface** serves as the introduction to this very thesis and to its structure.

Wrocław,
September 2024

Dąbrówka Biegańska

"This is a story of how a Baggins had an adventure,
and found himself doing and saying things altogether unexpected."

J.R.R. Tolkien

Contents

Part I

Introduction

CHAPTER 1

Exciton polaritons

1.1 Basic concepts

1.1.1 Excitons in semiconductor nanostructures

Excitons are quasiparticle states of electrons and holes, bound together via Coulomb interactions [1,2]. They are elementary excitations of a direct bandgap crystal and are the most widely studied in the context of semiconductor materials. These composite entities can be seen as being similar to atoms, featuring an electron and a positively charged hole, bound together by the electromagnetic force, in analogy to how electrons are held in orbit around atomic nuclei. They transport energy, but they don't transfer net electric charge, and as complex quasiparticles of two fermions they prove to have bosonic character [3].

The study of excitons spans a wide range of materials. Semiconductors form an important class of materials where the study of these excitations becomes particularly relevant. In semiconductors - materials with an energy bandgap - the electrons occupying energy levels within the valence band can absorb energy from an external source (e.g. photons from an incident light), and be relocated to the conduction band, leaving behind an empty state, known as a hole. When subsequently bound together by the Coulomb interaction, this process creates an exciton – a bound electron-hole pair with opposite charges. Its energy is typically below the semiconductor bandgap. The probability of the particle binding can be enhanced e.g. by localization of both electrons and holes.

Excitons typically can be well described by a hydrogen atomic model, with the lowest state resembling $1s$ orbital and a center of mass moving freely [1]. Their overall position and movement can be described by the movement of the center of mass. The state's kinetic energy can be then approximated as:

$$E_X = \frac{\hbar^2 \mathbf{K}^2}{2m_X}, \tag{1.1}$$

with m_X being the total excitons mass, consisting of electron and hole effective masses: $m_X = m_e + m_h$. $\mathbf{K}$ is a full exciton wavevector [1].

Furthermore, excitons are characterized by their binding energy, which is the energy required to separate the electron and the hole, thereby dissociating the exciton.

In the simple approach of a hydrogen model it can be approximated by the Rydberg energy [1, 4]:

$$E_B = Ry^* = \frac{\mu e^4}{2\epsilon^2\hbar^2} = \frac{e^2}{2\epsilon a_B}, \tag{1.2}$$

where μ is the reduced effective mass of an exciton, $\frac{1}{\mu} = \frac{1}{m_e} + \frac{1}{m_h}$. This definition introduces an exciton's Bohr radius, a_B, in direct analogy to the hydrogen model:

$$a_B = \frac{\epsilon\hbar^2}{\mu e^2}. \tag{1.3}$$

ϵ describes the electrical permittivity of the medium. In semiconductors this binding energy typically ranges from a few meV to a few tens of meV in a bulk material [1], widely differing across different materials. However, the binding energy can be influenced, e.g. by localization of electrons and holes, imposed by a structure design.

The latter fact is one of the important reasons why excitons are widely studied in the context of semiconductor nanostructures. The reduced-dimensionality systems, such as quantum wells (QWs), quantum dots, or nanowires confine the motion of electrons and holes in one or several dimensions, and impose quantization constraints on their motion, leading to discrete energy levels and modified density of states (DOS) [1, 5]. In QWs, thin semiconductor layers are sandwiched between two barriers, and the nanometre size of the layers restrict the motion of electrons and holes to a single plane. The subsequent discrete nature of the particle energy levels allows for precise control of the electron and hole energies, while reduced dimensionality increases the Coulomb interaction strength. This leads to an up to fourfold increase in exciton binding energy, compared to the bulk material [6–9], due to the shrinkage of the exciton's Bohr radius a_B.

In high-quality QWs, with excitons described by the hydrogen atomic model, the exciton's center of mass moves freely in the plane of the QW. The energy-momentum dispersion of these states may be then approximated by a kinetic energy of a free particle in a 2D plane, with quadratic dependence on the in-plane wavevector $k_\parallel$ (perpendicular to the growth direction of the QW) [1, 4]:

$$E_X(k) \approx E_X\left(k_\parallel = 0\right) + \frac{\hbar^2 k_\parallel^2}{2m_X}. \tag{1.4}$$

Additionally, imposing constraints on the particle movement by creating a nanostructure enhances exciton radiative recombination rates, making them efficient sources of light [7–9]. This also comes from the shrinkage of the exciton's Bohr radius - what increases the oscillator strength and the binding energy. Combined with the advantage of a big control over the exciton properties by adjusting the well's thickness and composition, this enables QW exciton's use in a wide range of applications, mostly in optoelectronic and photonic devices, such as lasers, detectors or modulators. Moreover, the ability to control exciton properties in QWs has led to the exploration of light-matter interactions and studies on novel quantum phenomena, such as in the area of exciton-polaritons, subject at the core of this thesis.

1.1.2 Photons in semiconductor microcavities

Photons are massless bosonic particles when moving freely. However, they can also become confined in space, e.g. by locating them in optical cavities. When inside an optical resonator, such as a Fabry-Perot cavity (light confinement between two mirrors), the electromagnetic modes become quantized, leading to well-defined energy levels for photons, in analogy to the quantized electron states [2]. The spatial distribution of these standing wave patterns depends on the specific geometry of the cavity.

Various cavity designs and types can by used, ranging from typical aforementioned Fabry-Perot cavities, through photonic crystal slabs, whispery gallery mode cavities, up to sophisticated custom designs, confining photons in different dimensions [2, 10]. In exciton-polariton research the 2D planar microcavities are most notoriously used, with photons confined in one of the dimensions between two reflectors, as the samples are typically produced as layered structures. In plane photons can propagate freely.

Eigenmodes of such a Fabry-Perot cavity are standing waves, which wavelength is directly related to the size of the resonator. Most generally, this condition is met for waves with wavelength λ_0 such that:

$$2n_C d_C = m\lambda_0, \tag{1.5}$$

where n_C and d_C are the refractive index and the width of the cavity respectively, and m are natural numbers $m = 1, 2, 3 \ldots$.

The reflecting surfaces can be made in a number of ways, starting from simple metallic mirrors. Within the semiconductor context the distributed Bragg reflectors (DBRs) are very often used as mirrors, since they can provide near unity reflectivity and can be monolitically integrated with the active region. DBR's include a number of repeated layers with alternating refractive indices, designed to create a constructive interference effect for waves reflected from many interfaces, what increases the overall reflection. A visualization of such a reflector is presented in Fig. 1.1 (a). Thicknesses of these layers need to satisfy the condition of constructive interference for backpropagating waves and destructive interference of the light passing through. In most typical case of two alternating materials this condition is met when:

$$n_1 d_1 = n_2 d_2 = \lambda_0/4, \tag{1.6}$$

where n_1 and n_2 are the refractive indices of the neighbouring layers, d_1 and d_2 are their respective widths and λ_0 is the central reflected wavelength.

Adding an additional spacer between two distributed mirrors creates a full cavity structure, with a schematic visualisation of such a design presented in Fig. 1.1 (b). It can be considered as a 1D photonic crystal with a central defect. Designing the layers' thicknesses, as well as adequately choosing materials and the number of pairs, allows for the confinement of light in a certain spectral range (called a stop-band, around a central wavelength following the Bragg condition (eq. 1.6)), but also affects the cavity quality and photon leakage. The confined standing wave - the cavity

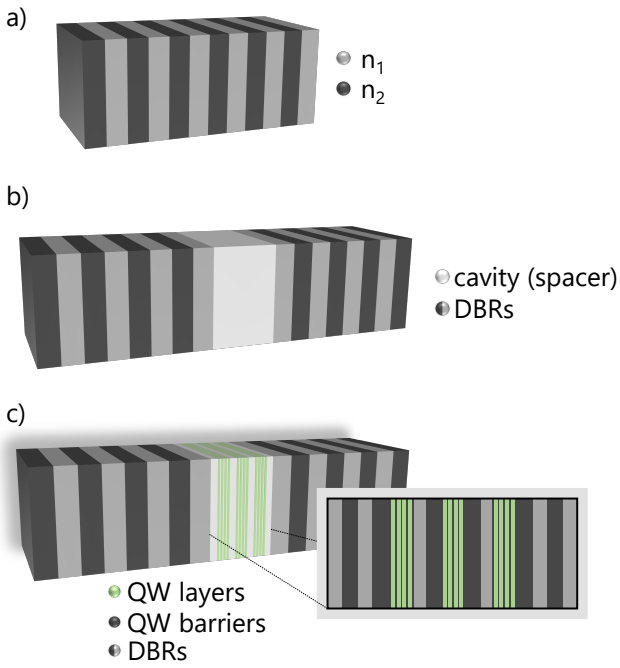

Figure 1.1. Schematic visualisation of the microcavity structure. (a) A single distributed Bragg reflector (DBR), formed from alternating layers of two materials with different refractive indices, n_1 and n_2. (b) Two DBRs with a spacer layer between them, forming a full optical microcavity. (c) Typical polariton microcavity structure, with quantum wells (QWs) embedded inside the cavity, overlapping with the maxima of the electromagnetic standing wave confined within the cavity. QWs can be replaced by other active layers, such as layered semiconductors or perovskite crystals, to act as an active medium providing excitons. In the pictured example multiple QWs are embedded (three stacks of four QWs), a design that is often used in monolithic structures to increase the exciton-photon coupling.

(photonic) mode with the wavelength λ_0 - is visible in the reflectivity spectrum as a sharp dip, even within the photonic stopband [2]. To confine light in the visible or close to the visible spectrum, the required DBR layer thicknesses are typically on the order of tens of microns, depending on the materials used. The increase of the number of pairs increases the overall reflection. The cavity layer is typically on the order of a photon wavelength.

Confinement of photons leads to a strong enhancement of the light intensity inside the cavity (of the resonant energy), with the oscillating decay inside the DBR mirrors. As the photons cannot propagate freely, their energy dispersion relation is modified. It can be approximated with a parabola for small in-plane momenta (wavevectors, $k_{\parallel}$), effectively making photons act as massive particles:

$$E_C(k) = \frac{\hbar c}{n_c}\sqrt{k_{\perp}^2 + k_{\parallel}^2} \approx E_C\left(k_{\parallel} = 0\right) + \frac{\hbar^2 k_{\parallel}^2}{2m_C}, \tag{1.7}$$

thus, introducing the concept of photon effective mass:

$$m_C = \frac{E_C\left(k_{\parallel} = 0\right)}{\frac{c^2}{n_c^2}} = \frac{hn_c}{cL_c}. \tag{1.8}$$

Here the effective mass of a cavity mode m_C clearly depends on the cavity refractive index n_c and an effective cavity length L_c (a sum of the physical cavity length L and the depth of the light penetration into the mirrors $L_c = L + \frac{\lambda_0}{2n_c}\frac{n_1 n_2}{|n_1 - n_2|}$). The mass is approximately four to five orders of magnitude smaller than an exciton's mass [2, 11–14].

Moreover, all microcavities can be characterized by their quality factor (Q-factor), defined as the ratio of the resonant cavity frequency to the linewidth (FWHM) of the cavity mode, quantifying the rate photon of leakage from the cavity [2, 15]. It is a measure of the cavity losses (photons escaped from the microcavity), and the typical planar microcavity Q-factor values range from 10^2 to 10^4. The higher the quality factor, the fewer photons are lost and the longer are the cavity photon lifetimes. Q strongly depends on the material system used and on the exact cavity geometry and design. The best quality factors in planar microcavities are typically observed in monolithic, DBR-based microcavities created with well developed III-V semiconductor based materials [10, 16, 17].

Apart from monolithic structures with DBRs, various cavity designs can be used, yet the concept of the light confinement remains core. Regardless of the exact design, the spatial confinement of photons serves as a basis for a wide range of applications, such as optoelectronic devices, efficient light sources or quantum information processing. The ease of cavity engineering and design enable huge mode tunability, further enhancing the confined photons application potential.

1.1.3 Strong coupling

Placing excitons and photons in the same space allows for the consideration of how they interact. Their confinement in a single structure leads to the enhanced light-matter interactions, hence it is often employed in studies on quantum electrodynamics [2]. In the most typical planar microcavity structures, one or more QWs are incorporated into the cavity layer, parallel to the cavity's plane. Such a design is schematically presented in Fig. 1.1 (c). The excitons confined in the QWs interact with the cavity photons, which lifetime is prolonged in the optical resonator. To achieve strong interaction between the excitons and photons, QWs are typically positioned at the antinodes of the cavity field, where its intensity exhibits maximum [2,18]. Additionally, the cavity mode's frequency and the QW exciton frequency need to be matched close to resonance to create conditions favourable for their coupling. High oscillator strength of the implemented QW and high quality of the microcavity further enhance the coupling between the photonic and the excitonic states [18].

Depending on the constituent particle energy and decay (accounting for the losses) one can distinguish either a weak coupling or a strong coupling regime between the two particles. Weak coupling leads to the enhancement of a spontaneous emission rate (faster emission of light from the cavity) - the so-called Purcell effect [2, 19]. The coupling stronger than the losses leads to creation of new states, the exciton polaritons.

Due to the light propagation, photon absorption and the exciton's radiative emission, the energy can be exchanged between confined QW excitons and microcavity photons. With sufficient coupling of the two (under the strong coupling conditions) the energy is continuously transferred back and forth between the two particles. In direct analogy to other strongly interacting systems, this transfer results in a characteristic Rabi oscillations in the time domain, accompanied by a normal mode splitting of the emerging states [2, 11–13, 20]. One can view it as an emergence of a new, complex quasiparticle, no longer distinguishable as a single excitonic or a photonic state - the so-called exciton polariton.

The mixed exciton-photon system results in creation of two eigenstates, the two branches of a polariton spectrum: a lower polariton (LP) and an upper polariton (UP). Their dispersions may be easily approximated, using a semi-classical model of two damped coupled oscillators (a photon and an exciton), but also in the quantum second quantization description, with bosonic creation and annihilation operators for photons and excitons. The former approach leads to a definition of a simple intuitive Hamiltonian:

$$H = \begin{pmatrix} E_C(\vec{k}) & V \\ V & E_X(\vec{k}) \end{pmatrix}, \tag{1.9}$$

where E_C and E_X are the cavity photon and exciton energies, and V quantifies their interaction strength (coupling).

In the latter, second quantization description approach, the analogous Hamilto-

nian can be written as:

$$H = \begin{pmatrix} \hat{a}_{\vec{k}}^{\dagger} & \hat{b}_{\vec{k}}^{\dagger} \end{pmatrix} \begin{pmatrix} E_C(\vec{k}) & \frac{\Omega}{2} \\ \frac{\Omega}{2} & E_X(\vec{k}) \end{pmatrix} \begin{pmatrix} \hat{a}_{\vec{k}} \\ \hat{b}_{\vec{k}} \end{pmatrix}, \tag{1.10}$$

where $\hat{a}_{\vec{k}}^{\dagger}$, $\hat{a}_{\vec{k}}$ and $\hat{b}_{\vec{k}}^{\dagger}$, $\hat{b}_{\vec{k}}$ are the creation and annihilation operators for photons and excitons with the wavevector $\vec{k}$, and the energies E_C and E_X respectively. Ω quantifies the particle coupling. Both the semi-classical and the full quantum theory frameworks give equivalent results.

As in planar samples the system is quantized in one direction (typically denoted as z) and photons and excitons are free to propagate in plane, the full wavevector $\vec{k} = (k_x,\ k_y,\ k_z)$ can be simplified to the in-plane and the perpendicular directions, $\vec{k} = \left(k_{\parallel}\ ,\ k_{\perp}\right)$, $k_{\parallel}\ = k_x^2 + k_y^2$, $k_{\perp} = k_z$. Moreover, as the photonic and excitonic dispersions can be approximated by quadratic dependencies with respect to the in-plane wavevector (for small k), as described in previous sections, $k_{\parallel} = k$ will be further used for simplicity of notation. Importantly, being one of the wavector projections, the in-plane wavevector is directly linked to the angle of incidence of light illuminating or being emitted from the structure θ (angle from the direction perpendicular to the sample surface), $k \propto sin\theta$. This allows for a direct measurement of the state dispersions in angle-resolved experiments, as will be showed in further sections.

As introduced in two previous sections, confinement of photons and excitons leads to their approximately parabolic energy-momentum dispersions, within the effective mass framework,

$$E_X\left(k\right) = E_{X0} + \frac{\hbar^2 k^2}{2m_X} \tag{1.11}$$

and

$$E_C\left(k\right) = E_{C0} + \frac{\hbar^2 k^2}{2m_c}, \tag{1.12}$$

where m_X is the total exciton mass and m_C is the effective mass of the cavity photon (eq. 1.8). Detuning between these two states is defined as:

$$\Delta(k) = E_C(k) - E_X(k). \tag{1.13}$$

When they couple (Hamiltonians 1.9 and 1.10), the resulting state dispersions of the lower and the upper polariton branches become non-parabolic, with the wavevector dependence calculated as:

$$E_{\substack{UP \\ LP}}(k) = \frac{1}{2}\left[E_X(k) + E_C(k) \pm \sqrt{\left(\hbar\Omega\right)^2 + \left(E_X(k) - E_C(k)\right)^2}\right]. \tag{1.14}$$

An example of such a dispersion is presented in Fig. 1.2. Solid green lines in Fig. 1.2 (a), (b) and (c) show the energy-momentum dependencies of eigenstates derived

with formula 1.14, with three different exciton-photon detunings $\Delta_0 = E_{C0} - E_{X0}$. Dashed lines present the dispersions of the uncoupled constituents - the cavity photon (blue) and the exciton (red). Due to the exciton's effective mass being much higher than that of the cavity photon $m_X \gg m_c$, the exciton energy can be approximated as nearly dispersionless. One can clearly see the final state repulsion, with characteristic avoided crossing of the polariton branches at resonance, and the deviation from the parabolic curve (especially at larger momenta). The avoided crossing is typical in strongly-interacting systems. When the interaction is not strong enough to overcome the dissipation, the modes cross (in the weak coupling regime or when uncoupled) and exciton polaritons are not formed.

Additionally, the inherent decay (lifetime) of both underlying quasiparticles should be taken into account, as the QW excitons recombine and the confined photons eventually leak from the cavity. This makes exciton polaritons a naturally dissipative system. As it is often done in open systems, the dissipation rates can be included as imaginary parts of the branch complex energy [21, 22]. One can then rewrite the energies as:

$$E_C{}' = E_C - i\gamma_C, \tag{1.15}$$

$$E_X{}' = E_C - i\gamma_X, \tag{1.16}$$

where γ_X and γ_C are the exciton and photon decay rates (inverse lifetimes) respectively.

Their incorporation into the same model finally yields:

$$E_{\substack{UP \\ LP}}{}' = \frac{1}{2}\left[E_X + E_C + i(\gamma_X + \gamma_C) \pm \sqrt{(\hbar\Omega)^2 + (E_X + \gamma_X - E_C - \gamma_C)^2}\right]. \tag{1.17}$$

In the formulas above Ω is the so-called Rabi frequency, which quantifies the particle coupling. It is envisioned as the splitting between the upper and lower branches when on resonance, called Rabi splitting $\hbar\Omega$. The Rabi frequency physically represents a dipole interaction strength [11, 13]. It is proportional to:

$$\Omega \propto \sqrt{\frac{f_{osc} N_{QW}}{L_c}}, \tag{1.18}$$

where N_{QW} is the number of QWs and f_{osc} is the exciton oscillator strength. The condition for the strong coupling is satisfied when:

$$\hbar\Omega > \gamma_X + \gamma_C, \tag{1.19}$$

meaning that the interaction needs to be higher than the losses. As one can clearly see from these conditions, the material parameters and the structure quality are crucial in the strength of exciton-photon coupling and an achievement of the strong coupling regime, as they influence both the oscillator strength and the lifetimes.

Moreover, polaritons are complex entities, inheriting their characteristics from the photonic and excitonic components. The exciton and photon contributions can be

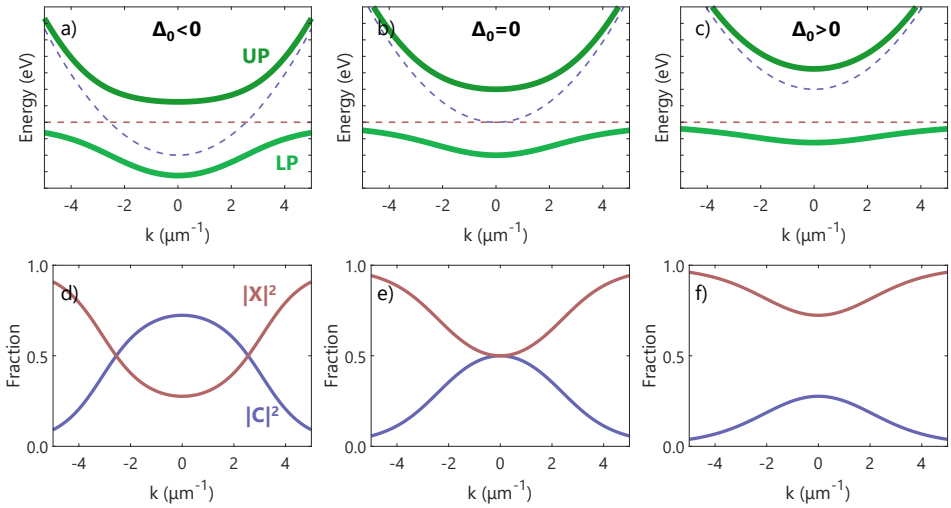

Figure 1.2. Polariton state dispersions. (a-c) Examples of a lower (LP) and an upper (UP) polariton branch dispersions (solid green lines) at three different exciton-photon detunings $\Delta_0 = E_{C0} - E_{X0}$: (a) $\Delta_0 < 0$ (a "photonic" detuning), (b) $\Delta_0 = 0$, (c) $\Delta_0 > 0$ (an "excitonic" detuning). The bare exciton (red) and bare microcavity photon (blue) dispersions are plotted with dashed lines. (d-f) Hopfield coefficients of the corresponding polariton dispersions. Red (blue) lines show the excitonic (photonic) Hopfield coefficient of the lower polariton branch $|X|^2$ ($|C|^2$).

quantified by the so-called Hopfield coefficients. These determine the exciton (X) and the photon (C) fraction in a lower polariton and can be defined as:

$$|X|^2 = \frac{1}{2}\left[1 + \frac{E_C - E_X}{\sqrt{(\hbar\Omega)^2 + (E_C - E_X)^2}}\right] = \frac{1}{2}\left[1 + \frac{\Delta(k)}{\sqrt{(\hbar\Omega)^2 + \Delta(k)^2}}\right], \tag{1.20}$$

$$|C|^2 = \frac{1}{2}\left[1 - \frac{E_C - E_X}{\sqrt{(\hbar\Omega)^2 + (E_C - E_X)^2}}\right] = \frac{1}{2}\left[1 - \frac{\Delta(k)}{\sqrt{(\hbar\Omega)^2 + \Delta(k)^2}}\right]. \tag{1.21}$$

The coefficients always satisfy a condition:

$$|X(k)|^2 + |C(k)|^2 = 1. \tag{1.22}$$

Their wavevector dependencies are presented in Fig. 1.2 (d-f), showing how the photonic and excitonic fractions change as a function of the momentum. The examples are plotted at different initial exciton-photon detunings (with corresponding eigenstate dispersions presented in Fig. 1.2 (a-c)).

The Hopfield coefficients significantly simplify the polariton description. With their use, polariton effective masses or lifetimes can be simply calculated from the initial state (photon and exciton) parameters with the Hopfield fractions used as weights, as is described in sections 1.2.4 and 1.2.5. Mathematically, Hopfield coefficients can be calculated as the Hamiltonian eigenvectors, showing the contribution of each basal state to the final eigenvalue.

1.2 Key properties

Previous section introduced the concept of the strong coupling between excitons and photons confined in optical microcavities and the emergence of new quasiparticles - exciton polaritons (which will be also called polaritons further on for simplicity). It introduced their unique dispersion relation, clearly deviating from the quasi-parabolic cavity photon modes. This section will discuss polaritons' key characteristics, emerging as a unique mixture of the photonic and excitonic properties.

1.2.1 Polariton spin

Polaritons possess a spin degree of freedom, stemming from optically active excitons coupled to photons. Typically, in QWs composed of the zinc-blend semiconductors (such as many III-V semiconductors, e.g. GaAs) the excitons can have spin projections of either ± 1 or ± 2, what is directly related to the exciton formation from conduction band electrons (with spin of $\pm 1/2$) with either heavy-hole ($\pm 3/2$) or light-hole ($\pm 1/2$) states in a semiconductor [1]. Since photons can carry only a spin angular momentum of $s = \pm 1$ (corresponding to the two circular polarization states), only the $j = \pm 1$ excitons couple to light. The $j = \pm 2$ states cannot be coupled to photons, hence are often referred to as dark excitons. Effectively, only bright excitons form polaritons. The influence of the dark exciton presence on the polariton coupling has recently gained interest [23, 24], but its discussion is beyond the scope of this thesis. Hence, polariton spin has two allowed integer projections on the cavity growth axis, effectively making polaritons a two-component (spinor) system, described by a pseudospin parameter [25].

It is important to note, that as the photonic component carries the spin angular momentum of the whole quasiparticle, one can directly measure the polariton spin by measuring the polarization of light escaping the microcavity. The pseudospin (or the polarization) degree of freedom can be very conveniently described by a so-called Stokes vector and represented on the Poincaré sphere [25, 26], presented in Fig. 1.3. In this formalism, the polarization (hence also the pseudospin) is described by a

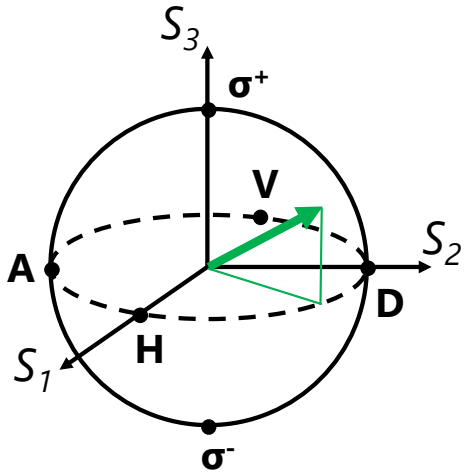

Figure 1.3. The Poincaré sphere, allowing a simple visualization of the last three Stokes' parameters, with their easy parametrization into spherical coordinates. An exemplary polarization state is shown with a green arrow.

four-component vector **S**:

$$\mathbf{S} = \begin{pmatrix} S_0 \\ S_1 \\ S_2 \\ S_3 \end{pmatrix}. \tag{1.23}$$

S_0 is the total light intensity, S_1 is the degree of linear polarization in the vertical (V) and horizontal (H) polarization basis $S_1 = \frac{I_H - I_V}{I_H + I_V}$, S_2 is the degree of linear polarization in the diagonal (D) and anti-diagonal (A) polarization basis $S_2 = \frac{I_D - I_A}{I_D + I_A}$, and S_3 describes the degree of polarization in the circular (left-circular σ^- or right-circular σ^+) polarization basis $S_3 = \frac{I_{\sigma^+} - I_{\sigma^-}}{I_{\sigma^+} + I_{\sigma^-}}$, while I is the intensity of the polarized light. H and V is a basis of two perpendicular linear polarizations, while D is the $+45°$ and A is the $-45°$ (with respect to the H/V axes) linear polarizations [27, 28].

A visualization of the Stokes vector on a Poincaré sphere is presented in Fig. 1.3 as a green arrow. Such a representation simplifies the description of the polarization state. On the sphere, points on the equator correspond to linearly polarized light, points at the poles represent circularly polarized light, and points on the rest of the sphere indicate other elliptical polarization states. Shorter vectors represent not fully polarized states. Three of the Stokes parameters ($S1$, $S2$, $S3$) correspond to the state's Cartesian coordinates.

Plotting the pseudospin vector in 3D allows for visualizing the pseudospin distribution in space or in momentum. Such a distribution is characteristic of the structure in question and can be described as the pseudospin rotation in the effective gauge field, as expanded in further subsections.

1.2.2 TE-TM splitting

When considering the polariton spin degree of freedom and the polarization of light in a cavity, the effect of the TE-TM splitting (or longitudinal-transverse splitting) needs to be introduced. In optical microcavities one can observe the energy splitting between transverse-electric (TE) and transverse-magnetic (TM) polarized modes in the dispersion for oblique angles - the effect known for polaritons, but also for purely photonic structures [2,25,29]. For polaritons, the effect arises from three contributing effects: (i) angle- and polarization-dependent phase delay upon reflection of light from the DBR layers ($\Delta\phi_{TM} = \Delta\phi_{TE} n_{21}/n_{22}$) - a purely photonic effect, (ii) the wavevector dependence of the long-range exciton exchange interaction and (iii) the difference in wavevector dependence of exciton oscillator strength for TE and TM modes [25,26,29]. The first of the listed effects is much larger than the latter two, and is intrinsic to a microcavity, hence it is often the only one taken under consideration. One can view it as a different effective length of the cavity for the TE and TM modes.

TE-TM splitting manifests in the polariton branch dispersion as a different curvature of the two linearly polarized branches, making the polariton effective masses different for the TE and TM polarized modes (typically $m_{TM} < m_{TE}$). An example of such a dispersion is presented in Fig. 1.4 (a-b). The two modes are represented by solid red and blue lines. The splitting between them is presented in (c-d) with a green dashed line as a function of the in-plane wavevector in two perpendicular directions (in-plane of the cavity, denoted as k_x and k_y).

In the effective mass approximation, at small in-plane wavevectors k (at small angles of incidence), the splitting between the TE and the TM modes increases with k (regardless of the direction), following a quadratic dependence. Its overall angle-dependence is non-monotonic - in an empty cavity (a purely photonic case) it increases like $sin^2(\theta)$, where θ is the angle of incidence (angle from the direction perpendicular to the sample surface), but depends on the mode energy. The TM mode can be higher or lower in energy, depending on the the detuning between the cavity mode from a central wavelength of the DBR stopband. [29].

The dependence in polariton microcavities is further affected by the wavevector dependence of the Hopfield coefficients (described in section 1.1.3). Since both the photonic and excitonic components are contributing to the overall splitting, its value also depends on the exciton-photon detuning. As mentioned, because of the photonic contribution, the splitting's magnitude is sensitive to the central wavelength of the DBR stopband and the detuning of the cavity mode from a central frequency. The impact of this photonic contribution and the weaker excitonic effects are weighted with the photonic and excitonic fraction coefficients.

The general Hamiltonian describing the TE-TM splitting may be written in a circular polarization basis as [26, 28–30]:

$$H_{TE-TM}(k) = \begin{pmatrix} H_0(k) & \boldsymbol{\beta}(k)\, e^{-2i\phi} \\ \boldsymbol{\beta}(k)\, e^{2i\phi} & H_0(k) \end{pmatrix} = H_0(k)\,\mathbf{I} + \boldsymbol{\Omega}_{\mathbf{eff}} \cdot \boldsymbol{\sigma} \tag{1.24}$$

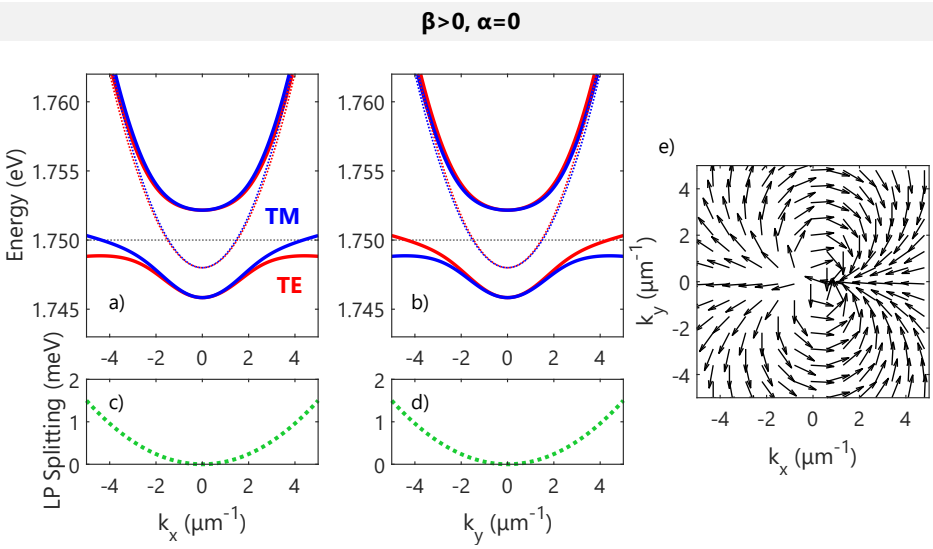

Figure 1.4. Visualization of the TE-TM splitting. (a-b) An example of a typical polariton dispersion in a negatively-detuned cavity, with two linearly-polarized modes (corresponding to the TE and the TM polarizations) plotted with solid red and blue lines respectively. Dashed lines show the dispersions of the constituent particles (the cavity photon and the exciton). A splitting between the two polariton eigenstates is presented in (c-d) with green dashed lines. The dispersions and the splittings are presented in two perpendicular directions in plane, k_x (a,c) and k_y (b,d). (e) A corresponding effective field texture, showing a rotation of the polariton pseudospin in plane.

where k is the in-plane wavevector ($k \equiv k_{\parallel}$) and ϕ - the in-plane angle (orientation of the in-plane wavevector), $\boldsymbol{\beta}(k)$ is the energy splitting between the TE and TM modes, $\mathbf{I}$ is the identity matrix and $\boldsymbol{\sigma}$ represents the Pauli matrix vector (with its components being Pauli spin matrices). H_0 is an initial Hamiltonian, describing either the photonic or the polaritonic system without the TE-TM splitting. $\boldsymbol{\Omega}_{\mathbf{eff}}$ can be then viewed as an effective in-plane magnetic field, acting on the particle spin:

$$\boldsymbol{\Omega}_{\mathbf{eff}}(k) = \Omega_{TE-TM}(k) = \boldsymbol{\beta}(k) \begin{pmatrix} cos2\phi \\ sin2\phi \\ 0 \end{pmatrix}. \tag{1.25}$$

Since the third component is zero, the field acts in-plane. The analogy with the real magnetic field is further expanded below.

Explicitly describing the exciton-polariton dispersions, one can characterize the lower branch with a single-particle Hamiltonian in a circular polarization basis [28,30]:

$$H(k) = \begin{pmatrix} E_{LP}(k) & -\beta k^2 e^{-2i\phi} \\ -\beta k^2 e^{2i\phi} & E_{LP}(k) \end{pmatrix}. \tag{1.26}$$

Here, E_{LP} is the dispersion of the lower polariton extracted from a coupled-oscillator model (see section 1.1.3) and β is the parameter quantifying the TE-TM splitting. The in-plane wavevector is expressed as $k = (k_x, k_y) = |k|\,(sin\phi, cos\phi)$. The two resulting eigenstates are presented in Fig. 1.4 (a-b). The TE-TM splitting has a rotational symmetry (visualised as a direct symmetry between two perpendicular directions in Fig. 1.4 (c,d)), and the two eigenstates are degenerate at $k = 0$.

Because the coupling of the polariton pseudospin to the in-plane wavevector is described in a mathematically analogous way to the spin-orbit coupling of electrons (where the effective magnetic field from their orbital motion interacts with their intrinsic angular momentum, giving rise to a spin splitting), it is very often referred to as the "photonic spin-orbit coupling" [25, 31] (see equation 1.24). In solid-state systems spin-orbit coupling transforms static electric fields in the laboratory frame into magnetic fields in the frame of a moving electron, which then interact with the spin of the electron. In optical systems the role of electron's spin is taken by the spin of photons, encoded in their polarization. Just as in electronic systems, also in optical ones (including polariton) this effect results in a variety of quantum phenomena, such as the realization of topological states [30, 32–34]. Depending on the symmetry, one can realize the so-called Dresselhaus- or the Rashba-type of coupling [25, 31, 35, 36]. In case of polariton systems, spin relaxation mechanism is similar to the Dyakonov–Perel spin relaxation mechanism for electrons in semiconductors, where the role of the effective Rashba and Dresselhaus fields is now played by the field created due to the TE–TM splitting. However, the TE-TM field created by the TE–TM splitting has a unique wavevector dependence, differing from the Dresselhaus or Rashba ones [25].

Since the spin (polarization) of polaritons is coupled to momentum and the Hamiltonian 1.24 is analogous to the effective magnetic field acting on particle spin, $\mathbf{\Omega_{eff}}$ governs polariton pseudospin's rotation in plane. The effect is presented in Fig. 1.4 (e). There, the distribution of polariton pseudospin in plane is plotted, when only the TE-TM field is present, with the dispersions plotted in (a-b)). The polarization winds around the point $k = (0, 0)$.

Importantly, the photonic spin-orbit effect leads to the optical analogue of the spin-Hall effect [37]. In electronic systems the spin Hall effect refers to a generation of an electronic spin current perpendicular to the charge current flow, due to the spin-dependent scattering of electrons by charged impurities or other defects, or due to spin–orbit effects on the carrier energy dispersion [25]. In polaritonic systems spin currents are carried by neutral particles (polaritons) and the spin separation takes place owing to a combination of elastic scattering of polaritons by structural disorder and the directionally-dependent influence of TE–TM splitting on the scattered polaritons. The elastic scattering of exciton polaritons is affected by the effective field $\mathbf{\Omega_{eff}}$ - if the initial polariton state has a zero spin and is characterized by some linear polarization, the scattered polaritons become strongly spin polarized. In effect, spin polarizations of the polaritons scattered clockwise and anticlockwise have different signs. It leads to a clear polarization texture in momentum space [25, 26, 37], confirmed in experiments.

The TE-TM splitting and the effective field can be directly observed experimen-

tally, by performing polarization-resolved measurements (in two orthogonal polarization bases, e.g. horizontal and vertical). Performing the measurements in horizontal/vertical, diagonal/antidiagonal and both circular bases allows for extracting all components of the polariton pseudospin, hence allows to directly map the effective field. Different polarizations of polaritons scattered in different directions (a hallmark of the optical spin Hall effect), has been observed and realized experimentally in different conditions [38–41], also in the condensated state (introduced in further parts of this thesis) [42, 43].

Moreover, one can further expand Hamiltonian 1.24 (and the effective field components 1.25), accounting for an additional birefringence or for a real magnetic field, simply by adding either nondiagonal or diagonal components to the matrix. The TE-TM splitting is inherently degenerate at $k_{\|} = 0$ and non-zero at larger momenta, but the cavity anisotropy (a birefiregent component) or the real magnetic field lifts this degeneracy at normal incidence and breaks its rotational symmetry. Such new contributions are described in the next section.

1.2.3 Cavity anisotropy and gauge fields

The model described in the previous section can be further expanded, accounting for additional terms.

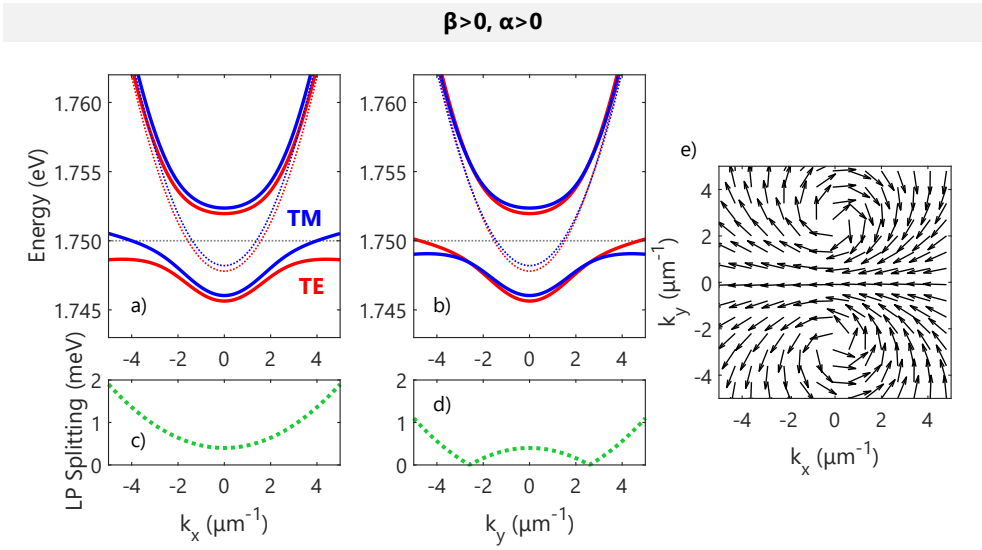

Figure 1.5. Visualization of the gauge field, with both the TE-TM splitting and the cavity anisotropy included. Panels are analougus to Fig. 1.4 and all the parameters are the same, apart from the nonzero X-Y splitting value. The anisotropy axis have been selected to act in direction y (direction x is perpendicular to the anisotropy axis, $\varphi = \pi/2$).

One of such terms results from the cavity birefringence or any inherent/imposed anisotropy. The TE-TM splitting has a rotational symmetry, creating two polarized states which are degenerate at $k = 0$, drawing away from each other at higher momenta (as presented in Fig. 1.4), regardless of the direction in-plane. However, this symmetry can be broken with the sample anisotropy [28, 30]. The birefringent term refers to a difference in effective cavity lengths for the ordinary and extraordinary waves, which can directly stem from the anisotropic crystal structure and is often unavoidable in crystalline systems. It can also be purposefully engineered into the structure [31,44]. The anisotropy, breaking the rotational symmetry, changes the symmetric (paraboloid-like) dispersion of the photonic (hence also polaritonic) modes. It acts as an additional splitting between linear polarizations associated with crystallographic axes (when stemming from the crystal structure), and can be described as a constant effective magnetic field term (often referred to as an X-Y splitting).

Anisotropy becomes one of the terms in the aforementioned Hamiltonians 1.24 and 1.26 and adds to the effective field $\mathbf{\Omega_{eff}}$ (1.25). Accounting for the TE-TM splitting and the intrinsic anisotropy (X-Y splitting) results in the Hamiltonian [28, 30, 36]:

$$H(k) = \begin{pmatrix} H_0(k) & \boldsymbol{\alpha}(k) + \boldsymbol{\beta}(k) e^{-2i\phi} \\ \boldsymbol{\alpha}(k) + \boldsymbol{\beta}(k) e^{2i\phi} & H_0(k) \end{pmatrix}, \tag{1.27}$$

Here $\boldsymbol{\alpha}$ describes the birefringence.

Explicitly describing lower polaritons translates to:

$$H(k) = \begin{pmatrix} E_{LP}(k) & \alpha e^{-i\varphi} - \beta k^2 e^{-2i\phi} \\ \alpha e^{i\varphi} - \beta k^2 e^{2i\phi} & E_{LP}(k) \end{pmatrix}, \tag{1.28}$$

where α quantifies the X-Y energy splitting and φ is the anisotropy orientation angle. The two eigenstates of this Hamiltonian are presented in Fig. 1.5.

As one can see, when the anisotropy is added on top of the TE-TM splitting, the two polarization-resolved modes dispersions are changed - as the degeneracy at $k = 0$ is broken, the branch dispersion now depends on the spatial direction (its relation to the anisotropy axis), what is visualized in Fig. 1.5. All parameters used are the same as in Fig. 1.4, but the anisotropy aligned with the y direction is included. Again, solid blue and red lines show the two polarized modes (a-b) and the splitting between them is presented with the green dashed line (c-d). A pseudospin rotation (the effective field) is presented in (e). One can see a clear difference between the two perpendicular directions (in-plane of the cavity, k_x and k_y).

At a specific angle, in the direction parallel to the anisotropy axis, the TE-TM and the X-Y fields exactly compensate, what results in a crossing of the two eigenstate dispersions, leading to the occurrence of a degeneracy point in momentum space. Such a unique state energy dependence, often described as a diabolical point, leads to a number of sophisticated phenomena [28, 30, 35, 36, 45]. The associated effective field acts on the pseudospin as a non-Abelian gauge field of the Rashba kind [28]. Around this crossing the polarization rotates, what can be described by a field analogous to a magnetic monopole, what is visualized in Fig. 1.5 (e). It remains in plane of the

sample. The effect of this field will be further explored in Parts II and III of this thesis.

Furthermore, one can introduce a real magnetic field, affecting polaritons via the Zeeman splitting, due to the excitonic component of polaritons. In QWs, placed in a real magnetic field, excitons with spins parallel or antiparallel to the magnetic field have different energies. This results in a Zeeman splitting of the exciton resonance, with value linearly proportional to the magnetic field. The Zeeman splitting of exciton states transfers to the Zeeman splitting observed for polaritons, weigthed with the excitonic Hopfield component [2, 46]. As the two spin components of excitons couple to photons with corresponding circular polarizations, the magnetic field imposes polarization of the polariton states, manifested as a change in the polarization of the detected light from a polariton microcavity [46]. The Zeeman split branches can be observed with the polarization-resolved measurements in the circular basis, in the presence of a magnetic field.

When added on top of the TE-TM field and the possible anisotropy, magnetic field makes the total effective field non-zero also out of plane [30]. All three contributions can be then accounted for in a full model with the Hamiltonian in a circular polarization basis (further expanding Hamiltonians 1.24 and 1.27):

$$H(k) = \begin{pmatrix} H_0(k) + \Delta_Z & \alpha + \beta(k)\, e^{-2i\phi} \\ \alpha + \beta(k)\, e^{2i\phi} & H_0(k) - \Delta_Z \end{pmatrix} = H_0(k)\,\mathbf{I} + \mathbf{\Omega_{eff}} \cdot \boldsymbol{\sigma}. \tag{1.29}$$

Here $\varphi = 0$ has been selected for simplicity of notation, aligning the x, y axis with the anisotropy axis. Δ_Z is the polariton Zeeman splitting (owing to the excitonic part). With no external magnetic field $\Delta_Z = 0$.

The full effective field can be then extracted as:

$$\mathbf{\Omega_{eff}}(\mathbf{k}) = \begin{pmatrix} \alpha + \beta(k)\ \ cos2\phi \\ \beta(k)\ \ sin2\phi \\ \Delta_Z \end{pmatrix}. \tag{1.30}$$

1.2.4 Polariton effective mass

In close resemblance to electrons in specific energy bands in a semiconductor, the concept of an effective mass of exciton polaritons is very often used. It characterizes the curvature of the polariton energy-momentum dispersion. As introduced briefly in section 1.1.3, in typical cases of strongly coupled polaritons in planar microcavities, the lower and upper polariton effective mass can be described as the harmonic mean of the mass of its exciton and photon components, weighted by the Hopfield coefficients [11, 13]:

$$\frac{1}{m_{LP}} = \frac{|C|^2}{m_X} + \frac{|X|^2}{m_C} \tag{1.31}$$

and

$$\frac{1}{m_{UP}} = \frac{|X|^2}{m_X} + \frac{|C|^2}{m_C} \tag{1.32}$$

(where $|X|^2$ and $|C|^2$ determine the exciton and the photon fraction in a lower polariton). Because the effective mass of a photon is much smaller than that of an exciton, the exciton-polariton effective mass is predominantly determined by the photonic part, making the lower polariton effective mass very small (on the order of $10^{-5}m_0$, where m_0 is the free electron mass), especially when the photonic fraction is high [2,13].

At small wavevectors, near the bottom of the dispersion, both polariton branches can be approximated as nearly parabolic, with evident discrepancies only at larger momenta. Hence, very often only the parabolic approximation is used. Nevertheless, the mass is broadly wavevector-dependent.

The concept of the effective mass can be generalized to any energy dispersion, as the measure of a band curvature, in direct similarity to semiconductor band studies in solid-state physics. A more general definition of mass can be then obtained with the use of a Taylor series expansion of the dispersion: $E(k) \approx E_0 + \frac{\hbar^2 k_0 (k-k_0)}{m_1(k_0)} + \frac{\hbar^2 (k-k_0)^2}{2m_2(k_0)} + \ldots$ [47]. The coefficients of each expansion order relate to a new mass parameter, with certain characteristic effects on the dynamics of the particle. In particular one can define:

$$m_1 = \hbar^2 k \left[\partial_k E(k)\right]^{-1}, \tag{1.33}$$

$$m_2 = \hbar^2 \left[\partial_k^2 E(k)\right]^{-1}. \tag{1.34}$$

The parameter m_1 is related to the classical motion of the wave packet, and determines the group velocity $v_g = \hbar k/m_1$. The parameter m_2 determines the acceleration of the packet when an external force is applied, as well as its diffusion rate. In case of a purely parabolic dispersion $m_1 = m_2$, but otherwise, m_1 and m_2 can have different signs, be zero, or even become infinite [47,48]. These concepts will be expanded in Part V of this thesis.

In exciton-polariton research the m_1 effective mass is most often considered. It becomes particularly important in the context of an additional potential landscape present in the microcavity, e.g. a lattice potential [11]. External potential largely affects the polariton dispersion (similarly to the electron bands in semiconductors), hence changes the mass. Favourable condensation of the negative-mass polaritons has been shown in a photonic lattice (at high symmetry points) [49], however the negative effective mass has also recently been observed in a planar structure [48]. This directly translates to an opposite sign of the particle's velocity and momentum in its dynamics, given by relation $m_1 v_g = \hbar k$ and can allow the observation of more sophisticated phenomena [50]. These topics are expanded in Part V.

1.2.5 Polariton lifetime

In direct analogy to the polariton mass, the polariton lifetime τ can be calculated as a harmonic mean of the exciton lifetime and photon lifetime (being a result of a leakage

of light through the cavity mirrors), weighted by the Hopfield coefficients [11, 13]:

$$\frac{1}{\tau_{UP}} = \frac{|C|^2}{\tau_X} + \frac{|X|^2}{\tau_C}, \tag{1.35}$$

$$\frac{1}{\tau_{LP}} = \frac{|X|^2}{\tau_X} + \frac{|C|^2}{\tau_C} \tag{1.36}$$

For lower polaritons the lifetime is typically inherited mostly from the photonic component, as the cavity photon lifetime is usually much shorter than the exciton lifetime inside a QW [2]. The former time is most typically on the order of up to single picoseconds in standard semiconductor microcavities and the latter - on the order of several tens of picoseconds up to nanoseconds in GaAs-based QWs, resulting in polariton lifetime on the order of 1-100 ps [13, 51, 52]. Total decay rate obviously depends on the exciton-photon detuning, as Δ governs the Hopfield fractions (see Fig. 1.2).

Because the photonic component plays a crucial role, the polariton lifetime is also highly affected by the cavity Q-factor. Constant leakage of photons makes cavity-polaritons a highly dissipative, open system, with the need of constant pumping to continue their investigation. However, it also allows for the direct measurement of polariton characteristics such as energy or phase (in real and momentum space), via optical experiments - as the observation in luminescence measurements is based typically on leaked photons.

Additionally, the lifetimes can be directly translated into the state decay rates, introduced in equation 1.17. The rates are proportional to the inverse lifetimes and can be investigated in optical experiments from the state linewidths. For example γ_X and γ_C are the exciton and photon decay rates (inverse lifetimes, multiplied by $\hbar$) respectively. Decay rates of lower and upper polariton states can be re-written as a weighted mean of γ_X and γ_C, weighted with the Hopfield coefficient.

1.2.6 Non-hermiticity

Due to the constant leakage of photons from the cavity, exciton-polaritons are an inherently open quantum system, which continuously decays and requires constant pumping of energy. Even though according to the principles of quantum mechanics the Hamiltonian describing a closed system's energies must be Hermitian, losses in open systems make them inherently non-Hermitian [53–55]. Polariton intrinsic non-Hermiticity for long has been unsung, but found a huge renewed interest in recent years [53, 56–59].

As in any open system, the losses can be accounted for by using the concept of complex energies. Even though the basic axiom of quantum mechanics requires the Hamiltonian (and other observables) of a system to be self-adjoint operators, represented by Hermitian matrices, in reality any physical system is in some way coupled to its environment. Many approaches has been suggested and used to take this into account, one of which being effective non-Hermitian Hamiltonians [60]. They provide

a conceptually simple and intuitive approach and have already led to profound insights and applications [61]. They enable to calculate the complex eigenenergies of the system, where the real part corresponds to the state energy value and the imaginary part quantifies the dissipation (loss) or gain. In case of exciton polaritons, it means accounting for and calculating both the real mode energies (e.g. as a function of particle's momentum) and the decay rates, in one complex parameter, introduced in equation 1.15. Both of them can be observed experimentally, e.g in optical experiments – the former directly, and the latter via the mode linewidth (proportional to inverse lifetime) [53]. This will be further employed in Part III of this thesis.

The solution of a simple two coupled oscillators Hamiltonian with the inclusion of the initial state linewidths, has already been introduced in section 1.1.3, with the lower and upper polariton dispersion formulas in equation 1.17, accounting for their imaginary parts.

Non-hermiticity of polaritons, combined with their versatility and usefulness in experimental studies, made them an ideal platform to study sophisticated non-Hermitian topologies [53, 61–64] and other extraordinary phenomena. Non-hermiticity has been shown to strongly modify the structure of the modes and spectral degeneracies, in effect affecting particle transport, localization and dynamical properties. It is linked to the existence of the exceptional points (non-Hermitian spectral degeneracies) of the modes, and paths a way to the study of non-trivial non-Hermitian topologies [61, 65–67]. Phenomena such as unidirectional transport, anomalous lasing/absorption and chiral modes have been observed and remain of a huge interest in the exciton-polariton research. A combination of topology and non-Hermicity is the topic of Part III of this thesis.

1.3 Material platforms

Exciton polaritons can emerge in any system, where excitons and photons interact. Due to fabrication and experimental concerns, availability, interest in particular characteristics or potential for useful application, several material platforms have been most widely studied. Some of the most advantageous and sought-after characteristics are: small exciton Bohr radius and large exciton binding energy (leading to high saturation density, necessary for the exciton presence even at high particle densities), high quality cavity (leading to long cavity photon and polariton lifetimes), strong exciton-photon coupling (for robust strong coupling) and large QW exciton oscillator strength, together with large polariton-phonon and polariton-polariton scattering cross sections (leading to efficient polariton thermalization) [13]. Of course the availability and costs of the fabrication technology remain a crucial factor.

The most widely used and studied systems since the very beginning have been the direct III-V direct-gap semiconductors, particularly the $Al_xGa_{1-x}As$ compounds, due to the best fabrication quality (via molecular-beam epitaxy growth) of both QWs and microcavities. Low lattice mismatches between the GaAs and AlAs materials, leading

to the achievement of nearly defect-free alternating layers, allowed the fabrication of very high Q-factor microcavities. To this day the most sophisticated polariton studies requiring high quality and long polariton lifetimes are achieved in this material system, following the very first observation of dynamic polariton condensation [68]. An important drawback of this material-system however is quite low exciton binding energy, which prevents the polariton observation (hence also condensation) at room temperature [13, 52]. The binding energy on the order of a few milielectronovolts is not sufficient to overcome the thermal energy at increased temperatures, leading to dissociation of excitons hence lack of the exciton-polariton presence. Necessity for cryogenic temperatures in studies and in potential devices is a huge drawback, both experimentally and from the useful application point of view [51]. There are several approaches to overcome this issue (such as achieving a very strong coupling regime [69], $\Gamma - X$ mixing [70], or implementation with novel materials), but still the low-temperature experiments remain the gold standard.

Another, historically exploited first, but less often used today system is CdTe (II-IV semiconductor) -based, typically with CdTe QWs and $Mg_xCd_{1-x}Te$ barrier and DBR layers. Even though the lattice mismatch between these materials is larger, it is compensated by a larger binding energy and a larger oscillator strength, as well as a larger refractive index contrast (leading to less layers needed in the DBRs) [13,51]. The first Bose-Einstein condensation (in quasi- thermal equilibrium) has been achieved in this material system [71], showing its potential. However, due to the less efficient polariton scattering, the condensation in the ground state is actually harder to observe, and the energy relaxation bottleneck is more persistent in this system [13]. It is also not a popular choice in typical optoelectronic devices, hence it has a lower potential in its integration with devices and application in technology.

Additionally, there have been studies on the development and use of certain wide-band-gap materials with low lattice constants, such as GaN, ZnSe or ZnO. As their exciton binding energy and oscillator strength are large, polariton lasing can be observed even at 300 K, though few such observations have been reported [72, 73]. A much higher concentration of impurities and crystal defects leads to much lower microcavity quality and the QWs integration is more challenging due to the lack of lattice matched DBR layers [13].

Some organic semiconductors have also been suggested and used, hosting the Frenkel/molecular excitons with a much larger binding energy and oscillator strength [74, 75]. More importantly, recently there is a growing interest in the use of new systems, such as thin layers of transition metal dichalcogenides [76, 77] or perovskites [78, 79] to develop polariton samples. Again, high exciton binding energy and oscillator strength make them advantageous and make polariton observation at room temperature possible. On the other hand, polariton condensation is challenging. Reports show that the nonlinearity in TMDCs and perovskite polariton microcavities are typically dominated by the phase-space filling effects and vanishing of the Rabi splitting, which makes the achievement of polariton condensation very difficult [80,81]. The key advantages of TMDC use are e.g. the strongly bound excitons, a range of possible materials with different band-gaps (covering a broad spectral region from near-IR

to visible), exciton sensitivity to the sample thickness, valley degree of freedom or the possibility of gating and electrical control [76, 80]. These materials are transparent, flexible, and mechanically strong, all making them advantageous for practical optoelectronic and nanophotonic applications. At the same time, they need to be implemented in microcavities - which remains a big challenge. Unlike the MBE-grown semiconductors, their exfoliation-based preparation method makes them unsuitable for monolithic microcavities growth. A wide range of approaches have been used, such as integration with an MBE-grown GaAs-based bottom DBR and plasmonic metallic top DBR, transfer of the top DBR on top of the flake, DBR growth in MOCVD chambers and other, but the final microcavity quality is still significantly smaller than the best GaAs-based structures [76].

In this thesis several different novel properties and qualities of polaritons have been studied. Three of the four result parts are connected by a similar experimental platform – all employing the GaAs-based monolithic microcavities. In particular two different structures have been considered: one ultrahigh quality structure with GaAs QWs and the other employing an AlGaAs compound. In both cases the material choice was of core importance to the study and the finding. The choice in the first one was necessary for studies of very sophisticated phenomena – ultralong polariton lifetime was crucial in an achievement of a high density highly uniform condensate in the Thomas-Fermi regime and the observation of condensation excitations (Part II of the thesis). The latter employed a sample designed for room-temperature condensation even in the GaAs-based platform, owing to the $\Gamma - X$ coupling, which allowed the formation of indirect X-excitons, core to the observed phenomenon (Part V). The exact structure characterization proved essential in the result interpretation and became an important piece of research (Part IV). The aforementioned coupling allowed also the studies at increased temperatures.

On the contrary, the platform investigated in Part III is different, as it employes lead-halide perovskite crystals embedded in an optical microcavity. This was necessery to increase the sample's anisotropy (as these orthorombic-structure crystals are known to be optically anisotropic). However, the experimental methods were the same as in other studies (work in Part II in particular), together with analysis methods and big part of the underlying phenomenon.

1.4 Applications

Finally, it is important to mention a large application potential of exciton polaritons and a wide range of ways how they can be used in science, industry or everyday life.

Since the very beginning, they were the most widely studied in the context of efficient lasers or light sources – due to their condensation and efficient coherent light emission. The topic of polariton condensation is discussed in detail in the next chapter (Chapter 2), with a section devoted to polariton lasing.

What is important is that the onset of coherent light emission and superlinear growth of the output power in polariton systems is expected and known to occur at much lower threshold powers than in traditional photon lasers, where a population inversion is needed [12,51,82]. This was the core promise of polariton research and its drive since their discovery [2], with the "holly grail" of near threshold-less lasing and ultra-efficient light sources being the goal. Unlike typical photon lasers, the threshold for polariton "lasing" can be made almost arbitrarily low, if the polariton lifetime is sufficiently increased (in contrast to the limit of the minimum carrier density at transparency, which needs to be surpassed to observe population inversion) [51]. The polariton decay rate is usually dominated by mirror losses, which can be mitigated with the sample quality.

Polariton lasing has been demonstrated in a wide range of materials and structures (e.g. see reviews [12, 51, 82]), with the lowest threshold densities achieved in high-quality GaAs-based samples, grown with epitaxial methods. However, despite the big promises, most polaritonic structures suffer from the presence of a phonon bottleneck, which hinders polariton relaxation (see section 2.2.2). Electrical injection has proved to be even more challenging, however, it was finally achieved, with the threshold powers comparable (or even favorable) to the best vertical cavity surface emitting lasers (VCSELs) [51,83]. Room temperature lasing has also been achieved in a range of material platforms [79, 84–87].

Furthermore, polariton lasing has been investigated in a wide range of contexts, such as in lattices, with promises of topological lasing [88–92], chiral lasing [93–95] or spin-helix lasing [35] in a range of platforms.

Polaritons have also been suggested as a medium allowing the creation of entirely new states of matter, such as in fractional quantum Hall states, even with a promise of looking for non-Abelian anyons [96]. These states can be used as quantum simulators, with polaritons being advantageous over atomic and optical systems.

Apart from lasing, polaritons have attracted significant attention e.g. for the realization of all-optical logic elements. First proposals investigated logical gates employing the binary information in the polarization of light [97]. Most studies however have suggested polariton diodes and polariton electronic switches that use the characteristic bistable or spin-multistable nonlinearity of exciton polaritons, to create logical elements [51]. The intrinsic polariton nonlinearity is expected to provide advantages in terms of switching times and threshold powers when compared to purely optical schemes. Furthermore, the polarization degree of freedom of polaritons, similarly to photons, can be used in a number of ways in spintronic devices [2, 43].

Another interesting application is the so-called quantum polaritonics, which harnesses quantum behaviour of polaritons, with no classical counterpart. The examples include obtaining an entanglement from pair scattering (e.g. [98]), showing an interference between two parametrically generated states that share the same signal [99], or - importantly - using Rabi oscillations to create quantum bits (qubits) [100]. These have potential applications in cryptography, computation and simulation.

Recently there is a lot of attention brought to the use of exciton polaritons in neuromorphic computing. Typically the challenge in developing optical artificial neural

networks for neuromorphic computing is the realization of a nonlinear activation function but combined with ultrafast operation. Since photons are very weakly interacting, purely photon-based optical neurons typically require large input power to reach the nonlinear regime, limiting their capability in terms of speed or energy efficiency. The strength of exciton-polariton nonlinearity is much higher, enabling their efficient use. Theoretical, but also experimental results have already been shown [97,101–104], with polaritonic neuromorphic computing outperforming linear classifiers [105].

Finally, from the scientific research perspective, huge advantages of polariton systems (over photons, atoms or electrons) make them ideal for the so called emulation and simulation [106]. Their experimental investigation may give important insights into other, less accessible platforms, systems or contexts, allowing profound conclusions. They act as the so-called analogue systems. As such, they have been investigated in a wide range of contexts, such as for the study of classical magnetism [106], non-trivial many-body physics (such as the fractional quantum Hall states mentioned above [107]) or even in experimental studies of black holes [108–110].

CHAPTER 2

Polariton condensates

The first chapter introduced the concept of exciton polaritons and their key properties, inherited mostly from the photonic and excitonic components. Importantly, as explained, they are quasiparticles composed of two bosons - hence they have an integer spin projection and are bosonic in nature. This fact governs their statistics, their behavior and the rules they obey.

In stark contrast to Fermi-Dirac statistics, resulting in the Pauli exclusion principle, bosons with same quantum numbers are allowed to occupy the same state. Moreover, their being in the same quantum state is more probable, due to the particle's indistinguishability [111]. In popular science it is often referred to as the "social" nature of bosons. The fact that a transition rate into an already occupied quantum state is enhanced by its occupation number is called bosonic stimulation [2, 112]. It is broadly the basis of a wide range of collective phenomena bosons undergo, most remarkable of which is condensation.

From the boson statistics Bose and Einstein first showed, how such particles are expected to undergo a phase transition in sufficiently high densities, or at sufficiently low temperatures [113, 114]. In this state a macroscopic number of particles occupy the same state (e.g. the ground state) and they behave collectively, as a single unified phase. The condensate is described by a single wavefunction and the state is known to have spontaneous macroscopic coherence.

This chapter will introduce the very basics of bosonic condensation, the specific case of condensation of polaritons and some of the properties of polariton condensates, crucial in further findings of this thesis. It will also highlight the advantages of polariton investigation in the condensate studies, with marked differences from other, typically regarded systems.

2.1 Bose-Einstein condensation

Following Bose and Einstein's theory [113, 114], all non-interacting bosons can be described by the distribution, defining the average occupation numbers (the expected number of particles in a single-particle energy state):

$$n_i\left(E,T\right)=\frac{1}{e^{\frac{E-\mu}{k_BT}}-1}, \tag{2.1}$$

where E and T are particle's energy and temperature, and μ is the chemical potential. The latter describes the energy required to add one particle without the change of entropy or volume.

Einstein has showed how an ideal Bose gas can undergo transition between the gas phase and the condensed state. The transition (called Bose-Einstein condensation) occurs when the mean spacing between the particles ($n^{1/3}$, with n being the gas density) decreases to a value comparable to the thermal de Broglie wavelength Λ [13, 115], defined as:

$$\Lambda\left(T\right) = \frac{h}{\sqrt{2\pi m k_B T}} = \sqrt{\frac{2\pi\hbar^2}{k_B m T}}. \tag{2.2}$$

At low temperatures (or high densities), the wavefuctions of separate particles start to overlap, finally forming one state, described by a single wavefunction, where the partcles act collectively. The critical temperature for condensation can be calculated from the above conditions – the condensate is formed when

$$T \leq T_{cr} = \frac{2\pi\hbar^2}{k_B m}\left(\frac{n}{2.612}\right)^{2/3}, \tag{2.3}$$

or alternatively (at a given temperature), when

$$n \geq n_{cr} = 2.612\frac{1}{\Lambda\left(T_{cr}\right)^3}. \tag{2.4}$$

In the above equations m is the boson's mass and the number constant comes from the Riemann zeta function $\varsigma\left(3/2\right) \approx 2.6124$.

Below the critical temperature (or above the critical density) a large fraction of bosons occupies a single quantum state, macroscopic in space and described by a single wavefunction. As a single state, the particles occupying it are phase-coherent. The process of condensation can be described as a phase transition, where the macroscopic occupation of the state is the order parameter. It is related to the symmetry breaking (hence it is a second-order phase transition [115]).

The number of particles in the condensate N_0 is dependent on temperature and can be expressed as [116]:

$$N_0 = N\left[1 - \left(\frac{T}{T_{cr}}\right)^{3/2}\right] \tag{2.5}$$

(with N being the total number of particles).

What is key to note is that the description of Bose-Einstein condensation was introduced for the ideal Bose gas of non-interacting particles. It was then expanded by Bogoliubov [117], who introduced a theory for weakly interacting gases – as discussed below in section 2.1.1.

2.1.1 BEC of weakly iteracting particles

The description of Bose-Einstein condensation was initially introduced for the ideal Bose gas of non-interacting particles and then expanded by Bogoliubov for dilute gases with weak interactions [117]. With interactions, the particle scattering becomes crucially important in the system investigation and the state occupation and critical conditions are modified, determined by the intra-particle interaction strength.

Bose-Einstein condensates (BECs) of weakly interacting bosons have been described by Pitayevskii [118] and Gross [119] with a famous Gross-Pitaevskii equation (GPE) – a classical partial differential equation for the superfluid order parameter. It can be derived as a mean-field limit to describe the dynamics of the condensate wave function $\Psi(\mathbf{r},t)$. It states [20, 116]:

$$i\hbar\frac{\partial}{\partial t}\Psi(\mathbf{r},t)=\left[-\frac{\hbar^2\nabla^2}{2m}+V_{ext}(\mathbf{r})+U\left|\Psi\right|^2\right]\Psi(\mathbf{r},t). \tag{2.6}$$

It is a nonlinear version of the Schrödinger equation – the kinetic term $\frac{\hbar^2\nabla^2}{2m}$ (with m being particle's mass) and the external potential V_{ext} are "expanded" by an additional, nonlinear term – $U\left|\Psi\right|^2$. This term describes the interaction strength between condensing particles and make the equation explicitly dependent on the particle density $n=\left|\Psi\right|^2$. The strength U can be also translated into the particle-particle scattering length a_s [20] (in 3D):

$$U=\frac{4\pi\hbar^2 a_s}{m}. \tag{2.7}$$

Furthermore, GPE can be seen as what the Maxwell equations are for quantum electrodynamics in nonlinear media, but for the matter [20].

Importantly, the GPE is quantitatively accurate when the occupation of modes other than the condensate is small (e.g. a_s is much shorter than the mean interparticle spacing) [20]. It is valid only at very low temperatures, as it does not include the temperature dependencies of all parameters.

From this equation one can look at the dynamics of the BEC. However, by imposing a small perturbation on the condensate wavefunction (the Bogoliubov approximation) one can calculate also the elementary excitations of the BEC. The simplest solution with no external potential $V_{ext}=0$ gives the dispersion relation of interacting Bose–Einstein-condensed particles - the famous so-called Bogoliubov spectrum:

$$\hbar\omega=\pm\sqrt{\frac{\hbar^2k^2}{2m}\left(\frac{\hbar^2k^2}{2m}+2Un\right)}. \tag{2.8}$$

It shows a quasi-linear dispersion (above and below the condensate), directly related to the interaction strength U. Further investigation of this spectrum can be found in section 2.3.

The bosonic character of exciton polaritons make them good candidates for condensation, what is expanded in further sections. As interacting particles, the condensate wavefunction is often derived with the use of GPE.

2.1.2 A note on BEC in two dimensions

Importantly, it is known that in the reduced dimensionality systems, such as a uniform 2D system of bosons, true Bose-Einstein condensation cannot occur, because the long-wavelength thermal fluctuations destroy a long-range order [13, 120]. This fact is a consequence of the Mermin-Wagner theorem, and it is particularly important in the context of realistic polariton condensates. Following it, in case of both 2D and 1D geometries the transition to BEC in a uniform system is only possible at zero temperature. In dimensions $d \leq 2$, long-range fluctuations can be created with little energy cost, so as they increase the entropy, they are favored. A non-zero density of states in the ground state prevents Bose-Einstein condensation in $d \leq 2$ systems.

However, if the Bose gas is spatially confined and it has a finite size and a finite number of single-particle states (as it is typically the case in realistic settings) the critical condition for the transition can be fulfilled at $T_{cr} > 0$, simply at a modified critical density, ($n_{cr} = \frac{2}{\Lambda(T)^2} \ln \frac{L}{\Lambda(T)}$ in the case of 2D box system of size L) [13]. Often it is then referred to as a quasi-BEC phase [13, 121].

Even though a planar microcavity exciton-polariton system is inherently two dimensional, the condensate's finite size allows this law to be adhered to – realistically the polariton condensate cannot occupy a largely extended state and the finite size makes it effectively three dimensional. Restriction of the system to a finite size, inhibits excitation of density and phase fluctuations and permits the formation of a condensate (or a quasicondensate) phase with a macroscopic coherence length [11]. The condensate size is typically governed by the optical excitation size (pumping spot size) or by the external potential (either natural to the sample or purposefully built-in/implemented) [11].

2.1.3 A note on other collective phases

Additionally, two other similar transition types, with some similarities to BEC, have been shown and investigated: the so-called BKT (from the names Berezinskii, Kosterlitz and Thouless) and BCS (Bardeen, Cooper and Schrieffer). First, Berezinskii, Kosterlitz and Thouless have shown how the formation of vortices can drive a phase transition unique to the 2D systems — the BKT transition [122, 123]. Below the critical temperature thermally excited vortices may form bound pairs (of oppositely circulating vortices), which stabilize a local order [13, 122, 124, 125]. In the context of exciton polaritons in a wide range of realistic cases, the system size is small enough that a quasi-BEC phase transition occurs typically before the BKT [13, 126]. However, the properties of the two phases differ and the mechanism of condensation in many systems is still actively debated [52, 127], yet it is beyond the scope of this thesis.

Secondly, in the interacting quantum gasses a transition between the BEC and the BCS phases can occur (named after Bardeen, Cooper and Schrieffer [128]), similarly to fermionic systems [129, 130]. The mechanism of such a transition is based on paring between fermionic species (a crossover from a degenerate Fermi gas described

by the standard BCS theory to a degenerate Bose gas with a BEC phase below a critical temperature). In the context of exciton polaritons, at sufficiently large exciton and holes densities (above a Mott density) the BEC-BCS crossover may take place, where degenerate Fermi gasses of electrons and holes are paired in the momentum space and an electron and hole plasma with screened Coulomb interactions coherently couples to a cavity-photon field [13, 131, 132]. However, the delicate after-effects of this distinction are not only beyond the scope of this work, but also the studied densities are significantly lower.

2.2 Polariton condensation

A wide range of particles and quasiparticles have been considered and used to achieve BEC, such as photons, excitons, bosonic atoms and other. Due to their composite nature exciton polaritons are bosons, hence they also undergo collective-coherence phenomena introduced in the previous section. Initially, they gained the most interest as a highly promising platform to study Bose-Einstein condensation in solid state systems, what significantly fuelled their research. In particular, several factors make them highly advantageous:

- the photonic component of exciton polaritons makes them easily accessible experimentally. The photons leaked from the microcavity carry all the information about the quantum particles, what can be easily probed in optical experiments. Emission (luminescence) experiments are the most often used, but also the reflection and transmission schemes are often employed. This allows for the experimental investigation of the energy, momentum, phase and spin of the formed condensate in a quick and relatively non-expensive manner - giving an insight into the condensate coherence, population distribution, polarization, transport, temporal decay or spatial distribution. It is very often contrasted with studies of atomic condensates, which prove to be a big challenge and require highly sophisticated methods (such as complex optical traps, cooling systems up to microkelvin scales, etc.).

- exciton polaritons have a very small effective mass in comparison to systems such as atoms or excitons, hence the critical density (temperature) for the condensation are much lower (higher), and much easier to achieve than in case of atomic or excitonic condensates;

- in a range of material systems, exciton binding energies are sufficiently large to allow for the strong exciton-photon coupling – hence also for polariton condensation – at elevated temperatures, up to a room temperature (see sections 1.3 and 1.4). This again stands in stark contrast to the vastly studied atomic gases, where temperatures necessary for condensation need to be on a sub-kelvin range. Even though challenging, employing polaritons allowed for many studies

of condensates at room temperature [79,84–87], what is obviously advantageous from both the experimental and the application point of view;

- the photonic component makes the extension of the phase-coherent wavefunction of polaritons much easier in space than for bare excitons, despite defects or disorder. By dressing the excitons with a microcavity vacuum field, the extended spatial coherence is more easily achieved, regardless of the realistic sample imperfections, which often limit quantum phase transitions [13].

Additionally:

- the dissipative nature of exciton polaritons makes them a unique system to study condensates in the delicate balance of pumping and loss (in and outside of a thermal equilibrium). It further enables studies of non-Hermitian effects (due to the inherently non-hermitian nature of polaritons, see section 1.2.6), also in the condensed phase. The open system properties are obviously a big challenge, but at the same time they allow novel studies and novel contexts exploration;

- as polaritons are often studied in high quality semiconductor samples in well-developed material platforms, they are a highly promising system for a range of possible applications (see section 1.4). Many of the proposed applications require the coherent, condensed state [51];

- owing to their excitonic component, polaritons – also in the condensed state – are sensitive to external magnetic or electric fields, allowing for their external control via these parameters. This stands in stark contrast to photonic condensates, with photons barely affected by the external stimuli. Combined with the polariton sample processing and design possibilities, this opens an endless range of settings in which they can be studied.

2.2.1 Condensation in driven-dissipative systems

Crucially, all first descriptions of a purely BEC state (described in the previous section) are true for bosons in a thermodynamic balance, at very low temperatures and for particles with infinite lifetime – occupying the condensed state indefinitely. It is clearly not the case for exciton polaritons – as shown in the first chapter, polaritons are inherently dissipative, with the lifetime determined mostly by the cavity photon lifetime (equation 1.36). The system needs constant pumping in order to maintain the condensate and to compensate for the losses. Therefore – it needs to be considered as a driven-dissipative system.

A use of the GPE (equation 2.6) in order to describe a polariton condensate wavefunction clearly needed to be expanded in order to account for the loss (or gain and loss). New terms had to be included, often phenomenologically, in the mean field approximation [20,115,133]. The most simple case with two additional terms, written

explicitly for the lower polariton wavefunction Ψ_{LP} (under the resonant pumping conditions), yielded [20]:

$$i\hbar\frac{\partial}{\partial t}\Psi_{LP}(\mathbf{r},t)=\left[-\frac{\hbar^2\nabla^2}{2m_{LP}}+V_{ext}(\mathbf{r})+U_p\left|\Psi_{LP}\right|^2-\frac{i\gamma_{LP}}{2}+i\eta_{LP}E_{inc}(\mathbf{r},t)\right]\Psi_{LP}(\mathbf{r},t). \tag{2.9}$$

Here, just as in 2.6, m_{LP} is the lower polariton effective mass (in the kinetic energy term) and V_{ext} is the external potential. U_p is the polariton-polariton interaction strength (in the nonlinear term dependent on particle density), which is related to the particle-particle scattering length a_s. Additionally, two terms need to be included: the term describing the loss rate, with γ_{LP} being the polariton dissipation (inverse lifetime, related to photon and exciton dissipation) and the pumping term proportional to the incident field E_{inc}, with η_{LP} quantifying the coupling of the polariton to incident radiation. They account for loss (dissipation) and gain (drive) respectively.

This general equation have been successfully used to describe exciton polariton condensates in a wide range of contexts, yet it has its limitations, with Ψ_{LP} varying slowly in space and time. It remains a mean-field approximation. If the pumping is done into an excitonic reservoir (further described in the next sections), with independent (and possibly slow) dynamics, it is often necessary to model the reservoir separately [20, 115]. Often it has been coupled with Semiclassical Boltzmann rate equations [13, 49, 134–136].

A typically-studied case of an incoherent, far off-resonant excitation of a polariton condensate results in a set of two coupled equations [11, 20]:

$$\begin{aligned}i\hbar\frac{\partial}{\partial t}\Psi_{LP}(\mathbf{r},t)=\Bigg[&-\frac{\hbar^2\nabla^2}{2m_{LP}}+V_{ext}(\mathbf{r})+U_p\left|\Psi_{LP}\right|^2-\frac{i\gamma_{LP}}{2}\\&+U_R n_R(\mathbf{r},t)+\frac{i}{2}Rn_R(\mathbf{r},t)\Bigg]\Psi_{LP}(\mathbf{r},t),\end{aligned} \tag{2.10}$$

$$\frac{\partial n_R}{\partial t}=-\left(\gamma_R+R\left|\Psi_{LP}\right|^2\right)n_R(\mathbf{r},t)+P(\mathbf{r},t), \tag{2.11}$$

with the first one describing the polariton wavefunction and the second one - the dynamics of the condensate reservoir. Here, n_R is the reservoir density and P is the optical pumping rate. The critical parameters defining the condensate dynamics, apart from the polariton dissipation γ_{LP}, are the reservoir excitons loss rate γ_R and the stimulated scattering rate R. A new term $Rn_R(\mathbf{r},t)$ describes the scattering from the incoherent reservoir to the condensate. U_R defines the polariton-reservoir interactions.

The next section investigates the particular case of the polariton condensation process and the complicated relaxation mechanisms necessary to achive a condensate.

2.2.2 Polariton condensation

Creating a polariton condensate is most typically achieved by using a non-resonant optical excitation (however electrical, or resonant excitation schemes are also possible and have been succesfully used). Incoming light with the above-bandgap energy can be absorbed by a semiconductor and a hot cloud of high-energy electron-hole pairs is generated. They subsequently scatter, dissipating their energy mainly via phonon emission. At lower energies, the Coulomb interactions become important and the high energy-high momentum excitons are being created. Particles scatter further, until they reach the optically active zone, the so-called light cone, in which their momentum can be carried by photons. Only then the excitons and the photons can couple and create polaritons [12].

Formed quasiparticles, mostly in the LP dispersion, scatter further, now mostly with acoustic phonons. However, this process is effective only until they reach the so-called "polariton bottleneck". In the vicinity of the inflection point (where the exciton and photon energy difference is on the order of the Rabi splitting), the dispersion becomes steep, and the photonic component of the LP becomes appreciable. This results in the reduction of the polariton lifetime, leaving less time for cooling, and the steep dispersion reduces the phonon density of states, leaving fewer phonons available to carry large amounts of energy and making the cooling process less efficient.

This is the reason for the polariton accumulation often observed around the bottleneck region [135]. Then a second mechanism becomes responsible for their further relaxation – the polariton-polariton scattering, which allows for occupation of dispersion around $k = 0$ [2, 12]. With the high enough population, polariton-polariton scattering becomes more probable. It can leave one particle in the vicinity of the dispersion minimum and the other at twice the bottleneck momentum, following the parametric scattering condition [2]. High momentum particles can be cooled again via phonon emission. Additionally, scattering with free carriers - also generated during pumping - may help in the relaxation process [52, 82].

Hence, at a certain particle density, conditions for bosonic stimulation are met, leading to the avalanche scattering process and subsequent macroscopic occupation of the ground state. With the condensate forming, polaritons are then scattered into it with the same phase, leading to a spontaneous coherence buildup [2, 52, 82]. Experimentally, the density can be easily changed via the pumping process, e.g increasing the optical excitation power or injecting more carriers electrically. This stands in contrast to typical atomic condensate realizations, where the critical conditions are met typically by decreasing the temperature.

Bosonic stimulation scattering process is what makes polaritons remarkably different from traditional photon lasers (what is further expanded in section 2.2.3).

The condensation process is associated with a distinct threshold behavior: a nonlinear rapid increase of particle population at a corresponding momentum, the rise of macroscopic coherence due to the macroscopic occupation of the same state, but also the state linewidth narrowing. Below the threshold, there is a broad distribution of polaritons in both energy and momentum. Increasing the pumping power may

then lead to a sudden narrowing of their distribution, a hallmark of condensation, when a large number of polaritons occupies the same quantum state. The appearance of the macroscopic order at threshold is interpreted as the symmetry breaking, hence the condensation is regarded as a second order phase transition [2, 12, 20, 52]. The first direct experimental observation of this process and the exciton-polariton BEC was achieved by Kasprzak et al. [71]. Since then it has been achieved in many experimental platforms, also at room temperature.

As already mentioned, the very complicated relaxation process has been successfully captured e.g. by the Semiclassical Boltzmann rate equations [13, 49, 134, 135]. The properties of the final condensate are often described by the aforementioned GPE, with terms accounting for gain and loss (equation 2.9).

A highly important result of the relaxation process described above is a crucial role of the reservoir - a population of particles that can relax into the condensate. In the most basic case of an optical excitation with a focused laser spot, the optically created excitons, the bottleneck polaritons and the condensed particles are all localized in the same place in space, what significantly influences the condensate properties [49, 136–139]. The particles then interact not only within the same phase, but also with the reservoir. Hence, any experimental measurements of the condensate need to take into the account also the non-condensed particles, vastly changing the measured characteristics, such as coherence. To overcome this limitation, the spatial separation of the condensate and the reservoir (pump) is often employed [138, 140]. It can be achieved with either studying ultra-high quality samples with largely extended condensates (and investigating propagating condensates outside of the pumping spot) [139] or by polariton trapping, e.g with the use of optical traps [11, 140]. The latter approach - particularly relevant in the context of this thesis - is expanded in section 2.6.

2.2.3 Polariton lasing

Regardless of the exact mechanism of the condensate formation, its emission consists of a coherent beam of light with spectrally narrow lines, similar to that of a standard laser. The condensation process is associated with a distinct threshold behavior: a sudden narrowing of the distribution, a nonlinear rapid increase of particle population (measured as a rapid increase of photoluminescence intensity), the state linewidth narrowing as well as the rise of macroscopic spatial coherence [2,12,52]. Hence, the coherent emission of condensed polaritons is very often referred to as “polariton lasing”, even though it does not constitute as a light amplification by stimulated emission of radiation [82]. There is no population inversion involved and the relaxation process leading to amplified light emission is starkly different [51, 52].

At the beginning of exciton-polariton condensates’ investigation there was a lot of debates and controversies regarding the nature of the coherent light emission, due to the system’s similarity to VCSELs (vertical-cavity surface emitting lasers). Even though the sample structures are typically very similar, in VCSELs the electrons and

the holes act as a gain medium and lasing occurs via population inversion, where many electron-hole pairs are excited [52, 82]. Coherent light is emitted by a well-known process of stimulated emission, where light in the cavity is amplified by the recombination of electron-hole pairs. The gain medium (electron-hole pairs) needs to be pumped sufficiently, such that the population inversion occurs, in order to coherently amplify photon emission. In contrast, to achieve polariton coherent emission, a large population of high-energy excitons is typically excited, but then the bosonic amplification of scattering process described in the previous section takes place, leading to the ground state occupation. Hence no population inversion is involved. The emission is achieved via the stimulated scattering (or stimulated cooling), rather than the stimulated emission [51, 52, 82]. The particle species that accumulates the coherence differs - in contrast to VCSELs, in polariton condensates the strong coupling is present, hence the coherence that accumulates is in the polaritons rather than the cavity photons. Thus, even though both a laser and a polariton condensate emit coherent light, there is a clear distinction between the coherent particle species.

There are other important differences between the two regimes, such as the the momentum-space distribution, onset of degeneracy or a Heisenberg-limited position and momentum uncertainty product [52]. Additionally, it's important to note, that all these differences are the most clear when the polariton lifetimes are sufficiently long and the thermalization occurs, leading to a truly BEC state. When polariton lifetimes are shorter, the distinction becomes less obvious, as the system may remain and operate outside of thermal equilibrium [52, 82]. Such an intermediate regime between a photon laser and BEC is often called *polariton laser* - when the strong coupling and macroscopic occupation of the polariton ground state is present, but without a thermalized population of polaritons. More on the precise distinction between the regimes can be found e.g. in refs. [13, 43, 52, 71, 82, 141].

Historically, the laser-like emission of polaritons was what drove the initial interest and investment in this field, as it offered a new way to create ultralow threshold coherent light sources, up to the limit of thresholdless lasing [2]. Most of their possible applications employ their efficient light emission above threshold. More on this topic can be found in section 1.4.

2.3 Condensate excitations

In section 2.1.1 the idea and the description of weakly interacting Bose gases have been introduced, initially considered by Bogoliubov for diluted gases [117]. The lowest-order approximation of the system's Hamiltonian when the interactions are included gives a ground state energy of the Bose gas and an equation of state [116]. A higher-order approximation on the other hand gives the excitation spectrum - the energy dispersion of excited states of the interacting Bose gas, introduced in equation 2.8 (with zero external potential). Importantly, the excited states of an interacting Bose gas can be described in terms of a gas of noninteracting quasiparticles (it can be in-

tuitively shown by explicitly using a second quantization approach, presented e.g. in ref. [116]). The excitation spectrum is approximately linear at low momenta (around $k = 0$) with the energy-momentum slope dependent on the strength of particle-particle interactions. The excitations dispersion has been explicitly introduced in equation 2.8.

The schematic visualization of the Bogoliubov spectrum, as a function of the wavevector, is presented in Fig. 2.1 (solid blue line). It is compared to a kinetic energy spectrum $\frac{\hbar^2 k^2}{2m}$ of the same exemplary particle (hence a spectrum with no interactions $U = 0$, a dotted orange line).

As visible in Fig. 2.1, the Bogoliubov dispersion at small momenta gives a linear, phonon-like form:

$$\epsilon(k) = v_s \hbar k = \sqrt{\frac{Un}{m}} \hbar k. \tag{2.12}$$

Velocity $v_s = \sqrt{Un/m}$ is the sound velocity of the condensate. The Bogoliubov theory predicts that the long-wavelength excitations of an interacting Bose gas are sound waves [116]. These excitations can be also regarded as Goldstone modes associated with breaking of a gauge symmetry, caused by the Bose–Einstein condensation [116].

The condensate excitations can be intuitively viewed either in a quasi-particle picture, as particles excited from the ground state condensate and occupying higher energy states, or as collective waves, higher frequencies, disturbing a single wavefunction of the collectively behaving ground state condensate.

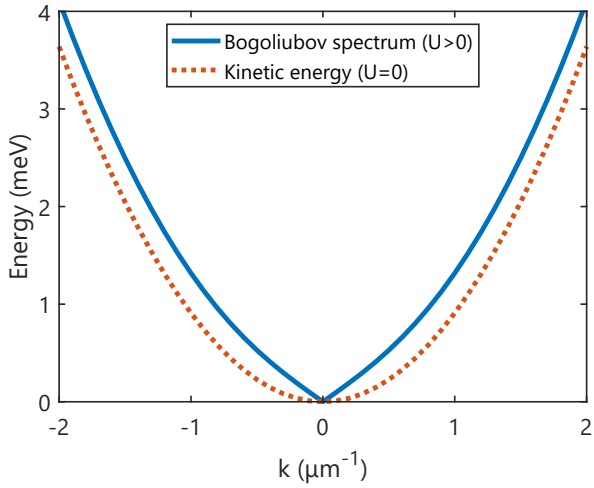

Figure 2.1. Bogoliubov dispersion of elementary excitations, with a quasi-linear dispersion at small momenta (solid line), compared to a parabolic dispersion (kinetic energy of the same particle, with no interactions, dotted line).

2.3.1 Superfluidity

Importantly, the Bogoliubov spectrum and its phonon-like form is the basis of the phenomenon of superfluidity (according to the Landau's criterion for superfluidity) - a dissipation-less flow of a fluid (flow without any loss of kinetic energy), hence fluid's zero viscosity [116]. It was initially observed for liquid helium-4 (He-II) [142–144], which is a boson, and the onset of the superfluidity was shown as a manifestation of its Bose–Einstein condensation. Similar phenomenon of superconductivity can be viewed as the superfluidity of a Fermi gas (coming from the fermion-pairing) [128,145].

Hence, the excitations of a BEC are flowing without the loss of energy and can flow against any defects, as long as the defects are sufficiently small. The defect size needs to be smaller than the so-called healing length ξ - also called the interaction length, as it is directly related to the interaction strength of the condensate. It is defined as [116]:

$$\xi = \sqrt{\frac{\hbar^2}{2mUn}} = \frac{1}{\sqrt{2}}\frac{\hbar}{mv_s}. \tag{2.13}$$

The healing length defines the transition between the phonon and the particle regimes in the Bogoliubov spectrum (low momentum vs high momentum as seen in Fig. 2.1). When the typical distance D, characterizing the density variations taking place in the system, is much larger than the healing length, the condensate wavefunction remains unaffected. This means the physical obstacles the condensate liquid encounters need to be smaller than ξ for the wavefunction not to be changed and for the dissipation-less flow to remain. When they become larger than ξ, the obstacles create discontinuities in the ground state wavefunction, and excite elementary waves or topological excitations, such as vortices or solitons [116, 146].

If $D \gg \xi$ (meaning that the density of the gas changes slowly in space), then the quantum pressure term becomes negligible. The neglection of the pressure term, together with the kinetic term, is referred to as the Thomas–Fermi approximation [116]. In this so-called Thomas-Fermi regime the chemical potential of a high-density condensate in the ground state is uniquely determined by the condensate mean-field energy [116, 147]. The condensate's behavior is then dominated by the interparticle interactions [147] - what is especially relevant in the context of this thesis and expanded in section 2.3 and in Part II. Entering the Thomas-Fermi regime allows for the measurements of the particle-particle interaction strength - also in polariton systems [116, 147, 148].

2.3.2 Excitations in exciton-polariton condensates

Even though exciton polaritons typically do not form a truly BEC state and are subject to gain and loss terms (see section 2.2.2), the polariton condensate is characterized by a spectrum very similar to the one introduced by Bogoliubov. In the particular case of polariton condensates, the excitation spectrum has been successfully calculated (e.g. by using a perturbative formalism of Bogoliubov-de Gennes

introduced before (within the mean-field approximation) from the GPE (equation 2.9)) [133, 149]. It results in form:

$$\epsilon(k) = \hbar\omega_{Bog} = \sqrt{\epsilon_{LP}\left(\epsilon_{LP} + 2U_p n\right)} \tag{2.14}$$

- the dispersion analogous to the Bogoliubov spectrum (see equation 2.8 and Fig. 2.1), but with the effective mass of the lower polariton branch as the particle's mass and the polariton-polariton interaction strength U_p specifically. ϵ_{LP} is the lower polariton energy dispersion (equation 1.14) shifted to its ground state's energy, $\epsilon_{LP}(k) = E_{LP}(k) - E_{LP}(0)$.

Quite crucially, due to the wavevector dependence of the lower polariton mass m_{LP} (see chapter 1.2.4) and the finite lifetime, the polariton condensate dispersion differs from a typical gas of massive particles. Apart from their non-parabolic dispersion, the inherently dissipative (open) nature and the finite lifetime of polaritons result in the the excitation modes to also have a non-zero imaginary part (they decay in time). With non-negligible losses, at low wavevectors (around $k = 0$) the excitation spectrum is flat in energy, increasing at finite momenta [133]. Hence, the long-wavelength excitations of the condensate are dispersion-less and have a diffusive character [133, 149, 150]. At higher momenta the dispersion approaches the quasi-linear Bogoliubov spectrum. However, these dissipative terms are beyond the scope of this thesis, and are not accounted for in further considerations.

The excitation dispersion calculated with equation 2.14 is presented in Fig. 2.2 with solid blue line. It accounts for the polariton dispersion non-parabolicity (wavevec-

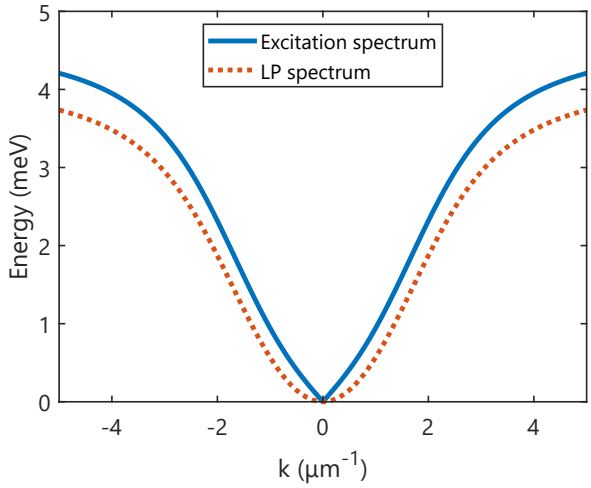

Figure 2.2. Dispersion of the exciton-polariton condensate excitations (solid line) compared to the dispersion of the uncondensed, low-density lower polaritons (dotted line). Both spectra are shown as an energy relative to the ground state.

tor dependence of the lower polariton effective mass), but it does not account for the finite lifetime (the imaginary part of the spectrum). It is compared with the dispersion of the lower polariton mode (spectrum with no polariton-polariton interactions $U_p = 0$, or the low-density regime) presented with dotted line.

One should also note, that both positive- and negative-energy excitation branches ($\pm\hbar\omega_{Bog}$) fulfill the evolution equations necessary to calculate the excitation spectrum, what corresponds to the positive and negative Bogoliubov branches. The physical elementary excitations correspond to the positive branch only [20, 116, 151], while the negative branch can be seen partly in similarity to the electron's holes in solid state. It is not a real excitation branch of the system: it corresponds to the emitted photons associated with the creation of real Bogoliubov excitations in the polariton system [152] and it is an intrinsic feature of an interacting condensate (it does not require the presence of a reservoir, but it requires nonzero interactions) [152]. The positive energy branch ($+\hbar\omega_{Bog}$) is typically described as a normal branch (NB) and the negative one ($-\hbar\omega_{Bog}$) as a ghost branch (GB). The occupation of the NB occurs via the process of thermal excitation (thermal depletion) [148, 153] and the GB is populated by the quantum depletion process [148], with parametric occupation of both the positive and the negative branches. The appearance of the GB in the photoluminescence spectrum of an exciton–polariton condensate can serve as a direct probe of quantum fluctuations (beyond mean-field effects), as have been evidenced experimentally [148].

The excitation spectra have been observed in several studies, employing different experimental methods and schemes [154–157]. Such an observation proves to be very challenging experimentally, as the condensate's strong emission hinders any other signal in optical experiments. Excitation emission is typically orders of magnitude lower than that of the condensate, what requires sophisticated experimental designs, such as a two-photon Bragg scattering technique [155] (in an atomic condensate) or covering the strong emission of the ground state condensate [148] (also further explored in Part II). The quasi-linear excitation branches not only lie at the core of the superfluidity phenomenon and can serve as its experimental evidence, but also their dispersions can been used to extract the inter-particle interaction strength U_p (also in the exciton polariton context) [147,148]. This topic is expanded and explored in Part II of this thesis.

2.4 Polariton-polariton interactions

Polaritons, as massive particles with partly excitonic and partly photonic characteristics, interact with other particles such as phonons, excitons or other polaritons. Photon interactions are known to be very weak and often neglected, so the polariton interactions are mainly a result of the excitonic component [13, 20]. Hence, polariton-polariton interactions are inherited directly from the exciton-exciton interactions [158].

A very clear signature of the interactions undergone within a polariton condensate is the characteristic blueshift of the emission above the condensation threshold – a hallmark of an interactiong bose gas [159]. The energy of the laser-like polariton emission increases with density (excitation), what stands in contrast to a typical photonic lasing case in a weak-coupling regime. In polaritonic systems, polariton-polariton interactions shift the condensate ground state energy - being repulsive, towards higher energies. The blueshift is density-dependent. For long it has been used to simply quantify the polariton-polariton interaction strength [14, 159–161], however, a huge drawback of the blueshift analysis to explore polariton-polariton interactions (with the non-resonant excitation) is a distinction between the interaction with the reservoir of uncondensed excitons and the polariton-polariton interactions within the condensate [159, 162]. It can be overcome by spatially separating the reservoir and the condensate population (as further explained in section 2.6).

Apart from the blueshift, a more reliable and direct signature of the polariton-polariton interactions is the renormalization of the polariton dispersion into a linear Bogoliubov profile [39, 155, 159] (see Fig. 2.2) or a superfluid behavior [39, 163], both introduced in the previous section and evidenced experimentally. Under the resonant pumping, polariton–polariton interactions lead to nonlinear effects such as bistability of the pumped mode [164, 165] and polariton parametric scattering [20, 25, 133, 166]. Superfluidity has been evidenced e.g. with the resonant Rayleigh scattering [167] or with the suppression of scattering from defects when the flow velocity is slower than the speed of sound [39], on top of the linearization of the dispersions (observation of the excitation branches, see section 1.1.1).

To estimate the interaction value, most of the first theoretical works have assumed the exciton-exciton interaction strength (in the Born approximation) as $g \sim 6E_b a_B^2$ [133, 134, 158, 160, 168], (where E_B is the excitonic binding energy and a_B is the excitonic Bohr radius, see section 1.1.1) with typical values in GaAs narrow quantum wells on the order of $g \sim 6\ \mu eV\mu m^2$ [147, 160] (assuming $E_B \approx 10\ meV$ and $a_B \approx 10\ nm$). More recent models show that the corrected proportionality factor is in fact 4π [169]. Additionally, an accurate description of 2D scattering is recently subject to intensive research [23, 169, 170]. Regardless, this approximation indicates that the polariton gas is intrinsically weakly interacting (as measured by the unitless parameter $g/\frac{\hbar^2}{2m} \sim 0.01 \ll 1$ [160, 171, 172]), as the polariton effective mass is typically several orders of magnitude lower than the vacuum electron mass. However, the interactions need to be compared to the kinetic energy term.

The interaction constant has been proven to be quadratically dependent on the excitonic fraction [147,148], a result in line with expectations, as the polariton-polariton interactions are mainly a result of the exciton-exciton interactions g. Hence, the polariton-polariton interaction strength U_p [147] ca be calculated as:

$$U_p = \frac{|X|^4 g}{2N_{QW}}, \tag{2.15}$$

where $|X|^2$ is the excitonic Hopfield coefficient (see section 1.1.3 and equation 1.20)

and N_{QW} is the number of quantum wells. The latter needs to be accounted for, as the excitons are confined in separate layers. The factor 2 accounts for the dominant role of triplet interactions [147].

The polariton-polariton interactions are most often described within the mean-field approximation. Then, at low particle density, the blueshift of ground state energy related to polariton-polariton interactions is linearly dependent on the particle density n [160]:

$$\Delta E = U_p n \tag{2.16}$$

Polariton-polariton interaction strength U_p is independent on density, as long as one assumes an absence of many-body correlations [160].

Experimentally the value have been often characterized from the polariton blueshift (e.g. [14,159–161]), but this approach is problematic due to the reservoir presence and the precise estimation of the density [159]. More accurate value estimations can be done with the Bogoliubov spectrum observations. In the Thomas-Fermi Regime of a high density condensate (see section 2.3), which is governed by interactions, U_p can be extracted with fitting the excitation dispersions [147, 148] using the equation 2.14. One can also minimize the influence of the reservoir in a pulsed excitation experiment, employing the "hole–burning effect" [138].

Figure 2.3 shows a comparison of some of the reported values of the polariton-polariton interaction strength, reproduced from ref. [147]. These values were obtained by various methods and the their range spans over several orders of magnitude, most of them exceeding the conventional theoretical theoretical estimate (solid line) by at least an order of magnitude. However, most of the measurements were performed on trapped condensates what can produce larger values due to the quantum confinement

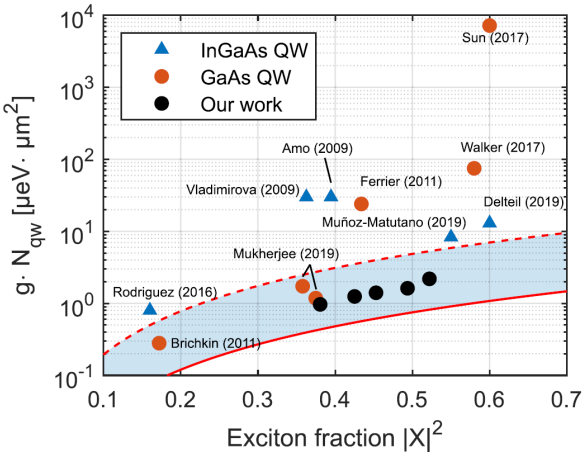

Figure 2.3. Comparison of some of the previously reported values of the polariton-polariton interaction strength, scaled by the number of quantum wells, as a function of the exciton fraction, reproduced from ref. [147] (black points correspond to the result of that work).

effect, together with the lack of the complete separation between the polariton and reservoir density. The measurements reported in ref. [147] (labelled as "Our work" in the reproduced Fig. 2.3) have been done in the Thomas-Fermi regime, with the fully eliminated influence of the incoherent excitonic reservoir.

Very importantly, the exciton-exciton interactions are known to be spin-dependent [173,174]. Because polaritons interact through their excitonic components, the strength of these interactions is also spin-dependent. As discussed in section 1.2.1, polaritons have two possible bright spin projections, as only the $j = \pm 1$ excitons couple to light. Hence, the interaction strengths for polaritons of the same (triplet) α_1 and opposite (singlet) α_2 spin are known to be different [25, 175–178].

There have been various attempts to estimate the values of α_1 and α_2 - both experimentally (e.g. [175, 176, 179–181]) and theoretically (e.g. [133, 158, 182–185]). The two most essential and consistent conclusions of most of the works are that $\alpha_1 > 0$ (the triplet polariton-polariton interactions are repulsive) and $|\alpha_1| \gg |\alpha_2|$ [134, 175, 177]. Some works also suggest that α_2 is negative [179], meaning that polaritons with opposite spins should weakly attract, but the sign is up to the debate and could change with exciton-photon detuning [175]. Such conditions lead to a linearly polarized Bose-Einstein condensate being the ground state of the system [25, 175]. However, the exact ratio of the α_1 and α_2 values and their signs have a crucial impact on the critical conditions for the condensation of exciton polaritons in microcavities [25, 175] and is known to strongly depend on the exciton-photon detuning. This can lead to different regimes with varying condensate polarization (e.g. a circular polarization of the ground state at a certain range of detunings) or its instability (e.g. a condensate collapse or fragmentation) [175,176,186]. The constants should not be strongly dependent on the in-plane wave vector of the interacting polaritons (if it remains inferior to the inverse exciton Bohr radius) [175].

The attraction between parallel-spin polaritons is typically weaker than the repulsion (at negative photon-exciton detunings) - and this is suggested as a basis of why the Bose-Einstein condensation of exciton polaritons in planar microcavities is possible [175]. The factors responsible for the antiparallel-spin polaritons repulsion are the mean-field electrostatic interaction (independent on spin) and direct exchange interaction. The factors responsible for attraction are the interaction via a biexciton state, the indirect exchange coupling via the dark states and the Van-der-Waals coupling (independent on spin and small) [175].

In most cases, the experimental investigation of the polariton-polariton interactions focused only the average strength of the interactions (meaning looking mostly at α_1, with much weaker α_2 being neglected) and the experiments to extract both of them are very scarce. The former approach (a single value) includes most of the works presented in Fig. 2.3. In some other works only the α_1 to α_2 ratio was being investigated and debated [175, 187] or their difference [176] and not the exact values. These used a scheme of resonant transmission of light through a microcavity in the strong coupling regime, which is challenging for most samples.

Expanding the accurate approach of studying the linearized Bogoliubov spectrum of the condensate excitations in the Thomas-Fermi regime, but considering also the

polarization resolution, allows to directly study both interaction constants experimentally. This method was proposed by this thesis as it is described in more detail in Part II.

2.5 Coherence

As already introduced, the bosonic condensation - including the exciton-polariton condensation - is associated with the buildup of the macroscopic coherence. When a large portion of particles occupies the same state, described by a single wavefunction, their phase is the same, allowing for the emission of the coherent radiation. It is well known, that the onset of a coherent laser emission in purely optical systems (such as VCSELs) is also associated with the appearance of long-range spatial coherence along the cavity plane - but the mechanism of the coherence buildup in such systems is different to polaritonic ones. In case of polaritons, the coherence comes from the stimulated scattering into the ground state, while in case of lasers - from the stimulated emission process (see section 2.2.3).

Hence, an important consequence of the Bose–Einstein condensation is the occurrence of coherence effects associated with the phase of the order parameter. Even in the very first experimental realization of the BEC of exciton polaritons (by Kasprzak et al. [71]), the authors reported an increase of the temporal coherence and the buildup of the long-range spatial coherence, together with the linear polarization (all indicating the spontaneous onset of a macroscopic quantum phase). They evidenced it in the spatial correlation measurements, using a Michelson interferometer. Such measurements have become a common practice in other studies since then, as a part of proving the condensation.

Spatial coherence is reflected by the classical first-order correlation function of the polariton emission, $g^{(1)}$, where the emission from two positions in space are interfered with one another [13,188,189]. In the low-density regime, the polaritons are expected to exhibit only the short-range correlations (with a correlation length given by the thermal de Broglie wavelength), while in the condensed phase, a complete coherence, up to the size of the condensate is expected [71,116]. The experimental investigation is typically done with the use of a retro-reflector in one arm of the Michelson interferometer, to invert the image in a centro-symmetric way [71] and measure a spatial autocorrelation.

Spatial coherence measurements can also directly show the fragmentation of the condensate, e.g. in unstable or trapped regimes [116], for example when the ratio of the inter-particle interaction strengths α_1 and α_2 don't allow for a stable condensate phase [176]. The robustness of Bose–Einstein condensation against fragmentation is ensured by two-body interactions [116].

Additionally, recently there have been a lot of attention put towards the effects of coherence relative to two or more condensates, such as with two overlapping condensates [116] or with several condensates trapped separately in optical

traps [106, 190, 191]. Effects such as coherent oscillations in an exciton-polariton Josephson junction have been described and shown [116, 192].

2.6 Polariton trapping

In case of microcavity polaritons, their existence is always connected to the confinement in plane of the microcavity, but in recent years a lot of attention and efforts has been put towards studying polaritons in additional, 2D or 1D potential landscapes [11]. The presence of an external potential is not necessary to observe the condensation, but a confinement allows for controlling, directing and structuring the flow of polaritons and their behavior [11, 13]. It can be used to trap and localize polaritons or their condensates.

Polariton's unique properties allow for a wide range of possibilities to influence their potential landscape. Several pathways of creating such a potential are possible and can be achieved by using either their photonic or excitonic parts. The examples of the ones most often used are: a use of a local strain [193], surface acoustic waves [194], electrostatic traps [195], structuring an excitonic reservoir [140], using low-dimensional active material [196], using photonic crystals [197], metal masks [198], etching micropillar cavities [199] or using hybrid approaches [200]. Many of them are reviewed in ref. [11].

In particular, optical traps with the reservoir shaping have proved to be very useful experimentally. When the condensate is excited optically, in the non-resonant excitation scheme, the pumping laser spot can be at the same time structured spatially on the sample, in order to localize the particle's population. Excitons are created at the position of the laser and the subsequent relaxation process (creating polaritons) occurs close to the spot - due to their large effective mass excitons are able to diffuse only small distances [138,140] (in comparison to polaritons or photons). Moreover, the presence of the exciton density and the high density blueshifted polaritons create a repulsive potential, altering further polariton movement, due to the polariton-exciton and polariton-polariton interactions. The repulsive interaction between the condensate and the reservoir particles enables the creation of effective potentials by exploiting a local reservoir-induced energy barrier [138]. The influence of the optical excitation's spatial (and temporal) distribution on the polaritons can be seen directly in coupled equations 2.10 and 2.11. The complex linear potential induced by the excitonic reservoir can be calculated as $\tilde{V}(\mathbf{r}) = U_R n_R(\mathbf{r}) + i\left[R n_R(\mathbf{r}) - \gamma_{LP}\right]$ (see equations 2.10 and 2.11), with both real and imaginary parts proportional to the pumping rate, $P(\mathbf{r})$, as $n_R(\mathbf{r}) \propto P(\mathbf{r})$ [53].

Very importantly in the context of this thesis, the additional potential can be employed specifically to trap polariton condensates, at the same time separating the studied quantum phase from the reservoir. As already introduced, an inherent presence of the exciton reservoir severely influences the condensate properties and measured characteristics. Investigating e.g. the condensate coherence or particle-

particle interactions needs to account for the "feeding" population, or to spatially separate the two - what can be achieved by the potential engineering. In the most typical cases of the condensate creation via a Gaussian-shaped optical pump spot, the reservoir and the condensing polaritons are at the same position and spatially overlap, what severely influences the condensate characteristics. Hence, spatially structured optical pumps can be useful to avoid this problem [138, 147, 162].

The most attention in these regard has been put to creating circular traps, by exciting the sample with a doughnut-shape laser beam [140], as schematically depicted in Fig. 2.4. It can be achieved with the use of conical lenses (axicons) [138, 140] or devices such as spatial light modulators (SLMs) [201] or digital micromirror devices (DMDs). Such a shaping can be used to localize polariton condensates in the centre, with the reservoir located at the edges. With high effective mass, excitons diffuse mostly around the excitation area, but most of them is unable to reach the center of the ring (provided that a sufficient ring diameter is used, typically on the order of $10 - 50\ \mu m$). Hence, the number of excitons in the centre of the trap is largely reduced.

The repulsion of polaritons from the ring-shaped exciton reservoir creates a ring-like trapping potential, and the uncondensed polaritons ballistically expand either towards its center or outside [140], schematically depicted in Fig. 2.4. Panel (a) is a visualization of the spatial distribution of the excitation (in real space, in-plane of the sample), creating a similar distribution of the excitons and blueshifted polaritons. The reservoir creates a repulsive potential, schematically depicted in Fig. 2.4 (b), with blueshifted particles moving either oudisde or toward the center of the ring. Those in center eventually collide with each other, subsequently condensing, if the density is sufficient [159, 202]. In order to create condensates fully spatially separated

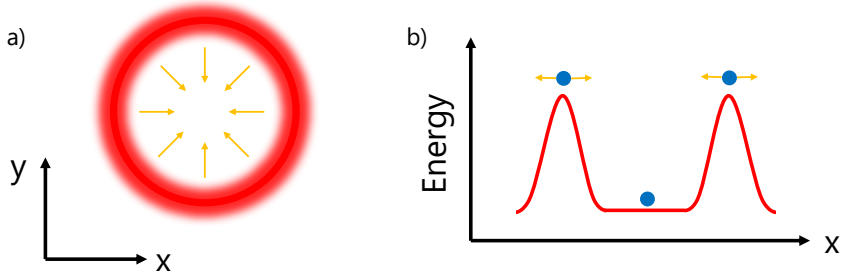

Figure 2.4. Schematic visualization of the ring-shape optical trapping of polariton condensates. (a) A spatial distribution of the optical excitation, with a donut-shape laser beam. Polaritons created in this area move ballistically towards the center of the trap (or outside), what is schematically visualized by yellow arrows. (b) A schematic visualization of the potential landscape, created by the reservoir. It alters the polariton movement, due to the repulsive polariton-exciton and polariton-polariton interactions. Polaritons moving towards the center can be trapped and create a high density condensate, separated from the reservoir.

from the reservoir one needs to use sufficiently large traps and a sufficiently strong pump, as the reservoir can still influence the condensate inside if conditions are not met [162]. Fully escaping the reservoir influence utilizes strong depletion of the reservoir (the effect of the so-called spatial hole burning) [138,147,162] in pulsed excitation conditions. This scheme proved to be useful in creating a high density condensate in a Thomas-Fermi regime, with no reservoir present [147].

CHAPTER 3

Outlook

The first chapter served as a general introduction to the topic of exciton polaritons and their condensates, giving a broad theoretical background and acquainting with some of their essential properties. However, it is important to note that these quasiparticles are extremely complex, and they are studied in a lot of contexts, systems, materials and schemes. Due to the polariton's complexity, the Introduction had to focus only on a selected number of topics, which are relevant to the further Results parts.

Prior to moving into the Results, the essential Methods will be discussed in a subsequent chapter, common to all the further included studies.

Then, the thesis will move into the Results, divided into four main topics. Each study is preceded by a more specific Introduction and finalized with the finding Summary.

CHAPTER 4

Methods

The studies described in this thesis are experimental works, with the findings based on the experimental observations. In all studies photoluminescence (PL) measurements of semiconductor samples were performed, in which the studied structures are optically pumped by the incoming laser excitation, and the structure emission is recorded in a spectroscopic setup. The employed optical setups have been build and tailored purposefully for the studies in question. In all studies the microphotoluminecsence (µPL) configuration has been used (having high spatial resolution due to the application of microscope objectives) and the setups were built in a reflection configuration.

4.1 Angle-resolved and spatially-resolved measurements

In spectroscopic studies of exciton polaritons the angle-resolved experiments are most often used, to directly measure the characteristic polariton energy-momentum dispersion. As introduced in section 1.1.3, the in-plane wavevector of the effectively two-dimensional (2D) polariton system is directly linked to the angle of incidence of light illuminating or being emitted from the structure θ (angle from the direction perpendicular to the sample surface). This allows for a direct measurement of the state dispersions in angle-resolved experiments, as:

$$k_{\parallel} = ksin\theta = \frac{2\pi}{\lambda} sin\theta. \tag{4.1}$$

Hence, by detecting the energy (or wavelength, λ) of the light emitted at each angle, one can reconstruct the whole energy-momentum dispersion of the respective state.

In order to do it experimentally, one can use lenses in a confocal configuration and image the Fourier plane of the sample's emission to study it in the reciprocal space (the so-called far field). Moreover, one can adjust the same setup to measure also the emission in real space (the so-called near field). Both are schematically depicted in Fig. 4.1. The simplest case (not depicted there) of an optical detection path consisting of a microscope objective (placed at the focal length from the sample) and an imaging lens (at its focal-length distance from the detector, e.g. a spectrometer) creates a simple microscope and allows to observe the emission in real space.

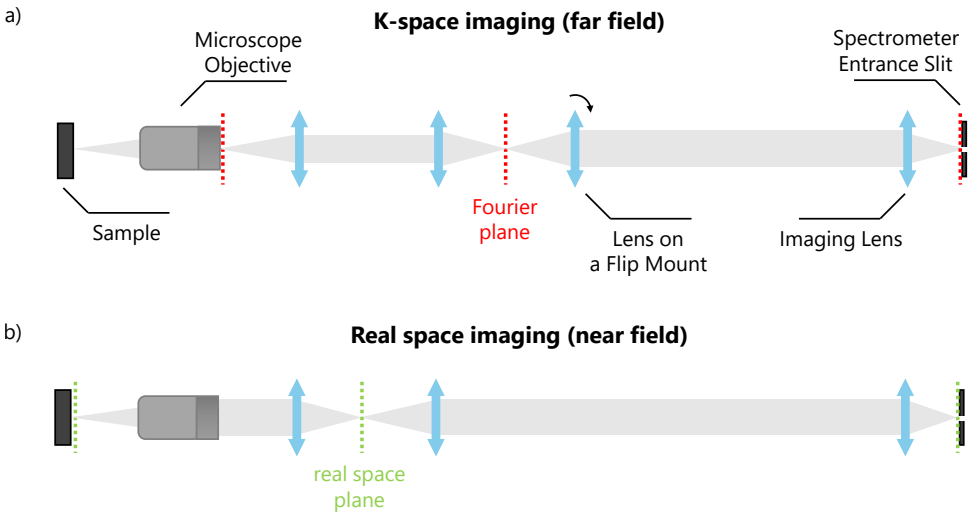

Figure 4.1. A schematic representation of the k-space (a) and real space (b) imaging. Even number of appropriately positioned lenses between the imaging objective and the detector entrance results in the Fourier plane imaging ((a), with the plane sketched with a red dotted line). Odd number allows for real-space plane imaging ((b), green dotted line).

Employing a 2-dimensional detector in such a system offers a spatial resolution in a single measurement. Then, by adding an additional lens at its focal length from the back of the objective (an infinity-corrected one), one can image the Fourier plane instead. According to the principles of geometric or Fourier optics, photons falling on a single lens at an given angle are focused in a point shifted from the central optical axis, at the lenses's focal length plane [203]. Hence, imaging this plane allows to image the angular distribution of the emission, directly translated into the momentum (wavevector k)-dependence. Adding further lenses in confocal configurations allows to observe either the far or the near field (real or momentum space), depending if the number of lenses is odd or even.

The most typically used k-space imaging setup consists of four lenses in a confocal configuration, as schematically presented in Fig. 4.1 (a). The imaged Fourier plane of the emission is sketched as a red dotted line. Using four lenses (instead of two) allows for additional momentum-space filtering of the emission, due to the creation of an intermediate Fourier plane (see Fig. 4.1 (a)). One can filter the signal in momentum space, if a spatial filter (e.g. an iris) is positioned in the conjugate plane.

Moreover, if one of the lenses (marked with a rotated arrow in Fig. 4.1 (a)) is placed on a removable mount (e.g. a flip mount), one can very easily switch between the real and k-space imaging. Changing the number of lenses between the objective and the detector to an even number allows to study the emission in real space, as shown in Fig. 4.1 (b). The number higher than one (e.g. three as in Fig. 4.1 (b)) allows to filter the emission in real space, using the intermediate real-space plane.

Such a plane in the latter configuration is sketched in Fig. 4.1 (b) with a green dotted line.

Now, the detection lenses in any configuration can be placed in the full PL optical setup to image both spaces and be adjusted for the experimental needs.

4.2 Optical experiments

The example of an optical setup used in the thesis experiments is presented in Fig. 4.2. In all measurements (apart from Part III), the sample was placed in the continuous flow liquid helium cryostat and cooled down to cryogenic temperature of $\sim 4.5\ K$ (or higher temperatures in temperature-dependent measurements). It was excited with a Ti:Sapphire laser, tuned to a reflectivity minimum of the microcavity, to reduce the loss due to the sample reflection. In Parts II and III a chopped CW laser was used, while Parts IV and V employed a pulsed Ti:Sapphire laser (with 76 MHz repetition rate), pumping an Optical Parametric Oscillator (OPO), to generate femtosecond-scale pulses of a desired wavelength. A high numerical aperture (NA) microscope objective was used to both focus the laser beam on a sample and collect the photoluminescence signal. The imaging setup consisted of four lenses in a confocal configuration, enabling near- and far-field emission imaging, as described in the section above. The signal was then imaged onto a monochromator slit and dispersed by a grating. The imaging was recorded by a high-efficiency EMCCD (Electron Multiplying Charge-Coupled Device), following the monochromator. In Part IV, the temporal resolution has been achieved by using a Si-cathode-based streak camera attached to a second exit of the monochromator.

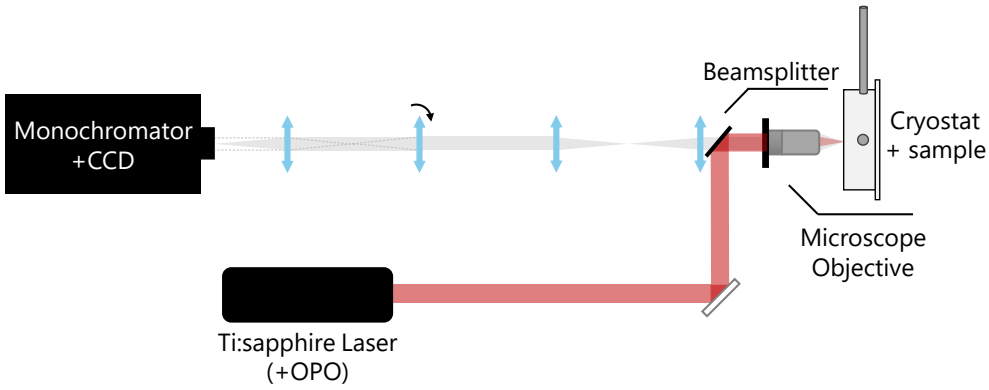

Figure 4.2. Schematic diagram of the experimental setup. The excitation laser beam is represented with a red line. The detected signal is marked in grey. The lens on a flippable mount is marked by the rotated black arrow. Adding or removing this lens allows to switch between the momentum- and real- spatial resolution.

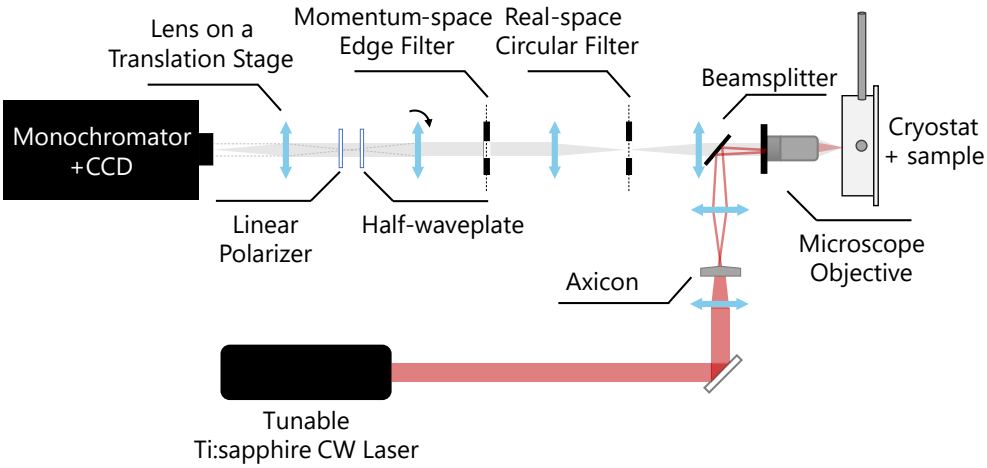

Figure 4.3. Schematic diagram of the experimental setup, allowing for the linear polarization-resolved measurements and for the real- and momentum-space filtering, as well as for the optical trapping. The ring-like shape of the excitation laser is achieved with the use of a conical lens (axicon) and two lenses in the excitation path. Moving the imaging lens on the translation stage allows for the optical tomography. This setup has been used in experiments described in Part II of this thesis.

Moreover, in Parts II and III, a polarization resolution of the measurements has been necessary, to study the spin properties of polaritons. As described in section 1.2.1, performing the measurements in four linear polarizations (horizontal-vertical H/V and diagonal-antidiagonal D/A basis, corresponding to the in-plane axes of the Poincaré sphere) allows to detect two Stokes parameters, S_1 and S_2 (see section 1.2.1 and Fig. 1.3). In the performed experiments, the polarization resolution has been achieved by placing a half-waveplate and a linear polarizer in the detection path, what is presented and marked in Fig. 4.3. Additionally, in Part III also the S_3 Stokes component has been measured. In order to do so, an additional quarter-waveplate has been added in the detection path, to perform the measurements in the circular (left-circular σ^- or right-circular σ^+) polarization basis.

Furthermore, the monochromator entrance slit allows to image only a single "slice" of the whole two-dimensional real/momentum space, selecting a vertical direction. In order to achieve a resolution in the direction perpendicular to the slit and detect spectra in the whole 2D momentum space, the imaging lens can be mounted on a translation stage in front of the monochromator (as marked in Fig. 4.3), allowing for the optical tomography [204]. Moving this lens in the horizontal direction allows to access, "slice by slice", the whole two-dimensional space (either real or reciprocal). This method has been used in Parts II and III of this thesis. Employing a motorized translation stage allows for the automation of the whole scan. Additionally, in Part II the signal has been filtered in the intermediate conjugate planes: with an optical

iris in the real space to reject the potential barrier signal, and a movable razor-blade edge in momentum space to reject the strong condensate emission around $k = 0$. The filters are also shown in the adjusted setup in Fig. 4.3.

Additionally, in Part II a circular optical trap has been created to minimize the overlap of polaritons with the excitonic reservoir, as described in section 2.6. In order to do so, an annular spatial distribution (a ring-like shape) of the laser on the sample has been created. It was achieved with the use of an axicon lens in a confocal configuration between two imaging lenses in the excitation path of the optical setup [147, 162], as presented in Fig. 4.3. This allowed for the laser beam shaping into a ring of $\sim 45\ \mu m$ in diameter.

The power density of the excitation laser has been adjusted with the use of reflective or polarization-based filters in the excitation path and measured with a power meter in front of the sample. The reflection of the pump laser from the sample has been achieved with selected spectral filters (e.g. a longpass filter) placed in the detection path.

4.3 Data analysis

The experimental data has been analysed, using Matlab and Origin software. All measured spectra (e.g. at each wavevector), after accounting for an experimental background, were fitted with appropriate curves, typically Lorentzian or Gaussian-shaped, in order to extract the energies, broadenings or intensities of the studied states. Further numerical analysis of the results has been done mostly using the Matlab software, with some custom-adjusted global fits implemented in the Origin software. All analysis has been adjusted to the specific experiment and data in question, with custom-made scripts. More specific data treatment or analysis performed in each study is described in respective parts and can be found in Methods and/or Supplementary Materials of the manuscripts.

Part II

Collective excitations of exciton-polariton condensates in a synthetic gauge field

Introduction

There have been an increasingly growing interest in the studies of the spin-orbit interactions in photonic systems and their use in designing synthetic Hamiltonians, nontrivial topologies, achieving and studying exceptional points or calculating the Berry curvature, among many others. Many of these remarkable phenomena have a potential and a goal to design photonic emulators of quantum Hamiltonians - a specific use of one system to study another, enabling to make general conclusions. Photonic systems offer a huge advantage of the experimental accessibility, as well as - very often - ease of design and tunability, in comparison to other solid state platforms. However, as photons' response to external fields and photon-photon interactions are typically very weak, exciton-polariton systems offer an additional big advantage in this regard, over the purely photonic systems. Their excitonic component makes them much more sensitive to a wide range of stimuli and adds a broad spectrum of possibilities for property tuning and influence via these external stimuli (such as electric and magnetic fields).

Importantly, polariton-polariton interactions and nonlinearities add an additional degree of freedom to tailor this system's properties and add to its complexity and its large potential, while still preserving the ease of the optical access. These interactions in fact allow for the particle relaxation and scattering, enabling the achievement of thermal quasi-equilibrium. Polaritons are known to condense much more easily than photons - even though both phases have been achieved, polariton condensates were experimentally demonstrated much sooner [71] than the photonic ones [205] and were more broadly investigated since.

Studies of polariton-polariton interactions are hugely important to understand their condensation and for all kinds of applications which employ the nonlinear properties of polaritons, such as optical switching and single-photon blockade devices [51]. Over the past few years, there have been several efforts and experimental approaches to establish the absolute value of the strength of these interactions, broadly introduced in section 2.4. However, as explained there, most of the studies disregarded the spin degree of freedom, while the interaction strengths for polaritons of the same (triplet) opposite (singlet) spin are known to be different. Creating a relatively easy experiment to measure the strength of spin-dependent interactions in any material platform would be critical to be able to study and potentially control this degree of freedom in future applications, yet the experimental efforts to extract both values, particularly both at the same time, proved to be scarce and challenging.

The polariton pseudospin, apart from its importance in the condensed phase, is vital in the aforementioned spin-orbit interaction (SOI) context also at low-density regime, as explained in sections 1.2.1 and 1.2.3. In solid state physics, SOI is a relativistic effect, which transforms static electric fields in the laboratory frame into magnetic fields in the frame of a moving electron. The magnetic fields interact with the spin of a studied particle, and result in a rich variety of quantum phenomena, including the realization of topological states [63, 206]. In optical microcavities, the momentum-dependent transverse-electric–transverse magnetic (TE-TM) splitting of the optical modes of the microcavity, together with a possible optical anisotropy (linear birefringence) of the cavity, create an effective magnetic field, which affects the polariton dynamics (see section 1.2.3 and Fig. 1.5). This is present also in the low-density regime, below the condensation threshold, mainly via the photonic component of the quasiparticles. Polariton pseudospin aligns with this effective field, what can be directly measured with the polarization of emitted light.

One can now combine the two contributions - (a) the presence of the effective gauge field, coming both from the inherent spin-orbit field and the cavity anisotropy, with (b) the importance of the spin-dependent interactions in a high density regime of the condensed phase. The inherent gauge field still affects polariton behavior, even if nonlinearities start to play an important role. Each of these contributions have been considered before separately, or purely theoretically, but never have all three components been realized experimentally in a single system. Former considerations focused mainly on the low density regime (and the effect of SOI on polaritons without interactions) or on the theoretical investigations in the high density regime (yet mostly without the cavity anisotropy).

Importantly in the context of this study, Shelykh et al. [177] showed how the difference in the interaction strengths for polaritons with parallel and antiparallel spins

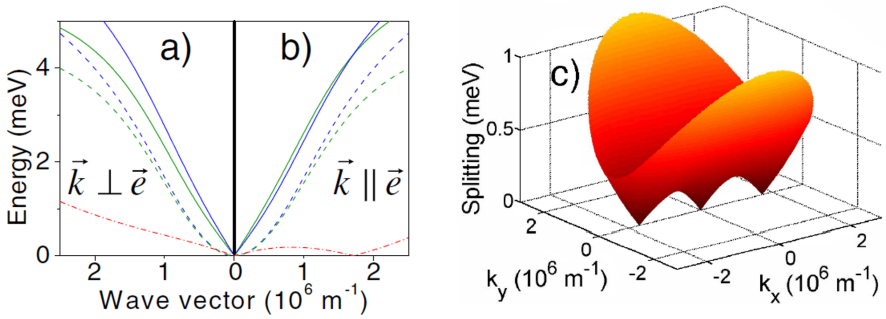

Figure 4.4. Bogoliubov split branches, reproduced from ref. [177]. Solid lines show renormalized lower-polariton branches and contrast them with the dispersion of bare lower-polariton modes (dashed lines) in the region of strong coupling. The anisotropic splitting between the Bogoliubov branches is shown in a dashdotted line. The wave vector is perpendicular to the condensate polarization in panel (a) and collinear with it in panel (b). Panel (c) shows the overall behavior of the splitting.

results in the anisotropy in the Bogoliubov spectrum of condensate elementary excitations. The authors considered theoretically, using the generalized Gross-Pitaevskii equation, a linearly polarized exciton-polariton condensate in a semiconductor microcavity. They showed a presence of two linearly polarized branches (eigenstates) of the excitations, with an anisotropic splitting between them, as one can see in Fig. 4.4. They did not include the cavity anisotropy – the two linearly polarized Bogoliubov branches were considered degenerate at $k = 0$. The results clearly show how the spin-anisotropy of the polariton-polariton interactions results in a remarkably different dispersion for excitation branches in directions parallel and perpendicular to the polarization axis of the condensate. Different dispersions of the two branches directly relate to different sound velocities of collective waves within the condensate (see equation 2.12). The quasi-linear Bogoliubov branches of two linear polarizations were found to only draw away from each other in the direction perpendicular to the polarization of the condensate, while they cross at a specific wavevector in the direction parallel. Hence, the splitting between the two branches (starting from zero at $k = 0$ for degenerate branches) only increases in one direction, while it comes back to zero at two points in momentum space (for positive and negative wavevector) in the parallel direction (as shown with red dash-dotted line in Fig. 4.4 (a) and (b)). Such a state crossing is known to be a diabolical point and is highly interesting from a theoretical and experimental standpoint. The authors also showed how this anisotropy noticeably affects the real-space dynamics of polariton condensates.

It's very important to note, that such a behavior of the states and their splitting may hugely resemble the effect of the gauge field (with the TE-TM and the anisotropy present) on the polariton branches in a low density regime. The lower polariton eigenstates also draw away from one another in one direction, while they cross in the direction perpendicular to it (as described in section 1.2.3), but the directions are then governed by the anisotropy axis (not the condensate polarization, as there is no condensate). However, one has to highlight, that the nature of these effects is completely different. One comes from the contributions of the TE-TM splitting and the spatial (often structural) anisotropy, while Shelykh et. al. considered the contributions of the spin-dependent interactions and the TE-TM field in a nonlinear regime, with no anisotropy present. In the former, the anisotropic branches are of the lower polariton modes, while in the latter - it's the renormalized branches of the excitations above the polarized condensate, that show the anisotropic behavior. This comparison will be further expanded below and in Fig. 4.6.

Figure 4.4, reproduced from Shelykh et al. [177], shows the calculated anisotropic dispersions of the Bogoliubov branches in two polarizations and the splitting between them. It also contrasts these renormalized lower-polariton branches (solid lines) with the dispersion of bare lower-polariton modes (dashed lines) in the region of strong coupling. The splitting between the renormalized states is shown in a dashdotted line. The results are presented as a function of the wavevector perpendicular to the condensate polarization in panel (a) and collinear with it in panel (b). Panel (c) shows the overall behavior of the splitting (in the whole two-dimensional momentum space).

Hence, the main conclusion of this theoretical study is that accounting for the polariton nonparabolic dispersion (strong coupling), the longitudinal-transverse splitting (TE-TM splitting, inherent to the microcavity), and the polarization-dependent interactions, one obtains substantial deviations of the quasiparticle spectrum from the typical Bogoliubov one. One can observe the anisotropy and strong polarization dependence of the dispersion, which results in characteristic asymmetric cross-like distributions of propagating polaritons in the real space [177]. The stark anisotropy can be observed even without any spatial anisotropy present in the non-interacting system.

Second important contribution has been done by Tercas et al. [28]. The authors considered theoretically the polariton dispersion relations when both the TE-TM splitting of the modes and the structure anisotropy of a semiconductor microcavity are considered. Those were found to combine into a non-Abelian gauge field for exciton-polaritons or cavity photons, as explained before in section 1.2.3. Quite similarly to the case of the interaction anisotropy considered above, such a field leads to the anisotropy of the dispersion spectra, but now even just for the TE and TM polarized modes of polaritons in the linear regime. The authors showed how the field texture can be tuned simply by rotating the sample and how it can range continuously from a Rashba to a monopolar field. So the polarization anisotropy of the lower-polariton branches can be observed when the TE-TM splitting and the cavity anisotropy are included. In essence it is inherently a photonic effect (so no strong coupling is necessary to observe it), but it proliferates into the polariton system. Even in the linear, non-interacting regime the gauge field's effect leads to remarkable focusing and conical diffraction effects.

This theoretical finding has been then experimentally evidenced e.g. by Gianfrate et al. [30]. Authors of this study showed the expected anisotropy of the lower polariton modes, subject to both the spin-orbit coupling and the inherent cavity anisotropy (in this case due to the inherent structure birefringence) in a high-quality planar microcavity with embedded GaAs QWs. They evidenced a small anisotropy of the lower polariton modes in the linear regime, which they then increased by an external magnetic field - another contributor to the overall gauge field (see equations 1.29 and 1.30, with Δ_Z being the Zeeman splitting). They used their findings to calculate a Berry curvature - an important topological metric. Additionally, they showed the polarization patterns in the momentum space (as values of the Stokes parameters), from which one can extract the pseudospin rotation in the gauge field.

Crucial findings of these two works are shown in Fig. 4.5. In (a) and (b), reproduced from Tercas et. al. [28], one can see the crossing branches of polaritons (or photons, as the approximation is parabolic) in the direction parallel to the anisotropy axis (a) and the effective non-Abelian gauge field in momentum space in (b). They are the calculated model curves. Figs. (c) and (d) are reproduced from Gianfrate et.al [30], showing the experimental evidence of these effects in a polariton microcavity. Inset in (c) additionally presents the splitting between the TE and TM branches, different in direction perpendicular and parallel to the anisotropy axis.

Furthermore, another important contribution to this topic which should be men-

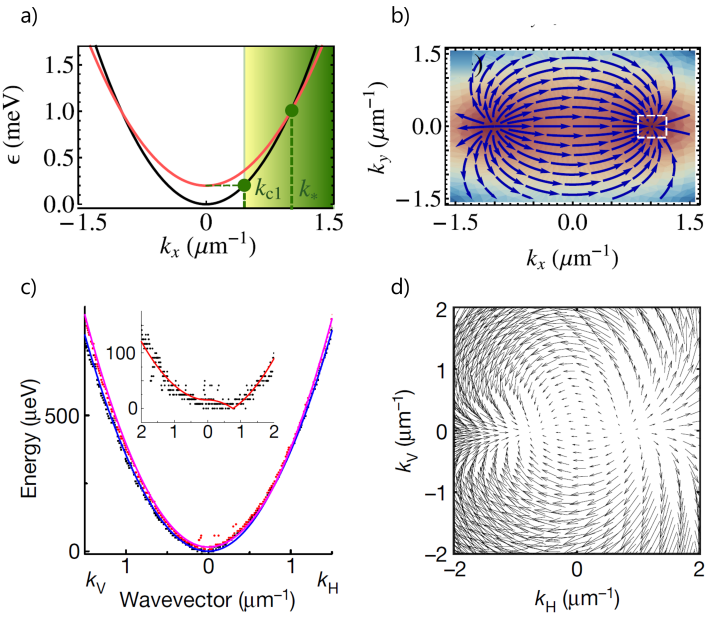

Figure 4.5. The non-Abelian gauge field effect on polariton eigenstates. (a) Polariton dispersion relation along the x direction (with $\varphi = 0$, hence, along the anisotropy axis), showing the two polariton branches crossing at the magic point k^*, reproduced from ref. [28]. The corresponding field texture is presented in (b) (also reproduced from this study). (c) and (d) are the experimental results of [30]. (c) Eigenmode energies (zero at about 1.6015 eV) along k_H and k_V (horizontal and vertical directions respectively). Inset: the energy splitting of the eigenmodes. Points are the experimental results, pink and blue lines are the fitted dispersions (model curves). (d) k-space in-plane pseudospin (S_1, S_2) texture, with monopolar texture around the crossing points.

tioned is the experimental and theoretical work by Polimeno et al. [36] in which the authors showed the effect of the non-Abelian gauge field on the exciton-polariton quantum flow in a polariton microcavity, affecting its trajectory. They did it in a perovskite-based smaple in which the inherent anisotropy (birefrengence) is known to be much bigger and the splitting is much higher. This was an experimental evidence of the effect of the field, not just the measurement of the field itself.

Now one should consider the most realistic case, where all the contributions are present and the polaritons enter the non-linear regime. It is typical that the cavity anisotropy is present and inherent to the optical microcavity (due to e.g. crystal birefringence) what results in the gauge field being non-Abelian, but the spin-anisotropic polariton-polariton interactions are crucial in the high density, renormalized regime. The interacting regime have been briefly considered in the Tercas et. al work described above [28], but only with the condensate put into motion in the vicinity of

the exceptional crossing-point. The authors showed how the spin-orbit coupling induces a breakdown of superfluidity and how the spatially homogeneous flows become unstable, evolving into spin textured states, such as stripes or domain walls.

However, such a case is essentially different from the ground-state condensate with close to zero momentum, with the renormalized excitation branches energetically above it. The authors calculated their dispersions in a general case (shown in the Supplemental Material [28]), but they proceeded to regard it solely at a specific wavevector. Importantly, their work is purely theoretical. The influence of the spin-dependent interactions on the overall effective field has not been evidenced, before the work presented in this part of the thesis.

Moreover, the authors did not suggest, how the experimental observation of the dispersion anisotropy could serve as a direct measure of both interaction constants - as it is also shown by this part of the thesis.

Finally, they used only a parabolic approximation of the dispersion (hence, a purely photonic case), while one can also account for the polariton dispersion non-parabolicity.

A summary and a comparison of all of the contributions described above is presented in Fig. 4.6, with an exemplary set of parameters. (a) and (b) show the low-density lower polariton branches (the calculated eigenstates of the equation 1.28), with (b) or without (a) the cavity anisotropy α. They are the LP dispersions (in two linear polarizations) in a low density regime, with no polariton-polariton interactions present. Contrary, (c-f) are the calculated eigenstates of the renormalized lower polaritons - the excitations above a condensate in a high density, nonlinear regime, governed by the polariton-polariton interactions. Spin-anisotropy of the interaction strengths is included (with $\alpha_1 > 0$ and $\alpha_1 \gg |\alpha_2|$). In (c) and (e) no structural anisotropy (birefringence) α is present (as considered by Shelykh et al. [177]), while (d) and (f) accounts for the TE-TM splitting, cavity anisotropy and the spin-anisotropic interactions. In (c) and (d) $\alpha_2 < 0$ (the opposite-spin polaritons weakly attract, as it is typically found in literature), however (e) and (f) additionally show the same results with positive α_2, showing how its sign governs the overall branch splitting. The model accounting for all contributions is explicitly presented in the Results section of this part of the thesis. In all figures solid lines are the model eigenstates and the dashed green lines show the splitting between them as a function of the in-plane wavevector. The results are presented in two directions - perpendicular and parallel to the anisotropy axis (which is then translated into and aligned with the polarization of the condensate in (c-f)).

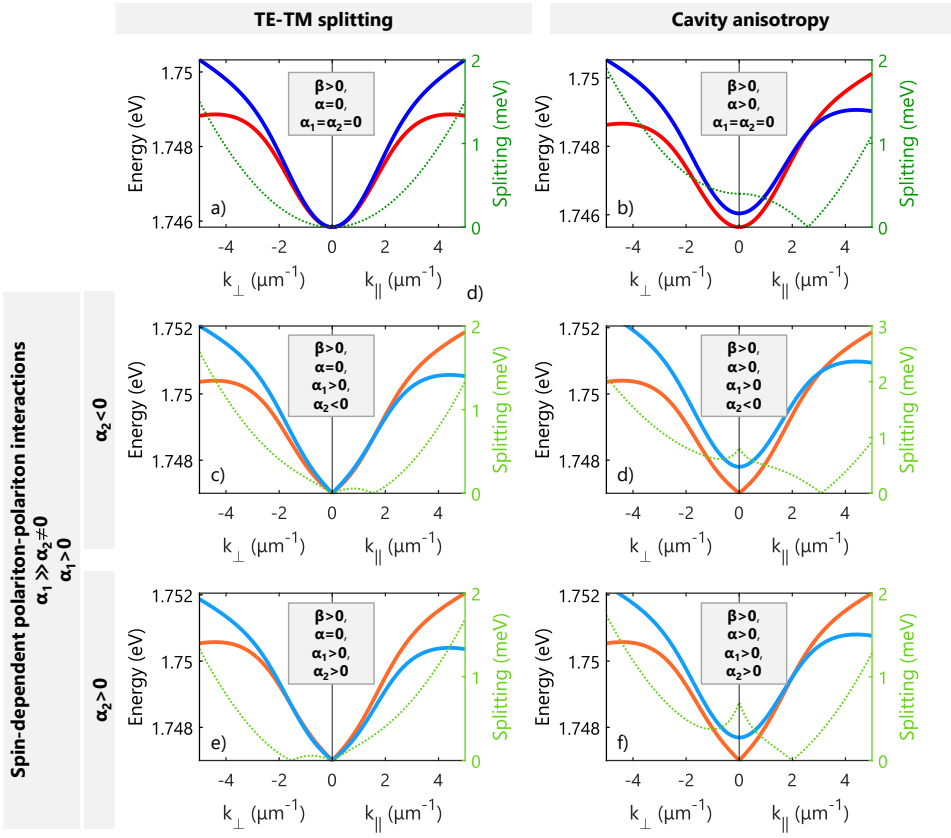

Figure 4.6. Comparison of the contribution of the TE-TM splitting, structural cavity anisotropy and the spin-dependent polariton-polariton interactions on the polariton eigenstates (in the circular polarization basis). Solid lines are the model eigenstates and the dashed green lines show the splitting between them as a function of the wavevector in two perpendicular directions in-plane. Parameters for all the graphs are: the exciton energy $E_{X0} = 1.750\ eV$, the cavity mode energy $E_{C0} = 1.748\ eV$, the effective refractive index (defining photon's effective mass) $n_C = 3.5$, the Rabi splitting $\hbar\Omega_R = 6\ meV$, the TE-TM splitting parameter $\beta = 30\ \mu eV\mu m^2$ and the Zeeman splitting $\Delta_Z = 0$ (no magnetic field). When nonzero: the structural anisotropy $\alpha = 0.2\ meV$ and the anisotropy angle $\varphi = 0$ (in b, d, f), the condensate energy $\epsilon_0 = 1.747\ eV$ and the polariton-polariton interactions are $\alpha_1 n = 500\ \mu eV$ (triplet) and $\alpha_2 n = \pm 100\ \mu eV$ (singlet) (in c-f). A large value of $\alpha_2 n$ has been selected to increase the visibility of its effect.

Contributions

This research has been a collaborative work. D. Biegańska (the author of this thesis) participated in designing the research question, she took part in rebuilding and modifying the optical setup (to adjust it to this study) and - supported by the coauthors - she performed all the experiments. Then she analysed the experimental data (using the Matlab software) with discussions and advice from all the authors. She wrote scripts helping to automate part of the analysis of the large amount of data. She employed the models available in literature to the specific data in question to fit it and extract the physical parameters, with discussions with all the authors. She also performed statistical analysis proving the validity of the applied model. She prepared all the graphs and wrote the initial version of the manuscript. All authors contributed to the final version of the text.

Results

Collective Excitations of Exciton-Polariton Condensates in a Synthetic Gauge Field

D. Biegańska,[1,2] M. Pieczarka,[1,2] E. Estrecho,[1] M. Steger,[3,†] D. W. Snoke,[3] K. West,[4] L. N. Pfeiffer,[4] M. Syperek,[2] A. G. Truscott,[5] and E. A. Ostrovskaya[1,*]

[1]*ARC Centre of Excellence in Future Low-Energy Electronics Technologies and Nonlinear Physics Centre, Research School of Physics, The Australian National University, Canberra, ACT 2601, Australia*

[2]*Department of Experimental Physics, Wrocław University of Science and Technology, Wybrzeże Wyspiańskiego 27, 50-370 Wrocław, Poland*

[3]*Department of Physics and Astronomy, University of Pittsburgh, Pittsburgh, Pennsylvania 15260, USA*

[4]*Department of Electrical Engineering, Princeton University, Princeton, New Jersey 08544, USA*

[5]*Laser Physics Centre, Research School of Physics, The Australian National University, Canberra, ACT 2601, Australia*

(Received 3 December 2020; revised 24 July 2021; accepted 21 September 2021; published 28 October 2021)

Collective (elementary) excitations of quantum bosonic condensates, including condensates of exciton polaritons in semiconductor microcavities, are a sensitive probe of interparticle interactions. In anisotropic microcavities with momentum-dependent transverse-electric–transverse-magnetic splitting of the optical modes, the excitations' dispersions are predicted to be strongly anisotropic, which is a consequence of the synthetic magnetic gauge field of the cavity, as well as the interplay between different interaction strengths for polaritons in the singlet and triplet spin configurations. Here, by directly measuring the dispersion of the collective excitations in a high-density optically trapped exciton-polariton condensate, we observe excellent agreement with the theoretical predictions for spinor polariton excitations. We extract the interaction constants for polaritons of the same and opposite spin and map out the characteristic spin textures in an interacting spinor condensate of exciton polaritons.

DOI: 10.1103/PhysRevLett.127.185301

Introduction.—Exciton polaritons (polaritons herein) are quasiparticles formed by excitons strongly coupled to confined photons, typically in a semiconductor optical microcavity. As interacting bosons, they form 2D nonequilibrium condensates analogous to Bose-Einstein condensates of ultracold atoms at sufficiently large particle densities above the phase transition threshold [1–4]. Furthermore, polaritons possess a spin degree of freedom inherited from optically active excitons coupled to photons [5–7]. Polariton spin has two allowed integer projections on the cavity growth axis, $\sigma_{\pm}$, making a polariton condensate effectively a two-component (spinor) gas described by a pseudospin parameter [1,8].

Polaritons interact through their excitonic components [6,9] with a spin-dependent strength [7,10–12]. The interaction strengths for polaritons of the same (triplet) α_1 and opposite (singlet) α_2 spin are related as $|\alpha_2| \ll \alpha_1$ [7,9,13]. Moreover, momentum-dependent transverse-electric–transverse magnetic (TE-TM) splitting of the optical modes of the microcavity [14] and optical anisotropy (linear birefringence) of the cavity create an effective magnetic field, which affects the polariton dynamics in the low-density regime, below the condensation threshold via the photonic component of the quasiparticles [15,16], similar to other optical systems [17,18]. In the high-density regime, above the condensation threshold, this synthetic field affects the condensate pseudospin dynamics [19–22] in addition to the effect of spinor polariton-polariton interactions. As a result, the single-particle dispersion of the polaritons in the low-density regime, as well as the dispersion of the collective excitations [23] of the condensate, are predicted to be strongly anisotropic [24–26]. Namely, the dispersion branches cross in one of the directions in the 2D momentum space at the so-called diabolical points, forming characteristic Dirac cones. The characteristic monopolar pseudospin texture around these crossing points in momentum space can be described in terms of an effective Rashba-like non-Abelian gauge field [25–27]. Studies of such gauge fields were previously limited to ultracold atomic Bose-Einstein condensates [28]. Observation of a synthetic (artificial) gauge field for polaritons in anisotropic microcavities offers the possibility to study topological phases of matter [29–31] and analog physics in optical systems [32]. However, despite the experimental progress in mapping the nontrivial spin textures in the single-particle (linear) regime [27], the predicted behavior of collective excitations in the interaction-dominated (nonlinear) regime above the condensation threshold has not been confirmed to date [33–36].

In this Letter, we observe the dispersion of collective excitations of a linearly polarized high-density polariton condensate in an optical trap. By performing polarization-resolved photoluminescence tomography, we detect the excitation branches in momentum space and observe a clear

asymmetry in the directions parallel and perpendicular to the cavity anisotropy axis. Moreover, we determine the triplet and singlet interaction strengths $\alpha_{1,2}$ and extract the spin textures and synthetic magnetic gauge field distribution in the nonlinear regime.

Experimental setup.—We use an ultrahigh-quality GaAs-based microcavity cooled down to ~4 K using a continuous-flow liquid helium cryostat. The very narrow linewidth of the polariton emission arising from the long cavity photon lifetime of > 100 ps in this sample [37,38] enables resolution of the non-negligible anisotropy of the polariton dispersion [27]. Off-resonant excitation of the sample with a continuous-wave laser beam, shaped by a conical lens into a ring of 45 μm in diameter, creates a round "box" optical trap [39,40] for polaritons. This trapping geometry minimizes the overlap of polaritons with the excitonic reservoir. We record the photoluminescence spectra in 2D momentum space by translating the imaging lens with respect to the monochromator slit. Polarization sensitivity is achieved by employing a half wave plate and a linear polarizer in the detection path, enabling us to record the spectra in four linear polarizations bases: horizontal and vertical and diagonal and antidiagonal with respect to the laboratory frame of reference. The experiments are performed on a region of the sample corresponding to a small, positive exciton-photon detuning of $\Delta = (2.70 \pm 0.21)$ meV and the excitonic Hopfield coefficient $X_0^2 \approx 0.585$, which defines the excitonic fraction of the polariton. Further details of the experiment can be found in the Supplemental Material [41].

Low-density regime.—Polariton eigenstates in the low-density limit can be described by a single-particle Hamiltonian in a circular polarization basis [25,27]:

$$H = \begin{pmatrix} \epsilon_{\mathrm{LP}}(k) & \frac{\Omega}{2} e^{-i\varphi} - \beta k^2 e^{-2i\theta_k} \\ \frac{\Omega}{2} e^{i\varphi} - \beta k^2 e^{2i\theta_k} & \epsilon_{\mathrm{LP}}(k) \end{pmatrix}, \quad (1)$$

where ϵ_{LP} is the lower-polariton dispersion extracted from a coupled-oscillator model, β is the TE-TM splitting parameter, and Ω is the cavity anisotropy constant. The source of Ω is the birefringence, which is caused by the small residual strain of the full multilayer structure [42–45]. The wave vector can be expressed as $\mathbf{k} = k(\cos\theta_k, \sin\theta_k)$, with θ_k denoting the in-plane propagation angle. The angle φ defines the anisotropy axis that depends on the sample orientation. By diagonalizing the Hamiltonian, one obtains two dispersive, linearly polarized eigenstates. The cavity anisotropy, Ω, breaks the cylindrical symmetry of the TE-TM splitting, resulting in both energy and polarization splitting at $k = 0$, as shown in Figs. 1(a),(c),(d). The two dispersion branches diverge in the direction perpendicular to the anisotropy axis ($k_\perp$), but cross in the direction parallel to it ($k_\parallel$). The crossing point occurs at $k_\parallel^* = \sqrt{\Omega/(2\beta)}$, where the effects due to TE-TM splitting and optical anisotropy cancel each other [Fig. 1(d)].

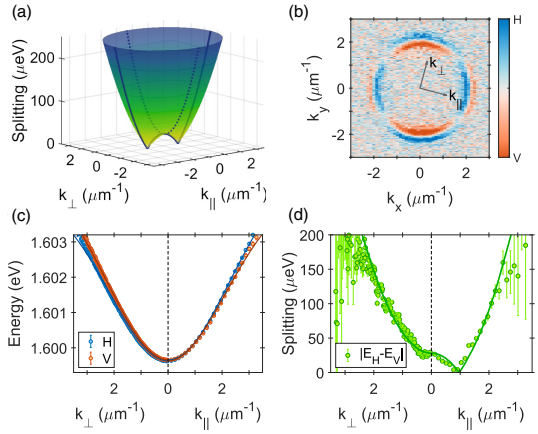

FIG. 1. Polariton dispersion in the low-density regime. (a) Energy splitting between the polariton eigenstates, calculated from Eq. (1), with the cross sections in the directions parallel (solid line) and perpendicular (dotted line) to the anisotropy axis. (b) Cross section of the Stokes vector component S_1 at the constant energy $E = 1.60154$ eV in the measurement (k_x, k_y) and anisotropy $(k_\parallel, k_\perp)$ frames of reference. (c) Polariton eigenstates and (d) their energy splitting extracted from the measured dispersions in the directions $k_\parallel$ and $k_\perp$. Solid lines are the model fits.

To apply this model to the experimental data, we fit the polarization-resolved spectra for each wave vector with a Lorentzian function and extract the energy of the eigenstate from the spectral peak. Subsequently, by fitting the measured dispersions with the eigenvalues of Eq. (1), as shown in Fig. 1(c), we find the values $\beta = (14.89 \pm 0.92)\ \mu\mathrm{eV}\,\mu\mathrm{m}^2$, $\Omega = (28.1 \pm 2.2)\ \mu\mathrm{eV}$, and $\varphi = -15°$. Hence, the crossing point occurs at $k_\parallel^* = 0.971\ \mu\mathrm{m}^{-1}$, and $k_\parallel$ is $-15°$ from the $+x$ axis [see the orientation of the frames of reference in Fig. 1(b)]. These measured parameters are essential for the analysis of the collective excitations in the high-density regime.

For each of the eigenstates, we also extract two components of the Stokes vector, S_1, S_2, which correspond to the polarization state or in-plane pseudospin of the polaritons. They are calculated from the polarized photoluminescence intensities I using the formulas $S_1 = (I_H - I_V)/(I_H + I_V)$ and $S_2 = (I_D - I_A)/(I_D + I_A)$. An example of the extracted texture of the S_1 component is presented in Fig. 1(b) and is consistent with the previous measurements in high-quality GaAs-based microcavities [27]. This is a typical texture arising from TE-TM splitting, which is the dominant effect at large $k > k_\parallel^*$. The full in-plane pseudospin textures of the single-particle eigenstates are shown in the Supplemental Material [41].

Condensate excitations.—By increasing the pump power above the condensation threshold, we create a high-density,

single-mode condensate in the Thomas-Fermi regime [39,46], formed in an optically induced potential trap. The condensate emission is highly polarized, with 95% of linear polarization oriented parallel to the anisotropy angle $\varphi = -15°$. A similar pinning of the condensate polarization to a given direction in the sample is routinely observed in different types of samples [47–51] and is not a signature of the expected stochastic buildup of polarization due to spontaneous symmetry breaking [52]. Here, we provide strong evidence that the pinning of the condensate polarization arises from the optical anisotropy of the cavity. This effect is undetectable in low-quality samples, where the anisotropic splitting Ω is much smaller than the spectral linewidths.

To study dispersion of the condensate excitations, we fix the pump power to the highest value available in our experiment (see the Supplemental Material [41]), where the interaction-induced effects are the strongest, and filter out the strong contribution of the condensate near $k = 0$ with an edge filter in momentum space. This allows us to detect the much weaker emission from the excitations without saturating the camera [46]. We use a vertically (horizontally) oriented edge to block the emission from $k_x < 0.55\ \mu\text{m}^{-1}$ ($k_y < 0.5\ \mu\text{m}^{-1}$). Tomographic scans are performed for each edge filter orientation and combined to reconstruct a 2D excitation spectrum. A constant-energy slice of the scans is presented in Fig. 2(a) showing the momentum-resolved S_1 texture and the edges (dashed lines) of the filter. A circular real-space aperture is also used to block the photoluminescence from the annular barrier of the optical trap.

The images of the collective excitation branches along $k_\perp$ at $k_\parallel = 0$ for horizontal and vertical polarizations are shown in Figs. 2(b),(c). The residual emission at the condensate energy has the characteristic Airy pattern arising from the diffraction on the real-space filter [46]. Above the condensate energy, clear Bogoliubov excitation branches are seen in both orthogonal polarizations. The negative or ghost branches [46] are also detectable but are extremely weak (see the Supplemental Material [41]); therefore, we focus on the much brighter normal branches in our detailed analysis. At a constant energy slice

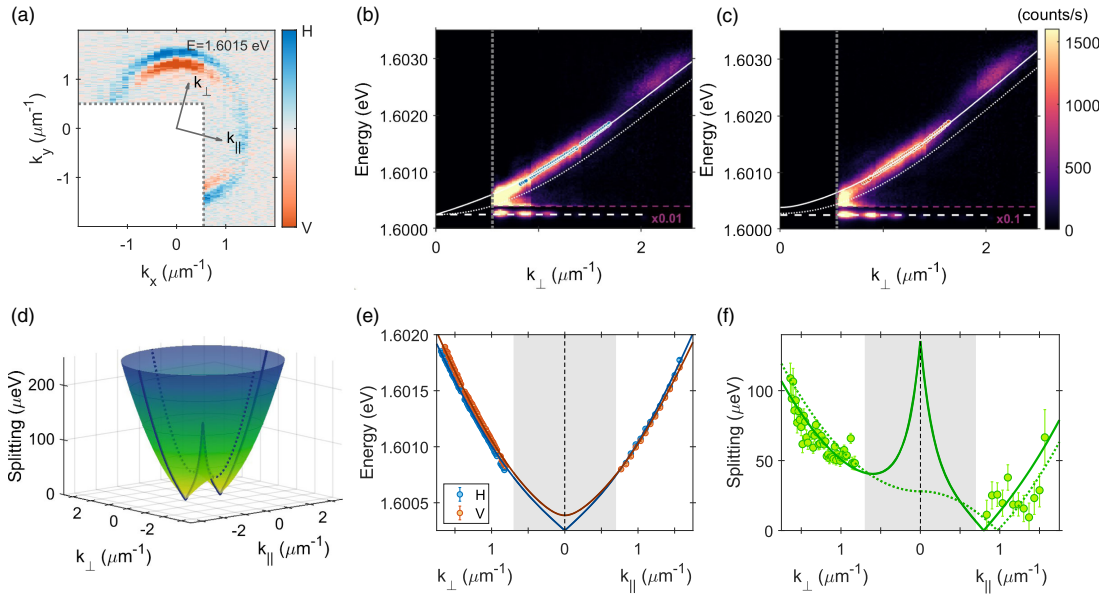

FIG. 2. Dispersion of collective excitations in the high-density regime. (a) Cross section of the Stokes vector component S_1 at the constant energy $E = 1.60154$ eV. Gray dotted lines mark the edges of the filtered area. The frames of reference are marked as in Fig. 1(b). (b),(c) Examples of the photoluminescence spectra at $k_\parallel = 0$ in (b) horizontal (H) and (c) vertical (V) polarization basis. Data points show energies extracted from fitting, white solid lines—the fitted model, and white dotted lines—single-particle dispersions. White dashed line marks the energy of the condensate $E = \mu = 1.600252$ eV and the gray dotted line is the edge of the spatial filter in momentum space. The condensate emission in the image is attenuated by a factor of 0.01 (b) and 0.1 (c). (d) Energy splitting between the excitations predicted by the model with the cross sections in the directions parallel (solid line) and perpendicular (dotted line) to the anisotropy axis. (e) Dispersions and (f) energy splitting between the collective excitations in the directions parallel and perpendicular to the condensate polarization direction with the corresponding theoretical fits (solid lines). Green dashed line in (f) shows the energy splitting for the single-particle states. Gray shaded area in (e),(f) marks the range of emission blocked by the edge filter.

[see Fig. 2(a)], the two branches have different polarizations and wave vectors. Equivalently, the dispersions are split as shown in Fig. 2(e). As predicted by theory and shown in Fig. 2(d), the energy splitting is highly anisotropic, which is confirmed by the experimental data in Fig. 2(f). As in the low-density limit (Fig. 1), the collective excitation branches diverge in the direction perpendicular to the anisotropy axis (along $k_\perp$) and cross in the orthogonal direction (along $k_\parallel$).

The experimental results can be modeled by solving the linearized equations for excitation eigenstates within the mean-field framework, as described in Ref. [25]. Taking into account the optical anisotropy and the TE-TM splitting, the excitations of a linearly polarized condensate at $k = 0$ result in four dispersion branches $\pm\epsilon^{L,U}$—two for positive and two for negative energies with respect to the condensate energy (chemical potential) $E = \mu$.

Expressed in the basis aligned to the cavity anisotropy axis, the positive excitation branches can be written as:

$$\epsilon^U(q) = \sqrt{(\Omega + \epsilon(q) \mp \beta q^2)(\Omega + \epsilon(q) \mp \beta q^2 + 2(\alpha_1 - \alpha_2)n)}$$
$$\epsilon^L(q) = \sqrt{(\epsilon(q) \pm \beta q^2)(\epsilon(q) \pm \beta q^2 + 2(\alpha_1 + \alpha_2)n)}, \qquad (2)$$

where $\epsilon(q) = \epsilon_{\mathrm{LP}}(q) - \epsilon_{\mathrm{LP}}(0)$, and $n_{\mathrm{tot}} = 2n$ is the total condensate density. Here the wave vector is aligned to the anisotropy axis such that $q = k_{\parallel,\perp}$, and the order of the $\pm$ and $\mp$ signs corresponds to $k_\parallel$ and $k_\perp$. The two branches inherit the anisotropic behavior of the single-particle dispersions, as shown by the energy splitting in k space [see Fig. 2(d)]. However, the crossing points k^* now also depend on the spin-dependent interaction constants.

Since the parameters β and Ω are known from the low-density measurements, we fit the measured dispersion of excitations using $\alpha_1 n$ and $\alpha_2 n$ as fitting parameters. Good agreement between the experimental data and the theoretical model is illustrated in Figs. 2(e),(f). One can observe a shift of the crossing points k^* with respect to the low-density case, directly induced by the polariton-polariton interactions in the condensed state. The resulting values are $\alpha_1 n = (322 \pm 12)\ \mu$eV for the polaritons in the triplet spin configuration and $\alpha_2 n = (9 \pm 15)\ \mu$eV in the singlet configuration, with the corresponding chemical potential $\mu = (\alpha_1 + \alpha_2)n - (\Omega/2) = (317 \pm 20)\ \mu$eV. The condensate density is measured [46] to be $\sim 2200\ \mu\mathrm{m}^{-2}$. This yields the interaction constants $\alpha_1 = (0.293 \pm 0.029)\ \mu\mathrm{eV}\,\mu\mathrm{m}^2$, while $\alpha_2 = (0.008 \pm 0.014)\ \mu\mathrm{eV}\,\mu\mathrm{m}^2$. These measured values are in good agreement with previous estimates. For polaritons in GaAs-based samples, it is common to neglect the singlet contribution to the total blueshift. This assumption is fully supported by our result, with α_2 around 2 orders of magnitude smaller than α_1. Our values yield the ratio $\alpha_2/\alpha_1 = (0.027 \pm 0.048)$, being positive and smaller than the common assumptions [7,9] for the GaAs system. The relative uncertainty of the ratio is high due to the uncertainty in individual interaction constants, which precludes a clear determination of its sign. However, taking into account the spin-dependent interactions and the nonzero (positive) value of α_2 is essential to properly model the polarization-resolved collective excitations spectra, as demonstrated by statistical analysis of the goodness of fit (see the Supplemental Material [41]). We note that the small, positive ratio of α_2/α_1 falls into the known region of stability of phase space for a linearly polarized condensate [7,12]. In contrast to previous reports, our approach enables a direct

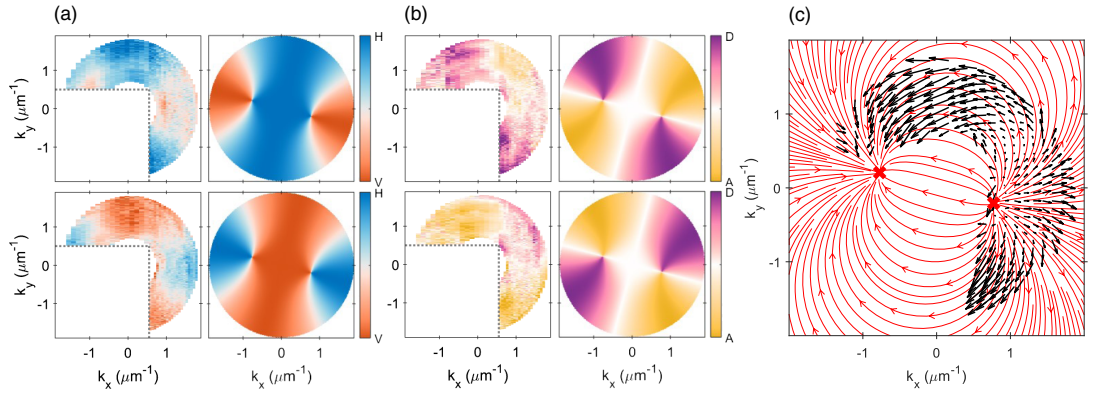

FIG. 3. (a) S_1 and (b) S_2 components of the Stokes vector for the collective excitations. Shown are experimental (left column) and theoretical (right column) results for the lower excitation branch ϵ^L (top row) and the upper branch ϵ^U (bottom row). Color scales are normalized to the maximum of the Stokes parameter, where the maximum Stokes amplitudes of the experimental results are around 40%. (c) Calculated pseudospin texture of ϵ^U (black arrows), plotted over the field texture obtained from the theoretical model. Red crosses mark the positions of the crossing points.

measurement of both values. The corresponding exciton-exciton interaction strengths, defined as $\alpha_{1,2}^{\mathrm{ex}} = N_{\mathrm{QW}}(\alpha_{1,2}/X_0^2)$ where $N_{\mathrm{QW}} = 12$ is the number of quantum wells, have the values of $\alpha_1^{\mathrm{ex}} = (10.3 \pm 1.1)\ \mu\mathrm{eV}\,\mu\mathrm{m}^2$ and $\alpha_2^{\mathrm{ex}} = (0.2 \pm 1.7)\ \mu\mathrm{eV}\,\mu\mathrm{m}^2$, which are in good agreement with previously reported values for the GaAs microcavities [39,53].

Spin texture of excitations.—The in-plane pseudospin of the collective excitations is characterized by the Stokes vector for the excitation eigenstates. Extracted polarization patterns are presented in the left columns of Figs. 3(a),(b), with the right columns showing the corresponding solution of the full theoretical model. To highlight the contrast in the patterns in spite of a very small splitting between the branches, we calculate the maximum Stokes vector components at the energies slightly offset from the eigenstates (the details of the analysis can be found in the Supplemental Material [41]). The experimental results show a good correspondence to the polarization patterns of the eigenstates expected from the model. The resulting pseudospin textures [Fig. 3(c)] show a pattern similar to that reported in the single-particle case [27]. However, the existence and position of the diabolical points with the associated effective monopolar magnetic field is now governed not only by the ratio of Ω and β but also by the polariton interactions since they arise from the collective (Bogoliubov) excitations of an interacting condensate. The exact crossing points and the corresponding monopoles in the pseudospin patterns are not directly accessible in our experiment, being too close to the strong condensate emission. Nevertheless, a clear manifestation of such a gauge field texture is visible in the experimental data [Fig. 3(c)].

Conclusions.—In this Letter, we have demonstrated anisotropy of collective excitations in a spinor exciton-polariton condensate, which results from the innate spin anisotropy of polariton interaction and the optical anisotropy (birefringence) of the microcavity under study. The optical anisotropy provides the strongest contribution to the anisotropy of the collective excitation branches in our GaAs-based system. Our experimental method enables a new, direct measurement of the interaction constants α_1 and α_2 for the polaritons in the triplet and singlet spin configurations and can be applied to other systems with different interaction strength ratios. In our sample, we confirmed a 2 orders of magnitude difference in the interaction strengths $\alpha_{1,2}$.

Furthermore, we extracted the pseudospin textures of the collective excitations in the polariton condensate resulting from the interplay between the effective magnetic field of the microcavity and spin-dependent interactions. The presence of diabolical points with the associated spin structure characteristic of a monopolelike magnetic field signifies that polariton systems in the high-density (nonlinear) regime can be used in future studies of synthetic gauge fields and topological physics [17,54]. The dominant role of the cavity birefringence in the anisotropy of collective excitations points to a straightforward way to design synthetic gauge fields for quantum liquids of light by tailoring the optical anisotropy of microcavities [32,55–58].

This work was supported by the Australian Research Council (ARC) through the Centre of Excellence Grant No. CE170100039. D. B., M. P., and M. S. acknowledge the support from the National Science Center, Grant No. 2018/30/E/ST7/00648, and M. P. acknowledges the support from the Foundation for Polish Science in the START program. The work of M. S., D. S., L. P. and K. W. was supported by the National Science Foundation (Grant No. DMR-2004570). The work of L. P. and K. W. was additionally supported by the Gordon and Betty Moore Foundation (GBMF-4420) and by the National Science Foundation MRSEC programme through the Princeton Center for Complex Materials (Grant No. DMR-0819860).

*Corresponding author.
elena.ostrovskaya@anu.edu.au
†Present address: National Renewable Energy Lab, Golden, Colorado 80401, USA.

[1] A. Kavokin, J. J. Baumberg, G. Malpuech, and F. P. Laussy, *Microcavities* (Oxford University Press, Inc., USA, 2008).
[2] D. Sanvitto, F. M. Marchetti, M. H. Szymańska, G. Tosi, M. Baudisch, F. P. Laussy, D. N. Krizhanovskii, M. S. Skolnick, L. Marrucci, A. Lemaître, J. Bloch, C. Tejedor, and L. Viña, Persistent currents and quantized vortices in a polariton superfluid, Nat. Phys. **6**, 527 (2010).
[3] A. Amo, D. Sanvitto, F. P. Laussy, D. Ballarini, E. d. Valle, M. D. Martin, A. Lemaître, J. Bloch, D. N. Krizhanovskii, M. S. Skolnick, C. Tejedor, and L. Viña, Collective fluid dynamics of a polariton condensate in a semiconductor microcavity, Nature (London) **457**, 291 (2009).
[4] J. Kasprzak, M. Richard, S. Kundermann, A. Baas, P. Jeambrun, J. M. J. Keeling, F. M. Marchetti, M. H. Szymańska, R. André, J. L. Staehli, V. Savona, P. B. Littlewood, B. Deveaud, and L. S. Dang, Bose-Einstein condensation of exciton polaritons, Nature (London) **443**, 409 (2006).
[5] I. A. Shelykh, A. V. Kavokin, Y. G. Rubo, T. C. H. Liew, and G. Malpuech, Polariton polarization-sensitive phenomena in planar semiconductor microcavities, Semicond. Sci. Technol. **25**, 013001 (2010).
[6] I. Carusotto and C. Ciuti, Quantum fluids of light, Rev. Mod. Phys. **85**, 299 (2013).
[7] M. Vladimirova, S. Cronenberger, D. Scalbert, K. V. Kavokin, A. Miard, A. Lemaître, J. Bloch, D. Solnyshkov, G. Malpuech, and A. V. Kavokin, Polariton-polariton interaction constants in microcavities, Phys. Rev. B **82**, 075301 (2010).
[8] L. Pitaevskii and S. Stringari, *Bose-Einstein Condensation and Superfluidity* (Oxford University Press, New York, 2016).
[9] B. Deveaud-Plédran, Polariton interactions in semiconductor microcavities, C. R. Phys. **17**, 874 (2016).

[10] P. Renucci, T. Amand, X. Marie, P. Senellart, J. Bloch, B. Sermage, and K. V. Kavokin, Microcavity polariton spin quantum beats without a magnetic field: A manifestation of Coulomb exchange in dense and polarized polariton systems, Phys. Rev. B **72**, 075317 (2005).

[11] N. Takemura, S. Trebaol, M. Wouters, M. T. Portella-Oberli, and B. Deveaud, Polaritonic Feshbach resonance, Nat. Phys. **10**, 500 (2014).

[12] O. Bleu, G. Li, J. Levinsen, and M. M. Parish, Polariton interactions in microcavities with atomically thin semiconductor layers, Phys. Rev. Research **2**, 043185 (2020).

[13] A. V. Sekretenko, S. S. Gavrilov, and V. D. Kulakovskii, Polariton-polariton interactions in microcavities under a resonant 10 to 100 picosecond pulse excitation, Phys. Rev. B **88**, 195302 (2013).

[14] G. Panzarini, L. C. Andreani, A. Armitage, D. Baxter, M. S. Skolnick, V. N. Astratov, J. S. Roberts, A. V. Kavokin, M. R. Vladimirova, and M. A. Kaliteevski, Cavity-polariton dispersion and polarization splitting in single and coupled semiconductor microcavities, Phys. Solid State **41**, 1223 (1999).

[15] C. Leyder, M. Romanelli, J. P. Karr, E. Giacobino, T. C. H. Liew, M. M. Glazov, A. V. Kavokin, G. Malpuech, and A. Bramati, Observation of the optical spin Hall effect, Nat. Phys. **3**, 628 (2007).

[16] A. Kavokin, G. Malpuech, and M. Glazov, Optical Spin Hall Effect, Phys. Rev. Lett. **95**, 136601 (2005).

[17] K. Rechcińska, M. Król, R. Mazur, P. Morawiak, R. Mirek, K. Łempicka, W. Bardyszewski, M. Matuszewski, P. Kula, W. Piecek, P. G. Lagoudakis, B. Piętka, and J. Szczytko, Engineering spin-orbit synthetic Hamiltonians in liquid-crystal optical cavities, Science **366**, 727 (2019).

[18] K. Y. Bliokh, F. J. Rodríguez-Fortuño, F. Nori, and A. V. Zayats, Spin-orbit interactions of light, Nat. Photonics **9**, 796 (2015).

[19] E. Kammann, T. C. H. Liew, H. Ohadi, P. Cilibrizzi, P. Tsotsis, Z. Hatzopoulos, P. G. Savvidis, A. V. Kavokin, and P. G. Lagoudakis, Nonlinear Optical Spin Hall Effect and Long-Range Spin Transport in Polariton Lasers, Phys. Rev. Lett. **109**, 036404 (2012).

[20] R. Hivet, H. Flayac, D. D. Solnyshkov, D. Tanese, T. Boulier, D. Andreoli, E. Giacobino, J. Bloch, A. Bramati, G. Malpuech, and A. Amo, Half-solitons in a polariton quantum fluid behave like magnetic monopoles, Nat. Phys. **8**, 724 (2012).

[21] P. Cilibrizzi, H. Sigurdsson, T. C. H. Liew, H. Ohadi, A. Askitopoulos, S. Brodbeck, C. Schneider, I. A. Shelykh, S. Höfling, J. Ruostekoski, and P. Lagoudakis, Half-skyrmion spin textures in polariton microcavities, Phys. Rev. B **94**, 045315 (2016).

[22] D. Schmidt, B. Berger, M. Bayer, C. Schneider, M. Kamp, S. Höfling, E. Sedov, A. Kavokin, and M. Aßmann, Dynamics of the optical spin Hall effect, Phys. Rev. B **96**, 075309 (2017).

[23] S. Utsunomiya, L. Tian, G. Roumpos, C. W. Lai, N. Kumada, T. Fujisawa, M. Kuwata-Gonokami, A. Löffler, S. Höfling, A. Forchel, and Y. Yamamoto, Observation of Bogoliubov excitations in exciton-polariton condensates, Nat. Phys. **4**, 700 (2008).

[24] I. A. Shelykh, Y. G. Rubo, G. Malpuech, D. D. Solnyshkov, and A. Kavokin, Polarization and Propagation of Polariton Condensates, Phys. Rev. Lett. **97**, 066402 (2006).

[25] H. Terças, H. Flayac, D. D. Solnyshkov, and G. Malpuech, Non-Abelian Gauge Fields in Photonic Cavities and Photonic Superfluids, Phys. Rev. Lett. **112**, 066402 (2014).

[26] D. Solnyshkov and G. Malpuech, Chirality in photonic systems, C. R. Phys. **17**, 920 (2016).

[27] A. Gianfrate, O. Bleu, L. Dominici, V. Ardizzone, M. De Giorgi, D. Ballarini, G. Lerario, K. W. West, L. N. Pfeiffer, D. D. Solnyshkov, D. Sanvitto, and G. Malpuech, Measurement of the quantum geometric tensor and of the anomalous Hall drift, Nature (London) **578**, 381 (2020).

[28] Y. J. Lin, K. Jiménez-García, and I. B. Spielman, Spin-orbit-coupled Bose-Einstein condensates, Nature (London) **471**, 83 (2011).

[29] M. Z. Hasan and C. L. Kane, Colloquium: Topological insulators, Rev. Mod. Phys. **82**, 3045 (2010).

[30] S. Klembt, T. H. Harder, O. A. Egorov, K. Winkler, R. Ge, M. A. Bandres, M. Emmerling, L. Worschech, T. C. Liew, M. Segev, C. Schneider, and S. Höfling, Exciton-polariton topological insulator, Nature (London) **562**, 552 (2018).

[31] C.-E. Bardyn, T. Karzig, G. Refael, and T. C. H. Liew, Topological polaritons and excitons in garden-variety systems, Phys. Rev. B **91**, 161413(R) (2015).

[32] A. Fieramosca, L. Polimeno, G. Lerario, L. D. Marco, M. D. Giorgi, D. Ballarini, L. Dominici, V. Ardizzone, M. Pugliese, V. Maiorano, G. Gigli, C. Leblanc, G. Malpuech, D. Solnyshkov, and D. Sanvitto, Chromodynamics of photons in an artificial non-Abelian magnetic Yang-Mills field, arXiv:1912.09684.

[33] V. Kohnle, Y. Léger, M. Wouters, M. Richard, M. T. Portella-Oberli, and B. Deveaud-Plédran, From Single Particle to Superfluid Excitations in a Dissipative Polariton Gas, Phys. Rev. Lett. **106**, 255302 (2011).

[34] M. Pieczarka, M. Syperek, L. Dusanowski, J. Misiewicz, F. Langer, A. Forchel, M. Kamp, C. Schneider, S. Hoefling, A. Kavokin, G. Sęk, Ł. Dusanowski, J. Misiewicz, F. Langer, A. Forchel, M. Kamp, C. Schneider, S. Höfling, A. Kavokin, and G. Sęk, Ghost Branch Photoluminescence from a Polariton Fluid under Nonresonant Excitation, Phys. Rev. Lett. **115**, 186401 (2015).

[35] P. Stepanov, I. Amelio, J.-G. Rousset, J. Bloch, A. Lemaítre, A. Amo, A. Minguzzi, I. Carusotto, and M. Richard, Dispersion relation of the collective excitations in a resonantly driven polariton fluid, Nat. Commun. **10**, 3869 (2019).

[36] D. Ballarini, D. Caputo, G. Dagvadorj, R. Juggins, M. D. Giorgi, L. Dominici, K. West, L. N. Pfeiffer, G. Gigli, M. H. Szymańska, and D. Sanvitto, Directional Goldstone waves in polariton condensates close to equilibrium, Nat. Commun. **11**, 217 (2020).

[37] B. Nelsen, G. Liu, M. Steger, D. W. Snoke, R. Balili, K. West, and L. Pfeiffer, Dissipationless Flow and Sharp Threshold of a Polariton Condensate with Long Lifetime, Phys. Rev. X **3**, 041015 (2013).

[38] M. Steger, C. Gautham, D. W. Snoke, L. Pfeiffer, and K. West, Slow reflection and two-photon generation of microcavity exciton-polaritons, Optica **2**, 1 (2015).

[39] E. Estrecho, T. Gao, N. Bobrovska, D. Comber-Todd, M. D. Fraser, M. Steger, K. West, L. N. Pfeiffer, J. Levinsen, M. M. Parish, T. C. H. Liew, M. Matuszewski, D. W. Snoke, A. G. Truscott, and E. A. Ostrovskaya, Direct measurement of polariton-polariton interaction strength in the Thomas-Fermi regime of exciton-polariton condensation, Phys. Rev. B **100**, 035306 (2019).

[40] M. Pieczarka, M. Boozarjmehr, E. Estrecho, Y. Yoon, M. Steger, K. West, L. N. Pfeiffer, K. A. Nelson, D. W. Snoke, A. G. Truscott, and E. A. Ostrovskaya, Effect of optically induced potential on the energy of trapped exciton-polaritons below the condensation threshold, Phys. Rev. B **100**, 085301 (2019).

[41] See Supplemental Material at http://link.aps.org/supplemental/10.1103/PhysRevLett.127.185301 for a detailed description of the experimental setup and the sample, additional experimental data, and details on data analysis, including statistical analysis of the goodness of fit.

[42] T. Pusch, E. La Tona, M. Lindemann, N. C. Gerhardt, M. R. Hofmann, and R. Michalzik, Monolithic vertical-cavity surface-emitting laser with thermally tunable birefringence, Appl. Phys. Lett. **110**, 151106 (2017).

[43] A. K. Jansen van Doorn, M. P. van Exter, and J. P. Woerdman, Tailoring the birefringence in a vertical-cavity semiconductor laser, Appl. Phys. Lett. **69**, 3635 (1996).

[44] J. Frougier, G. Baili, I. Sagnes, D. Dolfi, J.-M. George, and M. Alouini, Accurate measurement of the residual birefringence in VECSEL: Towards understanding of the polarization behavior under spin-polarized pumping, Opt. Express **23**, 9573 (2015).

[45] R. Balili, B. Nelsen, D. W. Snoke, R. H. Reid, L. Pfeiffer, and K. West, Huge splitting of polariton states in microcavities under stress, Phys. Rev. B **81**, 125311 (2010).

[46] M. Pieczarka, E. Estrecho, M. Boozarjmehr, O. Bleu, M. Steger, K. West, L. N. Pfeiffer, D. W. Snoke, J. Levinsen, M. M. Parish, A. G. Truscott, and E. A. Ostrovskaya, Observation of quantum depletion in a non-equilibrium exciton–polariton condensate, Nat. Commun. **11**, 429 (2020).

[47] J. Kasprzak, R. André, L. S. Dang, I. A. Shelykh, A. V. Kavokin, Y. G. Rubo, K. V. Kavokin, and G. Malpuech, Build up and pinning of linear polarization in the Bose condensates of exciton polaritons, Phys. Rev. B **75**, 045326 (2007).

[48] R. Balili, V. Hartwell, D. Snoke, L. Pfeiffer, and K. West, Bose-Einstein Condensation of Microcavity Polaritons in a Trap, Science **316**, 1007 (2007).

[49] J. Levrat, R. Butté, T. Christian, M. Glauser, E. Feltin, J. F. Carlin, N. Grandjean, D. Read, A. V. Kavokin, and Y. G. Rubo, Pinning and Depinning of the Polarization of Exciton-Polariton Condensates at Room Temperature, Phys. Rev. Lett. **104**, 166402 (2010).

[50] M. Klaas, O. A. Egorov, T. C. H. Liew, A. Nalitov, V. Marković, H. Suchomel, T. H. Harder, S. Betzold, E. A. Ostrovskaya, A. Kavokin, S. Klembt, S. Höfling, and C. Schneider, Nonresonant spin selection methods and polarization control in exciton-polariton condensates, Phys. Rev. B **99**, 115303 (2019).

[51] I. Gnusov, H. Sigurdsson, S. Baryshev, T. Ermatov, A. Askitopoulos, and P. G. Lagoudakis, Optical orientation, polarization pinning, and depolarization dynamics in optically confined polariton condensates, Phys. Rev. B **102**, 125419 (2020).

[52] H. Ohadi, E. Kammann, T. C. H. Liew, K. G. Lagoudakis, A. V. Kavokin, and P. G. Lagoudakis, Spontaneous Symmetry Breaking in a Polariton and Photon Laser, Phys. Rev. Lett. **109**, 016404 (2012).

[53] A. S. Brichkin, S. I. Novikov, A. V. Larionov, V. D. Kulakovskii, M. M. Glazov, C. Schneider, S. Höfling, M. Kamp, and A. Forchel, Effect of Coulomb interaction on exciton-polariton condensates in GaAs pillar microcavities, Phys. Rev. B **84**, 195301 (2011).

[54] J. Ren, Q. Liao, F. Li, Y. Li, O. Bleu, G. Malpuech, J. Yao, H. Fu, and D. Solnyshkov, Nontrivial band geometry in an optically active system, Nat. Commun. **12**, 689 (2021).

[55] M. Król, H. Sigurdsson, K. Rechcińska, P. Oliwa, K. Tyszka, W. Bardyszewski, A. Opala, M. Matuszewski, P. Morawiak, R. Mazur, W. Piecek, P. Kula, P. G. Lagoudakis, B. Piętka, and J. Szczytko, Observation of second-order meron polarization textures in optical microcavities, Optica **8**, 255 (2021).

[56] C. E. Whittaker, T. Dowling, A. V. Nalitov, A. V. Yulin, B. Royall, E. Clarke, M. S. Skolnick, I. A. Shelykh, and D. N. Krizhanovskii, Optical analogue of Dresselhaus spin–orbit interaction in photonic graphene, Nat. Photonics **15**, 193 (2021).

[57] F. Liu and J. Li, Gauge Field Optics with Anisotropic Media, Phys. Rev. Lett. **114**, 103902 (2015).

[58] Q. Liao, C. Leblanc, J. Ren, F. Li, Y. Li, D. Solnyshkov, G. Malpuech, J. Yao, and H. Fu, Experimental Measurement of the Divergent Quantum Metric of an Exceptional Point, Phys. Rev. Lett. **127**, 107402 (2021).

Supplementary material

SUPPLEMENTAL MATERIAL
Collective excitations of exciton-polariton condensates in a synthetic gauge field

D. Biegańska,[1,2] M. Pieczarka,[1,2] E. Estrecho,[1] M. Steger,[3,*] D. W. Snoke,[3]
K. West,[4] L. N. Pfeiffer,[4] M. Syperek,[2] A. G. Truscott,[5] and E. A. Ostrovskaya[1,†]

[1] *ARC Centre of Excellence in Future Low-Energy Electronics Technologies and Nonlinear Physics Centre, Research School of Physics, The Australian National University, Canberra, ACT 2601, Australia*
[2] *Department of Experimental Physics, Wrocław University of Science and Technology, Wyb. Wyspiańskiego 27, 50-370 Wrocław, Poland*
[3] *Department of Physics and Astronomy, University of Pittsburgh, Pittsburgh, PA 15260, USA*
[4] *Department of Electrical Engineering, Princeton University, Princeton, NJ 08544, USA*
[5] *Laser Physics Centre, Research School of Physics, The Australian National University, Canberra, ACT 2601, Australia*

I. SAMPLE AND EXPERIMENTAL DETAILS

The sample under study was an ultrahigh-quality $3\lambda/2$ GaAs-based microcavity, consisting of distributed Bragg reflectors with 32 (top) and 40 (bottom) pairs of alternating $Al_{0.2}Ga_{0.8}As$/AlAs layers and an active region of 12 GaAs/AlAs quantum wells with the nominal thickness of 7 nm. The sample was excited with a CW Ti:Sapphire laser, tuned to a reflectivity minimum of the microcavity (around 720 *nm*), chopped with an acoustic optical modulator at 10 kHz and 1% duty cycle to minimise thermal heating of the sample. The annular spatial distribution of the laser on the sample was achieved with the use of an axicon lens in a confocal configuration between two imaging lenses in the excitation path of the optical setup (see Supplemental Figure 1), as in our previous works [1, 2]. A NA = 0.5 microscope objective was used to both image the laser beam and collect the photoluminescence signal from the sample. The imaging setup consisted of four lenses in a confocal configuration, enabling near- and far-field emission imaging. The signal was filtered in the intermediate conjugate planes: with an optical iris in the real space to reject the potential barrier signal and a movable razor-blade edge in momentum space to reject the strong condensate emission around $k = 0$. The signal was then imaged onto the monochromator slit and dispersed by a grating. In order to achieve a resolution in the direction perpendicular to the slit and detect the spectra in 2D momentum space, the imaging lens was mounted on a translation stage in front of the monochromator, allowing the optical tomography. Measurements were performed in four linear polarizations (horizontal-vertical H/V and diagonal-antidiagonal D/A basis, corresponding to the in-plane axes of the Poincaré sphere [3]). The polarization resolution was achieved by employing a half-waveplate and a linear polarizer in the detection path. In the case of excitations measurements two sets of such scans were recorded: one with the condensate emission covered in either the horizontal or vertical direction in momentum space. The imaging was recorded by a high-efficiency EMCCD camera (Andor iXon Ultra 888), following a Princeton Instruments IsoPlane 320 monochromator. The sketch of the experimental setup is presented in Supplemental Figure 1.

II. DATA TREATMENT AND ANALYSIS

Each polarized spectrum (at each wavevector) was fitted with a Lorentzian curve in order to extract the energies of the two eigenstates. An example of the measured photoluminescence signal with the fitted curves is presented in Supplemental Figure 2(b). Since the splitting between the two states is small, especially close to the crossing points, where it becomes smaller than the linewidth, one cannot clearly resolve two distinct peaks in the photoluminescence signal. However, using the polarized spectra one can clearly extract two modes separated in energy. The same method was used to extract the eigenstates in the low- and high-density regimes. Error bars are 95% confidence intervals obtained for the peak positions from the Levenberg-Marquardt algorithm.

* Current address: National Renewable Energy Lab, Golden, CO 80401, USA
† elena.ostrovskaya@anu.edu.au

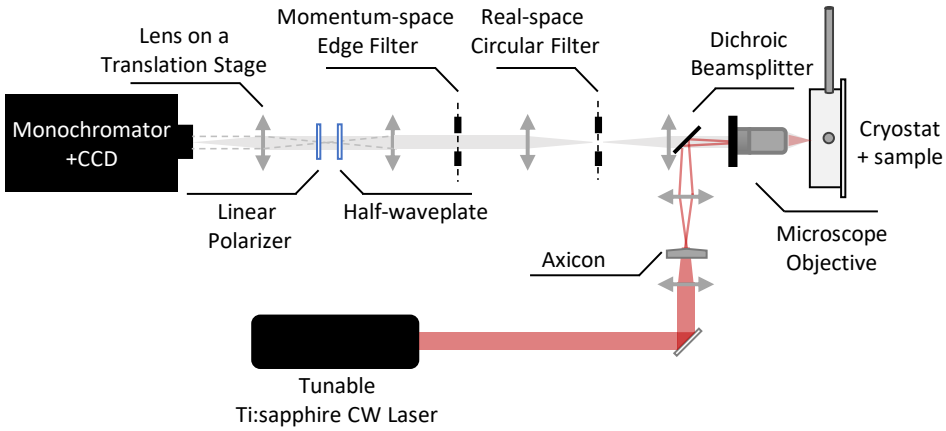

Supplemental Figure 1. Schematic diagram of the experimental setup.

After extracting the eigenstate energies in the directions perpendicular and parallel to the anisotropy axis, their dispersions were fitted with a solution of the model described in the main text (Eq. 1). Diagonalization of the Hamiltonian leads to a single-particle spectrum in the form of $\epsilon_{\pm}(k) = \epsilon_{LP}(k) \pm \sqrt{\frac{\Omega^2}{4} + \beta^2 k^4 - \Omega\beta k^2 \cos(2\theta_k - \varphi)}$), where $\epsilon_{LP}(k) = \frac{1}{2}\left(E_c(k) + E_X(k) - \sqrt{(E_c(k) - E_X(k))^2 + \hbar\Omega_{VRS}^2}\right)$, $E_c = E_{c0} + \frac{\hbar^2 k^2 c^2}{2E_{c0}n_c^2}$ is a cavity mode, and E_X corresponds to the exciton resonance energy. Using this formula for fitting low-density case data, the values of Ω and β were extracted, and used in the analysis of the collective excitation branches.

In the high-density regime, the full model (described in detail in Supplemental Material of ref. [4]) can be simplified to be written as follows:

$$L = \begin{pmatrix} -\epsilon - \alpha_1 n - \Omega/2 & -\alpha_2 n - \epsilon_a & -\alpha_1 n & -\alpha_2 n \\ -\alpha_2 n - \epsilon_b & -\epsilon - \alpha_1 n - \Omega/2 & -\alpha_2 n & -\alpha_1 n \\ \alpha_1 n & \alpha_2 n & \epsilon + \alpha_1 n + \Omega/2 & \alpha_2 n + \epsilon_b \\ \alpha_2 n & \alpha_1 n & \alpha_2 n + \epsilon_a & \epsilon + \alpha_1 n + \Omega/2 \end{pmatrix},$$

where $\epsilon_{a,b} = \beta(k_{||} \pm ik_{\perp})^2 - \Omega/2$. The eigenvalues of the matrix L correspond to the excitation eigenstates.

The full solution of this model can be further simplified by considering two directions that are relevant to the experimental observations, i.e. parallel and perpendicular to the optical anisotropy axis:

$$\epsilon^L(k_{||}) = \sqrt{\left(\epsilon + \beta k_{||}^2\right)\left(\epsilon + \beta k_{||}^2 + 2(\alpha_1 + \alpha_2)n\right)},$$

$$\epsilon^U(k_{||}) = \sqrt{\left(\Omega + \epsilon - \beta k_{||}^2\right)\left(\Omega + \epsilon - \beta k_{||}^2 + 2(\alpha_1 - \alpha_2)n\right)},$$

$$\epsilon^L(k_{\perp}) = \sqrt{(\epsilon - \beta k_{\perp}^2)(\epsilon - \beta k_{\perp}^2 + 2(\alpha_1 + \alpha_2)n)},$$

$$\epsilon^U(k_{\perp}) = \sqrt{(\Omega + \epsilon + \beta k_{\perp}^2)(\Omega + \epsilon + \beta k_{\perp}^2 + 2(\alpha_1 - \alpha_2)n)}.$$

Combined fitting of these four expressions to our eigenstates yielded values of $\alpha_1 n = (322 \pm 12)\,\mu eV$ and $\alpha_2 n = (9 \pm 15)\,\mu eV$. Estimated errors come from 95% confidence interval after accounting for the error on Ω and β values

(obtained from the previous fit). By using the same method as described in ref. [1] to calibrate the setup and calculate the density of the condensate, the measured value was found to be $n_{tot} = 2n \approx (2200 \pm 200)\ \mu m^{-2}$, finally yielding $\alpha_1 = (0.293 \pm 0.029)\ \mu eV\ \mu m^2$ and $\alpha_2 = (0.008 \pm 0.014)\ \mu eV\ \mu m^2$.

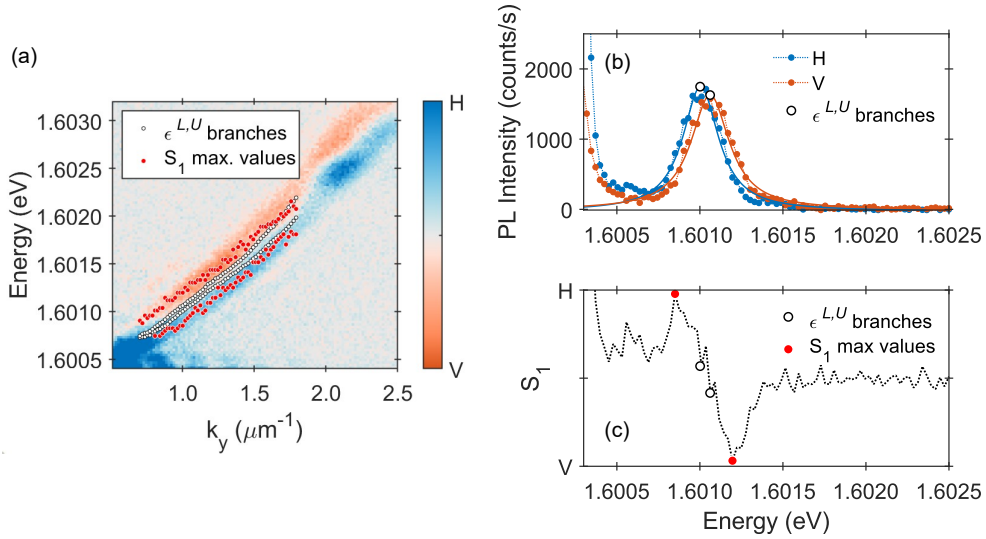

Supplemental Figure 2. (a) Cross-section of the Stokes vector component S_1 of a measured excitations' dispersion, along $k_x = 0\,\mu m^{-1}$. Energies of two eigenstates, extracted from the fitting procedure are marked with white circles, while red points show positions of maximum values of S_1 component at each point in momentum space. They are slightly shifted from the branches, and were used to calculate polarization maps in the main text. (b) An example of a single measured spectrum of elementary excitations for wavevector $k_x \approx 0\,\mu m^{-1}, k_y \approx 1\,\mu m^{-1}$, detected in horizontal (H) and vertical (V) polarization basis with calculated S_1 component presented in (c). Solid lines show fitted Lorentzian curves used to extract the eigenstates.

III. SPIN TEXTURES

In order to extract the pseudospin textures, the Stokes vector components were calculated for each of the excitation branches in the whole measured 2D momentum space. At the extracted energies of eigenstates, the S_1 and S_2 components were calculated using the intensities from the measured polarization-resolved spectra. However, as shown in Supplemental Figure 2, the finite broadening and small splitting between the branches results in partial overlapping of the states and the maximum value of the polarization degree is shifted from the eigenstate peak position in energy. Therefore, to enhance the visibility contrast of the patterns we used those maximum values to present the polarization maps and calculate the pseudospin textures in the main text (Fig. 3).

The polarization and pseudospin patterns were calculated in a similar manner for the low-density case, as presented in Supplemental Figure 3.

To compare the measured polarization patterns with the theoretical expectations, the maps in Fig. 3 in the main text were calculated from the full model as [4]:

$$S = \begin{pmatrix} S_1 \\ S_2 \\ S_3 \end{pmatrix} = \begin{pmatrix} 2\,Re\left(\psi_+ \psi_-^*\right) \\ 2\,Im\left(\psi_+^* \psi_-\right) \\ |\psi_+|^2 - |\psi_-|^2 \end{pmatrix},$$

where $\Psi = (\psi_+, \psi_-)^T$ is a polariton spinor.

They were rotated 15° to account for the difference in the measurement frames.

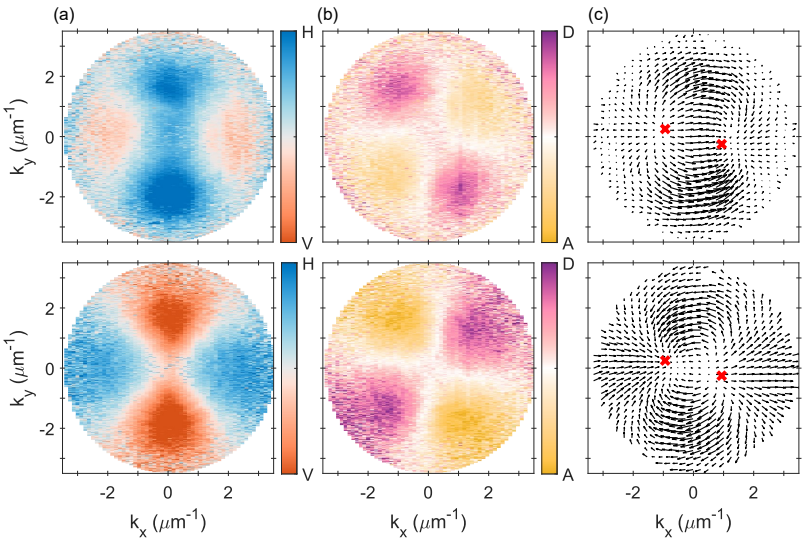

Supplemental Figure 3. (a) S_1 and (b) S_2 components of the Stokes vector for the low-density polaritons, at the ϵ_- (top row) and the ϵ_+ (bottom row) lower polariton branch. Corresponding pseudospin textures are presented in (c), with red crosses marking the positions of the crossing points.

IV. POWER DEPENDENCE

We have studied the power dependence of polarization- and momentum-resolved polariton photoluminescence along one direction in momentum space (along the monochromator slit in experimental frame of reference), without momentum filtering. It enabled us to study the threshold and the linear polarization degree of the condensate. Supplemental Figure 4 shows the dependence of integrated photoluminescence signal at $k = 0$ on the excitation power. Nonlinear increase of the emission intensity, combined with abrupt increase in the degree of linear polarization (see inset of Supplemental Figure 4), clearly mark the condensation threshold.

For further studies of excitations, presented in the main text, we have chosen the power corresponding to the last point on this series (marked with green) in order to achieve the highest condensate density.

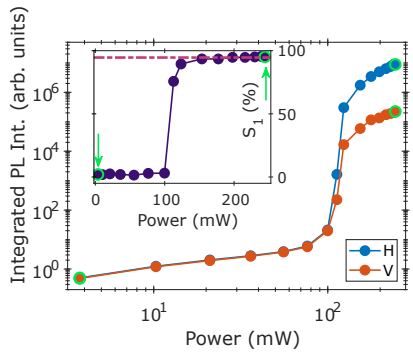

Supplemental Figure 4. Power dependence of the integrated photoluminescence intensity at $k = 0$, resolved in H- and V-polarizations. Inset: S_1 Stokes vector component of the polariton emission versus the excitation power. Dashed line shows the degree of linear polarization of a high-density condensate, saturating around 95%. Green circles and arrows indicate powers used for low-density and high-density measurements presented in the main text.

V. COMPARISON OF LOW-DENSITY AND HIGH-DENSITY DATA

Supplemental Figure 5 shows the comparison of low-density polariton and high-density excitation dispersions (shown separately in Figs. 1(c,d) and 2(e,f) of the main text). Energies of the eigenstates were shifted to the extracted condensate energy. The difference between the low and high density regimes is clear, as the shifts far exceed the eigenstate linewidths and experimental errors. Supplemental Figure 5(b) shows the energy splitting between the collective excitations in the directions parallel and perpendicular to the condensate polarization direction with the corresponding theoretical line following from fits (solid green), compared with the splitting of low-density polariton branches and their model (dotted purple line). With interactions included (model described in Section II), the resulting eigenstate splitting dependence on wavevector is clearly different from the low-density limit (Eq. 1 in the main text).

Moreover Supplemental Figure 5(b) also demonstrates how including polarization-dependent interactions (for polaritons in triplet and singlet state with corresponding α_1 and α_2 strengths) shifts the diabolical point. Dashed line shows the excitation branches' splitting which would result from considering our fitted model with $\alpha_2 = 0$. This highlights that considering polarization-dependent interactions is essential to reliably fit experimental data points.

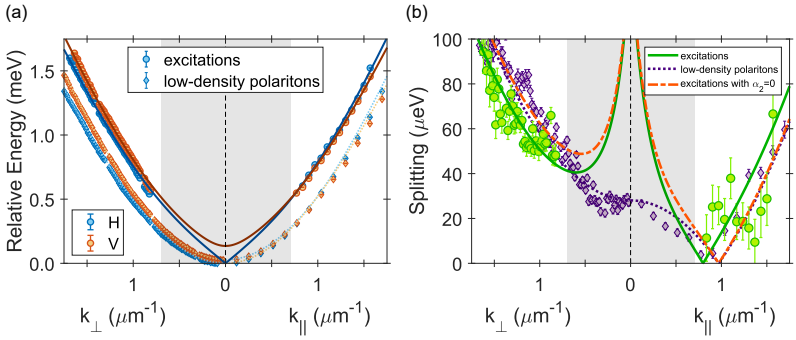

Supplemental Figure 5. Low-density polariton (diamonds) and high-density excitation (circles) eigenstate dispersions (a) and their splitting (b) in the directions parallel and perpendicular to the condensate polarization direction. Corresponding theoretical fits are shown with solid lines (excitation branches) and dotted lines (low-desity polariton branches). Red dashed line in (b) shows the energy splitting resulting from same excitation model (Eq. 2 of the main text) and parameters extracted from our fits, but with $\alpha_2 = 0$. Grey shaded area marks the range of emission blocked by the edge filter in high-density regime experiments.

To further prove the validity of our model, we have performed a statistical analysis of the goodness of the fit and compared models with and without the interactions. Supplemental Figure 6 presents several approaches to model our measured data. Panel (a) shows our fitted model, as in the main text, with the interaction constants included. We highlight that the fitting procedure was performed to the dispersion curves (Supplemental Figure 6(a)), as described in Section II, and the graph in Supplemental Figure 6(b) show the resulting energy splitting calculated from the fit. Supplemental Figures 6(c,d) show the model without polariton-polariton interactions, i.e., with the same polariton parameters extracted from the low-density measurements, but with $\alpha_1, \alpha_2 = 0$. It is therefore a model of non-interactiong polaritons, but with the energy of the $k = 0$ state ϵ_0 shifted to the measured condensate energy. It is very clear that the curve does not model our data correctly. Supplemental Figures 6(e,f) additionally present the model with no interactions but with the energy shift as a fitting parameter, yielding the value $\epsilon_0 = 1.60052\ eV$, which is blueshifted by 270 μeV from the observed condensate energy, and by 890 μeV from the low-density lower polariton. This model therefore results in a significant discrepancy with the observed blueshift. Furthermore, it does not yield the best fit to our experimental data, as shown in the analysis below. Finally, Supplemental Figures 6(g,h) additionally present a model with only triplet interactions taken into account, i.e., with $\alpha_2 = 0$ and $\alpha_1 n$ being the only fitting parameter (yielding the value $\alpha_1 n = (323 \pm 13)\ \mu eV$ - almost the same as in our original approach). Even though the fit to the excitation dispersion is similar to that achieved with our original approach, the energy splitting calculated from the fit and presented in Supplemental Figure 6(h) shows a clear descrepancy with our data, as further quantified and discussed below.

For each of the models presented in Supplemental Figure 6, we calculated the residual sum of squares (RSS), the mean residual square (MRS) (both measuring the discrepancy of the data points and the fitted line), and the R-squared (R^2) parameter, showing the overall goodness of fit. As each of the experimental points is subject to uncertainty, the fitting was performed through a weighted nonlinear least square procedure, with error bars included

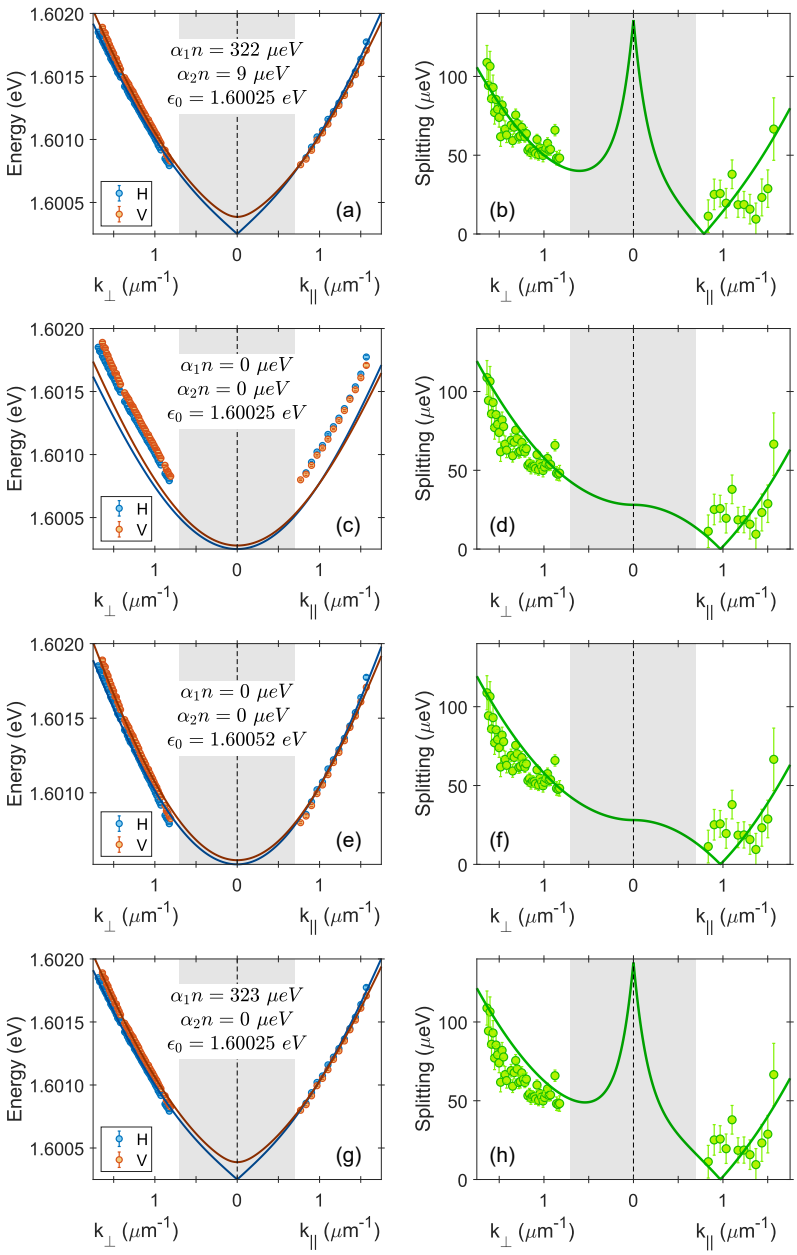

Supplemental Figure 6. Comparison of the model fits. Left panels (a,c,e,g) show the excitation dispersions, with datapoints extracted from the measurements and the corresponding theoretical curves shown as solid lines. Right panels (b,d,f,h) present the corresponding eigenstate splitting, with the model curves calculated from the dispersion fits. Panels (a,b) show the model used in the main text, with both interaction energies used as fitting parameters. Panels (c,d) and (e,f) show the models neglecting the interactions, with the $k = 0$ energy set to the measured condensate energy in (c) and used as a fitting parameter in (e). Panels (g,h) show the model without the singlet interactions, with the interaction energy $\alpha_1 n$ as the only fitting parameter.

as instrumental weights, $w_i = \frac{1}{\sigma^2}$, where σ is the size of an error bar. Calculated statistical measures were therefore also adjusted, taking these weights into account:

$$RSS = \sum_{i=1}^{m} w_i (y_i - \hat{y}_i)^2,$$

$$MRS = \frac{RSS}{m},$$

$$TSS = \sum_{i=1}^{m} w_i y_i^2 - \left(\sum_{i=1}^{m} (y_i w_i) / \sum_{i=1}^{m} w_i \right)^2 \sum_{i=1}^{m} w_i,$$

$$R^2 = 1 - \frac{RSS}{TSS},$$

where y_i are the datapoints, $\hat{y}_i$ are model points, TSS is the corrected total sum of squares, and m is the number of points.

The results are presented in Supplemental Table I, with the statistical parameters calculated for each of the models discussed above, as well as for the eigenstate splitting (not subject to fitting). The columns (a-h) in Supplemental Table 1 present the statistical measures corresponding to the fitting of different models to the experimental dispersion branches in Supplemental Figures 6(a,c,e,g) and the extracted energy splitting in Supplemental Figures 6(b,d,f,h), respectively.

	Fitted model $\alpha_1 n = 322\ \mu eV$ $\alpha_2 n = 9\ \mu eV$ $\epsilon_0 = 1.60025\ eV$	**No interactions** $\alpha_1 n = 0\ \mu eV$ $\alpha_2 n = 0\ \mu eV$ $\epsilon_0 = 1.60025\ eV$	**No interactions, fitted blueshift** $\alpha_1 n = 0\ \mu eV$ $\alpha_2 n = 0\ \mu eV$ $\epsilon_0 = 1.60052\ eV$	**Only triplet interactions** $\alpha_1 n = 323\ \mu eV$ $\alpha_2 n = 0\ \mu eV$ $\epsilon_0 = 1.60025\ eV$
Dispersions	(a)	(c)	(e)	(g)
Residual sum of squares RSS	2330.3	816160	7120.1	2829.1
Mean residual square MRS	19.58	6858.50	59.83	23.77
R^2	**0.9964**	**-0.2749**	**0.9889**	**0.9956**
Splitting	(b)	(d)	(f)	(h)
Residual sum of squares RSS	154.73	411.39	411.39	610.85
Mean residual square MRS	2.7146	7.2173	7.2173	10.717
R^2	**0.6639**	**0.1064**	**0.1064**	**-0.3268**

Supplemental Table I. Statistical analysis of the goodness of fit and model comparison. Best parameter values are highlighted in red.

Our original model yielded a value of $R^2 = 99.64\%$, as seen in column (a) of Supplemental Table I, which proves its statistical significance. It is the highest R^2 value of all considered approaches. As seen in column (b) of Supplemental Table I, R^2 for the resulting splitting is 66.39%, which means a larger discrepancy between the data points and the model, however, we stress that the small splitting values in $k_{\parallel}$ direction (close to zero due to the crossing point presence) greatly contribute to the overall discrepancy, as they come close to the experimental resolution limit. Importantly, we were able to measure such small splittings because of the polarization-resolved measurements, enabling the isolation of individual eigenstates in the polarization basis. Without polarization filtering, both branches are indistinguishable experimentally. In the $k_{\perp}$ direction, the splitting values can be seen as more reliable, and curve calculated from our fit closely follows the data (left side of the Supplemental Figure 6(b)).

As evident from column (c) of Supplemental Table I, neglecting the interactions results in a poor fit, with negative R^2 (meaning that the fit is worse than a horizontal line and does not explain the data variance) and the residual squares larger than those presented in column (a) by orders of magnitude. Even including an additional blueshift into the model (originating, for instance, from an excessive reservoir in the trap), results in ~ 3 times higher residual sum of squares and mean residual square as seen in column (e) of Supplemental Table I. More importantly, this low-density interactions-free polariton approach does not agree with the splitting data, yielding the R-squared parameter of only 10.64%, as seen in columns (d,f) of Supplemental Table I.

Finally, a model that does not include the singlet (opposite-spin) polariton-polariton interactions does fit the data with high statistical significance as can be seen in column (g) of Supplemental Table I. Nevertheless, the splitting data show a very high discrepancy with this model, with negative R^2, as reported in column (h) of Supplemental Table I. These results point to the significance of including a positive value of α_2 to correctly describe our data, even though its value is very small comared to α_1 and is characterised by a significant uncertainty.

The model used in our work, as highlighted in columns (a,b) of Supplemental Table I, yields by far the closest fit to the measured data, with almost perfect match in the fitted eigenstate data and a very good correspondence in the splitting calculated from it.

VI. GHOST BRANCHES

As mentioned in the main text, our experimental investigation of Bogoliubov excitation branches also results in observing the negative (ghost) branches in both orthogonal polarizations, with examples presented in Supplemental Figure 7. The visibility of these branches further confirms the presence of the polariton-polariton interactions. Their signal, however, is very weak and strongly affected by the diffracted condensate emission (especially in polarization parallel to the one of the condensate), therefore we do not analyse it in detail and focus on the much brighter normal branches.

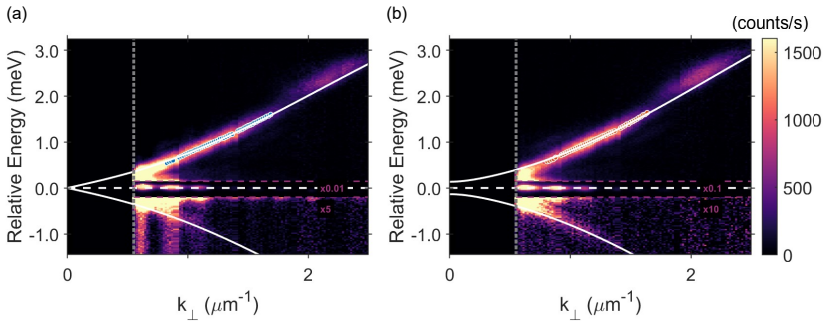

Supplemental Figure 7. Examples of the photoluminescence spectra at $k_{\parallel} = 0$ in (a) horizontal (H) and (b) vertical (V) polarization basis, with energies shifted to the condensate energy, showing both positive and negative (ghost) excitation branches. Data points show energies extracted from fitting of normal branches, white solid lines - the fitted model. White dashed line marks the energy of the condensate and grey dotted line is the edge of the spatial filter in momentum space. The condensate emission in the image is attenuated by a factor of 0.01 (a) and 0.1 (b), and the ghost branch emission is multiplied by a factor of 5 (a) and 10 (b).

[1] M. Pieczarka, M. Boozarjmehr, E. Estrecho, Y. Yoon, M. Steger, K. West, L. N. Pfeiffer, K. A. Nelson, D. W. Snoke, A. G. Truscott, and E. A. Ostrovskaya, Effect of optically induced potential on the energy of trapped exciton-polaritons below the condensation threshold, Physical Review B **100**, 085301 (2019).

[2] E. Estrecho, T. Gao, N. Bobrovska, D. Comber-Todd, M. D. Fraser, M. Steger, K. West, L. N. Pfeiffer, J. Levinsen, M. M. Parish, T. C. H. Liew, M. Matuszewski, D. W. Snoke, A. G. Truscott, and E. A. Ostrovskaya, Direct measurement of polariton-polariton interaction strength in the Thomas-Fermi regime of exciton-polariton condensation, Phys. Rev. B **100**, 035306 (2019).

[3] A. Gianfrate, O. Bleu, L. Dominici, V. Ardizzone, M. De Giorgi, D. Ballarini, G. Lerario, K. W. West, L. N. Pfeiffer, D. D. Solnyshkov, D. Sanvitto, and G. Malpuech, Measurement of the quantum geometric tensor and of the anomalous Hall drift, Nature **578**, 381 (2020).

[4] H. Terças, H. Flayac, D. D. Solnyshkov, and G. Malpuech, Non-Abelian gauge fields in photonic cavities and photonic superfluids, Phys. Rev. Lett. **112**, 066402 (2014).

Summary of the findings

In summary, the work presented in this Part served as a fundamental study of the polarization properties of a high-density exciton-polariton condensate in the Thomas-Fermi regime, governed by polariton-polariton interactions. It investigated the collective elementary excitations of a condensate with an intrinsic synthetic gauge field, directly showing the excitation branches spin anisotropy. This work:

- served as the first experimental observation of the polarization splitting and the anisotropic behavior of the condensate excitation dispersions in an optically confined condensate, previously explored only theoretically. This study experimentally evidenced a clear difference in the polarization-resolved excitation dispersions in different in-plane directions, showing two linearly-polarized Bogoliubov branches with different sound velocities of the collective condensate waves. The dispersion splitting was governed by the photonic TE-TM splitting, the inherent optical anisotropy and the spin-anisotropy of the polariton-polariton interactions, all of which were accounted for in the theoretical model. The strongest contribution to the anisotropy of the collective branches in this system has been found to come from the optical anisotropy part.

- presented a rotation of the polariton spin in an interacting regime of the condensate, directly showing a non-abelian gauge field with characteristic degeneracy points, around which the monopolar field texture is formed. Such a field has been shown before only in an non-interacting, low density regime of photonic states, with no evidence of the influence of polariton-polariton interaction anisotropy on the shape of the field prior to this work. The polarization texture has been directly evidenced from the Stokes vector components of the polariton pseudospin and showed superb correspondence to the results of the theoretical model.

- based on the experimental data, two interaction constants have been extracted, describing interaction strength of polaritons with the same or opposite spins. Previously, most experimental studies on polariton-polariton interactions focused solely on the average value, with no spin resolution, or only on their

ratio. This work offered a new, relatively straightforward way of measuring both constants in a polariton condensate, in future possible also in other material systems. It used a mean-field framework to describe the observed excitation eigenstates, allowing for the quantitative analysis of all the contributing effects. The extracted values of the interaction constants proved the theoretical predictions and common claims, that polaritons with the same spin interact with each other much more strongly than the particles with opposite spins. Additionally, the statistical analysis proved the applicability of the model and validity of the results.

- is important for further research and applications. The presence of diabolical points with the associated spin structure characteristic of a monopole-like magnetic field signifies that polariton systems in the high-density (nonlinear) regime can be used in future studies of synthetic gauge fields and topological physics. The dominant role of the cavity birefringence in the anisotropy of collective excitations points to a straightforward way to design synthetic gauge fields for quantum liquids of light by tailoring the optical anisotropy of microcavities. The measured values of the polariton-polariton interactions can be regarded as being of core importance in fundamental research.

Part III

Direct measurement of a non-Hermitian topological invariant in a hybrid light-matter system

Introduction

Topology is is a branch of mathematics describing the properties of a geometric object that are preserved under continuous deformations. It describes global characteristics of a whole class of systems and it is central to understanding and engineering materials that display robust physical phenomena immune to imperfections [33]. Different topological phases of matter are characterized by topological invariants - quantities that take on discrete values which do not change under continuous deformations of the space (hence remain invariant). They can be used to classify groups of objects and describe a global, topological property - objects with the same topological invariant are topologically equivalent [33]. The most common example of a topological invariant is the number of holes in an object, with a doughnut and a cup being members of the same class. Changing the topological invariant (e.g. by creating a new hole in an object) is known as a topological phase transition.

Topology has gained a huge interest after the discovery of topologically protected energy bands in electronic materials and solid state systems [123, 207–209]. With properties invariant to continuous deformations (such as stretching, twisting, crumpling, and bending) it allows the existence of topological phases immune to disorder. Imperfections or sample defects typically lower or even diminish the effectiveness of electronic devices, hence topological protection gave a lot of promise in potential applications. Topological phases in electronic materials has led to demonstrations of unique phenomena, such as a dissipationless current in topological insulators or an enhanced sensitivity to electromagnetic fields [210, 211].

Firstly studied in solid state systems, soon topological states have been presented also in photonic systems [32, 33], with potential applications in photonic devices. Topological effects such as topological protection, unidirectional transport or topological lasing can be realized in e.g. photonic crystals, coupled resonators, metamaterials and quasicrystals [33]. Soon it has also been suggested and realized in polariton systems [63, 206, 212–216]. Breaking the time-reversal symmetry, necessary to induce topological edge modes, has been done with an external magnetic field, or by breaking the inversion symmetry (e.g. by creating a lattice) [91, 206, 214, 215, 217].

In energy-conserving (Hermitian) systems, topological invariants are determined by the winding of the phase of the eigenstates in momentum space. The bulk–boundary correspondence dictates that the topological invariant called the winding number, which specifies the number of chiral edge modes, is completely determined by the bulk topological invariant - the Chern number [218, 219]. The winding has

been evidenced experimentally in a range of systems [218, 220–222].

However, the situation is different in dissipative, open systems which are not Hermitian (as introduced in section 1.2.6), in which the gain and the loss govern also the topological properties. In non-Hermitian systems, a topological invariant emerging from the winding of the complex eigenenergies has been predicted [65–67]. Some properties of the eigenstates stemming from the novel non-Hermitian topology - e.g. localization of modes [223] or the polarization half-charge [224] - have been experimentally observed in photonic and mechanical systems, however, a direct measurement of the non-Hermitian topological invariant in momentum space has not been demonstrated prior to this work, regardless of the physical system under investigation.

Extracting the non-Hermitian properties of photonic or polaritonic systems can be done by experimentally mapping both the energy and the linewidth of the spectrum, what correspond to mapping the real (energy) and imaginary (linewidth) parts of the eigenstates. As introduced in section 1.2.6, accounting for the inherent losses can be done by using a non-Hermitian framework [53, 60], where both the exciton and the photon resonances are described by complex energies $E' = E - i\gamma$. The real part E corresponds to the state energy, and the imaginary part - to its linewidth (inverse lifetime). One can now include these complex energies into full Hamiltonians, e.g. into the Hamiltonian describing the TE-TM splitting of the photonic or polaritonic states, combined with the anisotropy/birefringence (described in section 1.2.3 and in equation 1.27).

By simply measuring the photoluminescence spectra, one can extract both real and imaginary parts of the eigenstates from the fitting procedure. Mapping these values in momentum space - very similarly to the methods described in the previous part of this thesis - allows to extract the novel topological invariant — *fractional spectral winding* - when done near the exceptional points (the crossing points of the eigenstate dispersions). Additionally, mapping the polariton pseudospin in momentum space (again, with methods described in the previous parts) allows to map the artificial in-plane magnetic field acting on the polaritons. Here, the non-Hermiticity results in a unique appearance of circular polarization, maximized near the exceptional points, even without the presence of the external (real) magnetic field.

This work - in contrast to other works presented in this thesis - has been done in a perovskite material platform, with a lead-halide perovskite crystals embedded in an optical microcavity. These crystals are known to be optically anisotropic [79], having an orthorombic structure - what allows for a much higher X-Y splitting (the birefringence of the cavity medium). This effectively enlarges the overall eigenstate splitting and makes the exceptional points more distinct. Additionally, larger exciton binding energies in these materials allow for the polariton presence (and even condensation [79]) at room temperature - a condition used in this work.

Large structural anisotropy greatly increases the size of the effects described in section 1.2.3 and also in the previous part (Part II) of this thesis. The values of the branch splitting are higher, hence much easier to observe and extract experimentally. Even though no polariton-polariton interactions have been considered in this part (a low density regime) and the broad scope of this work is different, the experimental

methods are very similar to the ones employed in the previous part. By mapping the photoluminescence spectra in the momentum space, while resolving the polarization of the states, one can extract the effective magnetic field governing the polariton pseudospin. This highlights, how this technique is hugely versatile, and how it can be employed to study various novel characteristics of polaritons or photons.

It's also important to note, that this work significantly differs from the works by Tercas et al. [28] and Gianfrate et al. [30] (described in the Introduction to Part II) in two ways. First, in these works the authors used a parabolic approximation of the polariton states in the model (further used in the effective-SOI Hamiltonian), hence, considered a purely photonic effect of the gauge field, with no strong coupling between the photons and excitons needed. Here, apart from the gauge field effect on the photonic mode, photons are strongly coupled to excitons. Secondly and most importantly, this work considers also the imaginary part of the polariton states - hence their inherent non-Hermiticity - as it has not been done before.

Contributions

This research has been a collaborative work. D. Biegańska (the author of this thesis) participated in data analysis. She used the mathematical methods and scripts very similar to the ones used in other parts of this thesis (Part II in particular) and took an active part in analyzing the data. She participated in final corrections of the manuscript. She also participated in designing and performing the initial, test experiments (in preparation for this study), learning the skills which she has later used in Part II. All authors contributed to the final version of the text.

Results

PHYSICS

Direct measurement of a non-Hermitian topological invariant in a hybrid light-matter system

Rui Su[1]*†, Eliezer Estrecho[2]*†, Dąbrówka Biegańska[2,3], Yuqing Huang[1], Matthias Wurdack[2], Maciej Pieczarka[2,3], Andrew G. Truscott[4], Timothy C. H. Liew[1,5], Elena A. Ostrovskaya[2]*, Qihua Xiong[6,7,8]*

Topology is central to understanding and engineering materials that display robust physical phenomena immune to imperfections. Different topological phases of matter are characterized by topological invariants. In energy-conserving (Hermitian) systems, these invariants are determined by the winding of eigenstates in momentum space. In non-Hermitian systems, a topological invariant is predicted to emerge from the winding of the complex eigenenergies. Here, we directly measure the non-Hermitian topological invariant arising from exceptional points in the momentum-resolved spectrum of exciton polaritons. These are hybrid light-matter quasiparticles formed by photons strongly coupled to electron-hole pairs (excitons) in a halide perovskite semiconductor at room temperature. We experimentally map out both the real (energy) and imaginary (linewidth) parts of the spectrum near the exceptional points and extract the novel topological invariant—fractional spectral winding. Our work represents an essential step toward realization of non-Hermitian topological phases in a condensed matter system.

INTRODUCTION

The discovery of topologically protected energy bands and associated topological phases in electronic materials has led to demonstrations of unique phenomena, such as dissipationless current (*1*) and enhanced sensitivity to electromagnetic fields (*2*, *3*), that have the potential to revolutionize the electronics industry. Inspired by the discoveries in the field of condensed matter physics, the realization of topological effects in engineered photonic systems holds similar promise for photonic applications (*4*). On the other hand, growing understanding of the physics of non-Hermitian systems with gain and loss (*5*, *6*) has led to demonstration of novel functionalities, such as loss-induced lasing (*7*), enhanced sensing (*8*, *9*), and optical nonreciprocity (*10*, *11*). The past few years have witnessed the convergence of the two research directions, with notable theoretical and experimental advances in extending the notion of topology to non-Hermitian systems (*12*, *13*). The bulk-boundary correspondence, the principle relating the surface states to the topological classification of the bulk, was generalized to non-Hermitian systems (*14*–*17*) and has been explored for high-order systems (*18*, *19*). Furthermore, the associated non-Hermitian skin effect, the localization of bulk modes at the edges of an open boundary system, was observed in experiments (*20*–*22*). A unique non-Hermitian topology arising from the winding of the complex eigenvalues (eigenenergies) was theoretically predicted (*23*–*25*). This is in stark contrast to energy-conserving systems, where the topological invariants are determined by the winding of the phase of the eigenstates in momentum space, which has been directly measured in ultracold atomic (*26*, *27*), microwave (*28*), and photonic systems (*29*). The properties of the eigenstates stemming from the novel non-Hermitian topology, such as the polarization half-charge (*30*) and localization of modes (*31*), have been experimentally observed in photonic and mechanical systems. However, a direct measurement of the non-Hermitian topological invariant in momentum space is yet to be demonstrated, regardless of the physical nature of the system under investigation.

Exciton polaritons, hybrid light-matter particles arising from strong coupling of confined photons to excitons in a semiconductor, offer a promising platform for investigations of topology and non-Hermitian physics in condensed matter. Artificial lattice potentials (*32*–*34*) enable exciton polaritons to emulate topological quantum matter (*35*), although the topological gap only opens in very strong magnetic fields requiring a superconducting magnet and cryogenic temperatures. Under similar extreme conditions, exciton-polariton systems also enable a direct measurement of physical quantities directly related to topology, such as the quantum geometric tensor (*36*), including the nonzero Berry curvature (*36*–*38*). Moreover, because of the photonic and excitonic losses, exciton polaritons are inherently non-Hermitian. A non-Hermitian spectral degeneracy—an exceptional point (EP) (*7*, *39*), where both the eigenvalues and eigenvectors coalesce—was demonstrated in exciton-polariton systems (*40*, *41*) in parameter space. Since then, new proposals have emerged combining topology and non-Hermiticity of the system using artificial lattices (*42*–*44*). However, there are no experimental studies yet demonstrating the novel topology arising from non-Hermiticity in exciton-polariton systems.

In this work, we exploit exciton polaritons formed in optically anisotropic lead-halide perovskite crystals embedded in an optical microcavity to demonstrate the emergence of non-Hermitian topology in an exciton-polariton system at room temperature. First,

[1]Division of Physics and Applied Physics, School of Physical and Mathematical Sciences, Nanyang Technological University, Singapore 637371, Singapore. [2]ARC Centre of Excellence in Future Low-Energy Electronics Technologies and Nonlinear Physics Centre, Research School of Physics, The Australian National University, Canberra 2601, Australia. [3]Department of Experimental Physics, Faculty of Fundamental Problems of Technology, Wrocław University of Science and Technology, Wyb. Wyspiańskiego 27, 50-370 Wrocław, Poland. [4]Laser Physics Centre, Research School of Physics, The Australian National University, Canberra 2601, Australia. [5]MajuLab, International Joint Research Unit UMI 3654, CNRS, Université Côte d'Azur, Sorbonne Université, National University of Singapore, Nanyang Technological University, Singapore, Singapore. [6]State Key Laboratory of Low-Dimensional Quantum Physics and Department of Physics, Tsinghua University, Beijing 100084, P.R. China. [7]Beijing Academy of Quantum Information Sciences, Beijing 100193, P.R. China. [8]Beijing Innovation Center for Future Chips, Tsinghua University, Beijing 100084, P.R. China.
*Corresponding author. Email: qihua_xiong@tsinghua.edu.cn (Q.X.); elena.ostrovskaya@anu.edu.au (E.A.O.); surui@ntu.edu.sg (R.S.); eliezer.estrecho@anu.edu.au (E.E.)
†These authors contributed equally to this work.

we develop a non-Hermitian model for the two states of exciton-polariton pseudospin that accounts for the inherent losses in the system. The exciton-polariton pseudospin originates from the two allowed projections of its spin on the structure axis and is directly related to the polarization of the exciton-polariton emission, i.e., cavity photoluminescence (PL) (*45*). The model predicts the formation of two paired EPs in momentum space connected by the topologically protected bulk Fermi arcs (*30*). We also demonstrate theoretically that the topologies of the eigenstates (polarization winding) and the eigenenergies (spectral winding) are not equivalent, and the latter can persist when the former is absent. Then, by performing spectroscopic measurements of exciton-polariton PL, we experimentally confirm the existence of paired EPs and Fermi arcs linking them in momentum-resolved spectrum. Moreover, the non-Hermiticity results in the appearance of circular polarization, maximized near the EPs (*46*), which arises from the imaginary part of the artificial in-plane magnetic field acting on the exciton-polariton pseudospin. We provide a direct measurement of the novel non-Hermitian topological invariant—spectral winding—in a spatially homogeneous system and demonstrate the topological stability of the EPs and Fermi arcs against the gap-opening perturbations.

RESULTS

Non-Hermitian model for exciton-polariton dispersion

Losses are unavoidable in exciton-polariton systems because of the finite lifetimes of the cavity photons and excitons. These losses can be fully accounted for using non-Hermitian framework, where both exciton and photon resonances in the cavity are described by complex energies $\widetilde{E} = E - i\gamma$, with the real part corresponding to the resonance energy and the imaginary part to the linewidth (inverse lifetime). We therefore model the complex exciton-polariton dispersion (spectrum in momentum space) by using a 4 × 4 non-Hermitian Hamiltonian describing the coupling of the two polarization modes of the cavity photons to the corresponding modes of the exciton (*47*)

$$H(\boldsymbol{k}) = \begin{pmatrix} H_c(\boldsymbol{k}) & V\mathbf{1}_{2\times2} \\ V\mathbf{1}_{2\times2} & \widetilde{E}_x\mathbf{1}_{2\times2} \end{pmatrix} \tag{1}$$

where $\hbar\boldsymbol{k}$ is the in-plane momentum, $\mathbf{1}_{2\times2}$ is the 2 × 2 identity matrix, $\widetilde{E}_x = E_x - i\gamma_x$ is the complex exciton energy, and V is the exciton-photon coupling strength. For simplicity, we assume that the exciton spins are degenerate in energy, and the coupling strength is isotropic. We model the cavity photon by extending the Hermitian Hamiltonian (*48*, *49*) to properly account for the losses

$$H_c(\boldsymbol{k}) = \begin{pmatrix} \widetilde{E}_c(k) & \widetilde{\alpha} + \widetilde{\beta}(k)\, e^{-2i\phi} \\ \widetilde{\alpha} + \widetilde{\beta}(k)\, e^{2i\phi} & \widetilde{E}_c(k) \end{pmatrix} \tag{2}$$

where ϕ is the in-plane propagation angle, $\widetilde{E}_c(k) = \widetilde{E}_{c0} + \widetilde{\chi}(k)$ is the mean complex energy of the cavity photon, $\widetilde{\chi}(k)$ is a function related to the effective mass (real part) and the momentum-dependent loss rates (imaginary part), $\widetilde{\alpha}$ describes the complex energy splitting due to X-Y splitting, and $\widetilde{\beta}(k)$ describes transverse-electric transverse-magnetic (TE-TM) splitting. The X-Y splitting can arise from the birefringence in the cavity medium (*48*, *49*), for example, due to the anisotropic orthorhombic crystal structure of perovskites at room temperature (*33*, *50*), which leads to different cavity lengths for the ordinary and extraordinary waves and results in the splitting of both energies and linewidths at normal incidence ($k = 0$). The TE-TM splitting naturally arises from the polarization-dependent reflectivity of the dielectric mirrors at oblique angles, inducing an effective spin-orbit coupling (*48*–*50*) that increases with the angle of incidence (or k). The resulting energy splitting is sensitive to the position of the cavity resonance with respect to the distributed Bragg reflector (DBR) stopband, but the linewidth consistently increases (decreases) with momentum for TE (TM) modes (*47*). The model Eqs. 1 and 2 are derived by extracting the resonances in 4 × 4 transfer matrix simulations (*46*) (see Materials and Methods). The behavior of the energies and linewidths is presented in the Supplementary Materials.

In the strong coupling regime, the model Eqs. 1 and 2 result in four exciton-polariton branches (see the Supplementary Materials). In this work, we focus on the two lower polariton branches since the upper branches are not visible in PL experiments. The lower polaritons at lower momenta k can be described by a model similar to Eq. 2. However, the effective X-Y and TE-TM splitting parameters $\widetilde{\alpha}$ and $\widetilde{\beta}$ now also depend on the exciton-photon coupling strength V and exciton-photon detuning $\widetilde{E}_{c0} - \widetilde{E}_x$. In experiments, the exciton-photon coupling strength is typically fixed, but the exciton-photon detuning can be varied across the sample because of distinct cavity lengths. The effective 2 × 2 Hamiltonian can be recast into a more convenient form as $\widetilde{E} = \langle\widetilde{E}(\boldsymbol{k})\rangle 1_{2\times2} + \boldsymbol{G}(\boldsymbol{k}) \cdot \sigma$, where $\langle\widetilde{E}(\boldsymbol{k})\rangle$ is the mean lower polariton complex energy, $\sigma = [\sigma_x, \sigma_y, \sigma_z]^T$ is a vector of Pauli matrices, and

$$\boldsymbol{G}(\boldsymbol{k}) = [\widetilde{\alpha} + \widetilde{\beta}(k)\cos 2\phi, \widetilde{\beta}(k)\sin 2\phi, 0] \tag{3}$$

is the effective non-Hermitian gauge field. The complex spectrum can be written as $\widetilde{E}_\pm - \langle\widetilde{E}\rangle = \pm\sqrt{G_R^2 - G_I^2 + 2i\boldsymbol{G}_R \cdot \boldsymbol{G}_I}$, where G_R and G_I are the real and imaginary parts of the gauge field, respectively. In the Hermitian limit of negligible losses, the spectrum (energy eigenvalues) of the Hamiltonian with gauge field, Eq. 3, features two Dirac cones in momentum space, as shown by the energy surfaces in Fig. 1 (A and B). This lossless approximation has been successfully used to describe several experiments in exciton-polariton systems such as the optical spin-Hall effect (*45*), anomalous Hall effect (*36*), and the measurement of the quantum geometric tensor (*36*–*38*). Adding a real-valued σ_z component to the gauge field, Eq. 3, e.g., by inducing a Zeeman shift of the exciton energies with an out-of-plane magnetic field, would remove the Hermitian degeneracies at the Dirac point and thus open a topological gap (*36*–*38*). When polarization-dependent losses are non-negligible, the imaginary parts of the gauge field, Eq. 3, split each of the Dirac point into a pair of EPs, as shown in Fig. 1 (C and D). These EP pairs are topologically stable (*12*), in stark contrast to the Dirac points that are only stable when protected by symmetry. It takes a strong gap-opening perturbation (i.e., a real-valued σ_z term) to make the EPs approach each other (see Fig. 1E) and annihilate to open the gap (see Fig. 1F). A closer look at one of the pairs, as shown in Fig. 1 (C and D), reveals that the paired EPs are connected by open arcs called the bulk Fermi arc (*30*), where $\Delta E = 0$ (green), and the imaginary Fermi arc, where $\Delta\gamma = 0$ (orange), which form closed contours in momentum space (see Fig. 1G). The gap opens when the bulk Fermi arc shrinks and disappears, and the imaginary Fermi arc closes.

Non-Hermitian systems are characterized by two nonequivalent types of topological winding numbers: The first one is a topological

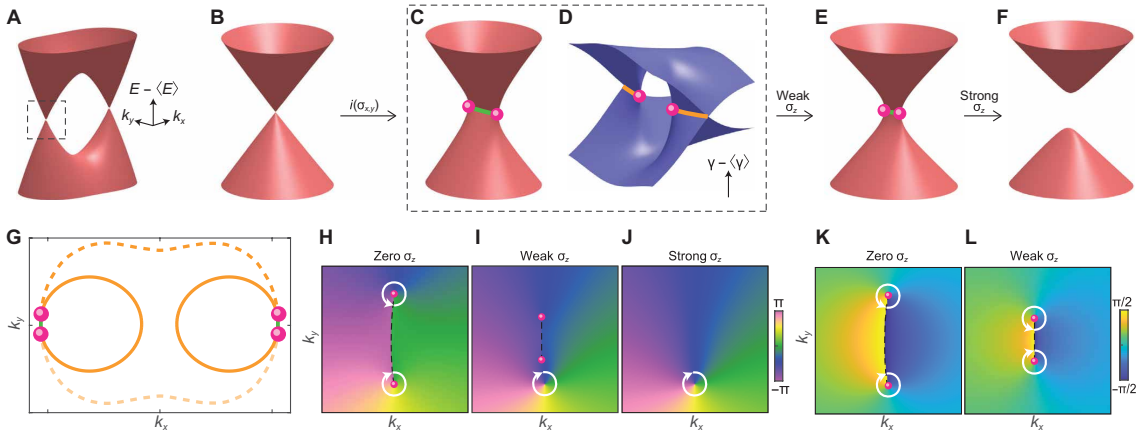

Fig. 1. Complex spectral structure near pairs of EPs in momentum space. (**A**) Energy (real part of the complex spectrum) of the exciton-polariton modes in a microcavity with linear birefringence, calculated using the model Eq. 1. The mean energy is subtracted for clarity. Energy crossings occur at two opposite regions in the 2D momentum space (k_x, k_y). (**B**) Enlarged view of the dashed region in (A) in the Hermitian limit, showing a Dirac point. (**C**) Energy of the dashed region in (A) in the non-Hermitian case, with nonzero $i\sigma_{x,y}$ components, showing the Dirac point splitting into a pair of EPs (pink dots) connected by the nodal line, bulk Fermi arc (green), where the energies cross. (**D**) Imaginary part of the complex spectrum corresponding to the linewidth for the dashed region in (A), showing the imaginary Fermi arc (orange), where the linewidths cross, emanating from the EPs (pink dots). (**E**) Energy of the system with a weak, real-valued σ_z term perturbation. (**F**) Same as (E) but with a strong perturbation leading to the annihilation of the EPs and opening of the gap. (**G**) Simplified complex energy structure of the two eigenstates, showing the bulk (green) and imaginary (orange) Fermi arcs connecting at the EPs and forming two closed contours. A single contour can also form (dashed orange) for the different sign of the parameters in Eq. 3. (**H** to **J**) In-plane pseudospin angle in momentum space of the upper eigenstate corresponding to (from left to right) (C), (E), and (F), respectively. (**K** and **L**) Spectral phase Arg($\Delta\tilde{E}$) in momentum space corresponding to (C) and (E), respectively. In (H) and (I), pink dots correspond to the EP, dashed lines correspond to the bulk Fermi arc, and white arrowed contours correspond to the half-charge (H, K, and L) and integer (I and J) windings around the singularities.

charge of the eigenstates (or pseudospin) arising around singularities in momentum space, and the second one is the non-Hermitian topological charge associated with eigenenergies. For the case of Eq. 3, there are pairs of singularities in the pseudospin texture, around which the in-plane pseudospin component winds. As shown in Fig. 1H for the upper eigenstate, the in-plane pseudospin angle rotates by ±π around the singularity due to the π discontinuity at the bulk Fermi arc, resulting in half-integer topological charges (*30*). The lower eigenstate exhibits the same topological charges at the same singularities (see the Supplementary Materials). Moreover, the pseudospin is polarized up or down at these points, which translates to circularly polarized PL emission (*51*), exactly at the momenta of the paired EPs (see the Supplementary Materials).

Adding a chiral (or σ_z) term to Eq. 3, which can be achieved by magnetically induced Zeeman splitting (*36*), or intrinsic chirality (optical activity) (*38*), moves the EPs in momentum space, but the pseudospin singularities remain at the same momenta, a phenomenon closely related to the haunting theorem in singular optics (*51*). The singularities reside in separate eigenstates, and the topological charge becomes integer-valued. These effects are demonstrated in Fig. 1I for a weak, real-valued σ_z perturbation, where one singularity disappears, since it migrates to the other eigenstate (see the Supplementary Materials), and the winding of the remaining one is −2π. The integer topological charges persist even if the gap opens. Moreover, with increasing magnitude of the σ_z term, the polarization at the EP becomes elliptical, and the discontinuity at the bulk Fermi arc continuously decreases toward zero where the gap opens, as shown in Fig. 1J (see also the Supplementary Materials). The half-integer winding, shared by the two eigenstates, is therefore unstable against any σ_z perturbation, where a nonzero σ_z term suddenly switches the winding from π to 2π (or to zero for the other eigenstate). This transition is reminiscent of the Hermitian case, where the σ_z perturbation immediately destroys the Dirac point and opens the gap.

In contrast to the topology of the eigenstates described above, the winding of the eigenenergies is deeply tied to the EP and is topologically stable. The topology is revealed by the "spectral phase" of the difference of the two complex energies Arg($\Delta\tilde{E}$) (*23*–*25*). As shown in Fig. 1 (K and L), the singularities of the spectral phase occur exactly at the EP with a π-spectral phase winding or half-integer topological charge, regardless of where the singularities of the eigenstates are located in momentum space. This is because the spectral phase jump at the bulk Fermi arc remains equal to π. These two features, the π-winding and the π-phase jump, persist even under a weak, real-valued σ_z perturbation, as shown in Fig. 1L. This is in contrast with the behavior of the eigenstates, where the π winding suddenly switches to 2π (Fig. 1, H and I), and the phase jump across the bulk Fermi arc decreases with a σ_z perturbation (see the Supplementary Materials).

At sufficiently strong σ_z perturbation, the EPs meet and annihilate, the gap fully opens, and the non-Hermitian topological charges disappear, but the topological charges of the eigenstates (polarization vortices) remain (see Fig. 1J). This demonstrates that the topologies of the eigenstates and the eigenenergies are separable, and measuring the topology of the eigenstates, in general, is not equivalent to measuring the non-Hermitian topology of the eigenenergies. In the following, we experimentally observe paired EPs in an exciton-polariton system with weak chirality and directly measure the non-Hermitian topological invariant by extracting the winding of complex eigenenergies from the PL spectrum.

Experimental observation of paired EPs

To demonstrate the EP pairs in the exciton-polariton dispersion experimentally, we use the microcavity schematically shown in Fig. 2A. It is formed by sandwiching a ~142-nm-thick $CsPbBr_3$ perovskite crystal between two SiO_2/Ta_2O_5 DBRs, as detailed in Materials and Methods. The crystal is optically anisotropic because of its orthorhombic symmetry (*33*, *52*, *53*), which leads to *X*-*Y* splitting of the exciton-polariton states (*33*, *50*). The exciton polaritons are excited by an off-resonant laser with the photon energy far above the perovskite exciton energy. The exciton-polariton energy distribution in momentum space is extracted from the PL of the sample. An emitted photon at polar angle θ, azimuthal angle ϕ (see schematics in Fig. 2B), and photon wavelength λ carries the exciton-polariton in-plane momentum $\hbar\boldsymbol{k} = \hbar\left(\frac{2\pi}{\lambda}\right)\sin\theta(\cos\phi, \sin\phi)$, with ϕ corresponding to the propagation angle. To distinguish between the pseudospin states of exciton polaritons, which translate to the polarization of the PL, the signal is recorded with linear polarizations along the horizontal-vertical (H-V) (orientation shown in Fig. 2B), diagonal-antidiagonal (D-A), and left-right circular polarizations (L-R). The sample is oriented so that the *X*-*Y* splitting, along with the spin-orbit coupling, results in energy crossing along (k_x, $k_y = 0$) but no crossing along ($k_x = 0$, k_y) in the linearly polarized exciton-polariton dispersions (*36*, *37*), as shown in Fig. 2C.

The non-Hermitian character of the exciton-polariton dispersion is reflected in the linewidths of the modes, which are also split at $k = 0$ (see fig. S2). Subtracting the mean value, i.e., $\gamma - \langle\gamma\rangle$, reveals that the linewidth dependence on k is also anisotropic as shown in Fig. 2D, such that the linewidth switches or crosses along the direction (k_x, $k_y = 0$) but not along ($k_x = 0$, k_y). The crossings in energy and linewidth along the same direction suggest that the Fermi arcs form two loops in momentum space, as shown by the insets of Fig. 2C. A similar behavior of energy and linewidth in momentum space was observed for the cavity photons in birefringent ZnO-based microcavities (*46*, *54*) in the weak coupling regime (i.e., without coupling to excitons). However, the paired EPs remained elusive in the strong coupling regime despite several experiments on exciton polaritons in anisotropic cavities (*36*–*38*, *55*). Related EPs in momentum space were observed in microcavities with embedded carbon nanotubes (*56*) and organic microcrystals (*57*), but strong exciton-photon coupling in these systems only occurs in one polarization. Our results demonstrate that the exciton polaritons can inherit the EPs from birefringent cavity photons.

The EPs predicted in Fig. 1 (C and D) are expected to exist near the energy crossings at $\boldsymbol{k}^* \approx (\pm 5.2, 0)\ \mu m^{-1}$ (see Fig. 2C). The position of the EP pair can be determined by carefully tracking the complex spectrum near this region. The extraction of peak energy and linewidth from the polarized PL measurements is detailed in Materials and Methods. Figure 3 shows the results of the measurements along five lines (labeled b to f) in *k*-space that intersect the Fermi arcs as schematically shown in Fig. 3A. The measurement in Fig. 3B is approximately along the bulk Fermi arc, where the mode energies approach each other while the linewidths clearly repel. At a slightly off-arc position, as shown in Fig. 3C, the mode energies always repel, but the linewidths cross at two points of the imaginary Fermi arc. Perpendicular to the bulk Fermi arc and close to the EP, the energies cross while the linewidths approach each other, as shown in Fig. 3D. Conversely, the modes cross in linewidth and approach in energy outside the bulk Fermi arc but close to the EP, as shown in Fig. 3F. Across the middle of the bulk Fermi arc, Fig. 3E clearly shows that the energies cross, but the linewidths repel. From these results (see fig. S5 for the 2D surfaces), we estimate the EP positions to be $\boldsymbol{k}_{EP} \approx (-5.2, 0.40)\ \mu m^{-1}$ and $\boldsymbol{k}_{EP} \approx (-5.2, 0.09)\ \mu m^{-1}$ with a bulk Fermi arc length of $\approx 0.31\ \mu m^{-1}$.

Pseudospin texture in the complex artificial gauge field

The existence of the EPs is further evidenced by the circular polarization of the exciton-polariton emission (*9*, *46*), which corresponds to the singularities of the eigenstates near the EPs (see Fig. 1, H and I) where the exciton-polariton pseudospin points either up or down. We define the pseudospin of the eigenstates using the Stokes parameters:

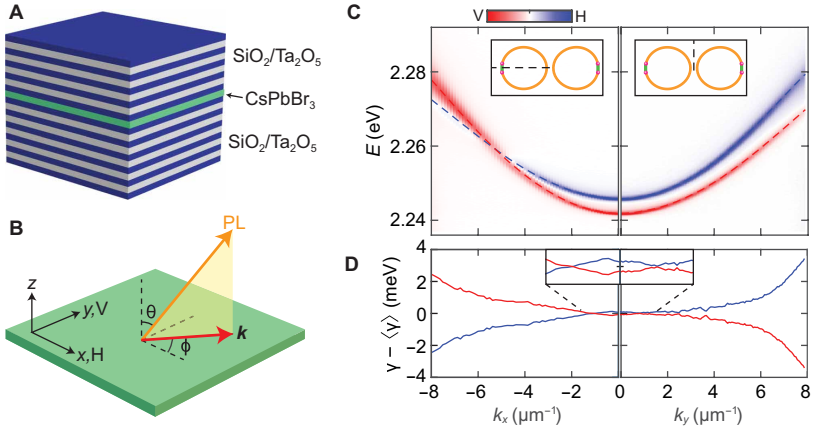

Fig. 2. Experimental investigation of the complex exciton-polariton eigenenergies. (**A**) Schematics of the planar microcavity made of SiO_2/Ta_2O_5 DBRs with an embedded $CsPbBr_3$ perovskite crystal. (**B**) Schematics of the laboratory (*x*, *y*, *z*) axis and the polarization measurement axis (H, V). The exciton-polariton in-plane momentum depends on the angles (θ,ϕ) of the PL emission. (**C**) Linearly polarized PL intensity (I_V-I_H) measured along (k_x, $k_y = 0$) and ($k_x = 0$, k_y). Dashed lines are the extracted peak energies of the two polarized modes. The dispersion is approximately symmetric for $k \rightarrow -k$. Inset: Schematics of the measurements in momentum space with respect to the Fermi arcs. (**D**) Linewidths of the modes in (C) with the mean subtracted. Inset: Enlarged region near $k = 0$.

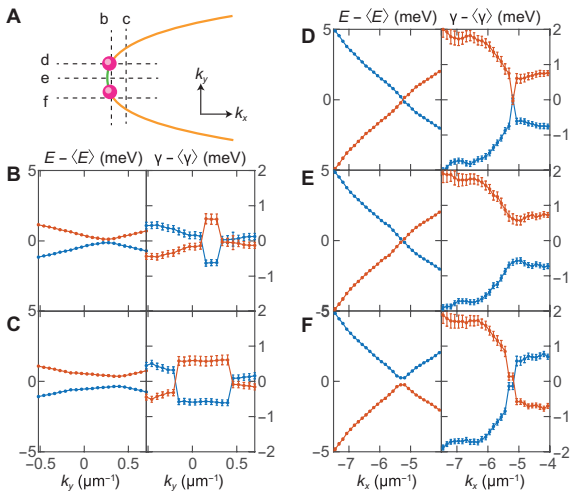

Fig. 3. Mapping out complex energies near the EP pair. (**A**) Schematics of the EP pair (pink dots) connected by the bulk (green) and imaginary (orange) Fermi arcs. Dashed lines (b to f) represent the lines (directions) in *k*-space, along which the measurements in (B) to (F) are performed. (**B** to **F**) Measured energies and linewidths (mean-subtracted) of the two modes: (B) Parallel to and very near the bulk Fermi arc; (C) parallel to the bulk Fermi arc intersecting the imaginary Fermi arc twice, which corresponds to two linewidth crossings and no crossing in energy; (D) perpendicular to the bulk Fermi arc very near the top EP, showing crossing in both energy and linewidth; (E) along the center of the real Fermi arc, showing crossing in energy and anticrossing in linewidth; (F) near the EP but outside the real Fermi arc showing no crossing in energy but crossing in linewidth. The complex eigenvalues are sorted so that a smooth crossing (D and E) or anticrossing (B, C, and F) in the real part is ensured. The values for *k* are as follows: (B) $k_x = -5.19$ μm^{-1}, (C) $k_x = -5.07$ μm^{-1}, (D) $k_y = 0.40$ μm^{-1}, (E) $k_y = 0.21$ μm^{-1}, and (F) $k_y = 0.09$ μm^{-1}. Error bars represent the 95% confidence interval fitting results.

$S_1 = (I_H - I_V)/(I_H + I_V)$, $S_2 = (I_D - I_A)/(I_D + I_A)$, and $S_3 = (I_R - I_L)/(I_R + I_L)$. In the Hermitian limit, and since Eq. 3 does not have a σ_z term, the eigenstates are orthogonal and purely linearly polarized (*48*), with the corresponding pseudospins confined to the S_1-S_2 plane of the Poincaré sphere (orthogonal polarizations are antipodal), as shown by the thin red and blue arrows in Fig. 4A. However, due to non-Hermiticity, the eigenstates of the Hamiltonian are not orthogonal, and the pseudospins of the eigenstates tend to point in the same direction toward one of the poles, as shown by the thick red and blue arrows in Fig. 4A. This leads to a nonzero S_3 Stokes component, while the projections on the S_1-S_2 plane remain antipodal. Hence, both eigenstates have the same S_3 components (dashed arrows in Fig. 4A), which, in this case, is a measure of the non-Hermiticity of the Hamiltonian. At the EP, full alignment occurs, resulting in a merged eigenstate pointing to the pole with a purely circular polarization, as shown by the purple arrow in Fig. 4A. The calculated circular polarization or S_3 component of the pseudospin texture of either eigenstate in *k*-space is shown in Fig. 4B. Maximum circular polarization occurs at the EPs and gradually decreases away from them. The EPs within the pair have opposite chirality, and the two pairs have opposite orientations.

The appearance of chirality in the model arises from the interplay between the real and imaginary components of the purely in-plane complex artificial magnetic field. If the real and imaginary fields are parallel or purely real or imaginary, the pseudospin of the eigenstates tends to align (parallel or antiparallel) to the field. However, if the two fields have perpendicular components, the pseudospins tend to align away from the real and imaginary parts and toward each other, which, in our case, effectively induces an out-of-plane component. The effective out-of-plane component is different from a real-valued out-of-plane magnetic field, where the pseudospins of the two modes remain antipodal on the Poincaré sphere. This non-Hermitian generalization allows an arbitrary control of the polarization (*58*) and can lead to rich spin dynamics not achievable with real-valued artificial magnetic fields. Note that in this off-resonant (incoherent) regime of exciton-polariton excitation, we are measuring the pseudospin of the eigenstates. This is in contrast to the resonant (coherent) regime, where a nonzero S_3 component can result from pseudospin precession in an in-plane field (*45*).

We take advantage of the non-Hermiticity, which results in non-orthogonal and chiral eigenstates, to directly measure the S_3 or spin texture of the exciton polaritons, as shown in Fig. 4C, by capturing the momentum space distribution without resolving the two modes. This method assumes that the two eigenstates at a momentum $\boldsymbol{k}$ are equally occupied, which is not always the case. However, it is effective for finding the pseudospin singularities shown in Fig. 1(H and I). A circular polarization texture qualitatively similar to the prediction of the model is observed using this method, with the local extrema near the EPs (black points in Fig. 4C). The discrepancy between the momenta of the EPs and the extrema of the S_3 texture is due to the close proximity of the EPs. The opposite circular polarization in the vicinity of the paired EPs tends to overlap and cancel each other. Hence, the measured $|S_3|$ is greatly reduced, and the extrema are offset away from the EPs (see the Supplementary Materials for supporting simulations). A similar low level of circular polarization degree near the EPs was observed for microcavity photons without coupling to excitons (*54*).

In addition to the spin texture due to the EPs, there is a background circular polarization (or chirality) that is not accounted for in the model Eqs. 1 and 2. This originates from the exciton emission of the bare perovskite (see the Supplementary Materials). The observed chirality can arise from the chirality of the excitons in lead-halide perovskites (*59*, *60*), but further experimental work is needed to verify its origin and derive an effective model for its spin texture. Here, we treat the chirality as a weak σ_z perturbation to Eq. 3, which can move the EPs toward each other and potentially open the gap in the Hermitian limit (see Fig. 1) (*38*). The clear observation of EPs in our experiment therefore demonstrates the topological stability of EP pairs against gap-opening (chiral) perturbations or any perturbation in general (*12*). The weak chirality places the experiment in the regime shown in Fig. 1(E, I, and L), where the topologies of the eigenstates and eigenenergies are not related to each other.

Observation of non-Hermitian topological invariant

Last, with the existence of the EPs verified using both the complex energies and pseudospin texture, we demonstrate the direct measurement of the non-Hermitian topological invariant arising from the EPs in momentum space. For the two-level system considered here, the non-Hermitian topological invariant, called the "spectral winding" or "vorticity" (*23*–*25*), is formally defined as

$$w = -\frac{1}{2\pi}\oint_C \nabla_{\boldsymbol{k}} \arg\left[\widetilde{E}_+(\boldsymbol{k}) - \widetilde{E}_-(\boldsymbol{k})\right] \cdot d\boldsymbol{k} \quad (4)$$

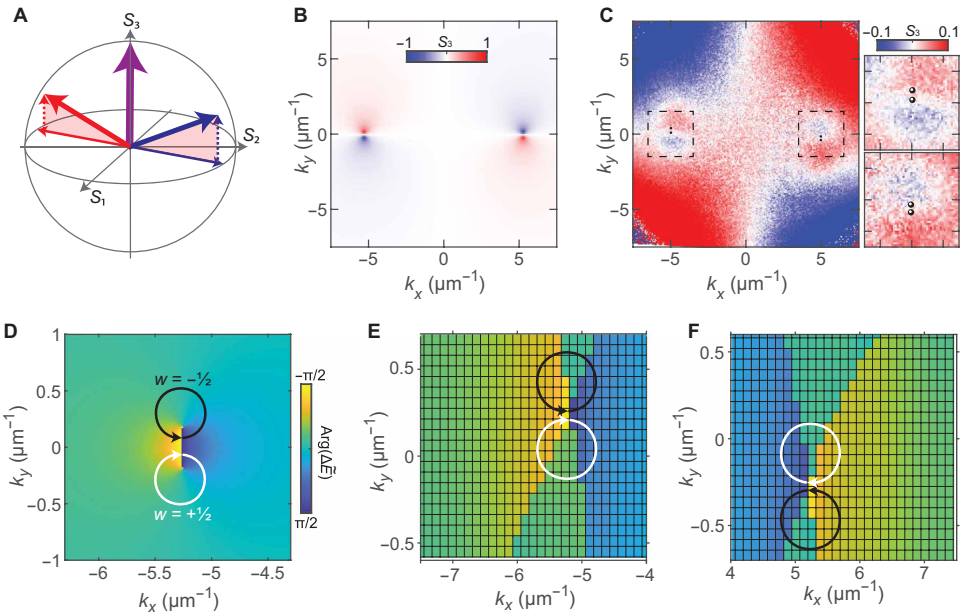

Fig. 4. Chirality and topology of the EPs. (**A**) Poincaré sphere with arrows representing the pseudospin of exciton polaritons away from the EP (thin red and blue), near the EP (thick red and blue), and at the EP (thick purple). Dashed vertical arrows are the effective out-of-plane field arising from the imaginary component of the complex in-plane artificial magnetic field. (**B**) Theoretical texture of circular polarization (S_3) arising from the inclusion of non-Hermiticity into the model of Eq. 1. (**C**) Measured energy-integrated circular polarization (S_3) showing the same spin structure as in (B) but with a weak S_3 background coming from the bare perovskite (see section: Pseudospin texture in the complex artificial gauge field). Right: Enlarged images of the marked regions showing the position of EPs (black points). (**D**) Theoretical values of arg($\tilde{E}_+ - \tilde{E}_-$) for one EP pair with the arrows schematically showing the fractional winding number. Parameters are the same as in Fig. 1 (C and D). (**E** and **F**) Measured values of arg($\tilde{E}_+ - \tilde{E}_-$) near the two pairs of EPs demonstrating the half-integer spectral winding around each EP.

where C is a closed loop in k-space. Naturally, this topological invariant is zero for Hermitian systems. The topology depends on the scalar field arg$[\tilde{E}_+(\boldsymbol{k}) - \tilde{E}_-(\boldsymbol{k})]$, a spectral phase that is well defined everywhere except at the EPs. Hence, the EPs are sources of non-Hermitian topological charges. For the paired EPs considered here, the theoretical spectral phase calculated from model Eq. 3 rotates in opposite directions around each EP, forming oppositely charged spectral vortices, as shown in Fig. 4D. The spectral vortices have a half-integer charge (*23*) since the spectral phase acquired around the loop enclosing a single EP is $\pm\pi$.

By carefully measuring the energies and linewidths in the vicinity of the EP pairs, we are able to extract the spectral phase and consequently determine the winding of the complex eigenenergies, as presented in Fig. 4 (E and F). The spectral phase winds around the EPs and jumps by approximately π at the bulk Fermi arc that connects the EPs. The small phase jumps away from the EP pair are experimental artifacts where we switch between H-V and D-A polarized measurements (see Materials and Methods) to extract the energies and linewidths. Using the definition in Eq. 4, we can assign a ±1/2 non-Hermitian topological charge to the EPs, as annotated in Fig. 4D and symbolized by the black and white arrows in Fig. 4 (E and F). Each pair of EPs therefore forms a "topological dipole," and the two dipoles have opposite orientations, as predicted by the model in Fig. 4B. Furthermore, the spectral winding around the whole EP pair is zero. Consequently, if the separation of the EP pair is not resolved in the experiment, the non-Hermitian topological invariant would not be measurable.

It is important to stress that the topological winding of the eigenenergies measured here should, in principle, be accompanied by the half-integer winding of polarization (*30*), as theoretically demonstrated in Fig. 1 (H and K). However, because of the background S_3, which introduces a weak σ_z term perturbation, the measured spectral winding is no longer related to the winding of the polarization (see Fig. 1, I and L). Hence, the non-Hermitian topological invariant observed in this work is fundamentally different from the winding of the eigenstates observed in photonic systems (*30*). Moreover, the measured half-integer topological invariant is unaffected by the chirality observed in the experiment, as theoretically demonstrated in Fig. 1L. This is not the case for the polarization winding that would become integer-valued even for weak chiral perturbation.

DISCUSSION

In summary, we have demonstrated the existence of paired EPs in the momentum-resolved exciton-polariton spectrum and directly measured the non-Hermitian topological invariant arising from the half-integer winding of the exciton-polariton complex eigenenergies around the EPs. We have also shown theoretically that the topology of the eigenstates and eigenenergies is separable, and hence, the signatures of inherent topology of EPs previously observed in the eigenstates of classical wave systems (*30*, *31*) are fundamentally different from our observation.

In contrast to previously demonstrated EPs in parameter space of exciton-polariton systems (*40*, *41*, *56*), the EPs in momentum

space observed here are expected to have a direct influence on the system's dynamics (*61*). Our observation can potentially lead to the realization of non-Hermitian topological phases (*24*) and the predicted nontrivial dynamics, such as a non-Hermitian skin effect (*62*), without the need for sophisticated microstructuring of the sample (*43*) or strong external magnetic fields (*35*). Moreover, we have demonstrated the manifestation of the imaginary part of the artificial gauge field that tends to align the exciton-polariton pseudospin pair toward each other and perpendicular to the field direction. This may lead to a new type of spin precession (*58*) and dynamics of exciton polaritons that is not possible in real magnetic fields. Combined with advanced methods for potential landscaping (*32*) and the possibility to extract a wide range of observables from the cavity PL, our work affirms exciton polaritons as a solid-state platform for exploring robust topological phenomena that do not occur in Hermitian systems. A recent experiment on organic microcavities with highly polarization-dependent (anisotropic) light-matter coupling (*57*) has demonstrated a diverging quantum metric at the EP, in stark difference to Hermitian systems (*31*).

Unlike previous observations of EPs in optical microcavities (*54*), our demonstration of a non-Hermitian topological invariant relies on hybrid light-matter particles, exciton polaritons, which exhibit strong interactions due to the exciton component (*63*). Therefore, our study offers a new platform for investigating the interplay between the non-Hermitian topology and nonlinearity, which may bring about unexpected phenomena, e.g., similar to self-adaptation in energy transfer (*64*). For example, under a strong circular polarized excitation, the unique strong spin-anisotropic nonlinearity in exciton-polariton systems (*48*, *55*) could potentially lead to an effective real σ_z perturbation with rich tunability. This could provide an efficient pathway for investigating Hermitian and non-Hermitian topological effects in the presence of σ_z perturbations and nonlinearity, even without the need of real magnetic fields.

Last, the strong interactions and very small effective mass of exciton polaritons have successfully enabled the demonstration of collective quantum effects, e.g., bosonic condensation (*65*) and superfluidity (*66*, *67*), at elevated temperatures, in particular, using lead-halide perovskites (*33*, *34*, *68*). Thus, our work paves the way for investigating the interplay between quantum many-body effects and non-Hermitian topology, which is, as yet, an unexplored frontier in non-Hermitian physics (*12*).

MATERIALS AND METHODS

Perovskite microcavity fabrication

Pairs (20.5) of SiO_2 and Ta_2O_5 were deposited on a silicon substrate as the bottom DBR using an electron beam evaporator (OHMIKER-50D). The 142-nm-thick cesium lead bromide perovskite crystal was grown with a vapor phase deposition method on a mica substrate and then transferred onto the bottom DBR by a dry-transfer process with Scotch tape (*33*). Subsequently, a 60-nm-thick poly(methyl methacrylate) protection layer was spin-coated onto the perovskite layer. Another 10.5 pairs of SiO_2 and Ta_2O_5 were deposited onto the structure by the electron beam evaporator, acting as the top DBR to complete the fabrication process.

Optical spectroscopy characterizations

The energy-resolved momentum space PL was mapped by using a home-built angle-resolved PL setup with a motorized translation stage to scan the whole 2D momentum space. In the detection line, a quarter–wave plate, a half–wave plate, and a linear polarizer were used for the detection of polarization-resolved PL mappings in momentum space. A continuous-wave laser (457 nm) with a pump spot of ~10 μm was used to pump the perovskite microcavity, passing through an optical chopper to minimize sample heating. The emission from the perovskite microcavity was collected through a 50× objective (numerical aperture = 0.75, Mitutoyo) and directed to a 550-mm focal length spectrometer (HORIBA iHR550) with a grating of 1200 lines/mm and a liquid nitrogen–cooled charge-coupled device of 256 × 1024 pixels. All measurements were conducted at room temperature.

Non-Hermitian theoretical model

The simple non-Hermitian model in Eqs. 1 and 2 for the exciton-polariton spectrum was derived by simulating the reflectance of a microcavity with an embedded anisotropic cavity spacer and the excitonic transition in the strong coupling regime. We follow the 4 × 4 transfer matrix method in (*46*) but with an addition of the exciton resonance modeled as a Lorentz oscillator.

The transfer matrix calculations and the theoretical model also capture the linewidth behavior of the experiment shown in fig. S4. Regardless of the direction, the linewidth increases with k as the exciton fraction of polariton increases. However, the experimental linewidth increases more or less linearly with k (see fig. S4), compared to the near-parabolic behavior of the numerical simulation. This can arise from the inhomogeneous broadening of the exciton resonance, which is not accounted for in the simulations.

Determination of mode energies and linewidths

To measure the energy and linewidth, we fit Lorentzian functions to the measured spectra at different points in k-space. The energy corresponds to the center, while the linewidth corresponds to the full width at half maximum of the fitted Lorentzian function. Away from the energy crossings, the spectrum displays two peaks and can be fitted with a double Lorentzian function, as shown in fig. S7. Near the energy crossings, there is only one apparent peak since the mode energy separation is smaller than the linewidth. To resolve the individual peaks, we take advantage of the orthogonal pairs (H-V or D-A) of polarized measurements. Each polarized spectrum is fitted with a single Lorentzian as shown in fig. S7, and the orthogonal pair with the largest energy splitting is chosen. This switching between H-V and D-A results in jumps in the extracted energies and linewidths (see Fig. 3, B to F) and small phase jumps in the spectral phase (see Fig. 4, E and F). This is because we are not measuring (or projecting) the eigenstates in their appropriate orthogonal basis. In principle, a full polarization tomography is needed, in addition to the 2D scan of the momentum space, to properly separate the modes and smoothen the jumps in the complex energy and spectral phase. However, this will greatly increase the measurement time and data from 3D to 4D. The current set of data is enough to verify the existence of EPs and measure the half-integer spectral winding in this system.

SUPPLEMENTARY MATERIALS

Supplementary material for this article is available at https://science.org/doi/10.1126/sciadv.abj8905

REFERENCES AND NOTES

1. Y. Tokura, K. Yasuda, A. Tsukazaki, Magnetic topological insulators. *Nat. Rev. Phys.* **1**, 126–143 (2019).
2. A. A. Burkov, Chiral anomaly and transport in Weyl metals. *J. Phys. Condens. Mater.* **27**, 113201 (2015).

3. C. K. Chan, N. H. Lindner, G. Refael, P. A. Lee, Photocurrents in Weyl semimetals. *Phys. Rev. B* **95**, (2017).
4. L. Lu, J. D. Joannopoulos, M. Soljacic, Topological photonics. *Nat. Photonics* **8**, 821–829 (2014).
5. Ş. K. Özdemir, S. Rotter, F. Nori, L. Yang, Parity–time symmetry and exceptional points in photonics. *Nat. Mater.* **18**, 783–798 (2019).
6. R. El-Ganainy, K. G. Makris, M. Khajavikhan, Z. H. Musslimani, S. Rotter, D. N. Christodoulides, Non-Hermitian physics and PT symmetry. *Nat. Phys.* **14**, 11–19 (2018).
7. B. Peng, Ş. K. Özdemir, S. Rotter, H. Yilmaz, M. Liertzer, F. Monifi, C. M. Bender, F. Nori, L. Yang, Loss-induced suppression and revival of lasing. *Science* **346**, 328–332 (2014).
8. W. Chen, Ş. Kaya Özdemir, G. Zhao, J. Wiersig, L. Yang, Exceptional points enhance sensing in an optical microcavity. *Nature* **548**, 192–196 (2017).
9. H. Hodaei, A. U. Hassan, S. Wittek, H. Garcia-Gracia, R. El-Ganainy, D. N. Christodoulides, M. Khajavikhan, Enhanced sensitivity at higher-order exceptional points. *Nature* **548**, 187–191 (2017).
10. C. E. Rüter, K. G. Makris, R. El-Ganainy, D. N. Christodoulides, M. Segev, D. Kip, Observation of parity–time symmetry in optics. *Nat. Phys.* **6**, 192–195 (2010).
11. B. Peng, Ş. K. Özdemir, F. Lei, F. Monifi, M. Gianfreda, G. L. Long, S. Fan, F. Nori, C. M. Bender, L. Yang, Parity–time-symmetric whispering-gallery microcavities. *Nat. Phys.* **10**, 394–398 (2014).
12. E. J. Bergholtz, J. C. Budich, F. K. Kunst, Exceptional topology of non-Hermitian systems. *Rev. Mod. Phys.* **93**, 15005 (2019).
13. A. Ghatak, T. Das, New topological invariants in non-Hermitian systems. *J. Phys. Condens. Matter* **31**, 263001 (2019).
14. S. Yao, Z. Wang, Edge states and topological invariants of non-Hermitian systems. *Phys. Rev. Lett.* **121**, 086803 (2018).
15. Y. Xiong, Why does bulk boundary correspondence fail in some non-Hermitian topological models. *J. Phys. Commun.* **2**, 035043 (2018).
16. F. K. Kunst, E. Edvardsson, J. C. Budich, E. J. Bergholtz, Biorthogonal bulk-boundary correspondence in non-Hermitian systems. *Phys. Rev. Lett.* **121**, 026808 (2018).
17. S. Yao, F. Song, Z. Wang, Non-Hermitian Chern bands. *Phys. Rev. Lett.* **121**, 136802 (2018).
18. T. Liu, Y.-R. Zhang, Q. Ai, Z. Gong, K. Kawabata, M. Ueda, F. Nori, Second-order topological phases in non-hermitian systems. *Phys. Rev. Lett.* **122**, 076801 (2019).
19. C. H. Lee, L. Li, J. Gong, Hybrid higher-order skin-topological modes in nonreciprocal systems. *Phys. Rev. Lett.* **123**, 016805 (2019).
20. M. Brandenbourger, X. Locsin, E. Lerner, C. Coulais, Non-reciprocal robotic metamaterials. *Nat. Commun.* **10**, 4608 (2019).
21. T. Helbig, T. Hofmann, S. Imhof, M. Abdelghany, T. Kiessling, L. W. Molenkamp, C. H. Lee, A. Szameit, M. Greiter, R. Thomale, Generalized bulk–boundary correspondence in non-Hermitian topolectrical circuits. *Nat. Phys.* **16**, 747–750 (2020).
22. L. Xiao, T. Deng, K. Wang, G. Zhu, Z. Wang, W. Yi, P. Xue, Non-Hermitian bulk–boundary correspondence in quantum dynamics. *Nat. Phys.* **16**, 761–766 (2020).
23. D. Leykam, K. Y. Bliokh, C. Huang, Y. D. Chong, F. Nori, Edge modes, degeneracies, and topological numbers in non-Hermitian systems. *Phys. Rev. Lett.* **118**, 040401 (2017).
24. Z. Gong, Y. Ashida, K. Kawabata, K. Takasan, S. Higashikawa, M. Ueda, Topological phases of non-Hermitian systems. *Phys. Rev. X* **8**, 031079 (2018).
25. H. Shen, B. Zhen, L. Fu, Topological band theory for non-Hermitian Hamiltonians. *Phys. Rev. Lett.* **120**, 146402 (2018).
26. M. Atala, M. Aidelsburger, J. T. Barreiro, D. Abanin, T. Kitagawa, E. Demler, I. Bloch, Direct measurement of the Zak phase in topological Bloch bands. *Nat. Phys.* **9**, 795–800 (2013).
27. M. Aidelsburger, M. Lohse, C. Schweizer, M. Atala, J. T. Barreiro, S. Nascimbène, N. R. Cooper, I. Bloch, N. Goldman, Measuring the Chern number of Hofstadter bands with ultracold bosonic atoms. *Nat. Phys.* **11**, 162–166 (2015).
28. W. Hu, J. C. Pillay, K. Wu, M. Pasek, P. P. Shum, Y. D. Chong, Measurement of a topological edge invariant in a microwave network. *Phys. Rev. X* **5**, 011012 (2015).
29. S. Mittal, S. Ganeshan, J. Fan, A. Vaezi, M. Hafezi, Measurement of topological invariants in a 2D photonic system. *Nat. Photonics* **10**, 180–183 (2016).
30. H. Zhou, C. Peng, Y. Yoon, C. W. Hsu, K. A. Nelson, L. Fu, J. D. Joannopoulos, M. Soljačić, B. Zhen, Observation of bulk Fermi arc and polarization half charge from paired exceptional points. *Science* **359**, 1009–1012 (2018).
31. A. Ghatak, M. Brandenbourger, J. van Wezel, C. Coulais, Observation of non-Hermitian topology and its bulk-edge correspondence in an active mechanical metamaterial. *Proc. Natl. Acad. Sci. U.S.A.* **117**, 29561–29568 (2020).
32. C. Schneider, K. Winkler, M. D. Fraser, M. Kamp, Y. Yamamoto, E. A. Ostrovskaya, S. Höfling, Exciton-polariton trapping and potential landscape engineering. *Rep. Prog. Phys.* **80**, 016503 (2016).
33. R. Su, S. Ghosh, J. Wang, S. Liu, C. Diederichs, T. C. H. Liew, Q. Xiong, Observation of exciton polariton condensation in a perovskite lattice at room temperature. *Nat. Phys.* **16**, 301–306 (2020).
34. M. Dusel, S. Betzold, O. A. Egorov, S. Klembt, J. Ohmer, U. Fischer, S. Höfling, C. Schneider, Room temperature organic exciton–polariton condensate in a lattice. *Nat. Commun.* **11**, 2863 (2020).
35. S. Klembt, T. H. Harder, O. A. Egorov, K. Winkler, R. Ge, M. A. Bandres, M. Emmerling, L. Worschech, T. C. H. Liew, M. Segev, C. Schneider, S. Höfling, Exciton-polariton topological insulator. *Nature* **562**, 552–556 (2018).
36. A. Gianfrate, O. Bleu, L. Dominici, V. Ardizzone, M. De Giorgi, D. Ballarini, G. Lerario, K. W. West, L. N. Pfeiffer, D. D. Solnyshkov, D. Sanvitto, G. Malpuech, Measurement of the quantum geometric tensor and of the anomalous Hall drift. *Nature* **578**, 381–385 (2020).
37. L. Polimeno, M. De Giorgi, G. Lerario, L. De Marco, L. Dominici, V. Ardizzone, M. Pugliese, C. T. Prontera, V. Maiorano, A. Moliterni, C. Giannini, V. Olieric, G. Gigli, D. Ballarini, D. Solnyshkov, G. Malpuech, D. Sanvitto, Tuning the Berry curvature in 2D perovskite. arXiv:2007.14945 (2020).
38. J. Ren, Q. Liao, F. Li, Y. Li, O. Bleu, G. Malpuech, J. Yao, H. Fu, D. Solnyshkov, Nontrivial band geometry in an optically active system. *Nat. Commun.* **12**, 689 (2021).
39. W. D. Heiss, Exceptional points of non-Hermitian operators. *J. Phys. A Math. Gen.* **37**, 2455–2464 (2004).
40. T. Gao, E. Estrecho, K. Y. Bliokh, T. C. H. Liew, M. D. Fraser, S. Brodbeck, M. Kamp, C. Schneider, S. Höfling, Y. Yamamoto, F. Nori, Y. S. Kivshar, A. G. Truscott, R. G. Dall, E. A. Ostrovskaya, Observation of non-Hermitian degeneracies in a chaotic exciton-polariton billiard. *Nature* **526**, 554–558 (2015).
41. T. Gao, G. Li, E. Estrecho, T. C. H. Liew, D. Comber-Todd, A. Nalitov, M. Steger, K. West, L. Pfeiffer, D. W. Snoke, A. V. Kavokin, A. G. Truscott, E. A. Ostrovskaya, Chiral modes at exceptional points in exciton-polariton quantum fluids. *Phys. Rev. Lett.* **120**, 065301 (2018).
42. P. Comaron, V. Shahnazaryan, W. Brzezicki, T. Hyart, M. Matuszewski, Non-Hermitian topological end-mode lasing in polariton systems. *Phys. Rev. Res.* **2**, 022051 (2020).
43. S. Mandal, R. Banerjee, E. A. Ostrovskaya, T. C. H. Liew, Nonreciprocal transport of exciton polaritons in a non-Hermitian chain. *Phys. Rev. Lett.* **125**, 123902 (2020).
44. L. Pickup, H. Sigurdsson, J. Ruostekoski, P. G. Lagoudakis, Synthetic band-structure engineering in polariton crystals with non-Hermitian topological phases. *Nat. Commun.* **11**, 4431 (2020).
45. C. Leyder, M. Romanelli, J. P. Karr, E. Giacobino, T. C. H. Liew, M. M. Glazov, A. V. Kavokin, G. Malpuech, A. Bramati, Observation of the optical spin Hall effect. *Nat. Phys.* **3**, 628–631 (2007).
46. S. Richter, T. Michalsky, C. Sturm, B. Rosenow, M. Grundmann, R. Schmidt-Grund, Exceptional points in anisotropic planar microcavities. *Phys. Rev. A* **95**, 023836 (2017).
47. G. Panzarini, L. C. Andreani, A. Armitage, D. Baxter, M. S. Skolnick, V. N. Astratov, J. S. Roberts, A. V. Kavokin, M. R. Vladimirova, M. A. Kaliteevski, Cavity-polariton dispersion and polarization splitting in single and coupled semiconductor microcavities. *Phys. Solid State* **41**, 1223–1238 (1999).
48. H. Terças, H. Flayac, D. D. Solnyshkov, G. Malpuech, Non-Abelian gauge fields in photonic cavities and photonic superfluids. *Phys. Rev. Lett.* **112**, 066402 (2014).
49. A. Fieramosca, L. Polimeno, G. Lerario, L. De Marco, M. De Giorgi, D. Ballarini, L. Dominici, V. Ardizzone, M. Pugliese, V. Maiorano, G. Gigli, C. Leblanc, G. Malpuech, D. Solnyshkov, D. Sanvitto, Chromodynamics of photons in an artificial non-Abelian magnetic Yang-Mills field. arXiv:1912.09684 (2019).
50. R. Su, S. Ghosh, T. C. H. Liew, Q. Xiong, Optical switching of topological phase in a perovskite polariton lattice. *Sci. Adv.* **7**, eabf8049 (2021).
51. M. V. Berry, M. R. Dennis, The optical singularities of birefringent dichroic chiral crystals. *Proc. R. Soc. Lond. Ser. A* **459**, 1261–1292 (2003).
52. M. A. Becker, R. Vaxenburg, G. Nedelcu, P. C. Sercel, A. Shabaev, M. J. Mehl, J. G. Michopoulos, S. G. Lambrakos, N. Bernstein, J. L. Lyons, T. Stöferle, R. F. Mahrt, M. V. Kovalenko, D. J. Norris, G. Rainò, A. L. Efros, Bright triplet excitons in caesium lead halide perovskites. *Nature* **553**, 189–193 (2018).
53. R. Su, C. Diederichs, J. Wang, T. C. H. Liew, J. Zhao, S. Liu, W. Xu, Z. Chen, Q. Xiong, Room-temperature polariton lasing in all-inorganic perovskite nanoplatelets. *Nano Lett.* **17**, 3982–3988 (2017).
54. S. Richter, H.-G. Zirnstein, J. Zúñiga-Pérez, E. Krüger, C. Deparis, L. Trefflich, C. Sturm, B. Rosenow, M. Grundmann, R. Schmidt-Grund, Voigt exceptional points in an anisotropic ZnO-based planar microcavity: Square-root topology, polarization vortices, and circularity. *Phys. Rev. Lett.* **123**, 227401 (2019).
55. D. Biegańska, M. Pieczarka, E. Estrecho, M. Steger, D. W. Snoke, K. West, L. N. Pfeiffer, M. Syperek, A. G. Truscott, E. A. Ostrovskaya, Collective excitations of exciton-polariton condensates in a synthetic gauge field. arXiv:2011.13290 (2020).
56. W. Gao, X. Li, M. Bamba, J. Kono, Continuous transition between weak and ultrastrong coupling through exceptional points in carbon nanotube microcavity exciton–polaritons. *Nat. Photonics* **12**, 362–367 (2018).
57. Q. Liao, C. Leblanc, J. Ren, F. Li, Y. Li, D. Solnyshkov, G. Malpuech, J. Yao, H. Fu, Experimental measurement of the divergent quantum metric of an exceptional point. *Phys. Rev. Lett.* **127**, 107402 (2020).

58. A. Cerjan, S. Fan, Achieving arbitrary control over pairs of polarization states using complex birefringent metamaterials. *Phys. Rev. Lett.* **118**, 253902 (2017).
59. P. C. Sercel, Z. V. Vardeny, A. L. Efros, Circular dichroism in non-chiral metal halide perovskites. *Nanoscale* **12**, 18067–18078 (2020).
60. J. Li, J. Li, R. Liu, Y. Tu, Y. Li, J. Cheng, T. He, X. Zhu, Autonomous discovery of optically active chiral inorganic perovskite nanocrystals through an intelligent cloud lab. *Nat. Commun.* **11**, 2046 (2020).
61. D. D. Solnyshkov, C. Leblanc, L. Bessonart, A. Nalitov, J. Ren, Q. Liao, F. Li, G. Malpuech, Quantum metric and wave packets at exceptional points in non-Hermitian systems. *Phys. Rev. B* **103**, 125302 (2021).
62. T. Hofmann, T. Helbig, F. Schindler, N. Salgo, M. Brzezińska, M. Greiter, T. Kiessling, D. Wolf, A. Vollhardt, A. Kabaši, C. H. Lee, A. Bilušić, R. Thomale, T. Neupert, Reciprocal skin effect and its realization in a topolectrical circuit. *Phys. Rev. Res.* **2**, 023265 (2020).
63. J. Wu, S. Ghosh, R. Su, A. Fieramosca, T. C. H. Liew, Q. Xiong, Nonlinear parametric scattering of exciton polaritons in perovskite microcavities. *Nano Lett.* **21**, 3120–3126 (2021).
64. S. Assawaworrarit, X. Yu, S. Fan, Robust wireless power transfer using a nonlinear parity–time-symmetric circuit. *Nature* **546**, 387–390 (2017).
65. J. Kasprzak, M. Richard, S. Kundermann, A. Baas, P. Jeambrun, J. M. J. Keeling, F. M. Marchetti, M. H. Szymańska, R. André, J. L. Staehli, V. Savona, P. B. Littlewood, B. Deveaud, L. S. Dang, Bose–Einstein condensation of exciton polaritons. *Nature* **443**, 409–414 (2006).
66. A. Amo, J. Lefrère, S. Pigeon, C. Adrados, C. Ciuti, I. Carusotto, R. Houdré, E. Giacobino, A. Bramati, Superfluidity of polaritons in semiconductor microcavities. *Nat. Phys.* **5**, 805–810 (2009).
67. G. Lerario, A. Fieramosca, F. Barachati, D. Ballarini, K. S. Daskalakis, L. Dominici, M. De Giorgi, S. A. Maier, G. Gigli, S. Kéna-Cohen, D. Sanvitto, Room-temperature superfluidity in a polariton condensate. *Nat. Phys.* **13**, 837–841 (2017).
68. R. Su, J. Wang, J. Zhao, J. Xing, W. Zhao, C. Diederichs, T. C. H. Liew, Q. Xiong, Room temperature long-range coherent exciton polariton condensate flow in lead halide perovskites. *Sci. Adv.* **4**, eaau0244 (2018).

Acknowledgments

Funding: Q.X. acknowledges the National Natural Science Foundation of China (no. 12020101003), strong support from the State Key Laboratory of Low-Dimensional Quantum Physics, and start-up grant from Tsinghua University. T.C.H.L. acknowledges the support from Singapore Ministry of Education via AcRF Tier 3 Programme "Geometrical Quantum Materials" (MOE2018-T3-1-002) and AcRF Tier 2 grants (MOE2017-T2-1-001, MOE2018-T2-02-068, and MOE2019-T2-1-004). E.E., E.A.O., M.W., and M.P. acknowledge support from the Australian Research Council (ARC) through the Centre of Excellence Grant CE170100039. M.P. also acknowledges support from the Foundation for Polish Science in the START programme. **Author contributions:** Q.X. and E.A.O. supervised and guided this research. R.S. and Y.H. designed the setup. R.S. fabricated the sample. R.S. and E.E. designed and performed the experiments. E.E., R.S., and D.B. analyzed and interpreted the data with input from M.W., M.P., A.G.T., T.C.H.L., E.A.O., and Q.X. E.E. developed the theoretical model and performed the theoretical calculations. E.E., R.S., and E.A.O. wrote the manuscript with input from all authors. **Competing interests:** The authors declare that they have no competing interests. **Data and materials availability:** All data needed to evaluate the conclusions in the paper are present in the paper and/or the Supplementary Materials.

Submitted 9 June 2021
Accepted 13 September 2021
Published 3 November 2021
10.1126/sciadv.abj8905

Supplementary material

Science Advances
AAAS

Supplementary Materials for

Direct measurement of a non-Hermitian topological invariant in a hybrid light-matter system

Rui Su*, Eliezer Estrecho*, Dąbrówka Biegańska, Yuqing Huang,
Matthias Wurdack, Maciej Pieczarka, Andrew G. Truscott, Timothy C. H. Liew,
Elena A. Ostrovskaya*, Qihua Xiong*

*Corresponding author. Email: Qihua_xiong@tsinghua.edu.cn (Q.X.); elena.ostrovskaya@anu.edu.au (E.A.O.); surui@ntu.edu.sg (R.S.); eliezer.estrecho@anu.edu.au (E.E.)

Published 3 November 2021, *Sci. Adv.* **7**, eabj8905 (2021)
DOI: 10.1126/sciadv.abj8905

This PDF file includes:

Numerical simulations and theoretical modelling

Examples of the simulated reflectance are shown in Fig. S1, with and without strong exciton-photon coupling. Without exciton-photon coupling, the reflectance dips correspond to the cavity photon modes, which can be modelled by Eq. (2) of the main text, as shown by the dashed lines in fig. S1**a**. In the strong coupling regime, the reflectance dips form 4 exciton-polariton branches, as shown in Fig. S1**b**. All branches can be modelled by Eq. (1) using the parameters of the cavity photon with the exciton-photon coupling strength V as the fitting parameter.

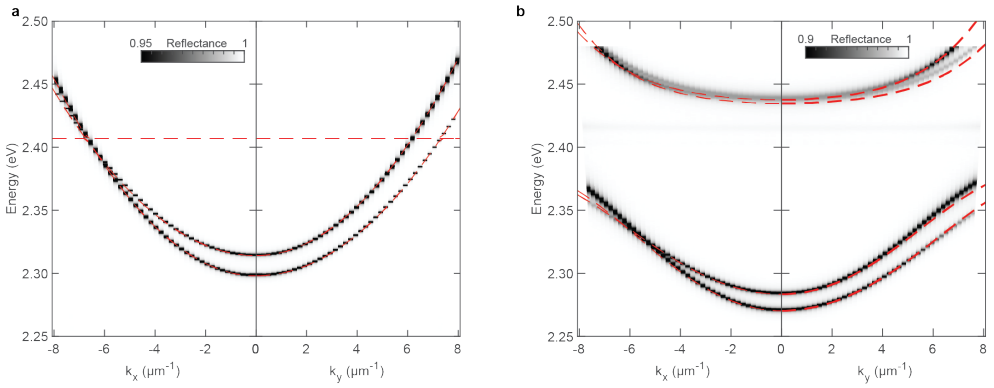

Figure S1: Simulated reflectance using the 4×4 transfer matrix method. a "Empty" anisotropic microcavity with exciton-photon coupling turned off. Dashed lines correspond to the exciton (known a priori) and cavity photon energies (fitted using Eq. 2 of the main text). **b** Same as **a** but with the exciton-photon coupling turned on. Dashed lines are energies extracted from the model, Eq. 1 of the main text, of the main text using the exciton and cavity photon energies extracted in (a), and the exciton-photon coupling strength V as the fit parameter.

We fitted Lorentzian profiles to the reflectance dips to extract the energy (peak centre) and linewidth (peak width), which are presented as data points in Fig. S2**a**, **b** and Fig. S2**c**, **d** for the weak and strong coupling regimes, respectively. Evidently, the energies of the lower polariton branches (see Fig. S2**c**) inherit the same behaviour from the cavity photon, but the crossing occurs at lower momenta for the polariton branches. However, the linewidth behaviour is different for the two cases. The linewidth of the TE (TM) polarised cavity photon increases (decreases) with momentum, resulting in the linewidths crossing along the k_y direction (see Fig. S2**b**). This means the Fermi arcs form a single closed contour in momentum space (see dashed contour in Fig. 1**G** of the main text). For the polariton branches, the linewidths increase with momentum, regardless of the polarisation. This is because the excitonic fraction (which has a large linewidth) increases with momentum. As a result, the polariton linewidths cross along the same direction as the energies,

suggesting that the Fermi arcs form two closed loops in momentum space, as illustrated by the solid arcs in Fig. 1**G** of the main text.

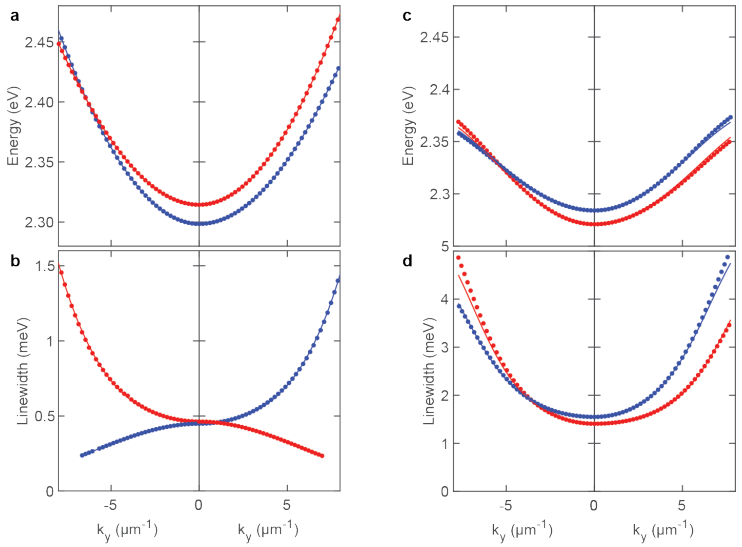

Figure S2: Extracted energies and linewidths from 4×4 transfer matrix simulations. a Extracted energies and **b** linewidths from the reflectance dips of the simulations with no exciton-photon coupling. Solid lines are fit to the complex dispersion using Eq. 2 of the main text. **c**, **d** Same as **a** and **b** but with strong exciton-photon coupling. Solid lines are fit to the complex dispersion using Eq. 1 of the main text using the cavity photon parameters extracted in **a**, **b**.

To confirm that the model, Eqs. (1,2) of the main text, describe the non-Hermitian dispersion of exciton polaritons, we fit the eigenvalues of Eq. (1,2) to the extracted complex dispersion. We used Eq. (2) of the main text to fit to the complex cavity photon dispersion, shown as solid lines in Fig. S2**a**, **b**, resulting in the following cavity photon parameters: $\tilde{E}_{c0}$ =(2.306-4.58×10^{-4}i) eV, $\tilde{\chi}_1$ =(2.3×10^{-3}-1.45×10^{-7}i) μm^{-2}.eV, $\tilde{\chi}_2$ =(8.76×10^{-7}-8.59×10^{-8}i) μm^{-4}.eV, $\tilde{\alpha}$ =(8×10^{-3} - 4.28×10^{-6}i) eV, $\tilde{\beta}_1$ =(1.76×10^{-4}-6.4×10^{-6}i) μm^{-2}.eV, $\tilde{\beta}_2$ =(5.01×10^{-7}-5.33×10^{-8}i) μm^{-4}.eV. The complex exciton energy is known a priori as an input to the simulation with a value of $\tilde{E}_x$ =(2.407-6.08×10^{-3}i) eV. We then use these parameters to fit to the eigenvalues of Eq. (1) to the complex lower exciton-polariton dispersion as shown in Fig. S2**b**, **c**, resulting in an exciton-photon coupling strength of V=61 meV. Note that the model starts to deviate from the exciton-polariton dispersion at higher momenta. This is due to the weak polarisation and momentum-dependent exciton-photon coupling strength, which is neglected in the model for simplicity.

For sufficiently large negative detuning of cavity photon with respect to the exciton energy, Eq. (2) of the main text can be used to describe the lower exciton-polariton branches. The 2×2 Hamiltonian

is easier to understand and can describe the energy crossings and topology of the exceptional points presented in this work. Moreover, it enables a simple theoretical model for the effective gauge field for exciton polaritons. The validity of the 2×2 approximation is demonstrated in Fig. S3, where the crossing and anti-crossing behaviour of the complex dispersion is qualitatively captured by the 2×2 Hamiltonian. The model greatly deviates from the simulations at higher momenta, such that the energy and linewidth crossings occur at different momenta compared to the simulations. Higher order terms can be added to the $\tilde{\chi}(k)$ and $\tilde{\beta}(k)$ terms to improve the model.

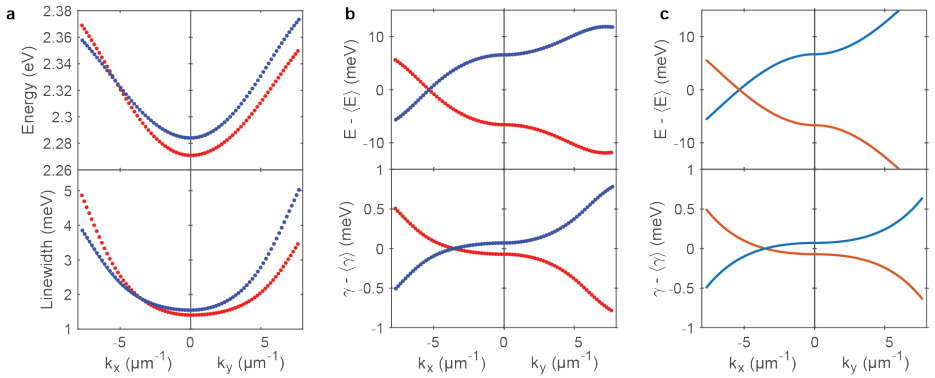

Figure S3: Simulated and theoretical exciton-polariton complex dispersion. (a) Energy and linewidth (FWHM) of the lower exciton-polariton modes (upper polariton not shown) extracted from the 4×4 transfer matrix simulation of an anisotropic microcavity with embedded excitons in the strong coupling regime. **(b)** Mean-subtracted energy and linewidth of the simulated data in **(a)**. **c,** Mean-subtracted energy and linewidth of the simple model (Eq. (1) of main text, after accounting for the losses), showing a similar behavior as that in **(b)**.

Supplementary experimental data

The transfer matrix calculations and the theoretical model also capture the linewidth behaviour of the experiment shown in Fig. S4. Regardless of the direction, the linewidth increases with k as the exciton fraction of polariton increases. However, the experimental linewidth increases more or less linearly with k (see Fig. S4), compared to the near parabolic behaviour of the numerical simulation. This can arise from the inhomogeneous broadening of the exciton resonance, which is not accounted 2 for in the simulations.

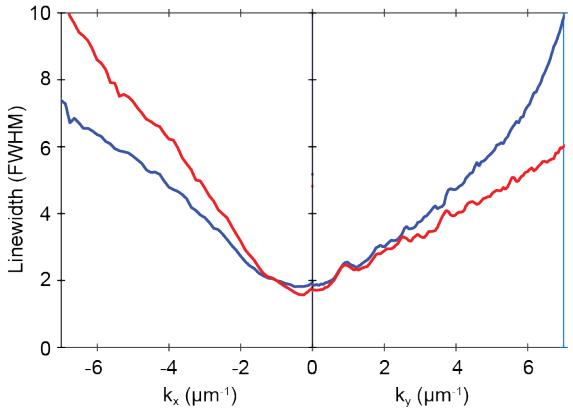

Figure S4: Experimentally measured linewidths. FWHM of the experimental data presented in Fig. 2**c** of the main text. The linewidths of both modes are split at $k = 0$ and increase with k as the excitonic fraction of the exciton-polariton increases.

The measured energies and linewidths near the paired EPs in momentum space are shown in Fig. S5. The complex energies are sorted following the same method in Fig. 3 of the main text to highlight the crossings in energy and linewidth.

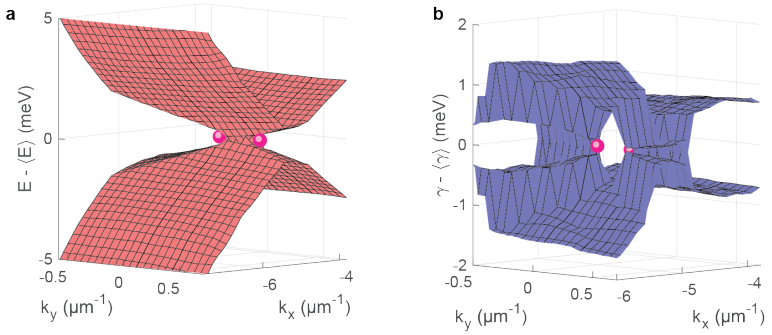

Figure S5: 2D complex spectra. Experimentally extracted **(a)** Energy and **(b)** linewidth surfaces in the vicinity of the paired exceptional points (pink dots).

The spin texture of the excitonic PL of $CsPbBr_3$ perovskite crystals in momentum space are shown in Fig. S6. This was measured directly in momentum space without spectral filtering. The same background spin texture is observed outside the paired EPs in Fig. 4**C** of the main text. Note that, as expected, this chirality does not depend on the orientation (by rotation) of the sample.

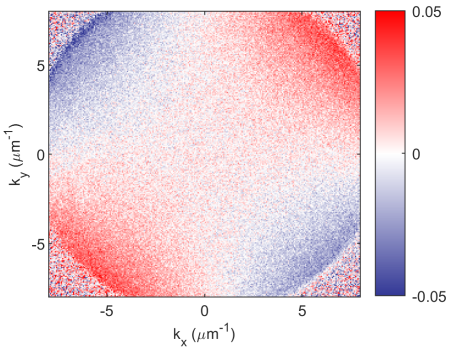

Figure S6: Weak inherent chirality of $CsPbBr_3$ perovskite crystals. S_3 texture in *k*-space of the energy-integrated photoluminescence of a bare perovskite crystal.

The extraction of the energy and linewidth is performed by fitting the spectrum at each point in momentum space. For regions away from the EPs, two peaks appear in the polarised spectrum, as shown in Fig. S7**a**, which can be fitted to a double Lorentzian function. Near the EPs, the two peaks overlap so only one peak appears in the measurements. These peaks can be distinguished using the pair of orthogonally linearly polarised measurements as shown in Fig. S7**b**, **c**. We then select the pair that produces the largest energy splitting.

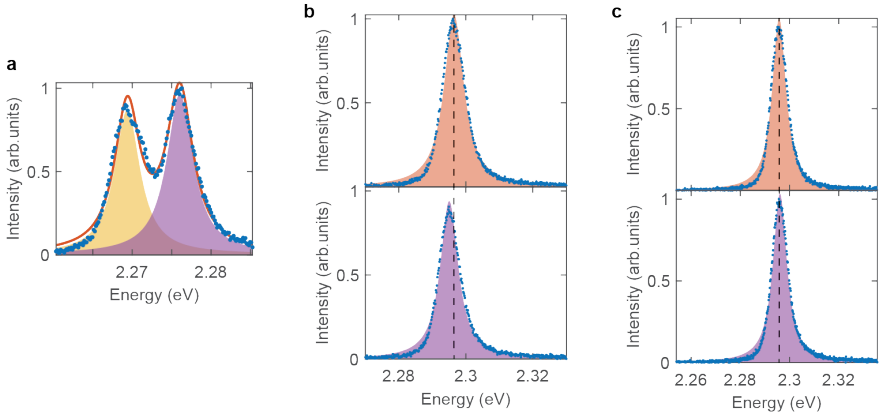

Figure S7: Fitting of spectral data. **(a)** Spectral profile (blue dots) at a *k* point away from energy crossings. The red line is the double Lorentzian function fit, and the shaded areas are the contributing Lorentzian functions. Crossed polarised spectral profiles at a *k* point **(b)** near and **(c)** very close to an exceptional point. A single Lorentzian function (shaded region) is used to fit the polarized data (blue dots). Dashed vertical lines correspond to the peak energy of the upper panel.

Topology of the eigenstates of the non-Hermitian model

For completeness, we show here the topology of the eigenstates corresponding to the discussions related to Fig. 1**H-L** of the main text. In Fig. S8, we show changes of the lower eigenstate with

increasing real-valued σ_z-term perturbation along with the topology of the eigenenergies, defined the spectral phase. Similar to Fig. 1**K**-**L** of the main text, the EPs in a pair each other (see Fig. S8**a**, **b**) and annihilate leading to a trivial non-Hermitian topology, i.e. zero spectral winding, as shown in Fig. S8**c**.

The in-plane pseudospin angle of the lower eigenstate (shown in Fig. S8**d**-**f**) is the opposite of that of the upper eigenstate (see Fig. 1**H**-**J**). Indeed, at some finite σ_z-term perturbation, the pseudospin singularity migrates to one of the eigenstates. The upper eigenstate (Fig. 1**I**) retains the negative (clockwise) winding while the lower eigenstate retains the positive winding. The singularity is accompanied by high circular polarisation degree, as shown by the spin textures (or S_3) in Fig. S8**g**-**l**. The sign of the circular polarisation follows the winding direction of the in-plane pseudospin angle. Note that since the pseudospin singularites do not follow the EP in momentum space for finite σ_z-term perturbation, the EP becomes elliptically polarised.

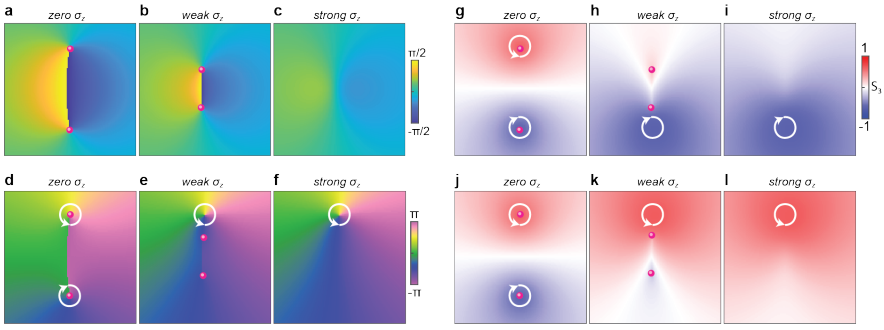

Figure S8: Topology in momentum space for increasing magnitude of gap-opening perturbation. **a-c** Spectral phase near a pair of EPs (pink dots) for different magnitudes of real-valued σ_z-term perturbation. Same data are presented in Fig. 1**k**, **l** of the main text. **d-f** In-plane pseudospin angle of the lower eigenstate corresponding to **a-c**, respectively. The plots for the upper eigenstate are presented in Fig. 1**h-j** of the main text; Pseudospin texture (or S_3) of the upper (**g-i**) and lower (**j-l**) eigenstates corresponding to **a-c**. White arrowed contours correspond to the winding direction around the pseudospin singularities.

The evolution of the windings of both eigenstates and eigenenergies as a function of a σ_z-perturbation are shown in Fig. S9a. For a vanishing σ_z-perturbation, both eigenstates share the same winding of π. However, for a nonzero σ_z-term, as soon as the EP moves away from the pseudospin singularity, the shared winding migrates to one of the eigenstates resulting in a winding of 2π for that eigenstate and zero for the other. The windings of 2π and 0 persist for any strength of σ_z-perturbation. The zero σ_z-term case is a transition point that demonstrates the instability of the π-winding of the eigenstates against σ_z-perturbation. This is reminiscent of the instability of Dirac points in the Hermitian case, where any σ_z-perturbation destroys the degeneracy and opens the gap. 8

In contrast, the π winding of the eigenenergies is more robust, requiring a finite σ_z-perturbation to change the winding number, as shown by the solid curve in Fig. S9a. The EPs meet and annihilate at this finite σ_z-perturbation, consequently destroying the bulk Fermi arc. This signifies the non-Hermitian topological transition and is accompanied by the sudden disappearance of the π jump of the spectral phase at the bulk Fermi arc, as shown in Fig. S9b. By contrast, the phase jump of the eigenstate at the bulk Fermi arc continuously decreases from π for any nonzero σ_z-perturbation, which demonstrate the stark difference between the topology of the eigenstates and eigenenergies.

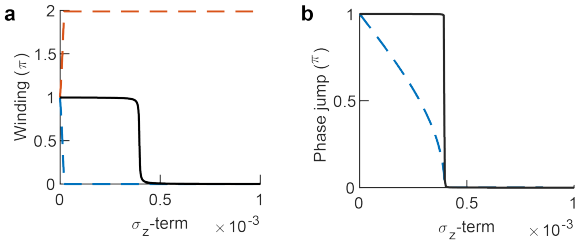

Figure S9: Evolution with σ_z-perturbation. **a** Numerically calculated winding of the eigenstates (dashed) and eigenenergies (solid) as a function of σ_z-perturbation. **b** Discontinuity jump of the in-plane pseudospin angle (dashed line) and spectral phase (solid) at the midpoint of the bulk Fermi arc as a function of σ_z-perturbation.

Magnitude of circular polarisation degree near the EPs

The order-of-magnitude reduction of the measured circular polarisation degree near the EPs can be explained by the close proximity of the exceptional points. The high circular polarisation near the EPs (due to the pseudospin singularities) has opposite handedness and finite extent in momentum space, as shown in the theoretical spin texture shown in Fig. 4**B** of the main text. Hence, the opposite spin textures due to the EPs tend to overlap and cancel each other. In the measurement, this will result in the reduction of the circular polarisation degree: the closer the pseudospin singularities in momentum space, the larger is the reduction in the measured circular polarisation.

We observe the same behaviour in the transfer matrix simulations, which simulates the experiment, as presented in Fig. S9. In the simulations, we varied the number of DBR pairs (from 4.5 to 6.5) and calculate the S_3 of reflectance at constant energy (near the EP energy). Increasing the number of DBR pairs decreases the linewidth and hence reducing the separation between the EPs. As clearly shown in Fig. S9, the maximum $|S_3|$ decreases with increasing number of DBR layers. This suggests that samples with very high Q-factor will bring the EPs very close to each other such that the EP pairs cannot be resolved in the experiment.

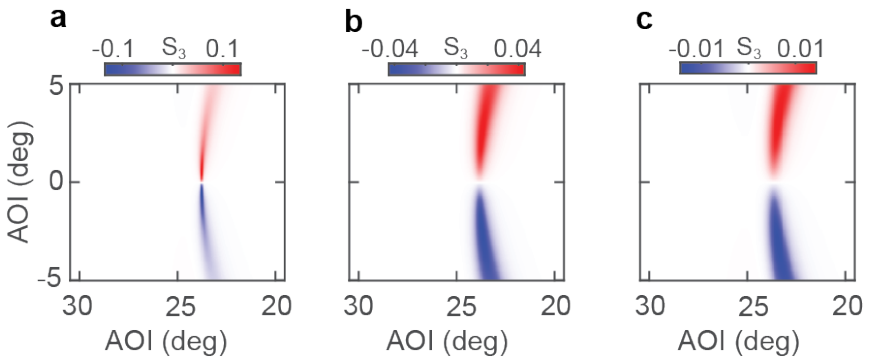

Figure S10: Simulated circular polarisation degree near the EPs. Simulated spin texture in momentum space at constant energy (near the EP energy) for an anisotropic microcavity with different number of DBR pairs: **a** 4.5 pairs, **b** 5.5 pairs, **c** 6.5 pairs.

Summary of the findings

In summary, the work presented in this Part focused on the non-Hermitian topological properties of a perovskite-based exciton-polariton system, governed by the polariton pseudospin, the optical (structural) anisotropy of an active material and the inherent system losses. It studied the optically-anisotropic lead-halide perovskite crystals, embedded in an optical microcavity, to demonstrate the emergence of non-Hermitian topology in an exciton-polariton system at room temperature. This work:

- served as the first direct measurement of a non-Hermitian topological invariant, called *spectral winding* (or *vorticity*). The invariant arose from the half-integer winding of the exciton-polariton complex eigenenergies around the exceptional points present in the system's gauge field. The invariant was extracted from the real and imaginary part of the eigenstates, which were measured directly in polarization-resolved experiments.

- directly showed a pseudospin texture of a complex artificial gauge field, governed by the TE-TM splitting and the anisotropy field, with a critical importance of the system's non-Hermiticity. It experimentally evidenced the existence of paired exceptional points in the momentum-resolved exciton-polariton spectrum, connected by the topologically protected bulk Fermi arcs. The findings suggested that the Fermi arcs form two loops in momentum space, a behavior similar to the one observed for the cavity photons in previous works, but solely in the weak coupling regime. This work has demonstrated for the first time that the exciton polaritons can inherit the exceptional points from birefringent cavity photons. Moreover, it showed how the non-Hermiticity results in the appearance of circular polarization in the effective field, maximized near the exceptional points, arising from the imaginary part of the artificial in-plane magnetic field acting on the exciton-polariton pseudospin.

- developed a non-Hermitian model to describe exciton-polariton dispersion and used it to extract the topological invariant from the experimental data. It also showed that the topologies of the system eigenstates (polarization winding) and eigenenergies (spectral winding) are not equivalent and are separable, meaning,

that the latter can persist when the former is absent. Hence, the inherent topology of these exceptional points is different from any previously observed points in the eigenstates of classical wave systems. The previously shown exceptional points in parameter space of exciton-polariton systems should not have a direct influence on the system's dynamics, in contrast to the ones in momentum space evidenced here.

- paves a way for future studies and can lead to the realization of non-Hermitian topological phases, nontrivial dynamics, non-Hermitian skin effect, etc., without the need for sophisticated sample microstructuring or strong external magnetic fields, as well as to explore robust topological phenomena that do not occur in Hermitian systems. Moreover this presentation in exciton-polariton system offers a new platform for investigating the interplay between the non-Hermitian topology and nonlinearity, with large importance of quantum many-body effects - an unexplored frontier in non-Hermitian physics so far.

Part IV

Optical properties and dynamics of direct and spatially and momentum indirect excitons in AlGaAs/AlAs quantum wells

Introduction

This work differs from other parts of this thesis, as it does not involve strong coupling between excitons and photons. However, it has been done as a key characterization of the active material of the full microcavity, later described in Part V. In Part V an initially unexpected effect has been observed in an AlGaAs/AlAs polariton microcavity designed for room temperature strong coupling and lasing [70]. To explore and understand the nature of the effect, the QW active medium had to be understood fully, prior to the coupling with the photonic modes. In order to do that, the top Bragg reflector of the full cavity has been etched, and the QW system on top of the bottom DBR has been investigated. It was assured that no measurable signatures of remaining photonic modes in the spectral vicinity of the QWs were observed and a purely QW system could be considered. This investigation proved to be vitally important in the result described in Part V.

The system in question consists of $Al_{0.20}Ga_{0.80}As$ QWs, separated by AlAs barriers. This material system has been purposefully used to take advantage of a so-called $\Gamma - X$ coupling in order to increase the exciton binding energy and allow for the existence of exciton polaritons at room temperature, even in a GaAs-based system. As described in detail in section 1.3, III-V semiconductors are highly advantageous in exciton-polariton research, as they offer the highest quality, scalability and reproducibility of all the semiconductor platforms. High quality of the epitaxial growth, precise control over the structure parameters, and small lattice mismatches necessary to achieve high quality factors of optical microcavities make them the best candidates for a wide range of applications [13, 51]. However, one important drawback of these systems is a relatively low exciton binding energy, on the order of a few milielectronovolts, preventing the polariton observation (hence also condensation) at room temperature [13, 52]. The binding energy is not sufficient to overcome the thermal energy at increased temperatures, leading to a dissociation of excitons. Most of the GaAs polariton studies require cryogenic temperatures, what hinders also the application potential. That is one of the reasons why other platforms, such as wider gap semicoductors (e.g. GaN) or transition metal dichalcogenide systems gained interest in the exciton-polariton context in recent years (see section 1.3). However, they still lack the superb qualities of the aforementioned AlGaAs compounds. There are several approaches to overcome the issue of the small binding energy in III-V systems, such as achieving a very strong coupling regime [69]. Another solution is the employment of the $\Gamma - X$ mixing [70, 225–227].

As GaAs is a direct bandgap semiconductor at the Γ point, while AlAs is characterised by an indirect bandgap with the global minimum of the conduction band in the X point of the Brillouin zone [228], the $Al_xGa_{1-x}As$ alloy is characterized by a direct-to-indirect bandgap transition at a specific proportion of the two binary semiconductors of around $x = 0.24$ [229,230]. Near the $\Gamma - X$ crossover, the quantum mechanical mixing of the Γ- and the X-valley electrons was reported to manifest in a large enhancement of the donor activation energies and the exciton binding energies [231]. Mixing of the Γ-valley electrons with the X- and L-valley leads to an increase of the electron effective mass which, in turn, should lead to an increase of the exciton binding energy, proportional to its effective mass (see section 1.1.1). The increased exciton binding energy allows for the exciton-photon coupling at significantly increased temperatures. Polariton lasing has been reported at 155 K in an $Al_{0.31}Ga_{0.69}As/Al_{0.4}1Ga_{0.59}As$ QW sample [232] and in 170 K in GaAs QWs placed in a $Al_{0.3}Ga_{0.7}As$ cavity with $AlAs/Al_{0.15}Ga_{0.85}As$ DBRs [233], yet the strong coupling in this system has been observed up to the room temperature [70].

At the same time, the nearly resonant, spatially separated levels, open a possibility for indirect excitons to emerge. In AlGaAs/AlAs QWs near the $\Gamma - X$ crossover the conduction band edge in the Γ valley creates a confinement potential for electrons in the QW material, but the confinement for the X-valley electrons is created in the AlAs barrier (as the material is indirect, with minimum in the X valley) [234–236]. Holes are confined within the Γ-valley in the QW material [234]. This leads to the existence of confined Γ-electron levels in the QW layer and the X-electron states in the barrier layer, provided appropriate layer widths and material composition are used. The near-resonant levels of Γ QW electrons and X AlGaAs states were studied in single and multi-QW structures [237–239], as well as in superlattices [225, 226, 240–244], showing the possibility of tunnelling [238] and interactions [226] between the confined electron states.

Electrons from both levels, designed to be close to resonance near the $\Gamma - X$ crossover, can interact with holes confined in the QW layer. This creates "standard", direct, Γ-valley excitons confined in QWs, but also the spatially and momentum indirect excitons, consisting of the X-valley electron in the barrier and the Γ hole in the QW. Because of the X valley anisotropy (in contrast to the isotropic Γ band) [225, 245, 246], X electrons with different effective masses can be confined in the barrier layer. This comes from the fact, that creation of the QW structure breaks the spatial symmetry and selects a direction in space. Hence, a crossection of the anisotropic effective mass paraboloid of the X AlAs electrons needs to be considered in two directions: the quantization direction and the direction perpendicular to it [225,236,247]. This anisotropy has been broadly studied in ref. [225] and the effective masses are summarized in Table 4.1, following this reference.

An important conclusion from this fact is that in AlGaAs/AlAs QWs (or superlattices) two different confined indirect excitons can be formed: one coming from the coupling between the QW holes and the $X_{X,Y}$ confined levels in AlAs (characterized by the (lighter) transverse mass m_t) and a second one, with the same holes coupled to the X_Z confined states (with (heavier) longitudinal mass m_l). Typically, only the

	[100] **mass (dispersion mass)**	[001] **mass (quantization mass)**
X_X (100)	m_l	m_t
X_Y (010)	m_t	m_t
X_Z (001)	m_t	m_l
Γ (000)	m_Γ	m_Γ

Table 4.1. Effective masses of the Γ and X valleys, re-written from ref. [225]. The mass along [001] is a quantization mass in the typical (001) superlattices or QWs. The [100] mass accounts for the dispersion along [100] direction.

heavy holes are taken into consideration, as their mass is higher and they form a ground state in the valence band of such a system [1, 228].

Regardless of the AlGaAs context, the spatially indirect excitons, with Coulomb-bound electrons and holes characterized by spatially separated wavefunctions, found an increased interest in recent years. They have been most often considered in a context of TMDC layers [248–251]. A strong dipolar nature of such excitations allows for the observation of new exciting phenomena, including a dipolar excitonic insulator [252], high-temperature superfluidity [253], and high-temperature Bose-Einstein condensation [254–256], among others. They are characterized by a high dipole moment, prolonged lifetime, high diffusion length and are bosonic in nature, as well as they provide good control of the exciton properties due to their sensitivity to an electric field and dielectric environment [251, 255, 257, 258]. All these characteristics lead to a big potential of indirect excitons in novel electronic and photonic devices [259,260]. In the particular context of this thesis, their existance in the AlGaAs/AlAs polariton microcavity allowed for a unique observation described in Part V.

Contributions

This research has been a collaborative work. D. Biegańska (the author of this thesis) was the main contributor in building the experimental setup and she performed all the spectroscopic experiments, with support from the coauthors. She analysed all the experimental data. She took part in all discussions of the the results, wrote the first version of the manuscript and prepared all figures. All authors reviewed the manuscript to its final form.

Results

Optical properties and dynamics of direct and spatially and momentum indirect excitons in AlGaAs/AlAs quantum wells

Dabrówka Biegańska[1,*], Maciej Pieczarka[1], Krzysztof Ryczko[1], Maciej Kubisa[1], Sebastian Klembt[2], Sven Höfling[2], Christian Schneider[3], and Marcin Syperek[1,+]

[1]Department of Experimental Physics, Faculty of Fundamental Problems of Technology, Wrocław University of Science and Technology, Wybrzeże Wyspiańskiego 27, 50-370 Wrocław, Poland
[2]Julius-Maximilians-Universität Würzburg, Physikalisches Institut and Würzburg-Dresden Cluster of Excellence ct.qmat, Lehrstuhl für Technische Physik, Am Hubland, 97074 Würzburg, Germany
[3]Institute of Physics, University of Oldenburg, D-26129 Oldenburg, Germany
[*]dabrowka.bieganska@pwr.edu.pl
[+]marcin.syperek@pwr.edu.pl

ABSTRACT

We present an experimental study on optical properties and dynamics of direct and spatially and momentum indirect excitons in AlGaAs/AlAs quantum wells near the crossover between $\Gamma-$ and X-valley confined electron states. The time-integrated photoluminescence experiment at $T = 4.8$ K revealed three simultaneously observed optical transitions resulting from (a) a direct exciton recombination, involving an electron and a hole states both located in the Γ-valley in the quantum well layer, and (b) two spatially and momentum indirect excitons, comprising of the confined electron states in the X-valley in the AlAs barrier with different effective masses and quantum well holes in the Γ-valley. This interpretation has been based on the optical pumping density-dependent, temperature-dependent and spatially-resolved photoluminescence measurements, which provided the characterization of the structure, crucial in potential system's applications. Additionally, the time-resolved photoluminescence experiments unveiled complex carrier relaxation dynamics in the investigated quantum well system, which is strongly governed by a non-radiative carrier recombination - the characteristics further critical in potential system's use. This solid state platform hosting both direct and indirect excitons in a highly tunable monolithic system can benefit and underline the operation principles of novel electronic and photonic devices.

Introduction

A discovery and recent interest in two-dimensional (2D) materials spark remarkable progress in research on excitons and the use of excitonic properties in optoelectronic devices. Particular attention has been paid to spatially indirect excitons with Coulomb-bound electrons and holes characterized by spatially separated wavefunctions. The strong dipolar nature of such excitations allows for the observation of new exciting phenomena, including a dipolar excitonic insulator[1], high-temperature superfluidity[2], and high-temperature Bose-Einstein condensation[3–5], among others. Moreover, due to their high dipole moment, prolonged lifetime, high diffusion length and bosonic nature, as well as good control of the exciton properties due to their sensitivity to an electric field and dielectric environment, indirect excitons can benefit and underline the operation principles of novel electronic and photonic devices[6,7]. In this new wave of exciting discoveries, the attention can be brought back to the relatively mature AlGaAs/AlAs quantum well (QW) system in which similar indirect excitons can be generated in a highly controllable environment. Surprisingly, the knowledge on the isolated AlGaAs/AlAs QW system and its excitonic properties is limited in the literature[8–12], with research focused mainly on superlattice systems, not on isolated QWs.

What is important is that this system offers fabrication capabilities that are still unreachable in 2D layered semiconductors. The use of III-V semiconductors, in particular with AlGaAs alloy materials in monolithically integrated structures is highly beneficial due to the high quality of epitaxial growth, precise control over the structure parameters, and small lattice mismatches necessary to achieve high quality factors of optical microcavities. They can be easily integrated into multilayer monolithic structures and are suitable for a wide range of well-developed microelectronic processing techniques. On the other hand, the important drawback in developing useful systems and studying new excitonic-based physical phenomena in these materials is a low exciton binding energy, particularly when compared with 2D materials such as transition-metal dichalcogenides or 2D perovskites. The typical energies on the order of a few millielectronvolt are too small compared to the thermal energy at increased temperatures, which results in the exciton's effective dissociation, preventing an elevated-temperature device

operation.

Nevertheless, several attempts have been made to overcome this issue. One of the approaches employs the $\Gamma - X$ band mixing[9,13,14]. As GaAs is a direct bandgap semiconductor at the Γ point, while AlAs is characterised by an indirect bandgap with the global minimum of the conduction band in the X point of the Brillouin zone, the $Al_xGa_{1-x}As$ alloy is characterized by a direct-to-indirect bandgap transition at a specific proportion of the two binary semiconductors of around $x = 0.24$[15,16]. Near the $\Gamma - X$ crossover, the quantum mechanical mixing of the $\Gamma-$ and the $X-$valley electrons was reported to manifest in large enhancement of the donor activation energies and the exciton binding energies[17]. At the same time, the nearly resonant spatially separated levels open a possibility for indirect excitons to emerge.

Near-resonant levels of Γ QW electrons and X AlGaAs states were studied in single and multi-QW structures[18–20], as well as in superlattices[13,14,21–25], showing the possibility of tunnelling[19] and interactions[14] between the confined electron states. Such interacting states have yet to be studied in more complex structures, such as enclosed microcavities, where complex dynamics seems crucial in the structure design and band structure engineering.

In this report, we bring the III-V-based system back to the spotlight, uncovering the properties that can underline the operation of exciton-based photonic devices. We studied the optical properties of AlGaAs/AlAs QWs, operating close to the $\Gamma - X$ coupling regime. Using photoluminescence experiments supported by theoretical calculations within the effective-mass framework, we unravel the nature of multiple resonances present in the structure spectra and interpret two of the lowest energy states as spatially- and momentum-indirect X-excitons. We characterize the density and temperature evolution of all the energy states, as well as their temporal decay and spatial diffusion. Our work points to the complex exciton and carrier dynamics in this system, hindered by nonradiative processes and further affected by localization effects. Such detailed investigation on the interplay between the energy states is important to understand the resulting complex dynamics in the full structure such as microcavity, under the additional interaction with photonic modes, particularly of the dipolar excitons. Investigating the system in a wide range of temperatures is necessary to carefully design and understand future high-temperature devices.

Results

Steady-state photoluminescence spectroscopy

The structure under study is schematically depicted in Fig. 1a). It consists of twelve 9 nm-wide $Al_{0.20}Ga_{0.80}As$ QWs, separated by 4 nm AlAs barriers, distributed in three stacks of four, comprising the active part of the structure. Good isolation of each QW, provided by the barriers, ensures negligible coupling of confined states between neighbouring QWs. The active part was monolithically integrated on a distributed Bragg reflector (DBR), enhancing emission involving confined QW states. More details on the sample can be found in the **Methods** section.

To probe the fundamental excitations in this QW system, we employ the steady-state photoluminescence (PL) experiment (see **Methods**). Figure 1b) displays the measured low-temperature ($T = 4.8$ K) PL spectrum of the AlGaAs/AlAs QW, registered under a quasi-resonant energy excitation at $E_{exc} = 2.00$ eV and an excitation power of $P_{exc} = 10\,\mu$W. The PL spectrum consists of three well-resolved features, with enhanced visibility due to the DBR. The features originate from the carrier recombination between QW-confined states. The highest-energy and highest-intensity PL band located at 1.8472 eV corresponds well to the Coulomb-correlated electron-hole (exciton) recombination in the vicinity of the Γ valley in the Brillouin zone. The transition involves the lowest-lying Γ-electron state and the topmost Γ-hole state confined in the AlGaAs QW. The assignment has been suggested by the energy match with the calculations performed during the initial design of the sample[26], as well as the PL band intensity dominating the spectrum. Therefore, it should reflect the recombination of momentum- and spatially direct Γ-exciton (annotated simply as Γ), having a high optical transition probability.

The presence of two PL bands located energetically below the Γ exciton is initially surprising. They are centred at energies of 1.8007 eV and 1.7843 eV respectively, redshifted by nearly 47 meV and 63 meV from the direct Γ exciton transition. Large energy separation with respect to Γ excludes their identification as charged-excitons or multi-exciton recombination since these are typically characterized by sub-10 meV binding energies[27,28]. The defect-assisted recombination would likely appear in a spectrum as a single broad transition instead of two clearly resolved bands, resembling the excitonic transitions in the AlGaAs/AlAs QW[29]. Therefore, we attribute the observed spectral features to the recombination of excitons involving the X-valley electrons and Γ-valley holes, observed previously in other AlGaAs nanostructures[10,11,20]. We further investigate the nature of these transitions in the following sections.

Calculations

To elucidate the nature of the two optical transitions energetically below the Γ exciton and to provide arguments for their identification, the QW band structure has been calculated within the effective mass approximation. Fig. 1c) shows the band alignment for $Al_{0.20}Ga_{0.80}As$ QW material and the AlAs barriers in the conduction (CB) and valence (VB) bands, including the electrons from both the Γ and X valleys of the Brillouin zone. It is important to note that while in the Γ valley the CB profile (Fig. 1c), solid grey line) creates a confinement potential for electrons in the QW material, the confinement for X-valley

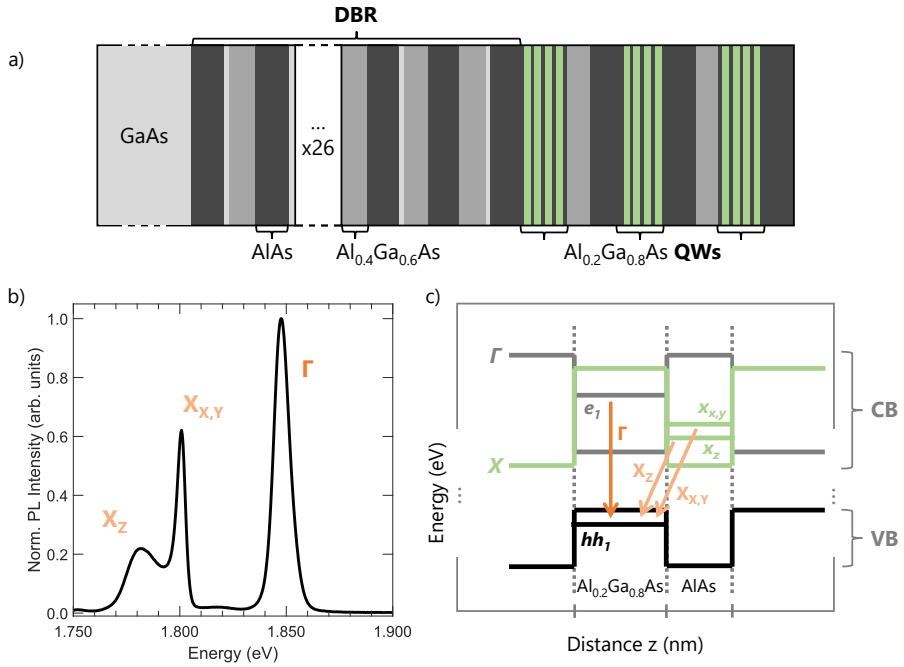

Figure 1

a) Schematic illustration of the investigated quantum well (QW) structure. b) Low temperature ($T = 4.8\ K$) photoluminescence (PL) spectra of the $Al_{0.20}Ga_{0.80}As$ /AlAs QWs registered at quasi-resonant excitation, $E_{exc} = 2.00\,eV$, and low excitation power $P_{exc} \approx 10\,\mu W$. c) Scheme of the band structure of one period of the structure with the single-particle levels marked with dashed lines the and optical transitions indicated with arrows. The solid black line represents the edge of the valence band (VB), while solid grey and green lines show the edges of the conduction band (CB) in the Γ and X valley, respectively.

electrons (Fig. 1c), solid green line) is created in the AlAs barrier[11,30,31]. Holes can be confined only within the Γ-valley in the QW material[11]. For clarity, only the topmost heavy hole (hh) band is presented, and unstrained materials are considered, in good agreement with the experimental implementation.

The band alignment is the basis for calculations of the single-particle confined states for Γ electrons (e_1) and holes (hh_1), and X electrons ($x_{x,y}$, x_z), as schematically depicted in Fig. 1c). The presence of two X-electron confined states results from the X-electron effective mass anisotropy, well known for the AlAs material[13,32,33]. As the quantization occurs in the growth direction perpendicular to the QW plane (the z-direction, [001] in the crystal structure), two X-electron masses need to be taken into account in calculations, in contrast to the isotropic Γ conduction band[13,31]. This results in a doublet of states for transverse, $x_{x,y}$, and longitudinal, x_z, electrons in the X valley. Their masses differ by a factor of 0.2268 in the AlAs layer (with a higher value of the longitudinal mass)[34], yielding the energy separation of approximately 28 meV between the calculated energy levels in the doublet. Our calculations do not include strain effects that can lead to further state separation[35].

Γ and X electrons in confined states can interact with Γ holes confined in the QW layer via Coulomb interactions, forming spatially and momentum direct and indirect excitons. In our calculations, we estimated the Coulomb corrections to single-particle energies using the Rydberg formula (see **Methods**). This simplified approach is likely to be an overestimation of the actual electron-hole Coulomb coupling for the indirect excitons due to the spatial separation between carriers[34,36]. On the contrary, the binding energy of the Γ exciton is underestimated due to the two-dimensional nature of the QW states[31]. Additionally, the $\Gamma - X$ coupling (neglected in our calculations) may affect the exciton energies[17]. More accurate evaluations of the exciton energies require complex self-consistent calculations, which are beyond the scope of this work[36–38]. Nevertheless, our simplified approach results in good agreement with experimental observations, as discussed below.

The calculated band structure and the energies of the optical transitions are confronted with the results of the PL measurement

in Table 1. The data shows that the Coulomb-corrected energy difference between the e_1 and the hh_1 states in the Γ-band corresponds very well to the spectral position of the most intensive PL band identified as Γ. As expected, the type-I confinement and the direct nature of the transition in the real and in the momentum space are linked to its high optical intensity. More importantly, the calculated energies of transitions involving the $x_{x,y}$ and x_z states in the X-valley and the Γ-valley heavy hole state (marked as $X_{X,Y}$, and X_Z in Fig. 1c)) are in good agreement with the PL band energies observed below the Γ. Both $X_{X,Y}$, and X_Z transitions are nominally indirect in the real and momentum space, which should lead to a low transition probability. However, several effects can increase this value. It is important to note that as the translational symmetry is broken in the growth direction (z), the X_Z recombination is allowed without phonon assistance, regardless of its indirect character in the momentum space, due to the weakening of the momentum selection rules[25,31,35,39]. Translational invariance of the Hamiltonian (hence the momentum selection rules) should not be broken in the plane of the structure, resulting in the need for phonon presence for the $X_{X,Y}$ transition to occur[25,31,35,39]. The excitonic states can therefore be described as pseudo-direct in the case of X_Z and indirect in the case of $X_{X,Y}$. Notably, both remain indirect in the real space.

Additionally, it is known that in the energetic vicinity of the electron states of the Γ and X valleys in the Al-rich AlGaAs semiconductor compounds, the $x_{x,y}$ and x_z states can have an admixture of the e_1 states, which increases the transition probability (this effect is not included in our calculations)[9,30,31,37]. What is more, the X-valley electrons can be shifted towards the AlGaAs/AlAs heterointerface due to the Coulomb interaction with holes confined in the QW layer, the localization at interface inhomogeneities (caused by chemical content fluctuations), and local electric field or strain fluctuations, which increases the overlap integral with the Γ valley hole states[9,19,39]. Interface inhomogeneities are expected to have the strongest influence on the x_z electron states, as their effective mass is the largest[13] (effect visualized in our spatial diffusion measurements, described in the next section).

Exciton	**PL peak energy** ($4.8\ K$)	**Calculated single-level transition energy** E	**Calculated exciton binding energy** E_{Ry}	**Calculated exciton recombination energy** $E - E_{Ry}$
$\Gamma(e_1 - hh_1)$	1.8472 eV	1.8521 eV	4.8 meV	1.8474 eV
$X_{X,Y}(x_{x,y} - hh_1)$	1.8007 eV	1.8130 eV	9.5 meV	1.8062 eV
$X_Z(x_z - hh_1)$	1.7843 eV	1.7847 eV	6.8 meV	1.7752 eV

Table 1. Measured and calculated energies of the three investigated optical transitions, including the energies calculated from single-particle states (E), calculated excitonic correctons (E_{Ry}) and the transition energies at $T = 4.8\,\mathrm{K}$.

Excitation power-dependent photoluminescence

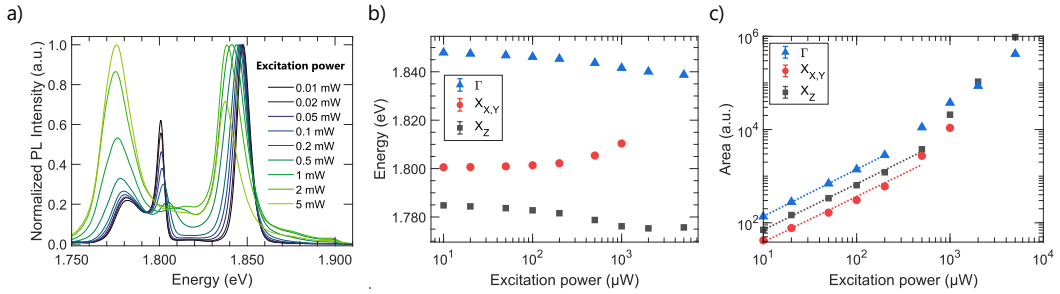

Figure 2. a) Excitation power-dependent photoluminescence (PL) spectra at $E_{exc} = 2.00\,\mathrm{eV}$ and $T = 4.8\,\mathrm{K}$. b) Change of the PL peak position with excitation power. c) Evolution of the PL intensity (represented as fitted peak area) of three respective bands as a function of P_{exc}. Dashed lines show the power-law fits to the experimental points at low excitation powers (in the linear growth regime), with slopes of $\gamma = 1.009(5)$, $0.997(5)$ and $0.99(1)$ for Γ, $X_{X,Y}$ and X_Z respectively.

The PL emission bands are examined as a function of the excitation power, P_{exc}, providing additional information on the nature of observed emission and the underlying optical transitions. Figure 2a) presents the spectra evolution with increasing P_{exc}. Three PL maxima, corresponding to the Γ, $X_{X,Y}$, and X_Z excitons, were fitted with Gaussian profiles and the extracted

energies are shown in Fig. 2b). One can observe that the middle-energy peak (corresponding to the $X_{X,Y}$ exciton) becomes unresolvable from the spectra under the strongest pumping. In contrast to the other two states, its energy blueshifts as a function of excitation power, what can be attributed to its dipolar nature and the repulsive interactions between quasiparticles, as was observed before for spatially indirect excitons[11,40,41]. Contrarily, both Γ and X_Z exciton energies present a small redshift with increasing excitation power, a behaviour not expected for indirect states. It is important to note that in the case of the X_Z excitons, their ground state nature makes them more prone to inhomogeneities, which affect their lifetime and transport properties. Higher probability of the transition due to the weakened momentum selection rules, shorter decay and higher localization can hinder their build-up, necessary for the repulsive interactions to be observed. Small redshift of the Γ and the X_Z PL bands at high excitation powers indicate the local sample heating under the elevated pumping.

Figure 2c) shows the spectrally integrated emission intensity of the three investigated bands as a function of P_{exc}, plotted in the log-log scale. Experimental points within the low excitation power range were fitted with the power law function $I \propto P_{exc}^{\gamma}$, where the γ value depends on the recombination mechanism[42,43]. For the defect-assisted mono-molecular recombination of photo-injected electrons or holes the coefficient is expected to be lower than 1. However, when the recombination is governed by the mixture of free and bound exciton annihilation, $1 < \gamma < 2$. Our fitting procedure yielded almost the same γ parameter for all three PL bands. Extracted values $\gamma = 1.009(5)$, $0.997(5)$ and $0.99(1)$ for Γ, $X_{X,Y}$ and X_Z respectively, clearly suggest that all the observed optical transitions have excitonic character in the considered low excitation power range.

The superlinear growth at increased P_{exc} (see Fig. 2c)) is quite surprising. It begins at an excitation power of approximately $\sim 3 \times 10^2\,\mu$W. At this power level, the calculated electron-hole pair density is estimated as $\sim 3.9 \times 10^{18}\,\mathrm{cm}^{-3}$ (see **Methods**), what approaches the Auger threshold limit for the QW system, estimated to be on the order of $\sim 10^{19}\,\mathrm{cm}^{-3}$[44,45]. Further increase of the excitation power, up to $P_{exc} = 10^3\,\mu$W, is expected to hypothetically reach this density limit and lead to a non-radiative recombination taking over the radiative processes, causing a sublinear increase in the PL intensity[45–47]. However, the observed superlinear increase contradicts these expectations, suggesting that the number of the photogenerated electron-hole pairs in the QW stack is significantly lower than the estimated value. It could result from the fast, non-radiative carrier relaxation following the pulse photoexcitation, which could efficiently lower the carrier population in the QW. According to this interpretation, a non-radiative state saturation may occur at an excitation density of $\sim 3 \times 10^2\,\mu$W, potentially leading to the increased PL intensity form the QW confined states with a further increase of the pumping power. These effects can be confirmed by studying the PL temporal decay, as described in section **Time-resolved photoluminescence**.

Temperature-dependent photoluminescence

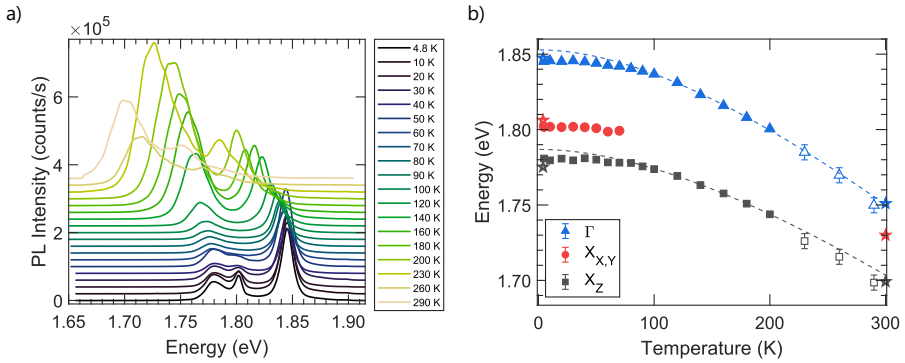

Figure 3. a) Temperature-dependent photoluminescence (PL) spectra at $E_{exc} = 2.00\,$eV and $P_{exc} = 150\,\mu$W. b) Temperature-induced energy shift of the PL bands. Points show the band energies extracted from fitting the spectra in a) with Gaussian profiles, open points mark the energies extracted from the spectra maximal intensity values and stars indicate the excitonic transitions calculated within the effective mass approximation. Dashed curves are the Varshni fits to the temperature dependences above 100 K.

To further characterize the studied system's excitonic features, we look at the temperature evolution of the PL spectra in the wide temperature range, with results presented in Fig. 3. As the temperature T increases, the energy of all resonances redshifts, as seen in Figs. 3a)-3b). At $T \approx 80\,$K, the $X_{X,Y}$ transition becomes unresolvable, while the neighbouring X_Z starts to dominate the spectrum. We highlight the fact that spectra presented in Fig. 3a) are not normalized, and the intensity of X_Z emission strongly increases at $T > 100\,$K reaching the maximum at $\sim 200\,$K. We hypothesize that the intensity increase originates from

the rising phonon density, making both the radiative transition from the X_Z exciton and the nonradiative transitions between e_1, $x_{x,y}$, and x_z electron levels more probable. Relaxation of electrons to the x_z state can be additionally increased by the decrease in energy separation between the Γ and X states with temperature (due to the different temperature variation of the Γ and X energy gaps in AlGaAs and AlAs layers respectively[25,48]), as well as by the quench of the $X_{X,Y}$ emission, making the inter-level transfer more effective. Additionally, these may be contributed to by an increased carrier density in the QW, owing to the temperature-driven release of carriers from nonradiative charge traps. The results of the excitation power-dependent and temperature-dependent time-resolved PL measurements suggest the existence of these traps (see sections **Excitation power-dependent photoluminescence** and **Time-resolved photoluminescence**). However, we also note, that absorption and effectiveness of the excitation strongly differ with temperature as the energy gaps shift, with E_{exc} crossing the band gap energy of the $Al_{0.40}Ga_{0.60}As$ spacer in the structure at $T \approx 220\,\mathrm{K}$, while the pumping energy in our experiment was set constant ($E_{exc} = 2.00\,\mathrm{eV}$). Hence, no definite conclusions based on the intensity evolution can be made. We note that the efficient high-temperature PL highlights the potential use of the structure in photonic devices at elevated temperatures, possibly up to room temperature.

Additionally, temperature dependences of the transition energies were fitted using the Varshni formula:[49] $E_t(T) = E_t(0) - \alpha T^2/(T+\beta)$ where E_t is the transition energy, and α and β are fitting constants related to the used semiconductor materials. The fitting results are presented in Fig. 3b) with dashed lines. Extracted α and β constants ($\alpha = 7.97 \times 10^{-4}\,\mathrm{eV\,K^{-2}}$ and $\beta = 399\,\mathrm{K}$ for the Γ state, and the $\alpha = 6.71 \times 10^{-4}\,\mathrm{eV\,K^{-2}}$ and $\beta = 425\,\mathrm{K}$ for the X_Z state) match well the reported material parameters of GaAs and AlAs[48,50]. Curves were fitted to the experimental points above 100 K, as at low temperatures the dependences deviate from the Varshni model. Transition energies lower than the theoretical values point to the likely additional localization effect and Coulomb correlations. At low temperatures, both Γ and X_Z excitons can be trapped, e.g. by spatial inhomogeneities of the QW interfaces or the chemical composition fluctuations, acting as localization centres, when the thermal energy is insufficient to overcome the energy potential minima[20,51]. Localisation effect is also affecting the diffusion of the excitonic complexes, showing the limited spatial extent of the low-temperature PL emission of both Γ and X_Z states, contrasted with the increase of the X_Z's diffusion at elevated temperatures, as presented and described in section **Exciton diffusion**, below. Localization energies suggested by the difference between the Varshni curves and the measured exciton emission at low temperatures are around 6 meV to 8 meV.

Finally, we estimate the expected exciton recombination energies at room temperature, using the same methods as described in the **Calculations** section. In contrast to previous estimations[26], we verify the system to be indirect (with the type-II transition from the quantized X-valley state in the barrier to the first heavy hole QW energy state as the lowest energy transition) in the whole studied temperature range up to the room temperature. At 300 K, the exciton energies estimated from our calculations are 1.751 eV, 1.730 eV and 1.6992 eV for the Γ, $X_{X,Y}$ and X_Z transitions respectively, matching nearly perfectly the PL resonances observed in the experiment (see Fig. 3b), open stars).

Exciton diffusion

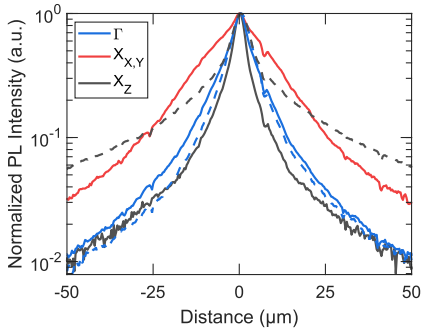

Figure 4. Spatial extent of the photoluminescence intensity, showing diffusion profiles of the three studied excitons, measured at low excitation power ($P_{exc} = 10\,\mu\mathrm{W}$) and the temperature of $T = 4.8\,\mathrm{K}$ (solid lines) and $T = 140\,\mathrm{K}$ (dashed lines). The $X_{X,Y}$ exciton is not visible at elevated temperatures.

The assignment of the observed QW transitions is further supported by the measured spatial profiles of the time-integrated PL emission at low temperatures and low excitation power density. The spatial extent of the PL signal of the three observed transitions at $T = 4.8\,\mathrm{K}$ is displayed in Fig. 4 (solid lines). One can see a clear difference between the emission profiles of the

studied states. The $X_{X,Y}$ excitons (the middle-energy-peak in Fig. 1b)) travel further away from the excitation spot than the Γ excitons before recombining, with their emission profile extending for more than 100 µm. The X_Z excitons are characterized by the smallest in-plane diffusion profile at low temperatures, even slightly smaller than that of the Γ excitons. Extended diffusion profiles are commonly observed for indirect excitons, having high momentum, and often being characterized by long radiative lifetimes, thus propagating macroscopic distances before recombination[4,52,53]. Several factors can influence the diffusion, including the in-plane effective mass, phonon density, exciton-phonon interaction and spatial localization of the states, as well as the efficiency of a non-radiative recombination[52,54,55]. The need for the phonon assistance in the $X_{X,Y}$ transition affects its recombination probability, hence the diffusion length, explaining its stark distinction from the other two profiles. In the case of the X_Z excitons, the aforementioned breaking of the momentum-selection rules makes them more similar to the Γ excitons, what is visualized in the narrower diffusion profile. Moreover, having the largest effective mass in the z-direction, their transport properties might be influenced by the spatial inhomogeneities of the QW interfaces, which act as localization centres[4,56], further affecting the diffusion.

The localization effect is clearly visualized by studying the diffusion profiles at elevated temperatures (experimental curves measured at $T = 140$ K shown in Fig. 4 with dashed lines). The diffusion of the X_Z state largely increases at elevated temperature and becomes significantly broader spatially than that of the Γ state, which remains narrow. The observation can be linked to the nature of an indirect state and the localization. Once the thermal activation overcomes the localization energy from local potential minima, the diffusion range of the X_Z exciton is expected to be longer than that of the direct excitons. On the other hand, it remains narrower than the $X_{X,Y}$ transition at low temperatures due to the difference in selection rules and in the effective mass. Full characterization of the temperature dependence is discussed in the previous section, where more localization effects become apparent. Overall, observed differences in the diffusion profiles support our interpretation of the nature of the direct and indirect excitons, as similar behaviour has been observed before in this material system[35].

Time-resolved photoluminescence

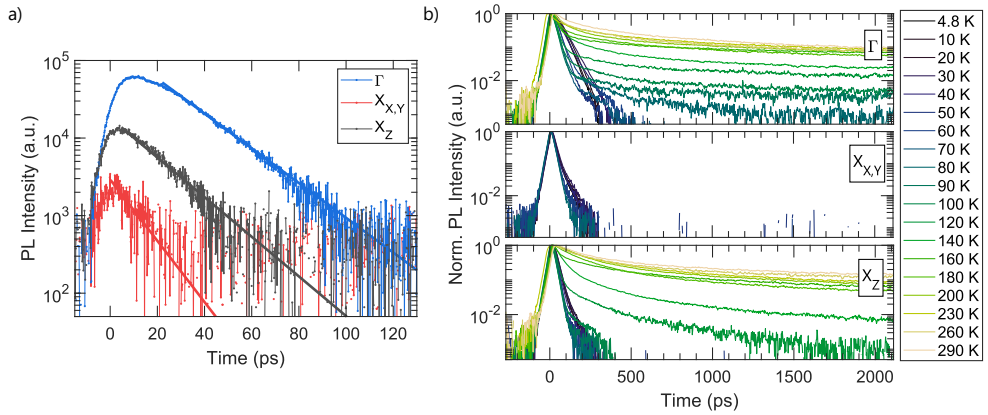

Figure 5. a) Temporal evolution of the photoluminescence (PL) intensity of the three studied transitions recorded at low temperature $T = 4.8$ K and excitation power $P_{exc} = 100$ µW. Solid lines show monoexponential decay curves, fitted to experimental data (points), with the time constants of 11 ps, 17 ps and 19 ps for $X_{X,Y}$, X_Z and Γ exciton respectively. b) Temporal PL decays of three investigated transitions with increasing temperature. Excitation energy ($E_{exc} = 2.00$ eV) and power ($P_{exc} = 150$ µW) were set constant throughout the series.

Finally, we explore the exciton recombination dynamics in the system. Figure 5a) shows the temporal evolution of the PL intensity for the Γ, $X_{X,Y}$ and X_Z transitions, following a ∼200 fs excitation pulse at low temperature ($T = 4.8$ K) and at the excitation power of $P_{exc} = 100$ µW.

All three transitions can be approximated by a mono-exponential decay with the characteristic decay time constant (τ_{PL}) of about 11 ps for the $X_{X,Y}$ transition and 17 ps for the X_Z. We note that such short decays are close to the temporal resolution of our detection system (of ∼7 ps), and are much smaller than the decay times expected for direct[28,57–59] and indirect transitions[9,19,39,60–62]. This observation reveals the likely presence of efficient nonradiative decay channels for the photoinjected carrier population in our system, dominating the measured dynamics and manifested by a shortening of the PL

decay.

Among the processes that could lead to the shortening of the PL decay time at cryogenic temperatures is an efficient depopulation of the QW reservoir through carrier relaxation into the states located below the fundamental QW bandgap, or the Auger-like processes, expected mainly in the high pumping regime. Importantly, the estimated maximum electron-hole pair density generated by our pump laser is on the order of $10^{18}\,\mathrm{cm}^{-3}$ (see **Methods**), what is at least an order of magnitude lower than the concentrations necessary for the Auger processes to take place[44,45]. Moreover, the Auger recombination is known to be followed by a drop of the PL efficiency with the pumping power density, a behaviour opposite to the clear increase observed in our structure, as presented in Figure 2c). The pump power-dependent PL experiment suggests that the number of the electron-hole pairs in the QW is significantly lower than the estimated values, as the time-integrated PL does not exhibit characteristic intensity saturation even up to $P_{exc} = 10^4\,\mu\mathrm{W}$ (see Figure 2c)). This indicates the likelihood of other non-radiative recombination processes, unrelated to the Auger ones, governing the carrier recombination just after the photoexcitation, and effectively decreasing the measured PL decay times. They could come from carrier relaxation to the states below the bandgap, such as defect states[63–65].

The Γ exciton is characterized by a slightly larger τ_{PL} of around 19 ps. However, its decay deviates from purely monoexponential at early times, with noticeably longer rise time (see the blue curve in Fig. 5a)). The elongated rise time for the Γ exciton is related to the inefficient capture of photo-generated carriers/excitons from the barrier, which may also stem from non-radiative processes happening in this layer, decreasing the overall capture probability. On the contrary, a relatively short capture time for the X valley can be driven by carrier relaxation in the barrier, additionally enhanced by the carrier transfer from the Γ to the X valley.

Furthermore, we studied the temporal evolution of the PL resonance intensity when the temperature is increased and the results can be seen in Fig. 5b), with corresponding time-integrated spectra presented in Fig. 3a). At elevated temperatures, the decays of all resonances become multiexponential, with the shorter component being on the same order of magnitude as the low temperature and the longer component strongly increasing up to several nanoseconds. This makes the net decay much longer, extending above the available 2 ns temporal window. Importantly, the $X_{X,Y}$ is characterised by the near resolution-limited decay for all temperatures at which it is observed, which can be explained by the ultrafast transfer of electrons to the true ground state, acting as an efficient nonradiative channel for this state. As the transition probability of the $X_{X,Y}$ state is lower due to the momentum-forbidden nature, the intra-level transitions become more effective. It further visualises the complex dynamics within the system, with possible transitions between closely neighbouring levels, especially when phonons help to conquer the energy barriers and carry particle momentum. Additionally, the temperatures corresponding to the stark elongation of the X_Z and Γ emission ($\sim$80 K to $\sim$100 K) match the localization energies estimated from the transition energy evolution as described in the section **Temperature-dependent photoluminescence**, pointing to the likelihood of localization effects playing an additional role in the change of dynamics with temperature, as it has been observed before[60]. Even more, the reservoir of trap states existing below the fundamental bandgap of the system, indicated by other measurements, could also contribute to the PL elongation. As the temperature rises, carriers may be released from the trap states and populate the QW confined states due to the increasing phonon bath. This process elongates the observed radiative lifetime[63–66].

Summary and Discussion

In this work, we investigated fundamental optical excitations in the AlGaAs/AlAs QWs near the regime of Γ-X valley coupling for confined electrons, using the time-integrated and time-resolved photoluminescence. Our experimental characterization is supported by theoretical calculations within the effective-mass framework.

The low-temperature PL experiments reveal three clearly resolved optical transitions, which we interpreted as direct and momentum- and spatially-indirect excitons. The strongest PL feature is attributed to the Γ exciton recombination. It has been previously observed in the microcavity-embbedded AlGaAs/AlAs QW[26] and its transition energy matches very well the calculated one. It dominates the spectrum at low temperature and low photo-excitation, as it is expected form a direct exciton transition of a high transition probability.

The other two transitions below the Γ exciton have not be thoroughly investigated in similar QW structures. Our study suggests their indirect nature and the X-valley-electrons origin. The middle energy transition, pinpointed as $X_{X,Y}$, have features corresponding well to the momentum and spatially indirect exciton, with the $x_{x,y}$-electron constituent. This state is expected to be purely indirect in space and in momentum, hence initially forbidden, yet allowed by a random potential which includes all wavevectors[39]. It does not mix with the Γ state by the structure potential[39] (in contrast to X_Z). In our experiments this state is characterized by a largely extended diffusion, and its energy blueshifts with density, as it is expected from dipolar species, affected by repulsive interactions. In both of those observations $X_{X,Y}$'s characteristics clearly differ from the other two states, as one can expect from their momentum-direct (or pseudo-direct) nature. At the highest excitation powers and increased temperatures it becomes unresolvable from the spectra, overwhelmed by the other two transitions. This can also be pinpointed to its indirect nature, as the momentum-selection rules make its recombination the least probable. With increased

phonon influence, the $x_{x,y}$ electrons can clearly relax or scatter into the other two states, preventing the $X_{X,Y}$ exciton radiative recombination (with $\Gamma - X_{X,Y}$ mixing allowed by the potential fluctuations due to interface roughness[19]).

Finally, we have identified the ground state of this system as the X_Z exciton, effectively recognizing the whole structure to be of the type-II (spatially indirect) and pseudo-direct in momentum. Symmetry (the structure potential) allows X_Z's recombination without the assistance of phonons and its mixing with the Γ state[19,20,39]. Accordingly, in all of our measurements its characteristics are similar to the highest Γ state, e.g. it presents similar diffusion profile at low temperatures and redshifts in energy at increased densities, due to the unintentional sample heating. The largest effective mass makes it the lowest energy state in the system[39]. It also makes it prone to the interface roughness and fluctuations and becoming localized. One can clearly see this effect in its observed narrow diffusion profile, the profile's expansion at increased temperatures, in the clear deviation from the Varshni curve at low temperatures, but also in a significant increase of its luminescence and decay time at elevated temperatures, as the excitons that are localized at low temperature become mobile at elevated temperatures[20]. The temperature of this increase in the decay constant corresponds well to the estimated localization energy of around 7 meV.

Our clear identification and characterization of these states are crucial in a careful design of future devices, where specific excitonic states are at the core of interest. Our system offers a superb monolithic platform in which three species of excitons, both direct and indirect, can be exploited. As a clear example, such a QW system can be integrated inside a microcavity, where the dipolar excitons coupled to the cavity field can provide new functionalities and device applications.

Methods

Sample growth

The investigated structure was grown by molecular beam epitaxy on a nominally undoped (001) GaAs substrate. The structure consists of twelve 9 nm-wide $Al_{0.20}Ga_{0.80}As$ QWs, separated by 4 nm AlAs barriers, distributed in three stacks of four. The stacks were initially placed in a $\lambda/2$-AlAs cavity surrounded by AlAs/$Al_{0.40}Ga_{0.60}As$ distributed Bragg reflectors (DBRs), consisting of 28/24 mirror pairs in the bottom/top reflector, including 3 nm GaAs smoothing layers after each mirror pair. Such a full microcavity structure was initially designed for room-temperature polaritonics, however, here we investigate the system prior to the coupling with the photonic modes. To characterize the QW system, the top DBR has been etched away, so the QW part on a bottom DBR-structure is studied in this work. The resulting structure is characterised by an enhanced luminescence extraction efficiency. Additionally, it was verified that no measurable signatures of remaining photonic modes in the spectral vicinity of the QWs were observed. Thus, one can assume no photonic mode coupling and focus on the QW emission. The structure with a top DBR mirror, providing a full cavity system, has been presented elsewhere[26].

Optical experiments

For the time-integrated (PL) and time-resolved photoluminescence (TRPL) experiments, the structure was held in a helium-flow optical cryostat, allowing for the sample temperature control in the range of 4.8 K to 300 K. The structure was excited by ~200 fs-long laser pulses with the pulse central wavelength of 620 nm ($E_{exc} = 2.00$ eV). The pulses were delivered by a synchronously-pumped optical parametric oscillator with a 76 MHz repetition frequency, pumped with a Ti:Sapphire laser. The optical excitation was focused on the sample surface via an infinity-corrected high-numerical-aperture (NA) objective (NA=0.65). The PL/TRPL signal was then collected by the same objective and directed to a 0.3 m-focal length monochromator for spectral resolution. The PL was registered by a thermo-electrically-cooled Si-based electron-multiplied-CCD camera or by a Si-cathode-based streak camera. The TRPL measurement system provided a time resolution of ~7 ps. Spatial resolution in the time-integrated spatial diffusion measurements was achieved using the two-dimensional CCD camera[67,68].

Band structure calculations

The band structure calculations were performed within the effective mass approximation. Due to the wide band gaps in the investigated materials the conduction band was assumed parabolic near the Γ and X points and the spin–orbit split-off (SO) energy is large enough to ignore the SO band. The remaining valence bands (heavy and light hole) were described in the Luttinger model[69]. The energies and wave functions of confined carriers were obtained numerically by solving the Schrödinger equation using the method reported in Ref.[70]. Standard material parameters[34] for GaAs and AlAs were used in the calculation and linear interpolation was applied for $Al_{0.20}Ga_{0.80}As$. The valence-band offset was calculated as 37% of the difference in band gaps in the well and barrier layers. The exciton binding energy was estimated from the formula $E_{Ry} = \mu e^4/2\varepsilon^2\hbar^2$, where μ is the in-plane reduced effective mass and ε is the dielectric constant.

Photo-excited electron-hole pair density estimation

The estimation of the maximum electron-hole pair density N_{e-h}, generated by our pump laser and used in sections **Excitation power-dependent photoluminescence** and **Time-resolved photoluminescence** has been done with a following formula:

$$N_{e-h} = \frac{P_{exc}}{A f E_{exc}} T_{obj} T_{glass} (1 - R_{sample}) e^{-\alpha d}, \tag{1}$$

where P_{exc} is the measured averaged excitation power, $A = \pi (\phi/2)^2$ is the laser spot area, $\phi = 4\,\mu\text{m}$ is its diameter, $f = 76\,\text{MHz}$ is the laser pulse repetition frequency, the excitation energy $E_{exc} = 2.00\,\text{eV} = 3.2038 \times 10^{-19}\,\text{J}$, $T_{obj} = 80\,\%$ is the objective transmission at 620 nm, the sample reflection under the normal incidence $R_{sample} = 30\,\%$[71] and the cryostat glass transmission is $T_{glass} = 96\,\%$. $\alpha = 2 \times 10^4\,\text{cm}^{-1}$ is the absorption coefficient for the $Al_{0.2}Ga_{0.8}As$ QW material at cryogenic temperatures[72] and d is the effective width of the absorption layer (QW stack), $d = 4 \cdot 3 \cdot 9$ nm=108 nm. The experiment with $P_{exc} = 100\,\mu\text{W}$ gives the maximum concentration of $N_{e-h} = 1.41 \times 10^{13}\,\text{cm}^{-2}$ ($N_{e-h}/d = 1.31 \times 10^{18}\,\text{cm}^{-3}$).

Data availability

The datasets generated during and/or analysed during the current study are available from the corresponding author on reasonable request.

References

1. Gu, J. *et al.* Dipolar excitonic insulator in a moiré lattice. *Nat. Phys.* **18**, 395–400, DOI: 10.1038/s41567-022-01532-z (2022).
2. Fogler, M. M., Butov, L. V. & Novoselov, K. S. High-temperature superfluidity with indirect excitons in van der waals heterostructures. *Nat. Commun.* **5**, 4555, DOI: 10.1038/ncomms5555 (2014).
3. Butov, L. V., Zrenner, A., Abstreiter, G., Böhm, G. & Weimann, G. Condensation of Indirect Excitons in Coupled AlAs/GaAs Quantum Wells. *Phys. Rev. Lett.* **73**, 304–307, DOI: 10.1103/PhysRevLett.73.304 (1994).
4. Butov, L. V., Lai, C. W., Ivanov, A. L., Gossard, A. C. & Chemla, D. S. Towards bose–einstein condensation of excitons in potential traps. *Nature* **417**, 47–52, DOI: 10.1038/417047a (2002).
5. Wang, Z. *et al.* Evidence of high-temperature exciton condensation in two-dimensional atomic double layers. *Nature* **574**, 76–80, DOI: 10.1038/s41586-019-1591-7 (2019).
6. Ciarrocchi, A., Tagarelli, F., Avsar, A. & Kis, A. Excitonic devices with van der waals heterostructures: valleytronics meets twistronics. *Nat. Rev. Mater.* **7**, 449–464, DOI: 10.1038/s41578-021-00408-7 (2022).
7. Liu, Y. *et al.* Excitonic devices based on two-dimensional transition metal dichalcogenides van der waals heterostructures. *Front. Chem. Sci. Eng.* **18**, 16, DOI: 10.1007/s11705-023-2382-0 (2024).
8. Masumoto, Y. & Tsuchiya, T. Optical study of alxga1-xas-alas ternary alloy multi-quantum-well structures around two γ–x crossovers. *J. Phys. Soc. Jpn.* **57**, 4403–4408, DOI: 10.1143/jpsj.57.4403 (1988).
9. Dawson, P., Moore, K. J., Foxon, C. T., 't Hooft, G. W. & van Hal, R. P. M. Photoluminescence decay time studies of type II GaAs/AlAs quantum-well structures. *J. Appl. Phys.* **65**, 3606–3609, DOI: 10.1063/1.342640 (1989).
10. Young, J. F., Charbonneau, S. & Coleridge, P. T. Determination of x_z-x_x,y energy separation and intervalley relaxation times in type-ii $al_xga_{1-x}as$/alas multiple quantum wells. *Phys. Rev. B* **42**, 11434–11437, DOI: 10.1103/PhysRevB.42.11434 (1990).
11. Lee, S. T. *et al.* Interband transitions in $al_xga_{1-x}as$/alas quantum-well structures. *Phys. Rev. B* **53**, 12912–12916, DOI: 10.1103/PhysRevB.53.12912 (1996).
12. Haetty, J. *et al.* Magnetic-field-induced localization of carriers in $al_{0.25}ga_{0.75}As$/AlAs multiple-quantum-well structures. *Phys. Rev. B* **56**, 12364–12368, DOI: 10.1103/PhysRevB.56.12364 (1997).
13. Ting, D. Z. Y. & Chang, Y.-C. Γ-X mixing in GaAs/$Al_xGa_{1-x}As$ and Al_xGa_{1-x} As/AlAs superlattices. *Phys. Rev. B* **36**, 4359–4374, DOI: 10.1103/PhysRevB.36.4359 (1987).
14. Ru, G. *et al.* Gamma-X band mixing in GaAs/AlAs superlattice. vol. 5260, 257, DOI: 10.1117/12.544034 (2003).
15. Fluegel, B., Alberi, K., Reno, J. & Mascarenhas, A. Spectroscopic determination of the bandgap crossover composition in mbe-grown alxga1-xas. *Jpn. J. Appl. Phys.* **54**, 042402, DOI: 10.7567/JJAP.54.042402 (2015).

16. Chand, N. *et al.* Comprehensive analysis of si-doped al$_x$ga$_{1-x}$As ($x = 0$ to 1): Theory and experiments. *Phys. Rev. B* **30**, 4481–4492, DOI: 10.1103/PhysRevB.30.4481 (1984).

17. Pearah, P. J. *et al.* Low-temperature optical absorption in AlxGa1-xAs grown by molecular-beam epitaxy. *Phys. Rev. B* **32**, 3857–3862, DOI: 10.1103/PhysRevB.32.3857 (1985).

18. Tada, T. *et al.* Tunneling process in AlAs/GaAs double quantum wells studied by photoluminescence. *J. Appl. Phys.* **63**, 5491–5494, DOI: 10.1063/1.340374 (1988).

19. Feldmann, J. *et al.* Γ-X-Γ electron transfer in mixed type I-type II GaAs/AlAs quantum well structures. *Solid State Commun.* **83**, 245–248, DOI: 10.1016/0038-1098(92)90846-2 (1992).

20. van Kesteren, H. W., Cosman, E. C., Dawson, P., Moore, K. J. & Foxon, C. T. Order of the X conduction-band valleys in type-II GaAs/AlAs quantum wells. *Phys. Rev. B* **39**, 13426–13433, DOI: 10.1103/PhysRevB.39.13426 (1989).

21. Birkedal, D. *et al.* Interwell excitons in GaAs superlattices. *Superlattices Microstruct.* **21**, 587–590, DOI: 10.1006/spmi.1996.0208 (1997).

22. Cingolani, R., Baldassarre, L., Ferrara, M., Lugarà, M. & Ploog, K. Type-I – type-II transition in ultra-short-period GaAs/AlAs superlattices. *Phys. Rev. B* **40**, 6101–6107, DOI: 10.1103/PhysRevB.40.6101 (1989).

23. Kato, H., Okada, Y., Nakayama, M. & Watanabe, Y. Γ - X crossover in GaAs/AlAs superlattices. *Solid State Commun.* **70**, 535–539, DOI: 10.1016/0038-1098(89)90945-9 (1989).

24. Peterson, M. W. *et al.* Miniband dispersion in GaAs/Al$_x$Ga$_{1-x}$As superlattices with wide wells and very thin barriers. *Appl. Phys. Lett.* **53**, 2666–2668, DOI: 10.1063/1.100189 (1988).

25. Danan, G. *et al.* Optical evidence of the direct-to-indirect-gap transition in GaAs-AlAs short-period superlattices. *Phys. Rev. B* **35**, 6207–6212, DOI: 10.1103/PhysRevB.35.6207 (1987).

26. Suchomel, H. *et al.* Room temperature strong coupling in a semiconductor microcavity with embedded AlGaAs quantum wells designed for polariton lasing. *Opt. Express* **25**, 24816, DOI: 10.1364/OE.25.024816 (2017).

27. Manassen, A., Cohen, E., Ron, A., Linder, E. & Pfeiffer, L. Exciton and trion spectral line shape in the presence of an electron gas in GaAs/AlAs quantum wells. *Phys. Rev. B - Condens. Matter Mater. Phys.* **54**, DOI: 10.1103/PhysRevB.54.10609 (1996).

28. Syperek, M. *et al.* Spin coherence of holes in GaAs/(Al,Ga)As quantum wells. *Phys. Rev. Lett.* **99**, DOI: 10.1103/PhysRevLett.99.187401 (2007).

29. Haverkort, J. E. M., Schuwer, M. P., Leys, M. R. & Wolter, J. H. Spatial variations of photoluminescence line broadening around oval defects in gaas/algaas multiple quantum wells. *Semicond. Sci. Technol.* **7**, A59, DOI: 10.1088/0268-1242/7/1A/011 (1992).

30. Ihm, J. Effects of the layer thickness on the electronic character in GaAs-AlAs superlattices. *Appl. Phys. Lett.* **50**, 1068–1070, DOI: 10.1063/1.97972 (1987).

31. O. Göbel, E. & Ploog, K. Fabrication and optical properties of semiconductor quantum wells and superlattices. *Prog. Quantum Electron.* **14**, 289–356, DOI: 10.1016/0079-6727(90)90001-E (1990).

32. Maezawa, K., Mizutani, T. & Yamada, S. Effective mass and ground state of AlAs quantum wells studied by magnetoresistance measurements. *J. Appl. Phys.* **71**, 296–299, DOI: 10.1063/1.350704 (1992).

33. Im, H., Klipstein, P. C., Grey, R. & Hill, G. Rotation of the conduction band valleys in alas due to X_X - X_Y mixing. *Phys. Rev. Lett.* **83**, 3693–3696, DOI: 10.1103/PhysRevLett.83.3693 (1999).

34. Piprek, J. *Semiconductor optoelectronic devices* (Elsevier, 2003).

35. Pietka, B. *Excitonic Complexes in Natural Quantum Dots Formed in Type II GaAs / AlAs. Physics [physics].* Ph.D. thesis, Université Joseph-Fourier - Grenoble I, Grenoble (2007).

36. Wu, F.-C., Xue, F. & MacDonald, A. H. Theory of two-dimensional spatially indirect equilibrium exciton condensates. *Phys. Rev. B* **92**, 165121, DOI: 10.1103/PhysRevB.92.165121 (2015).

37. Chang, C. P. & Lu, Y.-T. k-space formulation of Γ-x mixing for excitons in a thin gaas/alas quantum well. *Phys. Rev. B* **49**, 5438–5442, DOI: 10.1103/PhysRevB.49.5438 (1994).

38. Ponomarev, I., Deych, L., Shuvayev, V. & Lisyansky, A. Self-consistent approach for calculations of exciton binding energy in quantum wells. *Phys. E: Low-dimensional Syst. Nanostructures* **25**, 539–553, DOI: https://doi.org/10.1016/j.physe.2004.08.111 (2005).

39. Finkman, E. *et al.* Optical properties and band structure of short-period GaAs/AlAs superlattices. *J. Lumin.* **39**, 57–74, DOI: 10.1016/0022-2313(87)90033-0 (1987).

40. Butov, L. V., Imamoglu, A., Campman, K. L. & Gossard, A. C. Coulomb effects in spatially separated electron and hole layers in coupled quantum wells. *J. Exp. Theor. Phys.* **92**, 260–266, DOI: 10.1134/1.1354683 (2001).

41. Butov, L. V., Shashkin, A. A., Dolgopolov, V. T., Campman, K. L. & Gossard, A. C. Magneto-optics of the spatially separated electron and hole layers in gaas/al$_x$ga$_{1-x}$As coupled quantum wells. *Phys. Rev. B* **60**, 8753–8758, DOI: 10.1103/PhysRevB.60.8753 (1999).

42. Schmidt, T., Lischka, K. & Zulehner, W. Excitation-power dependence of the near-band-edge photoluminescence of semiconductors. *Phys. Rev. B* **45**, 8989–8994, DOI: 10.1103/PhysRevB.45.8989 (1992).

43. Spindler, C., Galvani, T., Wirtz, L., Rey, G. & Siebentritt, S. Excitation-intensity dependence of shallow and deep-level photoluminescence transitions in semiconductors. *J. Appl. Phys.* **126**, 175703, DOI: 10.1063/1.5095235 (2019).

44. Wang, P., Lee, K. K., Yao, G., Chen, Y. C. & Waters, R. G. Carrier recombination rate in gaas-algaas single quantum well lasers under high levels of excitation. *Appl. Phys. Lett.* **56**, 2083–2085, DOI: 10.1063/1.102979 (1990).

45. Borri, P., Ceccherini, S., Gurioli, M. & Bogani, F. Auger heating of carriers in heterostructures. *Solid State Commun.* **103**, 77–81, DOI: 10.1016/s0038-1098(97)00150-6 (1997).

46. Zhu, L. *et al.* Auger recombination at low temperatures in ingaas/inalas quantum well probed by photoluminescence. *J. Lumin.* **169**, 132–136, DOI: 10.1016/j.jlumin.2015.08.075 (2016).

47. Sumikura, H., Sato, T., Shinya, A. & Notomi, M. Time-resolved mid-infrared photoluminescence from highly strained inas/ingaas quantum wells grown on inp substrates. *Appl. Phys. Express* **14**, 032008, DOI: 10.35848/1882-0786/abe1e0 (2021).

48. Vurgaftman, I., Meyer, J. R. & Ram-Mohan, L. R. Band parameters for III–V compound semiconductors and their alloys. *J. Appl. Phys.* **89**, 5815–5875, DOI: 10.1063/1.1368156 (2001).

49. Varshni, Y. Temperature dependence of the energy gap in semiconductors. *Physica* **34**, 149–154, DOI: https://doi.org/10.1016/0031-8914(67)90062-6 (1967).

50. Lourenço, S. A. *et al.* Temperature dependence of optical transitions in AlGaAs. *J. Appl. Phys.* **89**, 6159–6164, DOI: 10.1063/1.1367875 (2001).

51. Colocci, M. *et al.* Temperature dependence of exciton lifetimes in gaas/algaas quantum well structures. *Europhys. Lett.* **12**, 417, DOI: 10.1209/0295-5075/12/5/007 (1990).

52. Ivanov, A. L. Quantum diffusion of dipole-oriented indirect excitons in coupled quantum wells. *Europhys. Lett.* **59**, 586, DOI: 10.1209/epl/i2002-00144-3 (2002).

53. Fasol, G., Fasolino, A. & Lugli, P. *Spectroscopy of Semiconductor Microstructures*, vol. 206 of *NATO ASI Series* (Springer US, Boston, MA, 1989).

54. Heller, W., Filoramo, A., Roussignol, P. & Bockelmann, U. Direct measurement of exciton diffusion in quantum wells. *Solid-State Electron.* **40**, 725–728, DOI: https://doi.org/10.1016/0038-1101(95)00351-7 (1996). Proceedings of the Seventh International Conference on Modulated Semiconductor Structures.

55. Smith, L. M. *et al.* Phonon-wind-driven transport of photoexcited carriers in a semiconductor quantum well. *Phys. Rev. B* **39**, 1862–1870, DOI: 10.1103/PhysRevB.39.1862 (1989).

56. Butov, L. V. & Filin, A. I. Energy relaxation and transport of indirect excitons in alas/gaas coupled quantum wells in magnetic field. *J. Exp. Theor. Phys.* **87**, 608–611, DOI: 10.1134/1.558700 (1998).

57. Vinattieri, A. *et al.* Exciton dynamics in gaas quantum wells under resonant excitation. *Phys. Rev. B* **50**, 10868–10879, DOI: 10.1103/physrevb.50.10868 (1994).

58. Deveaud, B. *et al.* Enhanced radiative recombination of free excitons in gaas quantum wells. *Phys. Rev. Lett.* **67**, 2355–2358, DOI: 10.1103/physrevlett.67.2355 (1991).

59. Citrin, D. S. Radiative lifetimes of excitons in quantum wells: Localization and phase-coherence effects. *Phys. Rev. B* **47**, 3832–3841, DOI: 10.1103/physrevb.47.3832 (1993).

60. Langbein, W., Kalt, H. & Hvam, J. M. Luminescence dynamics in type-ii gaas/alas superlattices near the type-i to type-ii crossover. *Phys. Rev. B* **54**, 14589–14594, DOI: 10.1103/PhysRevB.54.14589 (1996).

61. Baranowski, M. *et al.* Carrier dynamics between delocalized and localized states in type-II GaAsSb/GaAs quantum wells. *Appl. Phys. Lett.* **98**, 061910, DOI: 10.1063/1.3548544 (2011).

62. Mazuz-Harpaz, Y. *et al.* Radiative lifetimes of dipolar excitons in double quantum wells. *Phys. Rev. B* **95**, 155302, DOI: 10.1103/PhysRevB.95.155302 (2017).

63. Michler, P. *et al.* Nonradiative recombination via strongly localized defects in quantum wells. *Phys. Rev. B* **49**, 16632–16636, DOI: 10.1103/physrevb.49.16632 (1994).

64. Hangleiter, A. Recombination dynamics in gainn/gan quantum wells. *Semicond. Sci. Technol.* **34**, 073002, DOI: 10.1088/1361-6641/ab2788 (2019).

65. Zhang, S. K. *et al.* Radiative and nonradiative recombination processes in zncdse/zncdmgse multi-quantum-wells. *J. Appl. Phys.* **101**, DOI: 10.1063/1.2427098 (2007).

66. Rogowicz, E. *et al.* Carrier dynamics in thin germanium–tin epilayers. *ACS Appl. Electron. Mater.* **3**, 344–352, DOI: 10.1021/acsaelm.0c00889 (2021).

67. Pieczarka, M. *et al.* Lateral carrier diffusion in InGaAs/GaAs coupled quantum dot-quantum well system. *Appl. Phys. Lett.* **110**, 221104, DOI: 10.1063/1.4984747 (2017).

68. Rudno-Rudziński, W. *et al.* Carrier diffusion as a measure of carrier/exciton transfer rate in InAs/InGaAsP/InP hybrid quantum dot–quantum well structures emitting at telecom spectral range. *Appl. Phys. Lett.* **112**, 051103, DOI: 10.1063/1.5016436 (2018).

69. Luttinger, J. M. Quantum theory of cyclotron resonance in semiconductors: General theory. *Phys. Rev.* **102**, 1030–1041, DOI: 10.1103/PhysRev.102.1030 (1956).

70. Kubisa, M. *et al.* Photoluminescence investigations of two-dimensional hole landau levels in p-type single al$_x$ga$_{1-x}$As/GaAs heterostructures. *Phys. Rev. B* **67**, 035305, DOI: 10.1103/PhysRevB.67.035305 (2003).

71. Aspnes, D. E., Kelso, S. M., Logan, R. A. & Bhat, R. Optical properties of alxga1-x as. *J. Appl. Phys.* **60**, 754–767, DOI: 10.1063/1.337426 (1986).

72. Monemar, B., Shih, K. K. & Pettit, G. D. Some optical properties of the alxga1-xas alloys system. *J. Appl. Phys.* **47**, 2604–2613, DOI: 10.1063/1.322979 (1976).

Acknowledgements

D. B. and M. S. acknowledge financial support from the National Science Centre Poland within the (Grant No. 2018/30/E/ST7/00648). The Würzburg group acknowledges financial support by the German Research Foundation (DFG) under Germany's Excellence Strategy–EXC2147 "ct.qmat" (project id 390858490).

Author contributions statement

D. B. conducted all the spectroscopic experiments and analysed the experimental data, K.R. and M. K. performed the theoretical calculations, S. K., S. H and C. S provided the QW structure, D. B., M. P., S.K., C. S, S. H., and M.S. analysed and discussed the results. D.B. wrote the first version of the manuscript and prepared all figures. All authors reviewed the manuscript to its final form.

Additional information

The authors declare no competing interests.

Summary of the findings

The work presented in this Part focused on the excitonic characteristics of a QW system, which serves as an active material in the microcavity presented in the next Part of this thesis. This study investigated the system prior to the coupling with photonic modes. The structure was designed purposefully to increase the binding energy of the QW excitons, due to a near resonance of the $\Gamma-$ and X-valley band energy minimum, following a high Al content of the AlGaAs material. This work explored the optical properties and dynamics of the excitons in this system and:

- showed the presence of three states in the emission spectrum and used the power-dependent, spatially-resolved, temperature-resolved and time-resolved experiments, combined with theoretical calculations, to pinpoint their origin. It concluded, that three types of excitons are present in this QW system: an expected Γ-electron exciton confined in the QW layer (labeled as Γ), but also two momentum- and spatially-indirect excitons, lower in energy, stemming from X-valley electrons in the barrier layer with different effective masses, coupled to the confined QW holes (labelled as $X_{X,Y}$ and X_Z). Such indirect states have been studied in AlGaAs/AlAs superlattices before, but remained broadly unexplored in isolated QWs in a similar material system.

- showed a clear difference in the optical characteristics of the three studied states, in particular between the two indirect excitons. Namely, it showed a blueshift of the photoluminescence energy with excitation power of the $X_{X,Y}$ state, expected for a dipolar exciton, as well as its largely extended diffusion, also characteristic to indirect states. These characteristics follow directly from the momentum-selection rules, making the recombination of this state the least probable. The low recombination probability evidences also in the state's absence in the photoluminescence spectra at high densities or high temperatures. The pseudo-direct nature of the X_Z state makes its resemblance closer to the direct Γ exciton, and results in the respective redshift, narrow diffusion profile and strong emission also at increased temperatures.

- have identified the ground state of this system as the X_Z exciton, effectively recognizing the whole structure to be of the type-II (spatially indirect) and pseudo-direct in momentum.

- showed a linear dependence of the emission intensity of all three transitions with optical excitation density, expected for the excitonic transitions, followed by a possible non-radiative recombination taking over the radiative processes at high densities. The presence of efficient non-radiative recombination was further supported by the time-resolved measurements, which showed a fast, picosecond-scale photoluminescence decay of all three transitions on the order of the experimental setup resolution. Even though the indirect states are expected to present long lifetimes, the observed short decay in the luminescence experiments is likely to come from the non-radiative processes.

- it additionally showed, how also the localization effects play a role in Γ and X_Z characteristics, evidenced by the temperature-dependent and spatially resolved measurements. Namely, a deviation from Varshni curves at low temperatures, low diffusion of the X_Z state contrasted with a largely extended one at higher temperatures, as well as a significant increase of X_Z's luminescence and decay time at elevated temperatures, have all suggested that the excitons that are localized at low temperature become mobile at the elevated ones.

- provided the results of the theoretical calculations within the effective-mass framework, which showed a great correspondence with the experimental data. It also used simple models such as Varshni formulas to extract the material parameters (Varshni temperature constants and localization energies) of the states in question, largely in line with the previously reported parameters.

- has important implications not only in the full polariton microcavity, studied in the next Part, but also in other optoelectronic or photonic applications of such a system. The studied structure offers a superb monolithic platform in which three species of excitons, both direct and indirect, can be exploited at the same time, e.g. to underline the operation principles of novel electronic and photonic devices.

Part V

Anomalous dispersion via dissipative coupling in a quantum well exciton-polariton microcavity

Introduction

As shown throughout this thesis, in interacting quantum systems it is typical to observe level repulsion. With interactions, an avoided crossing between the energy levels of two strongly coupled eigenmodes is expected, and the size of the anticrossing gap is proportional to the strength of the coupling. In particular case of excitons in optical microcavities, standing at the core of this thesis, when the photonic and the excitonic modes are put close to resonance in energy and the quality is sufficient to prolong the excitation existence, the two modes couple and hybridize, forming exciton polaritons. The resulting energy levels anticross, avoiding degeneracy at resonance, and form characteristic polariton branches. The lower polariton dispersion is non-parabolic, yet for all the momenta the effective mass linked to band curvature remains positive.

However, there are also rare and more unique cases in which level attraction can be observed. Such observations have been done in a range of systems and settings, and there have been many approaches to explain such a phenomenon, such as the imaginary form of coupling [48,261], certain decay channels [48,262], artificial coupling using an external feedback circuit [263, 264] and various inclusions of non-Hermitian dissipative terms in the Hamiltonian [261]. All these approaches share a common characteristic - they account for some type of *dissipation* present in the studied system. When the dissipation becomes equally important to the coherent coupling, emergent states can attract, instead of repelling.

The effect of the level attraction has been observed in a wide range of physical systems. Initially studied mainly for magnons, and with most of the investigations in this context [265–267], but later it was observed also in microwave cavities [263], mechanical systems [268] or photonic crystal cavities containing single quantum dots [269]. In each case the exact form of dissipation differs, as well as the models suggested to describe it, however, an inherent existence and an importance of the decay remains a key factor. The broad range of contexts for these observations is not surprising - losses are inevitable in all open systems. Typically they are perceived as detrimental to the performance of the electronic or photonic devices, but recently the inherent non-Hermiticity of the system started to be considered advantageous. Controlling the losses has been suggested as a way to design novel properties or functionalities, e.g. in non-Hermitian photonics [270].

When levels with parabolic dispersions are being subject to a substantial loss, but the interlevel coupling and the energy proximity are both sufficient, they at-

tract, and the dispersion of one of the modes can invert, presenting an anomalous behaviour. Models show that this effect can lead to an inverted, anomalous wavevector dependence of one of the parabolic coupled modes, in effect resembling an inverted parabola [23, 48, 266, 267, 271]. Depending on the relative strength of the interaction and the dissipation, several regimes are expected, with either a single maximum of the energy-momentum dispersion at $k = 0$, or a non-monotonic anomalous function with maximas at finite wavevectors [261]. With the coherent coupling being sufficiently strong in comparison to the dissipation, the typical repulsion would hinder any effect.

One would expect, that exciton-photon systems are a great example of such a two parabolic modes system, and that with the level attraction, the dispersion of the eigenmodes would be hugely affected. Experimentally, for long such an observation has not been reported in microcavity polariton systems. Only recently the first hints have been presented, but they are still very scarce and limited. Several exact mechanisms have been suggested, different in each case, to explain the attraction. Importantly, all the experimental observations have been reported only in transition-metal dichalcogenide (TMDC) - based, rather low-Q microcavities.

First observation by Dhara et al. [272] was reported for trion polaritons in $MoSe_2$ layer, with the anomalous dispersion extracted from the photoluminescence spectra. The result is presented in Fig. 4.7 (a), reproduced from this study, showing a differentiated logarithm of the raw photoluminescence spectrum. One can see an inverted dispersion of one of the three modes. The supporting model, explaining the nature of the effect, is applicable only for many-particle excitons in heavily-doped samples, with complex interactions. A crucial role of the trion resonance is highlighted, interacting with an exciton and with a cavity photon (including many-body interactions with mediating polaritons). It's important to note, that the experimental result shown in Fig. 4.7 (a) is the differentiated logarithm of the raw data, calculated to increase the visibility and even then the linewidths of the final modes are very broad. The material platform and the sample quality strongly hinders the result.

Subsequent observation by Wurdack et al. [48] (reproduced in Fig. 4.7 (b)) showed negative-mass exciton-polaritons in an optical microcavity with a WS_2 monolayer. The effect has been reported in two samples with different exciton-photon detunings, and the observation was made at room temperature. In the photoluminecence spectra (see Fig. 4.7 (b)) the authors observed an anomalous dispersion of one polariton branch, with double maxima curves (maximas at finite wavevectors). To explain it, the authors suggested the mechanism of dissipative coupling via interactions of excitons with phonons, supported by a microscopic theory. They presented a model with exciton and photon modes coupled via imaginary interactions. Such an approach accounts for two decay channels present in the system - one related to the losses of photons (due to the microcavity imperfections) and one to the exciton-phonon interactions. Phonons are found to be the main contributor to the decay. They used a phenomenological approach to model the data, but they supported it with a microscopic theory. Importantly, this observation has been made at room temperature, and the interaction of TMDC excitons with phonons is known to be strong (in relation to e.g. GaAs-based systems, especially at low temperatures). Moreover, one has to

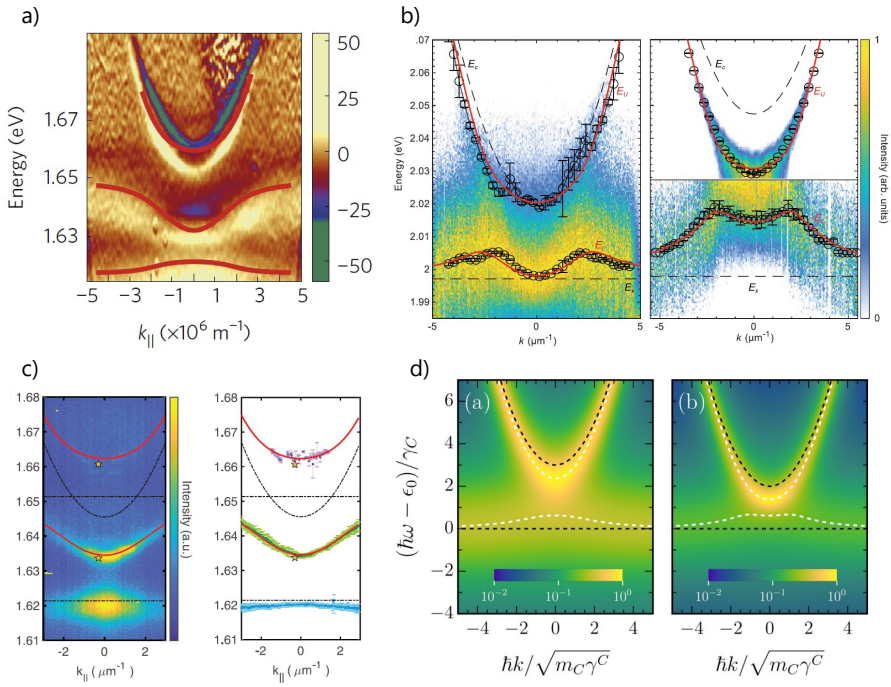

Figure 4.7. Reported observations of an anomalous dispersion in exciton-polariton microcavities. (a) Angle-resolved PL spectrum - the differentiated logarithm of the raw data to enhance the contrast - reproduced from ref. [272]. Solid line presents the model fitting. (b) Momentum-resolved PL spectra of two samples with different values of the exciton–photon detuning, reproduced from ref. [48]. The maximum intensity at each k value has been scaled to unity to visualise the shape of the lower branch. The black circles are the fitted peak positions of the two branches and the solid red lines are the fitted dispersion of the upper and lower polaritons. (c) Angle-resolved micro-PL spectra, reproduced from ref. [273]. The black dot-dashed lines show the bare cavity dispersion, $MoSe_2$ exciton emission and trion emission energies, the red solid lines show fitted upper and lower polariton modes. The extracted polariton energy is also plotted as a function of the in-plane wavenumber on the right-hand side. The error bars for the lower polariton and trion energies have been multiplied by a factor of 6 for increased visibility. (d) Calcultaed power spectra of the anomalous dispersions (with two sets of parameters), reproduced from ref. [261]. The color plots show the power spectra (color scale in arbitrary units), the dashed white lines correspond to the real parts of the theoretical model and the dashed-black lines represent the bare exciton and cavity photon kinetic energies.

note, that the spectra presented in Fig. 4.7 (b) are normalized, so that the maximum intensity at each k value has been scaled to unity, to visualise the shape of the lower branch. The effect is not starkly seen in the raw photoluminescence spectrum and the linewidths remain relatively broad.

Anomalous dispersion in a polariton sample has also been observed in ref. [273] (with the observation reproduced in Fig. 4.7 (c)), similarly in a TMDC monolayer, but it was not a subject of the work. The authors suggested that the mechanism of its occurence could be the same as in Dhara et al. [272], but they did not investigate the topic further. This only shows how such an effect is present and can be unexpectedly observed in a wide range of systems and samples, with more importance than previously thought, yet that it is still not very well understood.

Apart from these scarce observations, some theoretical predictions have been made in the context of exciton-polariton microcavities. In Bleu et al. [261] (a work inspired by discussions with the author of this thesis and coauthors of the research presented in this part) the authors showed how coupling of both resonances - the exciton and the cavity photon - to a shared photonic environment could lead to the anomalous shape of the dispersion. In such lossy cavities different regimes of the anomalous dispersion could be observed (with either a single or double maxima), depending on the ratio of the resonance decays. This setting was modelled by an imaginary form of coupling in a non-Hermitian model Hamiltonian. The examplary results of these calculations are presented in Fig. 4.7 (d) (with two regimes of the anomalous shape shown).

Additionally, in recent work by Binder et al. [274] the authors also considered the dispersion sign reversal of radiative resonances in two dimensions, as a consequence of a non-Hermitian coupling. They predicted how the 2D-layer polaritons without a cavity can exhibit mass-sign reversal similar to microcavity polaritons and have derived an analytic expression that sets conditions on the mass-sign reversal. However, their system is inherently different, as no cavity is present.

All of the works described above show, how this topic in the exciton-polariton context is now hotly debated. The limited reported works are very recent and there are still many unanswered questions. The experimental evidence is not only scarce, but also limited to rather low-Q microcavities with 2D materials. This limits both the effect's further experimental investigation, but also its potential application. These platforms are known to be rather inferior to monolithic III-V based systems in terms of quality, reproducibility and scalability. The investigated cases could be seen as rather "single-shot" samples, with little potential of scalability or precise tuning. The observations lack narrow sharp linewidths, as it is expected in non-monolithic, TMDC-based samples, especially at room temperature.

Furthermore, the models describing each of the cases are different. All of them describe a dissipative form of coupling between two modes, but the exact form, as well as the underlying phenomenon differ. Even though the level attraction and the anomalous band curvature can be phenomenologically described by the imaginary coupling between the two states, the physical basis of the effect is not always clear. Moreover, more models can be considered, when investigating a context of the level

attraction more broadly, beyond just the exciton-photon physical systems [266, 267].

Importanly in the context of this thesis, Yu et al. [271] have shown, how in a physical system, the dissipative type of coupling can be realized by coupling two oscillators reactively to a third, highly dissipative entity. They showed, how a real coupling of three oscillators (all with an intrinsic decay) can be regarded as an effectively complex coupling between two of the modes, provided that they are nearly resonant and that the dissipation of the third mode is sufficient. The third-party mode in cavity systems can even come from an invisible cavity mode, with extremely high leakage or dissipation. They regarded this model in a context of magnonic cavities, and used it to explain an experimental observation made in ref. [265]. Even though this mechanism has been successfully used to explain level attraction in magnon cavities, it has never been considered in the polariton context.

Crucially, this model explains the nature of the level attraction in a wide range of systems, showing how the dissipative coupling (often described in Hamiltonians as an imaginary coupling between two states [48, 261, 262, 267]) may result from a coherent coupling, but of three resonances. The presence of a highly dissipative mode, if pinpointed, can explain the attractive level crossing. In an intuitive, classical picture this model can be visualized as three damped oscillators (e.g. visualized as springs), coupled to each other, one of which is additionally in contact with a friction surface (hence, it is strongly damped). It is schamtically visualized in Fig. 4.8. The authors of ref. [271] call this type of coupling an *absement coupling* - the coupling force is proportional to the relative absement (the time integral of displacement) and can can be realized via a third oscillator with extra dissipation (as shown in Fig. 4.8). It differs from a *reactive* or a *velocity* types of coupling [271] between two oscillators, in which the mutual force is proportional to the oscillator's relative displacement or to their relative velocity respectively.

Finally, regardless of the explanation, the anomalous dispersion is inherently linked to a negative sign of the effective mass m_1, introduced in section 1.2.4. This parameter is related to the classical motion of the wave packet and determines the group velocity $v_g = \hbar k/m_1$ [47, 48]. Hence, the negative effective mass results in a complex and unique particle dynamics - the velocity and the force have different signs.

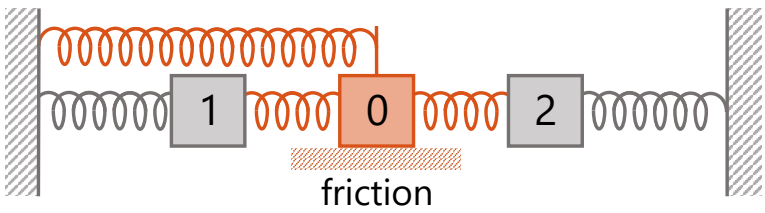

Figure 4.8. A simple classical depiction of the absement coupling, leading to the attractive level crossing, modelled as a coupling via a dissipative mode. The coupling between three numbered harmonic oscillators is schematically depicted, with damping visualized as springs. A dissipative mode is shown in orange, having contact with a friction surface.

The effect have been evidenced in Wurdack et al. [48], demonstrating propagation of the negative-mass polaritons in the direction opposite to their momentum. Such a unique feature can be used to further study nontrivial particle dynamics and hydrodynamics, or to investigate analogue systems. The optical accessibility of the polariton platform makes them an ideal system to specifically design and study analogous cases in other, less accessible systems [36, 275–277]. The effective mass engineering is a highly desirable and discussed topic, as it can be used e.g. to purposefully design non-Hermitian effects [58,63,278] (see also section 1.2.6), or obtain controllable exceptional points [49, 279–281]. Prior to the works described above, the negative effective mass in polariton microcavities has been obtained mainly by the potential landscape engineering [11], e.g. creating lattice potentials [199, 281, 282] or bound states in the continuum (in waveguides) [283]. Such an approach always requires additional sample processing steps, often hindering the effect tunability or limiting the systems in which it can be realized. The additional steps increase the cost and complexity of sample preparation. The engineering can also be realized via sophisticated excitation schemes [284], hugely increasing the complexity of the experiment.

An inverted, anomalous dispersion due to dissipative coupling adds one more possible way to engineer the effective mass and obtain negative m_1, even without any additional structuring. A specific context of high quality III-V semiconductor-based system would be additionally advantageous in this regard, as it offers the highest control of the design, structure parameters and the quality of the final structure.

Contributions

This research has been a collaborative work. D. Biegańska (the author of this thesis) initiated this study - during the characterization of a polariton microcavity, she observed the unexpected effect and she proceeded to its investigation and explanation. She was the main contributor in building the experimental setup and she performed all the spectroscopic experiments. She analysed the experimental data. Following crucial discussions with other authors she performed theoretical modeling of the results using the Matlab and Origin softwares. She took part in all discussions of the results, wrote the first version of the manuscript and prepared all figures. All authors reviewed the manuscript to its final form.

Results

Anomalous dispersion via dissipative coupling in a quantum well exciton-polariton microcavity

D. Biegańska,[1,*] M. Pieczarka,[1] C. Schneider,[2] S. Höfling,[3] S. Klembt,[3] and M. Syperek[1]

[1] *Department of Experimental Physics, Faculty of Fundamental Problems of Technology, Wrocław University of Science and Technology, Wybrzeże Wyspiańskiego 27, 50-370 Wrocław, Poland*

[2] *Carl von Ossietzky Universität Oldenburg, Fakultät V, Institut für Physik, 26129 Oldenburg, Germany*

[3] *Julius-Maximilians-Universität Würzburg, Physikalisches Institut and Würzburg-Dresden Cluster of Excellence ct.qmat, Lehrstuhl für Technische Physik, Am Hubland, 97074 Würzburg, Germany*

Although energy level repulsion is typically observed in interacting quantum systems, non-Hermitian physics predicts the effect of level attraction, which occurs when significant energy dissipation is present. Here, we show a manifestation of dissipative coupling in a high-quality AlGaAs-based polariton microcavity, where two polariton branches attract, resulting in an anomalous, inverted dispersion of the lower branch in momentum dispersion. Using angle-resolved photoluminescence measurements we observe the evolution of the level attraction with exciton-photon detuning, leading to changes in anomalous dispersion shape within a single sample. The dissipative coupling is explained by the interaction with an indirect exciton, acting as a highly dissipative channel in our system, and the observed dispersions are well captured within a phenomenological model. Our results present a new mechanism of dissipative coupling in light-matter systems and offer a tunable and well-controlled AlGaAs-based platform for engineering the non-Hermitian and negative mass effects in polariton systems.

INTRODUCTION

In interacting quantum systems, it is typical to observe level repulsion. When two modes couple and intermix, the resulting energy levels anticross, avoiding degeneracy at resonance. If the strongly interacting states are photons and excitons confined in planar microcavities, the resulting eigenstates appear as two exciton-polariton branches, schematically depicted in Fig. 1(a). Lower polaritons are characterized by a nearly parabolic dispersion at small wavevectors, with small and positive effective mass, inherited largely from the photonic component. At larger momenta characteristic inflection points appear, around which the second derivative of the energy dispersion changes sign, nevertheless, the mass that determines the group velocity remains positive for all momenta [1]. The mode dispersion and particle effective mass can be further engineered, typically by introducing an additional potential landscape in the system, such as lattice potentials, yet it requires additional sample processing or sophisticated excitation schemes [2–5].

However, in all open systems, losses are inevitable, and the interactions and eigenstates are strongly affected by dissipation. Optical systems in which light confinement can be effectively engineered, such as high-quality optical microcavities, are an ideal experimental platform to study dissipation-related coupling effects. When dissipation becomes equally important to the coherent coupling, the emergent states can attract (instead of repelling), even without additional potential. The attraction effect is analogous to classical in-phase oscillations of dissipatively coupled pendulums [6]. In light-matter systems the influence of dissipative coupling has been experimentally observed in photonic-crystal cavities containing single quantum dots [7]. In two-dimensional polaritonic systems however, while there were some first experimental hints in rather low-Q microcavities containing monolayer semiconductors [8, 9], clear studies in narrow-linewidth systems are elusive so far. The level attraction phenomenon has mainly been studied in other contexts, such as magnons [6, 10, 11], microwave cavities [12], opto-mechano-fluidic resonators [13] or mechanical systems [14]. Dissipative coupling has been suggested as a potential mechanism for entangled state creation, as a new tool in the design of superconducting qubits [10, 11], for development of metamaterials [10], but also as a mechanism beneficial in cavity spintronics [11].

When the coupling of two quantum mechanical oscillators with parabolic dispersions, subject to substantial loss, becomes complex, and the imaginary (dissipative) coupling is comparable to the real (coherent) coupling, the levels attract, and the dispersion of one of the modes can invert, presenting an anomalous behaviour. It is visualized in Fig. 1(b). The resulted band has a negative curvature parabolic wavevector dependence, directly representing the negative effective mass of the emergent state. However, even though the level attraction and the anomalous dispersion can be phenomenologically described by the imaginary coupling between the two states, the physical origin of the effect is not always clear and varies between systems. Interestingly, it has been shown how, in a physical system, the dissipative type of coupling can be realized by coupling two oscillators reactively to a third, highly dissipative entity [15], as schematically depicted in Fig. 1(c). The third-party mode in cavity systems can come from an invisible cavity mode with extremely high leakage or dissipation. This mechanism has been successfully used to explain the level attraction in

* dabrowka.bieganska@pwr.edu.pl

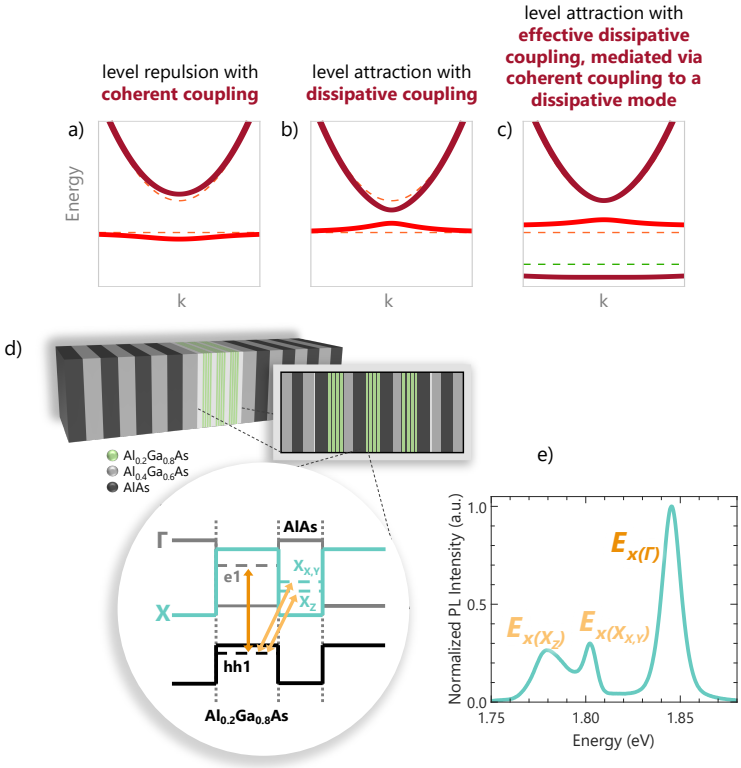

Figure 1. A schematic visualisation of the level attraction effect in an energy-momentum dispersion (a-c) and the investigated structure (d-e). (a) Levels of a strongly coupled system of two coherently coupled modes, showing level repulsion. (b) Level attraction of the same two modes, coupled with an imaginary coupling. (c) A schematic visualisation of a similar level attraction effect, but coming from a real coupling between three modes, one of which is strongly dissipative. Two initial modes in (a-c) are marked with dashed lines, and the third, dissipative mode in (c) is highlighted in green. (d) Schematics of the investigated microcavity, with a close-up of the active layer. In the system band structure solid lines show the edges of the X, Γ and valence bands of one period of the repeated layers. Dashed lines indicate the quantized electron ($e1$, $X_{X,Y}$, X_Z) and heavy hole ($hh1$) levels in two adjacent layers. Carriers occupying these levels subsequently form three excitons present within the system (indicated with orange arrows), when subject to Coulomb interactions. (e) The photoluminescence spectrum of the bare quantum well system, with the top Bragg reflector etched away. Three well-resolved features, labeled as $E_{x(\Gamma)}$, $E_{x(X_{X,Y})}$ and $E_{x(X_Z)}$, correspond to transitions of three excitonic species present in our sample.

magnon cavities [15], yet has never been considered in an exciton-polariton context.

Regardless of the mechanism, the negative mass of such an inverted state can be used in a wide range of studies on non-Hermitian effects or topology [16–18]. It manifests itself in the particle's dynamics, so that its group velocity and momentum have opposing directions [1, 9]. Next to substantial fundamental interest, this, in turn, can be employed to control wavepacket dynamics [1], hydrodynamics [19], or cause resonance trapping [20]. For all these applications, engineering the inverted dispersion is crucial, yet so far cavity engineering focused mainly on the potential engineering or spin-orbit interactions in polariton microcavities, rather than the dissipation. Precise control over the attraction strength would also be hugely beneficial.

In exciton-polariton settings, anomalous dispersion has been predicted [21], but it has been experimentally observed only very recently and only in transition-metal dichalcogenide samples [8, 9]. This medium lacks the exciton energy control and ease of the cavity design of a III-V based semiconductor and proved to be challenging in reproducibility. Moreover, in the experimental hints made so far, the effect was strongly obscured by inhomogeneously broadened lines, while their theoretical descriptions vary widely.

In this work, we unequivocally demonstrate the level attraction manifested as an inverted anomalous dispersion in the AlGaAs exciton-polariton system. We investigate the mechanism of dissipation in our structure, crucial for the attraction to occur. In contrast to previous studies, our III-V semiconductor sample not only hosts conventionally studied Γ-excitons in the QWs, coherently coupled to photons, but also lower-energy spatially- and momentum-indirect X-excitons, which are strongly prone to dissipation. We show that the source of dissipation in our structure is the lower-energy indirect state, acting as a draining channel for both photons and electrons. This highly dissipative mode allows for the dissipative coupling to become sufficiently strong to surpass the coherent exciton-photon coupling, and result in inverted eigenstate dispersion. Finally, we demonstrate the superiority of our material system in comparison to previous realisations, owing to its high tunability, ease of design, and huge potential for non-Hermitian phases engineering, by showing a change of the dispersion shape as a function of exciton-photon detuning.

RESULTS

Excitonic structure

We studied an AlGaAs/AlAs optical microcavity, designed for room temperature polaritonics [22]. However, in this work we focus on experimental observations made at cryogenic temperature of 4 K, benefiting from the narrow polaritonic linewidths. The sample schematic is depicted in Fig. 1(d) and a detailed description of the sample composition can be found in Methods.

Due to the high aluminium content affecting the band alignment, the structure hosts direct and indirect excitons in the quantum well (QW) [22–24]. Apart from the conventional direct excitons composed of Γ-valley electrons and heavy holes confined in the QW layer, the structure also hosts lower-energy spatially and momentum indirect X-excitons [24]. Since the order of X and Γ-valley energy minimum in the conduction band is reversed for the $Al_{0.2}Ga_{0.8}As$ QW and for the AlAs barrier material, the fundamental QW electron state resides in the barrier. This allows the formation of indirect excitons composed of X-valley electrons in the barrier Coulomb-correlated with Γ-valley heavy holes confined in the QW layer. Two lowest-energy optically active states relate to excitons consisting of X-valley electrons with different effective masses (longitudinal and transverse with respect to the spatial quantization axis), forming X_Z and $X_{X,Y}$ states respectively. The single-particle energy levels are visualized in the QW band structure in Fig. 1(d), using dashed lines. Measured spectrum of the bare QW active material is presented in Fig. 1(e), where all excitonic transitions are indicated. The indirect nature of these excitonic states has been investigated in detail in our previous work [24].

When embedded in a monolithic optical microcavity close to resonance with the Γ-state, direct excitons couple strongly to light, forming exciton-polariton quasiparticles [22]. These states are characterized by the normal-mode splitting and present typical polariton dispersions (as shown in Supplementary Material, section I). However, herein we study the structure at very large negative Γ-exciton – photon detunings, $\Delta_\Gamma = E_c - E_{x(\Gamma)} < 0$ (where E_c is the cavity mode energy and $E_{x(\Gamma)}$ is the energy of the direct exciton in the QW). In this regime, the light-matter interactions are dominated by the coupling of the cavity optical mode to the indirect X -valley excitons and the resulting states strongly differ from the typical exciton-polaritons under coherent light-matter coupling. The detuning is sufficiently large that the coherent coupling to the Γ-excitons becomes irrelevant. For convenience, throughout the rest of the paper, we will refer to the detuning as defined with respect to the higher-energy X-exciton, $\Delta_X = E_c - E_{x(X_{X,Y})}$.

Photoluminescence Measurements

To study the coupling between photons and X-excitons, we measured angle-resolved photoluminescence spectra in a wide detuning range, close to resonance with the X-excitons. When the photonic mode gets sufficiently close to the energy of the $X_{X,Y}$ excitonic resonance, a new lower energy state brightens up, with the dispersion curved in a distinctly inverted manner. An experimental example of such a momentum dispersion is presented in Fig. 2(a), together with the peak energies of the two branches, extracted with a fitting procedure (see Methods and Supplementary Material, section II). An apparent and monotonous redshift of this mode's energy with increasing wavevector can be seen in Fig. 2(b), a dependence opposite to the higher energy photonic-like state. The two levels attract, causing the mirroring of their wavevector energy dispersions, mimicking the dispersion sketched in Fig. 1(b). The negative curvature of such an inverted parabolic dispersion is directly linked to the negative effective mass of the lower mode - a rare phenomenon in exciton-polariton systems [8, 9, 25, 26].

Taking advantage of the cavity energy gradient (due to the thickness variation across the sample), we probed the negative mass states in a range of sample positions (detunings). As presented in Fig. 2(c), decreasing the detuning between the cavity mode and the $X_{X,Y}$-exciton energy Δ_X leads to an increase in attraction effect, with the anomalous shape of the lower branch becoming steeper and more distinct. Figure 2(c) shows the energies of two polaritonic branches extracted from fitting the PL measurements taken at different sample positions. Interestingly, around the positive photon to $X_{X,Y}$-exciton detuning of approximately 10 meV the curvature changes from the inverted parabola-like with one energy maximum at $k = 0$ to anomalous shape with two distinct and symmetric maxima at $k \neq 0$. Similar dispersion shapes

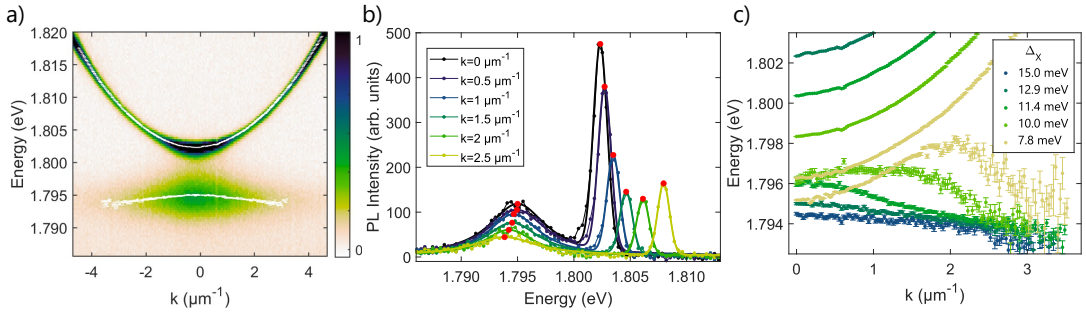

Figure 2. Experimental observation of the anomalous dispersion. (a) Momentum-resolved photoluminescence image at a chosen exciton-photon detuning (linear color scale). Spectra crossections taken at several wavevectors are presented in (b) (connected dots), together with fitted curves (solid lines). Red dots show the energies of the two deconvoluted modes, extracted from fitting, also marked in white in (a). (c) Extracted mode dispersions at several exciton-photon detunings Δ_X. Error bars indicate the fitting standard error.

have been observed before in different structures in both regimes [8, 9], yet never in the same material system, nor in a single sample. The corresponding change of the effective mass value with the detuning is presented in Supplementary Material, section VI.

At negative detunings Δ_X, only one branch appears in the photoluminescence spectrum, with the standard parabolic shape of the dispersion resembling the one of a photonic mode, as presented in Supplementary Material, section I. For further discussions, we focus solely on the level attraction region.

Model

To understand the source of level attraction, we have to recall the existence of the X_Z-electron exciton, with energy below both the $X_{X,Y}$ exciton and the photonic mode, which inclusion proves to be crucial in the theoretical description of the data. To describe our system and quantify the mechanism of level attraction, we used a general three coupled oscillator model, predicting the attractive level crossing via the existence of a dissipative mode [15]. Even though the level attraction has been previously described with the use of imaginary coupling between two oscillators [9, 21], in [15] the authors show how, in a physical system, the dissipative coupling can be realized by coupling two oscillators to a third highly dissipative one, even if the mode is invisible. In our case, the third-party mode could be identified as the X_Z -exciton.

The model can be represented by a 3×3 non-Hermitian matrix:

$$H = \begin{pmatrix} E_1 & V & g_1 \\ V & E_2 & g_2 \\ g_1 & g_2 & E_0 \end{pmatrix} = \begin{pmatrix} E_c - i\gamma_c & V & g_1 \\ V & E_{x(X_{X,Y})} - i\gamma_x & g_2 \\ g_1 & g_2 & E_{x(X_Z)} - i\gamma_0 \end{pmatrix}.$$

In this approach, two oscillators with intrinsic decay (with energies of E_1 and E_2) are coupled to each other coherently via V, and to the third oscillator E_0, which is strongly damped, $\gamma_0 \gg \gamma_c, \gamma_x$. Significant dissipation of the third state is crucial for the level attraction and for E_0's strong influence on the E_1 and E_2 dispersions, when the real coupling terms g_1 and g_2 are sufficiently large to surpass the coherent coupling V. In such conditions, these terms can effectively act as complex coupling between the two modes [9, 10, 15], provided that E_1 and E_2 are nearly resonant, what is further discussed in Supplementary Material, section III. In a regime of high coherent coupling between the two resonances and a weak dissipation of the third mode all eigenstates repel, as it is typically observed in exciton-polariton systems [27–31].

We schematically visualise the model and the involved oscillators in Fig. 3(a). In our structure, two coupled resonances are the photonic mode C and the $X_{X,Y}$ exciton, with energies and decay rates of E_c, $E_{x(X_{X,Y})}$ and γ_c, γ_x respectively. The lower-energy X_Z excitonic resonance acts as a dissipative mode and is characterized by the energy of $E_{x(X_Z)}$ and dissipation γ_0. The coupling between photons and $X_{X,Y}$ excitons inside the microcavity (V) is expected to be weak, due to the space- and momentum-indirect nature of the excitonic resonance. On the contrary, X_Z-exciton is expected to couple to light more efficiently, as the spatial symmetry breaking allows for its recombination without the assistance of phonons, due to the weakening of the momentum-conservation rules, re-

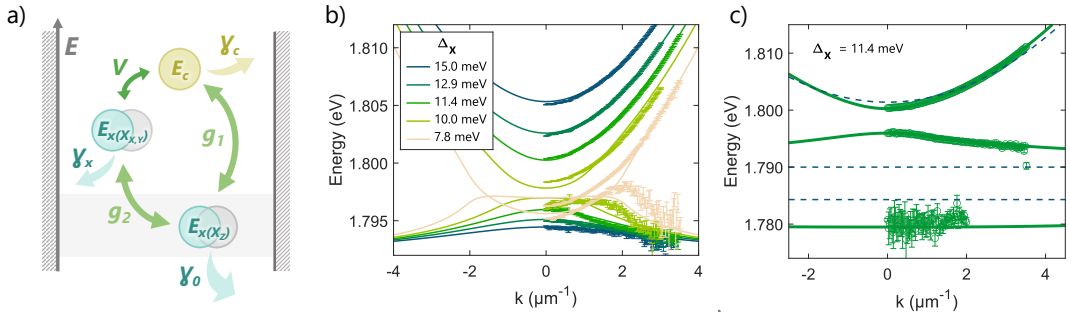

Figure 3. Level attraction modelling. (a) Schematic visualisation of the three coupled oscillators model and its application in our system. The coupled particles (photon (E_c, presented as a single circle) and two indirect excitons ($E_{x(X_{X,Y})}$ and $E_{x(X_Z)}$), represented as double circles) – are shown on a schematic energy scale, with their intrinsic decays sketched as broad arrows, while the couplings are presented as two-sided arrows. (b) Comparison of the model lines with experimental level branches at several exciton-photon detunings, plotted in corresponding colors. Model parameters are described in the main text. (c) Example dispersion at a single photon-$X_{X,Y}$-exciton detuning of 11.4 meV. Dashed lines mark the dispersions of a bare photonic mode and two indirect excitons, open points are the fitted peak positions of the three polaritonic branches, and solid green lines are the model dispersions. For clarity, the experimental data is only presented for positive k.

gardless of its indirect nature [24, 32, 33]. The coupling between the two indirect excitons is enabled via transfer of electrons between the states and transitions from the higher $X_{X,Y}$ to the lower X_Z electronic state, as evidenced by complex temporal dynamics [24] and previous studies [34–37]. Both couplings g_1 and g_2 are therefore expected to play a significant role in the system, with the g_1 value expected to be much larger than V. The energies of both excitonic resonances can be directly inferred from the photoluminescence measurements of the bare QW structure (see Fig. 1(e) and [24]).

Using this approach, we modelled our experimental dispersions, as presented in Fig. 3(b). Experimental points are the extracted peak energies of the two polaritonic branches at several exciton-photon detunings Δ_X, and solid lines show the fitted model eigenstates. Additionally, in Fig. 3(c) we show all three of the model eigenstates at the exciton-photon detuning of 11.4 meV, as well as the dispersions of a bare photonic mode and two indirect excitons (dashed lines). We note that in most measurements, the lowest-energy mode cannot be seen in the photoluminescence spectra, except near the $\Delta_X \approx 11$ meV detuning, hence we used only two states in the dispersion modelling.

Model results show very good correspondence with the measured dispersions. The model reflects well the anomalous shape of the lower branch dispersion and captures a clear transition between its monotonic (with a single maximum at $k = 0$) and non-monotonic (with maxima at finite wavevectors) $|k|$-dependence when decreasing Δ_X. At larger detunings the model dispersions match experimental points nearly perfectly, demonstrating the change in curvature around $k = 0$, linked to the dissipative level attraction. Discrepancies between the model and the experimental curves become visible only at smaller positive exciton-photon detunings ($\Delta_X \leq 10$ meV). This may arise from the fact, that to model our data we set all the parameters constant throughout this detuning range (apart from the photonic mode energy), which is a simplified approach. All three decay constants, as well as level energies, can vary across the sample, due to the local disorder and the layer width change. Nevertheless, the model describes our system very well in a large range of exciton-photon detunings, even when using only one set of parameters. Moreover, a high agreement between the model line and the third state detectable at the detuning $\Delta_X = 11.4$ meV presented in Fig. 3(c), despite not using this state in the fitting, further proves the applicability of our model.

The extracted exciton-photon couplings are $V = 0.1$ meV and $g_1 = 10.6$ meV, while the coupling between two X-excitons g_2 is 17 meV. As expected, the coherent coupling between the photonic mode and the spatially and momentum indirect $X_{X,Y}$ exciton is much smaller than other energies in our system. The highly dissipative X_Z state couples to light more efficiently, what is likely a result of the symmetry breaking effect described above. The most influential interaction comes from the nonradiative coupling between the two X-excitons. The extracted decay rates of all states are $\gamma_c = 0.1$ meV, $\gamma_x = 0.01$ meV and $\gamma_0 = 41$ meV. The model photon linewidth value corresponds to a lifetime of approximately ~ 6 ps, which is a value expected for this microcavity, subject to disorder and operating at large detuning from the designed wavelength [38]. A small line broadening of the $X_{X,Y}$ state originates from its longer lifetime, expected from its indirect nature. On the other hand, large broadening γ_0 of the X_Z exciton points to its dissipative role and it is crucial to obtain level attraction in our system. We note that the model value is larger

than the measured photoluminescence linewidth broadening of this state of $\sim 20\ meV$, measured with the top mirror removed from the cavity [24]. However, the observed emission linewidth cannot be directly translated into the homogeneous broadening. Photoluminescence broadening consists of both homogeneous and inhomogeneous parts, but, at the same time, can be narrowed by a Purcell effect, resulting from a formation of very low-Q-factor half-microcavity [27]. Large damping of this mode likely comes from the sensitivity of these states to structure inhomogeneities, stemming from their ground state nature, and affecting their lifetime and transport properties, as discussed in detail in [24] and shown before [39]. Overall, the model accurately describes our system and reveals the highly damped X_Z excitons as the source of the level attraction and the inverted polariton dispersion. The importance of the damped mode inclusion is presented in section IV of the Supplementary Material.

In addition, we considered the contribution of the three involved oscillators in the final system eigenvalues, by studying the Hopfield coefficients [40, 41]. Coefficient wavevector dependencies reflect the anomalous behaviour of the inverted anomalous branch, with the dissipative exciton fraction gaining importance in the anomalous region (at small wavevectors), particularly at small detunings. It further highlights the importance of the X_Z excitons in the observed effect. Hopfield dispersions at several detunings, as well as their more detailed discussion, can be found in section V of the Supplementary Material.

DISCUSSION

In summary, we have observed the anomalous dispersion of the polaritonic branch in an AlGaAs-based microcavity, characterized by the negative effective mass. Our AlGaAs-based semiconductor system offers precise high-quality growth and design of the layers, fine-tuning its properties, what will uniquely allow to tailor the coherent coupling and the optical Q-factor as well as the dissipation, by engineering the $X_{X,Y}$ and X_Z excitons. We have shown how the presence of and the coupling to the indirect excitonic state energetically below the excitonic and photonic resonances, which acts as a channel of loss, can manifest itself as a dissipative coupling between these states. Our hypothesis is supported by a phenomenological model of three coupled oscillators. The high dissipation rate of this indirect state is crucial to make the effective coupling non-Hermitian and overcome the coherent coupling. Furthermore, we have observed the evolution of the system eigenstates with varying detuning, showing the shift and the change of the eigenstate dispersion curvature. We show two regimes of anomalous dispersion shape, with eigenstate energy maxima at $k = 0$ and $k \neq 0$ in a single sample.

Previously, the anomalous dispersion of exciton polaritons in unstructured samples has been observed solely in transition metal dichalcogenide-based samples [8, 9, 26]. The supporting models were applicable only for many-particle excitons in heavily-doped samples with complex interactions [8], or for media with a strong influence of exciton-phonon interactions [9]. In our case of a III-V semiconductor-based system at cryogenic temperature, phonon influence is known to be much smaller, hence insufficient to lead to the dissipative coupling. Previously studied systems lacked the presence of a tunable and energetically-lower state providing a channel of loss, which proves to be crucial in our structure. Even more importantly, they also lacked the excellent linewidths, making the dispersion shape less distinct and rendering interpretations of the observed dispersions less robust.

Here, we present the effect of level attraction in a new experimental platform, with a new source of the dissipative coupling in the exciton-polariton context. Apart from narrow linewidths, our system provides a great opportunity for level attraction tuning, via changing the detuning between the resonances, owing to the sample's wedged growth. So far, the effective mass engineering had to involve additional sample processing steps (such as patterning or etching) or complicated excitation schemes, e.g. structured beams, which prove to be costly, imperfect, and often difficult to implement. In our case the mass can be engineered during the typical sample growth, with no further steps required. The change of the eigenstate dispersion curvature can be easily accessed by simply changing the position on the sample, allowing access to different anomalous dispersion curvatures in a single platform. Such a straightforward tuning was lacking in previous observations, and shows a clear path for future studies or device design.

Anomalous dispersion can be employed in novel studies of non-Hermitian effects [16, 17, 42], nontrivial dynamics and hydrodynamics [1, 43] and in studies of analogue systems [44–46]. It allows access to a plethora of studies on the exceptional points and related phenomena, such as winding of the complex eigenenergies, chiral modes, topological lasing, or enhanced perturbation, among others [18, 47–49]. The optical, easily experimentally-accessible platform of high quality and high adjustability presented in this work makes our finding relevant and desirable far beyond the exciton-polariton context. The observation can be considered to be an important contribution to the broad field of dissipative coupling effects, with losses and dissipation affecting practically all physical systems.

METHODS

Sample

The sample under study consists of twelve 9 nm-wide $Al_{0.20}Ga_{0.80}As$ QWs, separated by 4 nm AlAs barriers, distributed in three stacks of four (as visualized in Fig. 1(d)). The stacks are placed in a $\lambda/2$-AlAs cavity surrounded by $AlAs/Al_{0.40}Ga_{0.60}As$ distributed Bragg reflectors (DBRs), consisting of 28/24 mirror pairs in the

bottom/top reflector, including 3 nm GaAs smoothing layers after each mirror pair in the local minimum of the electromagnetic field. The whole microcavity structure was grown by molecular beam epitaxy on the GaAs substrate. Lack of wafer rotation during growth results in a gradual change of the cavity length across the sample, allowing for the experimental access to a wide range of exciton-photon detunings. The photoluminescence spectrum of the bare quantum well system presented in Fig. 1(e) was taken on a sample with the top Bragg reflector etched away [24].

Optical Measurements

The sample was placed in the continuous flow liquid helium cryostat and cooled down to 4.2 K. It was excited by laser pulses from the OPO pumped by a Ti:Sapphire pulsed laser with 76 MHz repetition rate, generating the wavelength of around 620 nm. The beam was focused on a sample via a NA = 0.65 objective. Structure photoluminescence was then collected by the same objective and imaged on a slit of a monochromator (with a 1200 lines/cm groove density diffraction grating) equipped with a high-efficiency EMCCD camera. Imaging the Fourier plane by using four confocal lenses in the detection path allowed for the angle-resolved measurements.

Dispersion extraction

Photoluminescence spectra at each wavevector were fitted with a sum of a Lorentzian (lower central energy) and Gaussian (higher energy) curves. The extracted peak energies were used for further modelling. The error bars presented throughout the manuscript come from the fitting standard error. An exemplary fit with the more detailed discussion on the fitting function selection can be found in the Supplementary Material, section II.

DATA AVAILABILITY

The datasets generated during and/or analysed during the current study are available from the corresponding author on reasonable request.

[1] D. Colas, F. P. Laussy, and M. J. Davis, Physical Review Letters **121**, 055302 (2018), arXiv:1801.04779.

[2] C. Schneider, K. Winkler, M. D. Fraser, M. Kamp, Y. Yamamoto, E. A. Ostrovskaya, and S. Höfling, Reports on Progress in Physics **80**, 016503 (2016).

[3] D. Tanese, H. Flayac, D. Solnyshkov, A. Amo, A. Lemaître, E. Galopin, R. Braive, P. Senellart, I. Sagnes, G. Malpuech, and J. Bloch, Nature Communications **4**, 1749 (2013).

[4] C. E. Whittaker, E. Cancellieri, P. M. Walker, D. R. Gulevich, H. Schomerus, D. Vaitiekus, B. Royall, D. M. Whittaker, E. Clarke, I. V. Iorsh, I. A. Shelykh, M. S. Skolnick, and D. N. Krizhanovskii, Phys. Rev. Lett. **120**, 097401 (2018).

[5] A. Gianfrate, H. Sigurðsson, V. Ardizzone, H. C. Nguyen, F. Riminucci, M. Efthymiou-Tsironi, K. W. Baldwin, L. N. Pfeiffer, D. Trypogeorgos, M. De Giorgi, D. Ballarini, H. S. Nguyen, and D. Sanvitto, Nature Physics **20**, 61–67 (2024).

[6] M. Harder, B. M. Yao, Y. S. Gui, and C.-M. Hu, Journal of Applied Physics **129**, 201101 (2021).

[7] T. Tawara, H. Kamada, T. Tanabe, T. Sogawa, H. Okamoto, P. Yao, P. K. Pathak, and S. Hughes, Opt. Express **18**, 2719 (2010).

[8] S. Dhara, C. Chakraborty, K. M. Goodfellow, L. Qiu, T. A. O'Loughlin, G. W. Wicks, S. Bhattacharjee, and A. N. Vamivakas, Nature Physics **14**, 130 (2018).

[9] M. Wurdack, T. Yun, M. Katzer, A. G. Truscott, A. Knorr, M. Selig, E. A. Ostrovskaya, and E. Estrecho, Nature Communications **14**, 1026 (2023).

[10] M. Harder, Y. Yang, B. M. Yao, C. H. Yu, J. W. Rao, Y. S. Gui, R. L. Stamps, and C.-M. Hu, Phys. Rev. Lett. **121**, 137203 (2018).

[11] Y.-P. Wang and C.-M. Hu, Journal of Applied Physics **127**, 130901 (2020).

[12] V. L. Grigoryan, K. Shen, and K. Xia, Phys. Rev. B **98**, 024406 (2018).

[13] Q. Lu, J. Guo, Y.-L. Zhang, Z. Fu, L. Chen, Y. Xiang, and S. Xie, ACS Photonics **10**, 699–706 (2023).

[14] F. Elste, S. M. Girvin, and A. A. Clerk, Phys. Rev. Lett. **102**, 207209 (2009).

[15] W. Yu, J. Wang, H. Y. Yuan, and J. Xiao, Phys. Rev. Lett. **123**, 227201 (2019).

[16] M. Parto, Y. G. N. Liu, B. Bahari, M. Khajavikhan, and D. N. Christodoulides, Nanophotonics **10**, 403 (2021).

[17] T. Gao, E. Estrecho, K. Y. Bliokh, T. C. H. Liew, M. D. Fraser, S. Brodbeck, M. Kamp, C. Schneider, S. Höfling, Y. Yamamoto, F. Nori, Y. S. Kivshar, A. G. Truscott, R. G. Dall, and E. A. Ostrovskaya, Nature **526**, 554 (2015).

[18] T. Long, X. Ma, J. Ren, F. Li, Q. Liao, S. Schumacher, G. Malpuech, D. Solnyshkov, and H. Fu, Advanced Science **9**, 2203588 (2022).

[19] D. Ballarini, D. Caputo, C. S. Muñoz, M. De Giorgi, L. Dominici, M. H. Szymańska, K. West, L. N. Pfeiffer, G. Gigli, F. P. Laussy, and D. Sanvitto, Phys. Rev. Lett. **118**, 215301 (2017).

[20] E. Persson, I. Rotter, H.-J. Stöckmann, and M. Barth, Phys. Rev. Lett. **85**, 2478 (2000).

[21] O. Bleu, K. Choo, J. Levinsen, and M. M. Parish, Phys. Rev. A **109**, 023707 (2024).

[22] H. Suchomel, S. Kreutzer, M. Jörg, S. Brodbeck, M. Pieczarka, S. Betzold, C. P. Dietrich, G. Sęk, C. Schneider, and S. Höfling, Opt. Express **25**, 24816

(2017).
[23] N. Chand, T. Henderson, J. Klem, W. T. Masselink, R. Fischer, Y.-C. Chang, and H. Morkoč, Physical Review B **30**, 4481 (1984).
[24] D. Biegańska, M. Pieczarka, K. Ryczko, M. Kubisa, S. Klembt, S. Höfling, C. Schneider, and M. Syperek, Optical properties and dynamics of direct and spatially and momentum indirect excitons in algaas/alas quantum wells (2024), arXiv:2404.01938 [cond-mat.mes-hall].
[25] D. Colas and F. P. Laussy, Phys. Rev. Lett. **116**, 026401 (2016).
[26] E. Y. Paik, L. Zhang, S. Hou, H. Zhao, Y. Chou, S. R. Forrest, and H. Deng, Advanced Optical Materials **11**, 2201440 (2023).
[27] A. V. Kavokin, J. Baumberg, G. Malpuech, and F. Laussy, *Microcavities*, 1st ed. (Oxford University Press, Oxford, 2008).
[28] M. Wurdack, N. Lundt, M. Klaas, V. Baumann, A. V. Kavokin, S. Höfling, and C. Schneider, Nature Communications **8**, 259 (2017).
[29] O. Koksal, M. Jung, C. Manolatou, A. N. Vamivakas, G. Shvets, and F. Rana, Phys. Rev. Res. **3**, 033064 (2021).
[30] Y. V. Zhumagulov, S. Chiavazzo, D. R. Gulevich, V. Perebeinos, I. A. Shelykh, and O. Kyriienko, npj Computational Materials **8**, 92 (2022).
[31] M. Höfner, S. Sadofev, B. Kobin, S. Hecht, and F. Henneberger, Applied Physics Letters **107**, 181109 (2015).
[32] B. Pietka, *Excitonic Complexes in Natural Quantum Dots Formed in Type II GaAs / AlAs*, Ph.D. thesis, Université Joseph-Fourier - Grenoble I (2007).
[33] G. Danan, B. Etienne, F. Mollot, R. Planel, A. M. Jean-Louis, F. Alexandre, B. Jusserand, G. Le Roux, J. Y. Marzin, H. Savary, and B. Sermage, Physical Review B **35**, 6207 (1987).
[34] J. Feldmann, M. Preis, E. Göbel, P. Dawson, C. Foxon, and I. Galbraith, Solid State Communications **83**, 245 (1992).
[35] E. Finkman, M. Sturge, M.-H. Meynadier, R. Nahory, M. Tamargo, D. Hwang, and C. Chang, Journal of Luminescence **39**, 57 (1987).
[36] A. Wysmołek, B. Chwalisz, M. Potemski, R. Stępniewski, A. Babiński, S. Raymond, and V. Thierry-Mieg, Acta Physica Polonica A **106**, 367 (2004).
[37] G. Peter, E. Göbel, W. Rühle, J. Nagle, and K. Ploog, Superlattices and Microstructures **5**, 197 (1989).
[38] G. Panzarini, L. C. Andreani, A. Armitage, D. Baxter, M. S. Skolnick, V. N. Astratov, J. S. Roberts, A. V. Kavokin, M. R. Vladimirova, and M. A. Kaliteevski, Physics of the Solid State **41**, 1223 (1999).
[39] S. T. Lee, J. Haetty, A. Petrou, P. Hawrylak, M. Dutta, J. Pamulapati, P. G. Newman, and M. Taysing-Lara, Phys. Rev. B **53**, 12912 (1996).
[40] M. I. Vasilevskiy, D. G. Santiago-Pérez, C. Trallero-Giner, N. M. R. Peres, and A. Kavokin, Phys. Rev. B **92**, 245435 (2015).
[41] J. J. Hopfield, Phys. Rev. **112**, 1555 (1958).
[42] L. Feng, R. El-Ganainy, and L. Ge, Nature Photonics **11**, 752 (2017).
[43] M. A. Khamehchi, K. Hossain, M. E. Mossman, Y. Zhang, T. Busch, M. M. Forbes, and P. Engels, Phys. Rev. Lett. **118**, 155301 (2017).
[44] L. Pickup, H. Sigurdsson, J. Ruostekoski, and P. G. Lagoudakis, Nature Communications **11**, 4431 (2020).
[45] M. J. Jacquet, T. Boulier, F. Claude, A. Maître, E. Cancellieri, C. Adrados, A. Amo, S. Pigeon, Q. Glorieux, A. Bramati, and E. Giacobino, Philosophical Transactions of the Royal Society A: Mathematical, Physical and Engineering Sciences **378**, 20190225 (2020).
[46] P. St-Jean, A. Dauphin, P. Massignan, B. Real, O. Jamadi, M. Milicevic, A. Lemaître, A. Harouri, L. Le Gratiet, I. Sagnes, S. Ravets, J. Bloch, and A. Amo, Phys. Rev. Lett. **126**, 127403 (2021).
[47] R. Su, E. Estrecho, D. Biegańska, Y. Huang, M. Wurdack, M. Pieczarka, A. G. Truscott, T. C. H. Liew, E. A. Ostrovskaya, and Q. Xiong, Science Advances **7**, eabj8905 (2021).
[48] F. Baboux, D. D. Bernardis, V. Goblot, V. N. Gladilin, C. Gomez, E. Galopin, L. L. Gratiet, A. Lemaître, I. Sagnes, I. Carusotto, M. Wouters, A. Amo, and J. Bloch, Optica **5**, 1163 (2018).
[49] V. Ardizzone, F. Riminucci, S. Zanotti, A. Gianfrate, M. Efthymiou-Tsironi, D. G. Suàrez-Forero, F. Todisco, M. De Giorgi, D. Trypogeorgos, G. Gigli, K. Baldwin, L. Pfeiffer, D. Ballarini, H. S. Nguyen, D. Gerace, and D. Sanvitto, Nature **605**, 447 (2022).

ACKNOWLEDGEMENTS

D. B., M.P. and M. S. acknowledge financial support from the National Science Centre Poland within the Grant No. 2018/30/E/ST7/00648. C.S. and S.K. gratefully acknowledge funding by the German Research Association (DFG) within the project SCHN1376 13.1 and KL 3124/3-1 (El Pollo Loco). S.H. and S.K. acknowledge financial support by the DFG under Germany's Excellence Strategy - EXC2147 ct.qmat (Project No. 390 858 490). S.H. acknowledges financial support by the DFG project HO 5194/12-1.

AUTHOR CONTRIBUTIONS STATEMENT

D. B. conducted all the spectroscopic experiments and analysed the experimental data. D.B. and M.P. performed theoretical modeling of the results. S. K., S. H, and C. S provided the sample. D.B., M.P., M.S. analyzed the results and all authors contributed to their discussion. D.B. wrote the first version of the manuscript and prepared all figures. All authors reviewed the manuscript to its final form.

ADDITIONAL INFORMATION

The authors declare no competing interests. Supplementary Information is available for this paper.

Supplementary material

SUPPLEMENTAL MATERIAL
Anomalous dispersion via dissipative coupling in a quantum well exciton-polariton microcavity

D. Biegańska,[1,*] M. Pieczarka,[1] C. Schneider,[2] S. Höfling,[3] S. Klembt,[3] and M. Syperek[1]

[1] *Department of Experimental Physics, Faculty of Fundamental Problems of Technology, Wrocław University of Science and Technology, Wybrzeże Wyspiańskiego 27, 50-370 Wrocław, Poland*
[2] *Carl von Ossietzky Universität Oldenburg, Fakultät V, Institut für Physik, 26129 Oldenburg, Germany*
[3] *Julius-Maximilians-Universität Würzburg, Physikalisches Institut and Würzburg-Dresden Cluster of Excellence ct.qmat, Lehrstuhl für Technische Physik, Am Hubland, 97074 Würzburg, Germany*

I. PHOTOLUMINESCENCE MEASUREMENTS AT DIFFERENT DETUNINGS

Owing to a stopped rotation of the wafer during an active layer growth, resulting in a gradual change of the cavity length across the sample, we were able to access a very large range of exciton-photon detunings. We measured

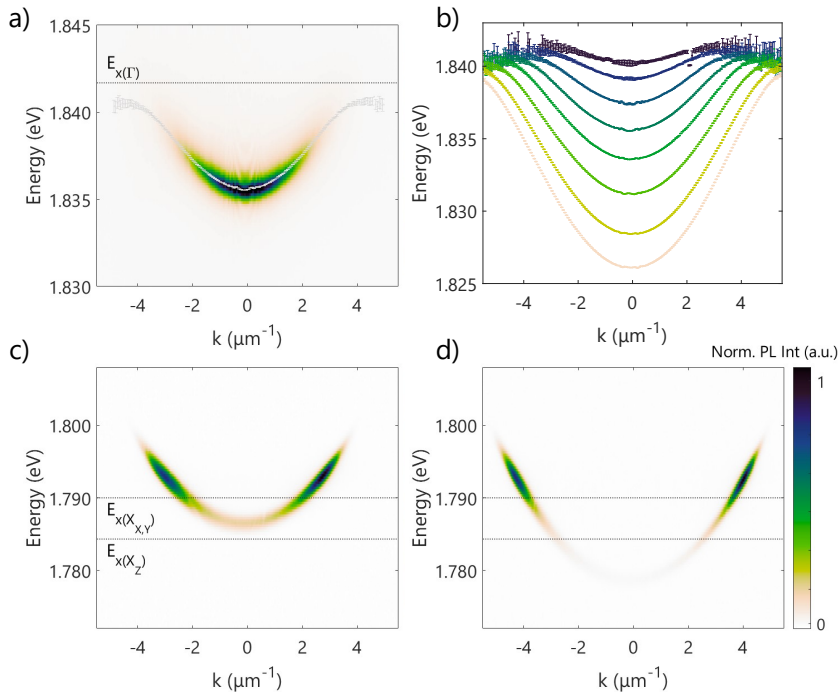

Supplementary Figure 1. (a) Momentum-resolved photoluminescence spectra in the strong coupling regime with the Γ-electron exciton, which energy is marked by a dashed line. Points mark the energy of the lower polariton branch, extracted by Lorentzian-curve fitting at each wavevector. (b) Dispersions of the lower polariton branch in the strong coupling regime in Δ_Γ (Γ-electron-exciton to photon) detuning range of around 11 (upmost curve) to −18 *meV* (lowest curve). (c), (d) Examples of photoluminescence spectra with photon energy below the $X_{X,Y}$- (c) and below both $X_{X,Y}$- and X_Z-electron-excitons (d).

* dabrowka.bieganska@pwr.edu.pl

momentum-resolved photoluminescence spectra with the photonic mode scanning the energies of the whole cavity stopband.

As described in the main manuscript, when the photonic mode is sufficiently close to the direct Γ-electron exciton energy of 1.8472 eV, one can observe the result strong coupling. Supplementary Figure 1(a) shows an example of far-field photoluminescence in this region, with the extracted energies of the lower polariton branch plotted as points. Additionally, lower polariton dispersions at several exciton-photon detunings ($\Delta_\Gamma = -18 \rightarrow 11\ meV$) are presented in Supplementary Figure 1(b). One can see a clear change in the branch curvature, typical for the strong coupling regime in exciton-polariton studies. The extracted vacuum Rabi splitting at 4.2 K is $\hbar\Omega_\Gamma \approx 12\ meV$.

When the energy of the photonic mode is lower, and gets closer to the indirect $X_{X,Y}$-exciton, we observe anomalous dispersion of one of the eigenstates, as described in the main manuscript and presented there in Figure 2. However, in the negative detuning range in this region, $\Delta_X < 0$, when the photon energy is lower than that of the $X_{X,Y}$-exciton, only one parabolic branch appears in the photoluminescence spectra. Two examples of such measurements are presented in Supplementary Figure 1(c) and (d). In the whole figure dotted lines mark the energies of three excitons present in the sample.

II. PHOTOLUMINESCENCE FITTING AND DISPERSION EXTRACTION

To extract the energy dispersions of the three branches investigated in the main text, we fitted the photoluminescence spectra at each wavevector with a sum of a Lorentzian (lower central energy) and a Gaussian (higher energy) curves. An example of such a fitting is presented in the main manuscript in Figure 2(b). Additionally, two of the curves presented there are also shown in Supplementary Figure 2, together with the individual fitted profiles.

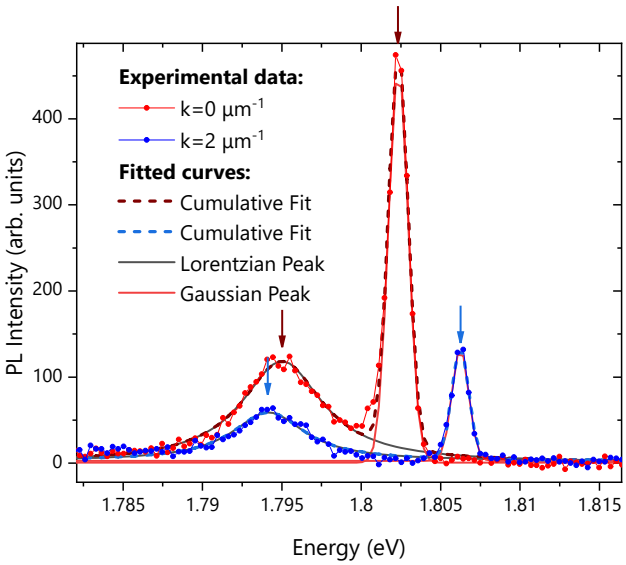

Supplementary Figure 2. Measured photoluminescence spectra taken at wavevectors $k = 0\ \mu m^{-1}$ and $2\ \mu m^{-1}$, at a detuning $\Delta_X = 11.4\ meV$, together with the fitted curves. Solid grey and red lines show the individual peaks of the convolution, while the dashed curves correspond to the final fitted model. Arrows indicate the peak central energies, extracted from the fitting, of the two peaks (shown also as red dots in Figure 2(b) of the main manuscript and used for further modelling).

The choice of band profiles was carefully selected to obtain the highest agreement with the experimental data, while also minimizing the number of free fitting parameters. Voigt profiles are known to describe both the homogeneous and the inhomogeneous broadening of the experimental state lines, but their implementation adds significantly to the complexity of the fit. At selected wavevectors the double Voigt profile fitting was performed, giving peak energy results analogous to the Gaussian and Lorentzian sum fitting. However, the experimental data matching was poorer with the Voigt curves, visualized in lower goodness-of-fit metrics. At some momenta Voigt fit convergence was not achieved, due to the larger number of free fitting parameters in comparison to the Lorentzian and Gaussian curves. It is

expected, that when the line shape is mostly Gaussian or Lorentzian and one of the broadenings is significantly higher than the other one, the Voigt model is over-parameterized and the convergence is not achieved. To better describe the experimental data and use consistent analysis for all wavevectors and all detunings, we choose the Gaussian and Lorentzian sum (with the fitted peak energy values used throughout the main manuscript).

The error bars presented throughout the manuscript come from the fitting standard error and the eigenstates energies come solely from the fitting procedure.

III. MODEL TRANSFORMATION

In ref. [1] with the presentation of the three-mode quantum model, authors show how the 3×3 matrix can be transformed by performing a unitary transformation to block-diagonalize the three-mode system into the two-mode and one-mode subsystems, effectively decoupling the third mode. When the coupling with the mode 0 (the strongly dissipative mode) is weak, such a transformation can be realized in the perturbation method using the Schrieffer-Wolff transformation. The decoupling of the third dissipative mode effectively renormalizes the coupling between modes 1 and 2 and modifies their eigenfrequencies with the additional dissipation (contributing as imaginary parts and guaranteeing the non-negativeness of the dissipation of the model). The authors show how such simplification is valid when $V \ll g_1,\ g_2$, but the coupling to the third state is sufficiently weak (so that the condition for the generator, perturbative and non-perturbative parts of the Hamiltonian is met, see Supplementary Material of ref. [1]). When $V = 0$, effective coupling between the two oscillators g_{12} becomes imaginary when $|E_{1,2} - E_0| \ll |\gamma_{1,2} - \gamma_0|$ and this is realized when mode 0 has large dissipation (γ_0). Hence, to observe attraction, γ_0 should be large such that $|\gamma_{1,2} - \gamma_0|$ is dominated by γ_0, but not so large such that the coupling strength g_{12} is still sizable. Overall it shows a huge importance of the relative ratios of the mode broadenings and their energy differences, on top of the coupling values.

In our case, due to the high importance of the third resonance (the X_Z exciton), and its sizable coupling to both the photon and the exciton, such a perturbative approximation cannot be made. The 2×2 matrix with the effective imaginary coupling ($g_{12} = V + \frac{1}{2} g_1 g_2 \sum_{i=1,2} \frac{1}{E_i - E_0}$) is not sufficient to describe our system, as the coupling values are sizeable when compared to other energy scales in our system. To visualize it, in Supplementary Figure 3 we present the solution of the transformed 2×2 matrix model (with effective imaginary coupling g_{12}), using the same parameters as extracted from the 3×3 model fitting (see main text). We compare it to the full 3×3 matrix solution, presented with dashed lines. The simplified model (solid) lines clearly deviate from the unsimplified approach (dashed curves) which fits best to our experimental data.

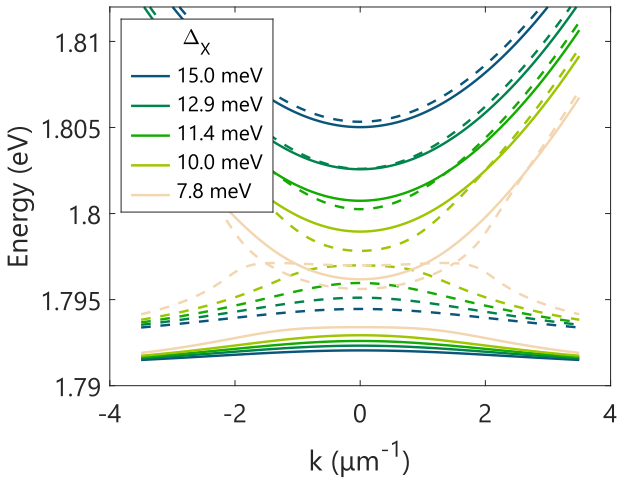

Supplementary Figure 3. Comparison of the 3×3 model solution (dashed lines) with the eigenstates of the model simplified into a 2×2 matrix, by using a Schrieffer-Wolff transformation (described in detail in ref. [1] Supplementary Material, solid lines). All parameters can be found in the main manuscript.

However, even though such a transformation cannot be made in our case, it visualizes the nature of the effect.

Anomalous dispersion and band attraction has been previously described by imaginary coupling between two oscillators (see e.g. [2, 3]). In [1] the authors show, how in a real physical system the dissipative coupling can be realized by coupling both oscillators reactively to a third highly dissipative entity. The third-party mode can even be an invisible mode (in our case we identified it as the X_Z-exciton), with high leakage or dissipation. Its effect on the other two resonances is analogous to the imaginary coupling between them - even if the exact transformation into a 2×2 system cannot be made in our case.

IV. NON-HERMITICITY AND COUPLING IMPORTANCE

To further visualize the importance of the dissipation of all three modes in the observed attraction effect, in Supplementary Figure 4 we show the solution of the model with varying decay and coupling conditions. Panel (b) shows model curves with no dissipation of the X_Z exciton (the dissipative mode), followed by the model solution with no dissipation of all three resonances (fully real model) in (c). The curves are compared to the model fitted to the

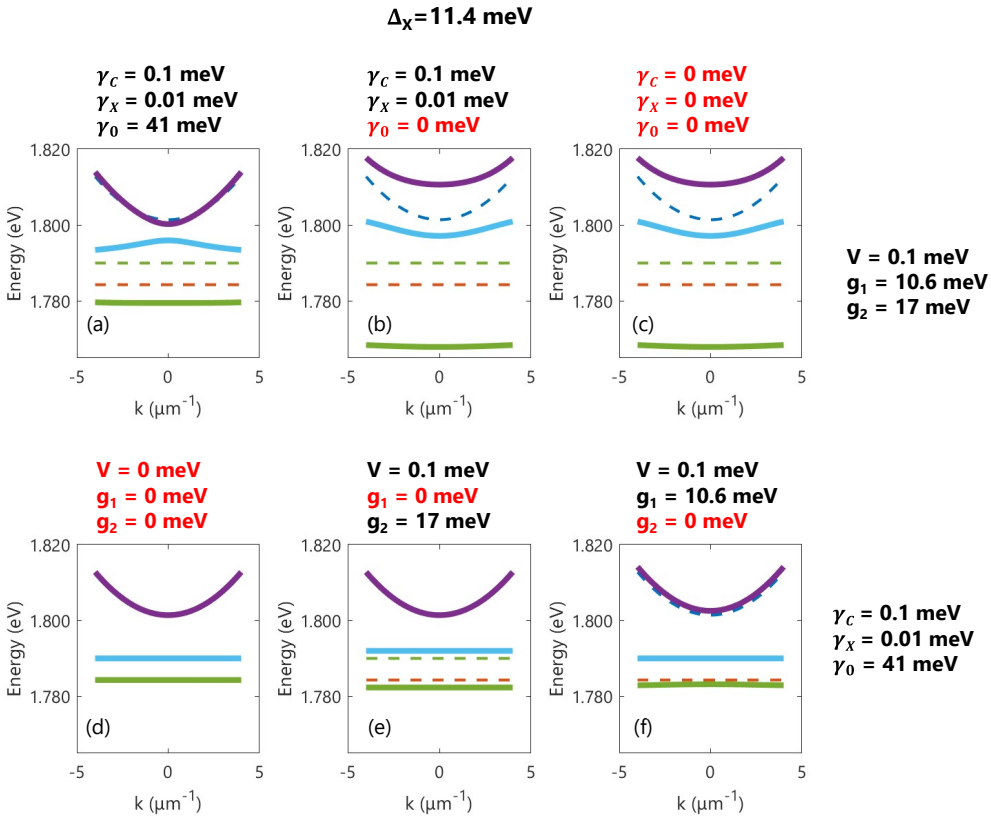

Supplementary Figure 4. Solution of the model with varying decay and coupling conditions, showing the importance of the dissipation and coupling. Solid lines show the dispersions of three eigenmodes, while dashed lines present the initial resonances. Parameters different from the fitted model values (the ones extracted from the experimental data) are marked in red. All curves were calculated at the same detuning between the $X_{X,Y}$ exciton and the photonic mode of 11.4 meV. (a) Model with the fitted parameter values. (b) Model with no dissipation of the lowest energy mode (XZ), $\gamma 0 = 0$. (c) Model with no dissipation of all involved oscillators (fully real model). (d) Model with no coupling between the involved oscillators (fully decoupled modes). (e) Model with no coupling between the X_Z exciton and photon, $g1 = 0$. (f) Model with no coupling between the X_Z and XZ excitons, $g2 = 0$.

experimental data in (a). All three coupling constants V, g_1 and g_2 in (a-c) were fixed, with values extracted from the fitting to the experimental data. One can clearly see, how the non-hermiticity of the system is crucial in the effect observation, with the largest impact of the huge decay of the dissipative mode. Without its contribution, the level attraction cannot be observed and the dispersions become trivial.

Moreover, in panels (d-f) we additionally show the comparison of the solved model with fixed decay constants γ_C, γ_X and γ_0, but varying coupling constants. In panel (d) the modes are fully decoupled, showing the most trivial case of three initial resonances. Panels (e) and (f) show how the lack of coupling between the dissipative mode and the photon (e) or the $X_{X,Y}$ exciton (f) affects the dispersion. One can clearly see how the middle energy branch (solid blue line) in both cases becomes trivial and is hugely redshifted in comparison to the observed data (see panel (a)).

V. HOPFIELD COEFFICIENTS

In addition to our model eigenvalues, we studied also the respective Hopfield coefficients, to gain insight into the contribution of the three involved oscillators in the final modes. By calculating eigenvectors and plotting respective oscillator components we study the dispersion of each contribution. The results at two different experimental detunings ($\Delta_X = 10.0\ meV$, corresponding to a single-maximum dispersion shape of the anomalous branch energy and $\Delta_X = 7.8\ meV$, corresponding to the double-maximum curve) are presented in Supplementary Figure 5.

Left panels (a,e) show the calculated energy dispersions (with three eigenstates labelled as branch 1, branch 2 and branch 3), followed by the Hopfield coefficients for each branch separately in the next columns. In our considerations it's particularly important to look at the mode contributions into the inverted, anomalous branch with the negative effective mass (branch 2, (c) and (g)). Not surprisingly, the excitonic fraction related to the $X_{X,Y}$ exciton is higher than the other two components, due to the energetic closeness between this branch and the initial resonance. However, particularly in the anomalous region around k=0, both other resonances gain importance. Increased contribution of

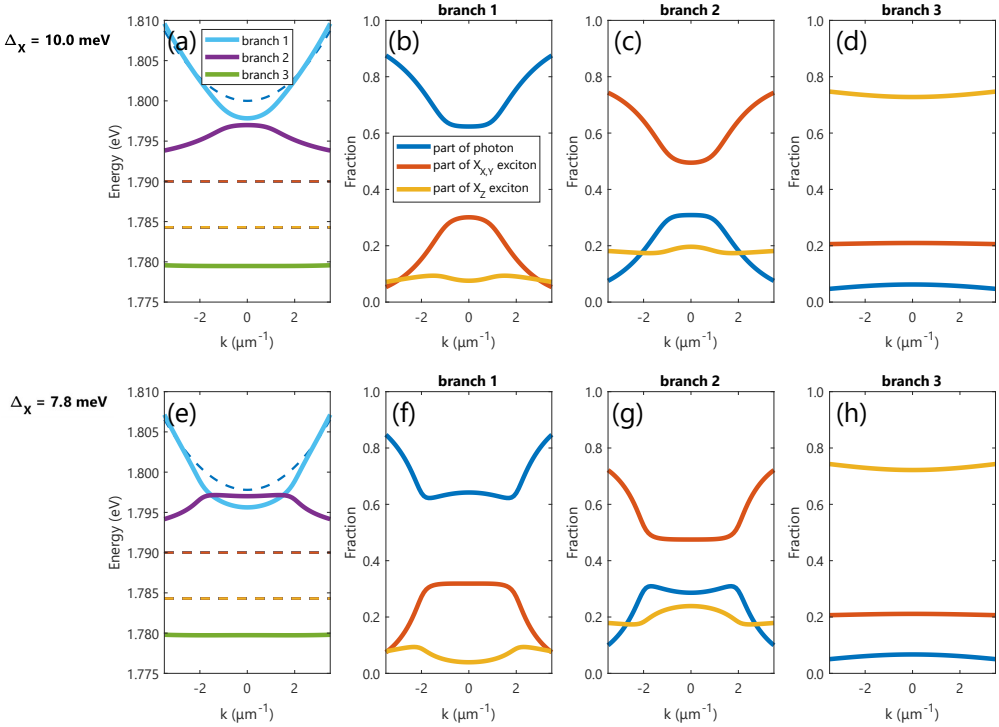

Supplementary Figure 5. Eigenstate dispersions (a,e) and the Hopfield coefficients (b-d,f-h) of each state at two exciton-photon detunings $\Delta_X = 10.0\ meV$ (a-d) and $\Delta_X = 7.8\ meV$ (e-h).

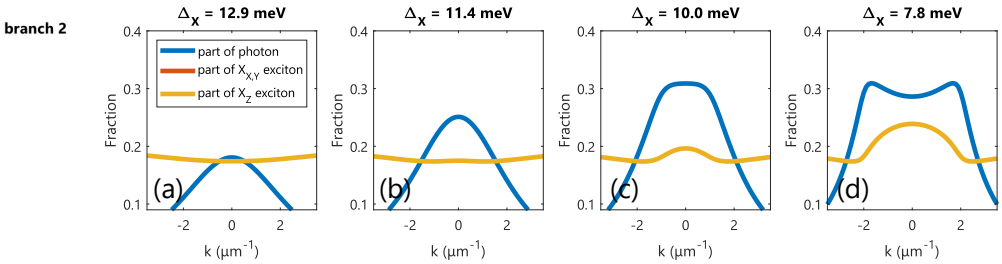

Supplementary Figure 6. Closeup of the Hopfield coefficient dispersions of branch 2 at four exciton-photon detunings. (c) and (d) are the closeup of Supplementary Figure 5 (c) and (g) respectively.

the photon fraction can be considered a typical and an expected behaviour, as it enlarges when the energy proximity of photon to this final eigenstate is higher. However, the excitonic fraction linked to the X_Z exciton (yellow curve) presents the anomalous dependence near $k = 0$, visible especially at the smaller detuning (bottom row, panels (e-h)). Its value is enhanced in the anomalous region, even though branch 2 diverts from the X_Z resonance, which is a behaviour opposite from a standard Hermitian Hamiltonian. To further visualize this effect we additionally plot the closeup of this region in Supplementary Figure 6, showing only the photonic and the X_Z-excitonic fractions of the branch 2 at four exciton-photon detunings (including the two presented in Supplementary Figure 5).

Increased contribution of the lowest-energy exciton into the anomalous branch in the crucial region, reflecting the inverted shape of the dispersion, pinpoints its interpretation as the dissipative mode. Even though our model cannot be simplified into a 2×2 matrix with imaginary coupling as described in Section III of this Supplementary Material, this increased contribution clearly justifies our approach of treating X_Z state as the dissipative mode, crucial to observe level attraction.

VI. EFFECTIVE MASS

Knowing the energy band dispersions one can calculate the particle's effective mass, which is a direct measure of band curvature. A definition of mass, in analogy to solid state systems, can be obtained with the use of a Taylor series expansion of the dispersion [2, 4]: $E(k) \approx E_0 + \frac{\hbar^2 k_0 (k-k_0)}{m_1(k_0)} + \frac{\hbar^2 (k-k_0)^2}{2m_2(k_0)} + \ldots$. The coefficients of each expansion order relate to a new mass parameter, with certain characteristic effects on the dynamics of the particle. In exciton-polariton research the ones most typically defined are:

$$m_1 = \hbar^2 k \left[\partial_k E(k)\right]^{-1} \tag{1}$$

$$m_2 = \hbar^2 \left[\partial_k^2 E(k)\right]^{-1}. \tag{2}$$

The parameter m_1 is related to the classical motion of the wave packet, and determines the group velocity $v_g = \hbar k / m_1$. The parameter m_2 determines the acceleration of the packet when an external force is applied, as well as its rate of diffusion. In case of a purely parabolic dispersion $m_1 = m_2$, but otherwise, m_1 and m_2 can have different signs, be zero, or even become infinite. In typical cases of two strongly coupled oscillators in polariton microcavity the m_1 mass of lower polaritons remains positive for all momenta (while the m_2 effective mass changes sign around the inflection points).

In our case, the m_1 parameter of the anomalous dispersion branch is negative, as it is shown in Supplementary Figure 7. There, in panels (b), (d) and (f) we present the calculated mass m_1 of the inverted branch (branch 2) as a function of the wavevector, with corresponding energy dispersions presented in (a), (c), and (e) respectively. The results are presented at three of the studied detunings Δ_X: 11.4 meV (a-b), 10.0 meV (c-d) and 7.8 meV (e-f). The masses were calculated from the fitted model curves.

One can clearly see, that the group-velocity mass of the anomalous state is negative. With larger detunings $\Delta_X = 11.4$ meV and 10.0 meV the mass $m_1 < 0$ for all momenta (Supp. Fig. 7 (a-d)). At the smaller detuning of 7.8 meV (Supp. Fig. 7 (e-f)) m_1 changes sign at a wavevector $|k^*| \approx 1.34$ μm^{-1} (indicated with the red dotted lines). The closeup of the branch 2 effective mass is also presented in panel (g).

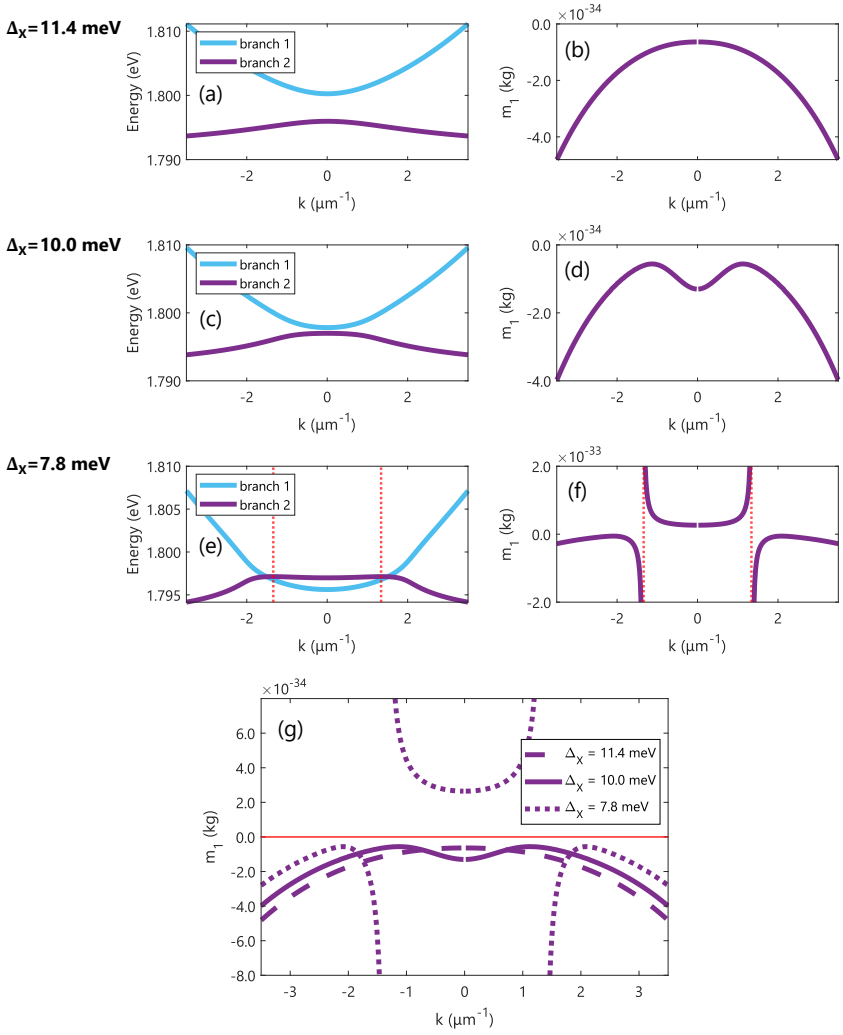

Supplementary Figure 7. Effective mass parameter m_1 wavevector dependence of the investigated anomalous branch (branch 2), at three exciton-photon detunings $\Delta_X = 11.4\ meV$ (a-b), $\Delta_X = 10.0\ meV$ (c-d) and $\Delta_X = 7.8\ meV$ (e-f). Calculated masses are presented in (b), (d) and (f), with corresponding energy dispersions shown in (a), (c) and (e). Red dashed lines in panels (e-f) show the wavevector, at which m_1 parameter of the anomalous branch changes sign. The closeup of these three m_1 wavevector dependencies comparing the three exciton-photon detunings is additionally presented in (g).

Given the relation $m_1 v_g = \hbar k$, negative mass $m_1 < 0$ means that the particle's velocity and momentum have an opposite sign. Then, the particles will move in the direction opposite to v_g, such that the particles displaced to the positive direction with respect to the excitation spot will have an average velocity towards the same direction [2, 5].

Change of sign of the m_1 parameter at the detuning of 7.8 meV (Supp. Fig. 7 (e-f)) occurs near the inversion peak in the branch dispersion, marked with red dashed lines. However we also note, that this is the detuning at which the discrepancies between the model and the experimental curves are the highest, as discussed in the main text. Regardless, it visualizes the change of the anomalous dispersion of this branch from the single maximum to

double-maxima shape and a huge potential of our system to study the exceptional points and related phenomena.

[1] W. Yu, J. Wang, H. Y. Yuan, and J. Xiao, Phys. Rev. Lett. **123**, 227201 (2019).
[2] M. Wurdack, T. Yun, M. Katzer, A. G. Truscott, A. Knorr, M. Selig, E. A. Ostrovskaya, and E. Estrecho, Nature Communications **14**, 1026 (2023).
[3] O. Bleu, K. Choo, J. Levinsen, and M. M. Parish, Physical Review A **109**, 10.1103/physreva.109.023707 (2024).
[4] D. Colas, F. P. Laussy, and M. J. Davis, Physical Review Letters **121**, 055302 (2018), arXiv:1801.04779.
[5] M. Wurdack, E. Estrecho, S. Todd, T. Yun, M. Pieczarka, S. K. Earl, J. A. Davis, C. Schneider, A. G. Truscott, and E. A. Ostrovskaya, Nature Communications **12**, 10.1038/s41467-021-25656-7 (2021).

Summary of the findings

In summary, the research study presented in this Part focused on the coupling between the indirect excitons described in Part IV and photonic modes of a full polariton microcavity. It investigated a unique effect of level attraction, resulting in an anomalous dispersion of the polaritonic state, and studied the topic of dissipative coupling in an exciton-polariton system context. This work:

- served as the first experimental observation of the anomalous dispersion in a polariton microcavity which was based on high quality semiconductor QWs. An inverted dispersion is a clear manifestation of level attraction - a rare phenomenon in an interacting system context. Prior to this work, an anomalous dispersion of a polariton state has been shown only in the transition metal dichalcogenide material-based samples in a very limited number of works, with ongoing debates about the effect's origin. This work has evidenced clearly resolved inverted energy-momentum dispersions, characterized by the negative effective mass of such state. This material system is largely superb to previously investigated dichalcogenide layers in linewidths, structure quality, reproducibility and potential use.

- showed an evolution of the anomalous state's dispersion with the exciton-photon detuning, evidencing a change from the inverted-parabola to the double-maxima energy-wavevector dependencies with decreasing detuning in a single sample. Both regimes has never been explored in a single experimental study before, and the tuning of the exciton-photon detuning of the anomalous state has not been possible.

- pinpointed the origin of the effect, showing a pivotal importance of a dissipative mode presence in the finding, which effectively made the coupling between the photonic and the excitonic states dissipative. Based on the characterization from Part IV, it recalled the presence of a lower-energy indirect state, which high dissipation rate proved to be crucial in the finding, mediating the dissipative coupling effect. The experimental data has been modelled with a three coupled oscillators model, previously regarded solely outside of the exciton-polariton

context. The modelling reflected well the anomalous shape of the lower branch dispersion and captured a clear transition between its monotonic (with a single maximum at $k = 0$) and non-monotonic (with maxima at finite wavevectors) $|k|$-dependence when decreasing detuning, fully supporting the hypothesis of the dissipative mode's key influence on the effective exciton-photon coupling. Moreover, this explanation has been further supported by showing an influence of each coupling strength in the model eigenstates, as well by the dissipative exciton fraction gaining importance in the anomalous region (especially at small detunings), when considering the Hopfield coefficients. Finally, the coupling constants between all states have been quantified with the data modelling.

- offered a relatively easy way of tuning the polariton state dispersion in an anomalous limit and paths a new way to tailor a state dispersion and engineer an effective mass in a mixed light-matter system, without the need of additional sample processing steps. This can be used in future studies of non-Hermitian effects, exceptional points, non-trivial dynamics and hydrodynamics, or in studies of analogue systems. The III-V-based semiconductor platform makes it an ideal platform for future studies and applications.

- adds an important contribution to the newly opened discussion of the dissipation effects in polariton states, as well as to much broader field of dissipative coupling and level attraction effects in open systems, presenting a new platform in which it can be studied.

Part VI

Summary and Conclusion

In this thesis I aimed to study novel properties of exciton polaritons and their condensates, in unique contexts not explored before. I investigated several of their properties - all with important implications for further research or in potential applications, as highlighted throughout this thesis.

First, in Part II, I performed the first experimental observation of the polarization splitting and the anisotropic behavior of the polariton dispersions in a high-density Thomas-Fermi regime of an optically confined condensate. With purely theoretical predictions of this effect reported in literature prior to this work, I evidenced experimentally a clear difference in the polarization-resolved excitation dispersions in different in-plane directions. The dispersion splitting was governed by the photonic TE-TM splitting, the inherent optical anisotropy and the spin-anisotropy of the polariton-polariton interactions, all of which I accounted for and modelled. I presented a rotation of the polariton spin in an interacting regime of the condensate, presenting a non-abelian gauge field with characteristic degeneracy points, around which the monopolar field texture is formed. Such a field has been shown before only in the non-interacting, low density regime of photonic states, with no evidence of the influence of polariton-polariton interaction anisotropy on the shape of the field shown so far. Moreover, I used the theoretical model to extract two interaction constants from the experimantal data - the interaction strength of polaritons in a singlet and in a triplet configuration. It was a novel approach and a demonstration of a new way of measuring both constants in a single experiment. Previously, the experimental works focused on a two strengths' ratio, or the difference between them, and the experimental schemes to achieve it were very complicated. Most works focused solely on the average value, with no spin resolution. My experiments have confirmed, that polaritons with the same spin interact with each other much more strongly than the particles with opposite spins. This new approach can be used in other material systems in the future. The diabolical points and a unique effective field texture can also be further explored in future works, both in research and in potential applications, with the interaction anisotropy adding an additional degree of freedom to previously considered low-density-regime gauge field. The measured values of the polariton-polariton interactions are of core importance in fundamental research.

Using the same methods, I contributed to the first direct measurement of a non-Hermitian topological invariant, called *spectral winding* (or *vorticity*), in a polariton system, as described in Part III. My analysis was used to experimentally show the existence of paired exceptional points in the momentum-resolved exciton-polariton single-particle spectrum, stemming from the TE-TM splitting and the anisotropy field - a field similar to the one described in the previous part, but with a key importance of the system's non-Hermiticity. This allowed for the first measurement of the non-Hermitian topological invariant, arising from the half-integer winding of the exciton-polariton complex eigenenergies around these exceptional points. The experimental methods and analysis were very similar to the ones used in Part II, but with the imaginary part of the eigenstates also taken into consideration. Again, the effective field texture was shown in the momentum space (here in a low density limit with a large effect of the structural anisotropy), and a big attention has been put to

the points around which the field winds. The result has been used to show theoretically that the topology of these eigenstates and eigenenergies is separable - meaning, that the inherent topology of these exceptional points is different from any previously observed points in the eigenstates of classical wave systems. The previously shown exceptional points in parameter space of exciton-polariton systems differ from the ones in momentum space evidenced here, as the latter are expected to have a direct influence on the system's dynamics. This can be used in further research or applications. Moreover, the measurement of the imaginary part of the artificial gauge field allowed for the conclusion, that it tends to align the exciton-polariton pseudospin pair toward each other and perpendicular to the field direction, what is of fundamental importance in basic research. It may lead to a new type of spin precession and dynamics of exciton polaritons that is not possible in real magnetic fields. In the future, this study could be combined with the interaction-dominated limit explored in the previous Part, to investigate the interplay between the quantum many-body effects and the non-Hermitian topology, unexplored in non-Hermitian physics so far.

This work differed from the other parts as it was not done in a III-V GaAs-based material system, but the methods used remained the same. The perovskite material used here was of core importance in the finding, as its structural anisotropy significantly increased the visibility of the effect, allowing for the observation.

Then, I focused on another novel setting of exciton polaritons, this time in a microcavity designed for room-temperature strong coupling. Such a design was allowed by the increased binding energy of the QW excitons, due to a near resonance of the $\Gamma-$ and X-valley band energy minimum, allowing for the $\Gamma - X$ coupling of the QW states - the implications of which were not explored in full detail in polariton microcavities before. I made an initially unexpected observation of an anomalous shape of the state dispersion and investigated the topic further to be able to fully understand it.

In order to do that, first, I had to characterize the QW system in question. In Part IV I presented the optical properties of the QWs, prior to the coupling with photonic modes. I showed three states present in the emission spectrum and the results of the power-dependent, spatially-resolved, temperature-resolved and time-resolved experiments, performed in order to pinpoint their origin and understand their dynamics. Paired with the theoretical calculations, these experiments allowed for the conclusion, that three types of excitons are present in this QW system: an expected Γ-electron exciton confined in the QW layer, but also two momentum- and spatially-indirect excitons, lower in energy, stemming from X-valley electrons in the barrier layer with different effective masses, coupled to the confined QW holes. My experiments allowed for this conclusion, but also served as a detailed characterization of all the states. The finding has important implications not only in the aforementioned unexpected effect in a full polariton microcavity, but also in other optoelectronic or photonic applications of such a system. Isolated AlGaAs/AlAs has not been widely explored in literature before (with research focusing mainly on a GaAs platform or superlattice systems) and the implications of the $\Gamma - X$ valley energy minimum crossover proximity has not been explored before in such a detail in a single similar QW structure.

Apart from the state origin, I evidenced also an important impact of non-radiative processes and state localization, governing the system's dynamics. This is of core importance in any future applications of a similar system.

Finally, the characterization made in Part IV allowed me for a detailed investigation of the full polariton microcavity, with the AlGaAs QW states coupled to the photonic modes. In Part V I evidenced experimentally the anomalous dispersion of one of the states in a polariton microcavity, for the first time in a high quality III-V semiconductor-based sample. An inverted dispersion of a polariton state has been shown before only very recently and in a very limited number of works, solely in the transition metal dichalcogenide material-based systems. The effect's origin has been debated. Here, I used the hypothesis of the dissipative mode presence and its core importance in the finding, effectively making the coupling between the photonic and the excitonic states dissipative. Such an approach has not been used in the exciton polariton context before. I pinpointed the dissipation to come from a lower-energy X-electron exciton, investigated in Part IV. I observed the anomalous dispersion in a range of exciton-photon detunings, which could be easily tuned with a position on a sample, what has not been done in any prior work in a single structure. I evidenced a change of the dispersion shape with detuning, showing both the inverted-parabola and the double-maxima energy-wavevector dependencies. Again, both regimes has not been explored in a single study before, apart from purely theoretical considerations. Finally, I used the model previously regarded solely outside of the exciton-polariton context, to support the hypothesis of the dissipative mode's key influence on the effective exciton-photon coupling. It allowed me to quantify the coupling constants between all involved states, further supporting the suggested explanation. This work offered an easy way of tuning the polariton state dispersion in an anomalous limit and paths a new way to tailor a state dispersion and engineer an effective mass in a mixed light-matter system, without the need of additional sample processing steps. It could be used in a wide range of further contexts and applications. The study adds an important contribution to the newly opened discussion of the dissipation effects in polariton states and the atypical level attraction in such systems, which starts to arise broadly. Very personally, it is a successful end of a huge quest throughout my hole Doctoral Studies, to be able to understand the unique effect I have observed unexpectedly at the beginning, what I believe I finally achieved.

All the works described in this thesis add new insights into the exciton-polariton research field and have broad implications: in this field, in applications, but also in other, analogous contexts.

Appendices

APPENDIX A

List of international research visits

International internships during the Doctoral Studies:

- Internship in the **Low Dimensional Structures and Devices** Group, Department of Physics and Astronomy, **University of Sheffield**, United Kingdom

  Date: Oct-Dec 2019,

  Topic: Topological polaritonics - investigating the exciton-polaritons in lattices of coupled zero-dimensional microresonators,

  Supervisors: Prof. Dmitry Krizhanovskii and Dr Charles Whittaker,

- Internship in the **Polariton BEC** Group at the Nonlinear Physics Centre, Research School of Physics, **The Australian National University**, Canberra, Australia

  Date: Jan-Jul 2020,

  Topics: Collective excitations of exciton-polariton condensates in a synthetic magnetic field, Anisotropy of exciton-polariton emission in perovskite structures,

  Supervisor: Prof. Elena Ostrovskaya.

- Internship in the **Advanced Photonics Lab** at the Institute of Nanotechnology **CNR-NANOTEC**, Lecce, Italy

  Date: Sept-Dec 2021,

  Topics: Exciton polaritons and their condensates in a synthetic gauge field, Universal scaling and coherence evolution of an exciton-polariton condensate after quench,

  Supervisors: Dr Dario Ballarini,

International internships prior to the Doctoral Studies:

- Internship at the Technische Physik, **Universität Würzburg**, Germany

  Date: Aug-Sept 2017,

  Topic: Preparation and spectroscopic measurement of atomically thin transition metal dichalcogenides,

  Supervisor: Dr Christian Schneider,

- Internship in the **Low Dimensional Structures and Devices** Group, Department of Physics and Astronomy, **University of Sheffield**, United Kingdom

  Date: Feb-Mar 2019,

  Topics: Nonlinear and quantum optics of hybrid light-matter states in nanophotonic structures,

  Supervisors: Prof. Dmitry Krizhanovskii and Dr Charles Whittaker.

APPENDIX B

List of relevant prizes and scholarships

Prizes and Scholarships received during the Doctoral Studies:

- **May 2024:** START Stipend for young, talented researchers, by Foundation for Polish Science,
- **Nov 2023:** Max Born's Scholarship (by Student Scholarship Program) for doctoral students with outstanding achievements,
- **Nov 2022:** The Prize of the Rector of Wrocław University of Science and Technology for the Best PhD Students,
- **Nov 2022:** Honorable Mention in Max Born's Scholarship (by Student Scholarship Program) for doctoral students with outstanding achievements,
- **Dec 2021:** The Prize of the Dean of Faculty of Fundamental Problems of Technology at the Wrocław University of Science and Technology for the Best PhD Students.

APPENDIX C

List of international conference presentations

Contributed Talks:

- D. Biegańska et.al, "Elementary excitations of exciton-polariton condensates in a synthetic gauge field", **International Conference on Optics of Excitons in Confined Systems OECS 17**, Dortmund, Germany, virtual format, Aug-Sept 2021,
- D. Biegańska et.al, "Elementary excitations of exciton-polariton condensates in a synthetic gauge field", **Quantum Optics X**, Toruń, Poland, virtual format, Sept 2021,
- D. Biegańska et.al, "Condensation and ballistic propagation of exciton polaritons in AlGaAs microcavity at high temperatures", **49th International School & Conference on the Physics of Semiconductors "Jaszowiec 2021"**, virtual format, Sept 2021,
- D. Biegańska et.al, "Elementary excitations of exciton-polariton condensates in a synthetic gauge field", **22nd International Conference on Physics of Light-Matter Coupling in Nanostructures PLMCN22**, Varadero, Cuba, Apr 2022,
- D. Biegańska et.al, "High-temperature condensation, ballistic propagation and non-hermitian effects of exciton polaritons in AlGaAs-based microcavities", **22nd International Conference on Physics of Light-Matter Coupling in Nanostructures PLMCN22**, Varadero, Cuba, Apr 2022,
- D. Biegańska et.al, "Anomalous dispersion and dissipative coupling in AlGaAs exciton-polariton structure", **51st, International School and Conference on the Physics of Semiconductors "Jaszowiec 2023"**, Szczyrk, Poland, Jun 2023,

Poster Presentations:

- M. Pieczarka, D. Biegańska et.al, "Spatial Diffusion of Photogenerated Carriers in Coupled Quantum Well -Quantum Dot Structures", **45th, International School and Conference on the Physics of Semiconductors "Jaszowiec 2016"**, Szczyrk, Poland, Jun 2016,
- D. Biegańska et.al, "Lateral Diffusion of Photogenerated Carriers in Coupled Quantum Dot – Quantum Well Structures Emitting at 1.55 m", **46th, International School and Conference on the Physics of Semiconductors "Jaszowiec 2017"**, Szczyrk, Poland, Jun 2017,
- D. Biegańska et.al, "Optical properties of $MoTe_2$ monolayers in various dielectric environments", **48th, International School and Conference on the Physics of Semiconductors "Jaszowiec 2019"**, Szczyrk, Poland, Jun 2019,
- D. Biegańska et.al, "Towards an (Al,Ga)As-based Exciton-Polariton Laser Operating At Room Temperature", **10th International Conference on Spontaneous Coherence in Excitonic Systems ICSCE10**, Melbourne, Australia, Jan 2020,
- D. Biegańska et.al, "Collective excitations of exciton-polariton condensates in a synthetic gauge field", **Condensates of Light Workshop**, Utrecht University, virtual, Dec 2020,
- D. Biegańska et.al, "Direct measurement of the anisotropic elementary excitations in an exciton-polariton condensate in a synthetic gauge field", **49th International School & Conference on the Physics of Semiconductors "Jaszowiec 2021"**, virtual format, Sept 2021,
- D. Biegańska et.al, "Elementary excitations of exciton-polariton condensates in a synthetic gauge field", **Bose-Einstein Condensation 2021 BEC2021**, Sant Feliu de Guixols, Spain, hybrid format, Sept 2021,
- D. Biegańska et.al, "Anomalous dispersion in AlGaAs exciton-polariton structure", **International Conference on Optics of Excitons in Confined Systems OECS 18**, Lecce, Italy, Jun 2023,
- D. Biegańska et.al, "Anomalous dispersion and dissipative coupling in quantum well exciton-polariton structure", **7th International Workshop On The Optical Properties Of Nanostructures OPON 2024**, Wrocław, Poland, Feb 2024.

Bibliography

[1] P. Y. Yu and M. Cardona, *Fundamentals of Semiconductors*. Graduate Texts in Physics, Berlin, Heidelberg: Springer Berlin Heidelberg, 2010.

[2] A. Kavokin, J. J. Baumberg, G. Malpuech, and F. P. Laussy, *Microcavities*. USA: Oxford University Press, Inc., 2008.

[3] C. Anton-Solanas, M. Waldherr, M. Klaas, H. Suchomel, T. H. Harder, H. Cai, E. Sedov, S. Klembt, A. V. Kavokin, S. Tongay, K. Watanabe, T. Taniguchi, S. Höfling, and C. Schneider, "Bosonic condensation of exciton–polaritons in an atomically thin crystal," *Nature Materials*, vol. 20, p. 1233–1239, May 2021.

[4] C. Kittel, *Introduction to solid state physics*. Nashville, TN: John Wiley & Sons, 8 ed., Oct. 2004.

[5] T. Ihn, *Semiconductor Nanostructures*. London, England: Oxford University Press, Nov. 2009.

[6] G. Bastard, E. E. Mendez, L. L. Chang, and L. Esaki, "Exciton binding energy in quantum wells," *Physical Review B*, vol. 26, p. 1974–1979, Aug. 1982.

[7] B. Deveaud, F. Clérot, N. Roy, K. Satzke, B. Sermage, and D. S. Katzer, "Enhanced radiative recombination of free excitons in gaas quantum wells," *Phys. Rev. Lett.*, vol. 67, pp. 2355–2358, Oct 1991.

[8] R. Miller and D. Kleinman, "Excitons in gaas quantum wells," *Journal of Luminescence*, vol. 30, p. 520–540, Feb. 1985.

[9] H. Mathieu, P. Lefebvre, and P. Christol, "Simple analytical method for calculating exciton binding energies in semiconductor quantum wells," *Physical Review B*, vol. 46, p. 4092–4101, Aug. 1992.

[10] K. J. Vahala, "Optical microcavities," *Nature*, vol. 424, p. 839–846, Aug. 2003.

[11] C. Schneider, K. Winkler, M. D. Fraser, M. Kamp, Y. Yamamoto, E. A. Ostrovskaya, and S. Höfling, "Exciton-polariton trapping and potential landscape engineering," *Reports on Progress in Physics*, vol. 80, p. 016503, nov 2016.

[12] D. Bajoni, "Polariton lasers. hybrid light–matter lasers without inversion," *Journal of Physics D: Applied Physics*, vol. 45, p. 409501, Sept. 2012.

[13] H. Deng, H. Haug, and Y. Yamamoto, "Exciton-polariton bose-einstein condensation," *Reviews of Modern Physics*, vol. 82, p. 1489–1537, May 2010.

[14] D. W. Snoke, V. Hartwell, J. Beaumariage, S. Mukherjee, Y. Yoon, D. M. Myers, M. Steger, Z. Sun, K. A. Nelson, and L. N. Pfeiffer, "Reanalysis of experimental determinations of polariton-polariton interactions in microcavities," *Physical Review B*, vol. 107, Apr. 2023.

[15] H. Megahd, D. Comoretto, and P. Lova, "(invited)planar microcavities: Materials and processing for light control," *Optical Materials: X*, vol. 13, p. 100130, Jan. 2022.

[16] D. Sanvitto, A. Daraei, A. Tahraoui, M. Hopkinson, P. W. Fry, D. M. Whittaker, and M. S. Skolnick, "Observation of ultrahigh quality factor in a semiconductor microcavity," *Applied Physics Letters*, vol. 86, May 2005.

[17] B. Nelsen, G. Liu, M. Steger, D. W. Snoke, R. Balili, K. West, and L. Pfeiffer, "Dissipationless flow and sharp threshold of a polariton condensate with long lifetime," *Phys. Rev. X*, vol. 3, p. 041015, Nov 2013.

[18] V. Savona, L. Andreani, P. Schwendimann, and A. Quattropani, "Quantum well excitons in semiconductor microcavities: Unified treatment of weak and strong coupling regimes," *Solid State Communications*, vol. 93, pp. 733–739, mar 1995.

[19] Anonymous, "Proceedings of the american physical society," *Physical Review*, vol. 69, p. 674–674, June 1946.

[20] I. Carusotto and C. Ciuti, "Quantum fluids of light," *Reviews of Modern Physics*, vol. 85, pp. 299–366, feb 2013.

[21] C. M. Bender, D. C. Brody, and H. F. Jones, "Complex extension of quantum mechanics," *Physical Review Letters*, vol. 89, Dec. 2002.

[22] N. Liu, M. Luo, Z. Wang, and J.-Q. Liang, "Hermitian and pseudo-hermitian hamiltonians of su(1,1) system—spectrum, exceptional point, quantum–classical correspondence," *Results in Physics*, vol. 56, p. 107292, Jan. 2024.

[23] O. Bleu, G. Li, J. Levinsen, and M. M. Parish, "Polariton interactions in microcavities with atomically thin semiconductor layers," *Phys. Rev. Res.*, vol. 2, p. 043185, Nov 2020.

[24] K. Choo, O. Bleu, J. Levinsen, and M. M. Parish, "Polaronic polariton quasiparticles in a dark excitonic medium," *Physical Review B*, vol. 109, May 2024.

[25] I. A. Shelykh, A. V. Kavokin, Y. G. Rubo, T. C. H. Liew, and G. Malpuech, "Polariton polarization-sensitive phenomena in planar semiconductor microcavities," *Semiconductor Science and Technology*, vol. 25, p. 013001, dec 2009.

[26] C. E. Whittaker, *Pattern formation , photonic spin-orbit coupling and topological states in semiconductor microcavities and micropillar lattices*. doctoral thesis, Department of Physics and Astronomy, University of Sheffield, july 2018.

[27] R. A. Chipman, W. S. T. Lam, and G. Young, *Polarized light and optical systems*. Optical Sciences and Applications of Light, London, England: CRC Press, July 2018.

[28] H. Terças, H. Flayac, D. D. Solnyshkov, and G. Malpuech, "Non-Abelian gauge fields in photonic cavities and photonic superfluids," *Phys. Rev. Lett.*, vol. 112, p. 066402, Feb 2014.

[29] G. Panzarini, L. C. Andreani, A. Armitage, D. Baxter, M. S. Skolnick, V. N. Astratov, J. S. Roberts, A. V. Kavokin, M. R. Vladimirova, and M. A. Kaliteevski, "Cavity-polariton dispersion and polarization splitting in single and coupled semiconductor microcavities," *Physics of the Solid State*, vol. 41, pp. 1223–1238, Aug 1999.

[30] A. Gianfrate, O. Bleu, L. Dominici, V. Ardizzone, M. De Giorgi, D. Ballarini, G. Lerario, K. W. West, L. N. Pfeiffer, D. D. Solnyshkov, D. Sanvitto, and G. Malpuech, "Measurement of the quantum geometric tensor and of the anomalous Hall drift," *Nature*, vol. 578, pp. 381–385, Feb 2020.

[31] K. Rechcińska, M. Król, R. Mazur, P. Morawiak, R. Mirek, K. Łempicka, W. Bardyszewski, M. Matuszewski, P. Kula, W. Piecek, P. G. Lagoudakis, B. Piętka, and J. Szczytko, "Engineering spin-orbit synthetic Hamiltonians in liquid-crystal optical cavities," *Science*, vol. 366, no. 6466, pp. 727–730, 2019.

[32] T. Ozawa, H. M. Price, A. Amo, N. Goldman, M. Hafezi, L. Lu, M. C. Rechtsman, D. Schuster, J. Simon, O. Zilberberg, and I. Carusotto, "Topological photonics," *Reviews of Modern Physics*, vol. 91, Mar. 2019.

[33] L. Lu, J. D. Joannopoulos, and M. Soljačić, "Topological photonics," *Nature Photonics*, vol. 8, p. 821–829, Oct. 2014.

[34] M. Hafezi, S. Mittal, J. Fan, A. Migdall, and J. M. Taylor, "Imaging topological edge states in silicon photonics," *Nature Photonics*, vol. 7, p. 1001–1005, Oct. 2013.

[35] M. Muszyński, M. Król, K. Rechcińska, P. Oliwa, M. Kędziora, K. Łempicka-Mirek, R. Mazur, P. Morawiak, W. Piecek, P. Kula, P. G. Lagoudakis, B. Piętka, and J. Szczytko, "Realizing persistent-spin-helix lasing in the regime of rashba-dresselhaus spin-orbit coupling in a dye-filled liquid-crystal optical microcavity," *Phys. Rev. Appl.*, vol. 17, p. 014041, Jan 2022.

[36] L. Polimeno, A. Fieramosca, G. Lerario, L. D. Marco, M. D. Giorgi, D. Ballarini, L. Dominici, V. Ardizzone, M. Pugliese, C. T. Prontera, V. Maiorano, G. Gigli, C. Leblanc, G. Malpuech, D. D. Solnyshkov, and D. Sanvitto, "Experimental investigation of a non-abelian gauge field in 2d perovskite photonic platform," *Optica*, vol. 8, pp. 1442–1447, Nov 2021.

[37] A. Kavokin, G. Malpuech, and M. Glazov, "Optical spin Hall effect," *Phys. Rev. Lett.*, vol. 95, p. 136601, Sep 2005.

[38] C. Leyder, M. Romanelli, J. P. Karr, E. Giacobino, T. C. H. Liew, M. M. Glazov, A. V. Kavokin, G. Malpuech, and A. Bramati, "Observation of the optical spin Hall effect," *Nature Physics*, vol. 3, pp. 628–631, Sep 2007.

[39] A. Amo, D. Sanvitto, F. P. Laussy, D. Ballarini, E. d. Valle, M. D. Martin, A. Lemaître, J. Bloch, D. N. Krizhanovskii, M. S. Skolnick, C. Tejedor, and L. Viña, "Collective fluid dynamics of a polariton condensate in a semiconductor microcavity," *Nature*, vol. 457, pp. 291–295, Jan 2009.

[40] C. E. Whittaker, T. Dowling, A. V. Nalitov, A. V. Yulin, B. Royall, E. Clarke, M. S. Skolnick, I. A. Shelykh, and D. N. Krizhanovskii, "Optical analogue of dresselhaus spin–orbit interaction in photonic graphene," *Nature Photonics*, vol. 15, pp. 193–196, Mar 2021.

[41] A. Amo, T. C. H. Liew, C. Adrados, E. Giacobino, A. V. Kavokin, and A. Bramati, "Anisotropic optical spin hall effect in semiconductor microcavities," *Physical Review B*, vol. 80, Oct. 2009.

[42] H. Flayac, D. D. Solnyshkov, I. A. Shelykh, and G. Malpuech, "Transmutation of skyrmions to half-solitons driven by the nonlinear optical spin hall effect," *Physical Review Letters*, vol. 110, Jan. 2013.

[43] E. Kammann, T. C. H. Liew, H. Ohadi, P. Cilibrizzi, P. Tsotsis, Z. Hatzopoulos, P. G. Savvidis, A. V. Kavokin, and P. G. Lagoudakis, "Nonlinear optical spin Hall effect and long-range spin transport in polariton lasers," *Physical Review Letters*, vol. 109, p. 036404, jul 2012.

[44] K. Lekenta, M. Król, R. Mirek, K. Łempicka, D. Stephan, R. Mazur, P. Morawiak, P. Kula, W. Piecek, P. G. Lagoudakis, B. Piętka, and J. Szczytko, "Tunable optical spin hall effect in a liquid crystal microcavity," *Light: Science and; Applications*, vol. 7, Oct. 2018.

[45] M. Król, H. Sigurdsson, K. Rechcińska, P. Oliwa, K. Tyszka, W. Bardyszewski, A. Opala, M. Matuszewski, P. Morawiak, R. Mazur, W. Piecek, P. Kula, P. G. Lagoudakis, B. Piętka, and J. Szczytko, "Observation of second-order meron polarization textures in optical microcavities," *Optica*, vol. 8, pp. 255–261, Feb 2021.

[46] B. Piętka, D. Zygmunt, M. Król, M. R. Molas, A. A. L. Nicolet, F. Morier-Genoud, J. Szczytko, J. Łusakowski, P. Zięba, I. Tralle, P. Stępnicki, M. Matuszewski, M. Potemski, and B. Deveaud, "Magnetic field tuning of exciton-polaritons in a semiconductor microcavity," *Physical Review B*, vol. 91, Feb. 2015.

[47] D. Colas, F. P. Laussy, and M. J. Davis, "Negative-Mass Effects in Spin-Orbit Coupled Bose-Einstein Condensates," *Physical Review Letters*, vol. 121, p. 055302, jul 2018.

[48] M. Wurdack, T. Yun, M. Katzer, A. G. Truscott, A. Knorr, M. Selig, E. A. Ostrovskaya, and E. Estrecho, "Negative-mass exciton polaritons induced by dissipative light-matter coupling in an atomically thin semiconductor," *Nature Communications*, vol. 14, p. 1026, Feb 2023.

[49] F. Baboux, D. D. Bernardis, V. Goblot, V. N. Gladilin, C. Gomez, E. Galopin, L. L. Gratiet, A. Lemaître, I. Sagnes, I. Carusotto, M. Wouters, A. Amo, and J. Bloch, "Unstable and stable regimes of polariton condensation," *Optica*, vol. 5, pp. 1163–1170, Oct 2018.

[50] M. Wurdack, N. Lundt, M. Klaas, V. Baumann, A. V. Kavokin, S. Höfling, and C. Schneider, "Observation of hybrid tamm-plasmon exciton- polaritons with gaas quantum wells and a mose2 monolayer," *Nature Communications*, vol. 8, p. 259, Aug 2017.

[51] D. Sanvitto and S. Kéna-Cohen, "The road towards polaritonic devices," *Nature Materials*, vol. 15, pp. 1061–1073, oct 2016.

[52] T. Byrnes, N. Y. Kim, and Y. Yamamoto, "Exciton–polariton condensates," *Nature Physics*, vol. 10, p. 803–813, October 2014.

[53] T. Gao, E. Estrecho, K. Y. Bliokh, T. C. H. Liew, M. D. Fraser, S. Brodbeck, M. Kamp, C. Schneider, S. Höfling, Y. Yamamoto, F. Nori, Y. S. Kivshar, A. G. Truscott, R. G. Dall, and E. A. Ostrovskaya, "Observation of non-hermitian degeneracies in a chaotic exciton-polariton billiard," *Nature*, vol. 526, pp. 554–558, Oct 2015.

[54] R. El-Ganainy, K. G. Makris, M. Khajavikhan, Z. H. Musslimani, S. Rotter, and D. N. Christodoulides, "Non-hermitian physics and pt symmetry," *Nature Physics*, vol. 14, p. 11–19, Jan. 2018.

[55] C. M. Bender, "Making sense of non-hermitian hamiltonians," *Reports on Progress in Physics*, vol. 70, p. 947–1018, May 2007.

[56] Y.-M. R. Hu, E. A. Ostrovskaya, and E. Estrecho, "Wave-packet dynamics in a non-hermitian exciton-polariton system," *Physical Review B*, vol. 108, Sept. 2023.

[57] R. Bao, H. Xu, W. Verstraelen, and T. C. H. Liew, "Topological enhancement of exciton-polariton coherence with non-hermitian morphing," *Physical Review B*, vol. 108, Dec. 2023.

[58] X. Xu, R. Bao, and T. C. H. Liew, "Non-hermitian topological exciton-polariton corner modes," *Physical Review B*, vol. 106, Nov. 2022.

[59] H. Cao and J. Wiersig, "Dielectric microcavities: Model systems for wave chaos and non-hermitian physics," *Reviews of Modern Physics*, vol. 87, p. 61–111, Jan. 2015.

[60] F. Roccati, G. M. Palma, F. Ciccarello, and F. Bagarello, "Non-hermitian physics and master equations," *Open Systems and Information Dynamics*, vol. 29, Mar. 2022.

[61] E. J. Bergholtz, J. C. Budich, and F. K. Kunst, "Exceptional topology of non-hermitian systems," *Reviews of Modern Physics*, vol. 93, Feb. 2021.

[62] R. Su, E. Estrecho, D. Biegańska, Y. Huang, M. Wurdack, M. Pieczarka, A. G. Truscott, T. C. H. Liew, E. A. Ostrovskaya, and Q. Xiong, "Direct measurement of a non-hermitian topological invariant in a hybrid light-matter system," *Science Advances*, vol. 7, no. 45, p. eabj8905, 2021.

[63] S. Klembt, T. H. Harder, O. A. Egorov, K. Winkler, R. Ge, M. A. Bandres, M. Emmerling, L. Worschech, T. C. Liew, M. Segev, C. Schneider, and S. Höfling, "Exciton-polariton topological insulator," *Nature*, vol. 562, no. 7728, pp. 552–556, 2018.

[64] T. Long, X. Ma, J. Ren, F. Li, Q. Liao, S. Schumacher, G. Malpuech, D. Solnyshkov, and H. Fu, "Helical polariton lasing from topological valleys in an organic crystalline microcavity," *Advanced Science*, vol. 9, no. 29, p. 2203588, 2022.

[65] Z. Gong, Y. Ashida, K. Kawabata, K. Takasan, S. Higashikawa, and M. Ueda, "Topological phases of non-hermitian systems," *Physical Review X*, vol. 8, Sept. 2018.

[66] H. Shen, B. Zhen, and L. Fu, "Topological band theory for non-hermitian hamiltonians," *Physical Review Letters*, vol. 120, Apr. 2018.

[67] D. Leykam, K. Y. Bliokh, C. Huang, Y. Chong, and F. Nori, "Edge modes, degeneracies, and topological numbers in non-hermitian systems," *Physical Review Letters*, vol. 118, Jan. 2017.

[68] H. Deng, G. Weihs, C. Santori, J. Bloch, and Y. Yamamoto, "Condensation of semiconductor microcavity exciton polaritons," *Science*, vol. 298, p. 199–202, Oct. 2002.

[69] J. Khurgin, "Excitonic radius in the cavity polariton in the regime of very strong coupling," *Solid State Communications*, vol. 117, p. 307–310, Jan. 2001.

[70] H. Suchomel, S. Kreutzer, M. Jörg, S. Brodbeck, M. Pieczarka, S. Betzold, C. P. Dietrich, G. Sęk, C. Schneider, and S. Höfling, "Room temperature strong coupling in a semiconductor microcavity with embedded algaas quantum wells designed for polariton lasing," *Opt. Express*, vol. 25, pp. 24816–24826, Oct 2017.

[71] J. Kasprzak, M. Richard, S. Kundermann, A. Baas, P. Jeambrun, J. M. J. Keeling, F. M. Marchetti, M. H. Szymańska, R. André, J. L. Staehli, V. Savona, P. B. Littlewood, B. Deveaud, and L. S. Dang, "Bose–einstein condensation of exciton polaritons," *Nature*, vol. 443, p. 409–414, Sept. 2006.

[72] S. Christopoulos, G. B. H. von Högersthal, A. J. D. Grundy, P. G. Lagoudakis, A. V. Kavokin, J. J. Baumberg, G. Christmann, R. Butté, E. Feltin, J.-F. Carlin, and N. Grandjean, "Room-temperature polariton lasing in semiconductor microcavities," *Physical Review Letters*, vol. 98, Mar. 2007.

[73] G. Christmann, R. Butté, E. Feltin, J.-F. Carlin, and N. Grandjean, "Room temperature polariton lasing in a ganálgan multiple quantum well microcavity," *Applied Physics Letters*, vol. 93, Aug. 2008.

[74] R. Pandya, R. Y. S. Chen, Q. Gu, J. Sung, C. Schnedermann, O. S. Ojambati, R. Chikkaraddy, J. Gorman, G. Jacucci, O. D. Onelli, T. Willhammar, D. N. Johnstone, S. M. Collins, P. A. Midgley, F. Auras, T. Baikie, R. Jayaprakash, F. Mathevet, R. Soucek, M. Du, A. M. Alvertis, A. Ashoka, S. Vignolini, D. G. Lidzey, J. J. Baumberg, R. H. Friend, T. Barisien, L. Legrand, A. W. Chin, J. Yuen-Zhou, S. K. Saikin, P. Kukura, A. J. Musser, and A. Rao, "Microcavity-like exciton-polaritons can be the primary photoexcitation in bare organic semiconductors," *Nature Communications*, vol. 12, Nov. 2021.

[75] Z. Jiang, A. Ren, Y. Yan, J. Yao, and Y. S. Zhao, "Exciton-polaritons and their bose–einstein condensates in organic semiconductor microcavities," *Advanced Materials*, vol. 34, Dec. 2021.

[76] F. Hu and Z. Fei, "Recent progress on exciton polaritons in layered transition-metal dichalcogenides," *Advanced Optical Materials*, vol. 8, Sept. 2019.

[77] Q. Zhang, S. Dong, G. Cao, and G. Hu, "Exciton polaritons in mixed-dimensional transition metal dichalcogenides heterostructures," *Optics Letters*, vol. 45, p. 4140, July 2020.

[78] M. Laitz, A. E. K. Kaplan, J. Deschamps, U. Barotov, A. H. Proppe, I. García-Benito, A. Osherov, G. Grancini, D. W. deQuilettes, K. A. Nelson, M. G. Bawendi, and V. Bulović, "Uncovering temperature-dependent exciton-polariton relaxation mechanisms in hybrid organic-inorganic perovskites," *Nature Communications*, vol. 14, Apr. 2023.

[79] R. Su, S. Ghosh, J. Wang, S. Liu, C. Diederichs, T. C. H. Liew, and Q. Xiong, "Observation of exciton polariton condensation in a perovskite lattice at room temperature," *Nature Physics*, vol. 16, p. 301–306, Jan. 2020.

[80] C. Schneider, M. M. Glazov, T. Korn, S. Höfling, and B. Urbaszek, "Two-dimensional semiconductors in the regime of strong light-matter coupling," *Nature Communications*, vol. 9, July 2018.

[81] K. W. Song, S. Chiavazzo, and O. Kyriienko, "Microscopic theory of nonlinear phase space filling in polaritonic lattices," *Physical Review Research*, vol. 6, Apr. 2024.

[82] H. Deng, G. Weihs, D. Snoke, J. Bloch, and Y. Yamamoto, "Polariton lasing vs. photon lasing in a semiconductor microcavity," *Proceedings of the National Academy of Sciences*, vol. 100, p. 15318–15323, Dec. 2003.

[83] G. Yang, M. MacDougal, and P. Dapkus, "Ultralow threshold current vertical-cavity surface-emitting lasers obtained with selective oxidation," *Electronics Letters*, vol. 31, p. 886–888, May 1995.

[84] A. M. Berghuis, G. W. Castellanos, S. Murai, J. L. Pura, D. R. Abujetas, E. van Heijst, M. Ramezani, J. A. Sánchez-Gil, and J. G. Rivas, "Room temperature exciton–polariton condensation in silicon metasurfaces emerging from bound states in the continuum," *Nano Letters*, vol. 23, p. 5603–5609, June 2023.

[85] L. Polimeno, A. Coriolano, R. Mastria, F. Todisco, M. De Giorgi, A. Fieramosca, M. Pugliese, C. T. Prontera, A. Rizzo, L. De Marco, D. Ballarini, G. Gigli, and D. Sanvitto, "Room temperature polariton condensation from whispering gallery modes in cspbbr3 microplatelets," *Advanced Materials*, vol. 36, Apr. 2024.

[86] M. Wei, W. Verstraelen, K. Orfanakis, A. Ruseckas, T. C. H. Liew, I. D. W. Samuel, G. A. Turnbull, and H. Ohadi, "Optically trapped room temperature polariton condensate in an organic semiconductor," *Nature Communications*, vol. 13, November 2022.

[87] T.-C. Lu, Y.-Y. Lai, Y.-P. Lan, S.-W. Huang, J.-R. Chen, Y.-C. Wu, W.-F. Hsieh, and H. Deng, "Room temperature polariton lasing vs photon lasing in a zno-based hybrid microcavity," *Optics Express*, vol. 20, p. 5530, February 2012.

[88] P. Gagel, O. A. Egorov, F. Dzimira, J. Beierlein, M. Emmerling, A. Wolf, F. Jabeen, S. Betzold, U. Peschel, S. Höfling, C. Schneider, and S. Klembt, "An electrically pumped topological polariton laser," *Nano Letters*, vol. 24, p. 6538–6544, May 2024.

[89] J. Wu, S. Ghosh, Y. Gan, Y. Shi, S. Mandal, H. Sun, B. Zhang, T. C. H. Liew, R. Su, and Q. Xiong, "Higher-order topological polariton corner state lasing," *Science Advances*, vol. 9, May 2023.

[90] T. H. Harder, M. Sun, O. A. Egorov, I. Vakulchyk, J. Beierlein, P. Gagel, M. Emmerling, C. Schneider, U. Peschel, I. G. Savenko, S. Klembt, and S. Höfling, "Coherent topological polariton laser," *ACS Photonics*, vol. 8, p. 1377–1384, Apr. 2021.

[91] K. Peng, W. Li, M. Sun, J. D. H. Rivero, C. Ti, X. Han, L. Ge, L. Yang, X. Zhang, and W. Bao, "Topological valley hall polariton condensation," *Nature Nanotechnology*, May 2024.

[92] M. Dusel, S. Betzold, T. H. Harder, M. Emmerling, J. Beierlein, J. Ohmer, U. Fischer, R. Thomale, C. Schneider, S. Höfling, and S. Klembt, "Room-temperature topological polariton laser in an organic lattice," *Nano Letters*, vol. 21, p. 6398–6405, July 2021.

[93] Y. Wang, H. Zheng, Z. Tang, R. Wang, X. Luo, Y. Shen, X. Yang, K.-K. Liu, S. Wang, S. Deng, C.-X. Shan, and H. Zhu, "Spin-polarization-induced chiral polariton lasing at room temperature," *ACS Photonics*, vol. 10, p. 1936–1943, May 2023.

[94] K. Łempicka Mirek, M. Król, L. De Marco, A. Coriolano, L. Polimeno, I. Viola, M. Kędziora, M. Muszyński, P. Morawiak, R. Mazur, P. Kula, W. Piecek, P. Fita, D. Sanvitto, J. Szczytko, and B. Piętka, "Electrical polarization switching of perovskite polariton laser," *Nanophotonics*, vol. 13, p. 2659–2668, Feb. 2024.

[95] X. Ma, Y. V. Kartashov, A. Kavokin, and S. Schumacher, "Chiral condensates in a polariton hexagonal ring," *Optics Letters*, vol. 45, p. 5700, Oct. 2020.

[96] M. D. Fraser, S. Höfling, and Y. Yamamoto, "Physics and applications of exciton–polariton lasers," *Nature Materials*, vol. 15, p. 1049–1052, Sept. 2016.

[97] T. C. H. Liew, A. V. Kavokin, and I. A. Shelykh, "Optical circuits based on polariton neurons in semiconductor microcavities," *Physical Review Letters*, vol. 101, July 2008.

[98] T. C. H. Liew and V. Savona, "Multipartite polariton entanglement in semiconductor microcavities," *Physical Review A*, vol. 84, Sept. 2011.

[99] S. Savasta, O. D. Stefano, V. Savona, and W. Langbein, "Quantum complementarity of microcavity polaritons," *Physical Review Letters*, vol. 94, June 2005.

[100] S. Demirchyan, I. Chestnov, A. Alodjants, M. Glazov, and A. Kavokin, "Qubits based on polariton rabi oscillators," *Physical Review Letters*, vol. 112, May 2014.

[101] A. Opala, S. Ghosh, T. C. Liew, and M. Matuszewski, "Neuromorphic computing in ginzburg-landau polariton-lattice systems," *Physical Review Applied*, vol. 11, June 2019.

[102] R. Mirek, A. Opala, P. Comaron, M. Furman, M. Król, K. Tyszka, B. Seredyński, D. Ballarini, D. Sanvitto, T. C. H. Liew, W. Pacuski, J. Suffczyński, J. Szczytko, M. Matuszewski, and B. Piętka, "Neuromorphic binarized polariton networks," *Nano Letters*, vol. 21, p. 3715–3720, Feb. 2021.

[103] A. Opala and M. Matuszewski, "Harnessing exciton-polaritons for digital computing, neuromorphic computing, and optimization [invited]," *Optical Materials Express*, vol. 13, p. 2674, Aug. 2023.

[104] R. Mirek, A. Opala, M. Furman, M. Król, K. Tyszka, B. Seredyński, W. Pacuski, J. Suffczyński, J. Szczytko, M. Matuszewski, and B. Piętka, "Neural networks based on ultrafast time-delayed effects in exciton polaritons," *Physical Review Applied*, vol. 17, May 2022.

[105] D. Ballarini, A. Gianfrate, R. Panico, A. Opala, S. Ghosh, L. Dominici, V. Ardizzone, M. De Giorgi, G. Lerario, G. Gigli, T. C. H. Liew, M. Matuszewski, and D. Sanvitto, "Polaritonic neuromorphic computing outperforms linear classifiers," *Nano Letters*, vol. 20, p. 3506–3512, Apr. 2020.

[106] N. G. Berloff, M. Silva, K. Kalinin, A. Askitopoulos, J. D. Töpfer, P. Cilibrizzi, W. Langbein, and P. G. Lagoudakis, "Realizing the classical XY Hamiltonian in polariton simulators," *Nature Materials*, vol. 16, no. 11, pp. 1120–1126, 2017.

[107] P. Knüppel, S. Ravets, M. Kroner, S. Fält, W. Wegscheider, and A. Imamoglu, "Nonlinear optics in the fractional quantum hall regime," *Nature*, vol. 572, p. 91–94, July 2019.

[108] D. D. Solnyshkov, H. Flayac, and G. Malpuech, "Black holes and wormholes in spinor polariton condensates," *Physical Review B*, vol. 84, Dec. 2011.

[109] M. Jacquet, M. Joly, F. Claude, L. Giacomelli, Q. Glorieux, A. Bramati, I. Carusotto, and E. Giacobino, "Analogue quantum simulation of the hawking effect in a polariton superfluid," *The European Physical Journal D*, vol. 76, Aug. 2022.

[110] A. Svetlichnyi, A. Chaika, and A. Yakimenko, "Acoustic analogs of extremal rotating black holes in exciton-polariton condensates," *Physical Review B*, vol. 109, June 2024.

[111] R. P. Feynman, R. B. Leighton, and M. Sands, *The Feynman lectures on physics; New millennium ed.* New York, NY: Basic Books, 2010. Originally published 1963-1965.

[112] H.-J. Miesner, D. M. Stamper-Kurn, M. R. Andrews, D. S. Durfee, S. Inouye, and W. Ketterle, "Bosonic stimulation in the formation of a bose-einstein condensate," *Science*, vol. 279, p. 1005–1007, Feb. 1998.

[113] Bose, "Plancks gesetz und lichtquantenhypothese," *Zeitschrift für Physik*, vol. 26, p. 178–181, Dec. 1924.

[114] A. Einstein, *Quantentheorie des einatomigen idealen Gases*. No. t. 1, Verlag der Akademie der Wissenschaften, in Kommission bei Walter de Gruyter u. Company, 1924.

[115] N. P. Proukakis, D. Snoke, and P. Littlewood, eds., *Universal themes of Bose-Einstein condensation*. Cambridge, England: Cambridge University Press, Apr. 2017.

[116] L. Pitaevskii and S. Stringari, *Bose-Einstein Condensation and Superfluidity*. Oxford University Press, jan 2016.

[117] N. Bogoliubov, "On the theory of superfluidity," *J. Phys. (USSR)*, vol. 11, pp. 23–32, 1947.

[118] P. Pitaevskii, "Vortex lines in an imperfect bose gas," *Journal of Experimental and Theoretical Physics*, vol. 13, pp. 451–454, 1961.

[119] E. P. Gross, "Structure of a quantized vortex in boson systems," *Il Nuovo Cimento*, vol. 20, p. 454–477, May 1961.

[120] N. D. Mermin and H. Wagner, "Absence of ferromagnetism or antiferromagnetism in one- or two-dimensional isotropic heisenberg models," *Physical Review Letters*, vol. 17, p. 1133–1136, Nov. 1966.

[121] Z. Hadzibabic and J. Dalibard, "Two-dimensional bose fluids: An atomic physics perspective," *La Rivista del Nuovo Cimento*, vol. 34, p. 389–434, June 2011.

[122] J. M. Kosterlitz and D. J. Thouless, "Ordering, metastability and phase transitions in two-dimensional systems," *J. Phys.*, vol. 6, pp. 1181–1203, Apr. 1973.

[123] J. M. Kosterlitz, "Nobel lecture: Topological defects and phase transitions," *Reviews of Modern Physics*, vol. 89, Oct. 2017.

[124] V. L. Berezinsky, "Destruction of long range order in one-dimensional and two-dimensional systems having a continuous symmetry group. I. Classical systems," *Sov. Phys. JETP*, vol. 32, pp. 493–500, 1971.

[125] J. M. Kosterlitz and D. J. Thouless, "Long range order and metastability in two dimensional solids and superfluids. (application of dislocation theory)," *Journal of Physics C: Solid State Physics*, vol. 5, p. L124–L126, June 1972.

[126] A. Kavokin, P. G. Lagoudakis, G. Malpuech, and J. J. Baumberg, "Polarization rotation in parametric scattering of polaritons in semiconductor microcavities," *Phys. Rev. B*, vol. 67, p. 195321, May 2003.

[127] W. H. Nitsche, N. Y. Kim, G. Roumpos, S. Höfling, A. Forchel, and Y. Yamamoto, "Observation of bkt transition in bec of exciton-polaritons in a semiconductor microcavity," in *CLEO: 2013*, pp. 1–2, 2013.

[128] J. Bardeen, L. N. Cooper, and J. R. Schrieffer, "Theory of superconductivity," *Physical Review*, vol. 108, p. 1175–1204, Dec. 1957.

[129] M. M. Parish, *The BCS–BEC Crossover*, p. 179–197. IMPERIAL COLLEGE PRESS, Sept. 2014.

[130] M. Randeria and E. Taylor, "Crossover from bardeen-cooper-schrieffer to bose-einstein condensation and the unitary fermi gas," *Annual Review of Condensed Matter Physics*, vol. 5, p. 209–232, Mar. 2014.

[131] J. Keeling, P. R. Eastham, M. H. Szymanska, and P. B. Littlewood, "Bcs-bec crossover in a system of microcavity polaritons," *Physical Review B*, vol. 72, Sept. 2005.

[132] T. Byrnes, T. Horikiri, N. Ishida, and Y. Yamamoto, "Bcs wave-function approach to the bec-bcs crossover of exciton-polariton condensates," *Physical Review Letters*, vol. 105, Oct. 2010.

[133] M. Wouters, "Resonant polariton-polariton scattering in semiconductor microcavities," *Phys. Rev. B*, vol. 76, p. 045319, Jul 2007.

[134] C. Ciuti, V. Savona, C. Piermarocchi, A. Quattropani, and P. Schwendimann, "Role of the exchange of carriers in elastic exciton-exciton scattering in quantum wells," *Phys. Rev. B*, vol. 58, pp. 7926–7933, Sep 1998.

[135] F. Tassone, C. Piermarocchi, V. Savona, A. Quattropani, and P. Schwendimann, "Bottleneck effects in the relaxation and photoluminescence of microcavity polaritons," *Physical Review B*, vol. 56, p. 7554–7563, Sept. 1997.

[136] M. Matuszewski and E. Witkowska, "Universality in nonequilibrium condensation of exciton-polaritons," *Physical Review B*, vol. 89, Apr. 2014.

[137] R. Bhuyan, M. Lednev, J. Feist, and K. Börjesson, "The effect of the relative size of the exciton reservoir on polariton photophysics," *Advanced Optical Materials*, vol. 12, Oct. 2023.

[138] E. Estrecho, T. Gao, N. Bobrovska, M. D. Fraser, M. Steger, L. Pfeiffer, K. West, T. C. H. Liew, M. Matuszewski, D. W. Snoke, A. G. Truscott, and E. A. Ostrovskaya, "Single-shot condensation of exciton polaritons and the hole burning effect," *Nature Communications*, vol. 9, Aug. 2018.

[139] D. Ballarini, D. Caputo, C. S. Muñoz, M. De Giorgi, L. Dominici, M. H. Szymańska, K. West, L. N. Pfeiffer, G. Gigli, F. P. Laussy, and D. Sanvitto, "Macroscopic two-dimensional polariton condensates," *Phys. Rev. Lett.*, vol. 118, p. 215301, May 2017.

[140] A. Askitopoulos, H. Ohadi, A. V. Kavokin, Z. Hatzopoulos, P. G. Savvidis, and P. G. Lagoudakis, "Polariton condensation in an optically induced two-dimensional potential," *Physical Review B*, vol. 88, p. 041308, jul 2013.

[141] K. Sawicki, J.-G. Rousset, R. Rudniewski, W. Pacuski, M. Ściesiek, T. Kazimierczuk, K. Sobczak, J. Borysiuk, M. Nawrocki, and J. Suffczyński, "Triple threshold lasing from a photonic trap in a te/se-based optical microcavity," *Communications Physics*, vol. 2, Apr. 2019.

[142] P. Kapitza, "Viscosity of liquid helium below the -point," *Nature*, vol. 141, p. 74–74, Jan. 1938.

[143] J. F. ALLEN and A. D. MISENER, "Flow of liquid helium ii," *Nature*, vol. 141, p. 75–75, Jan. 1938.

[144] K. V. Krutitsky, "Ultracold bosons with short-range interaction in regular optical lattices," *Physics Reports*, vol. 607, p. 1–101, Jan. 2016.

[145] D. D. Osheroff, R. C. Richardson, and D. M. Lee, "Evidence for a new phase of solid he^3," *Physical Review Letters*, vol. 28, p. 885–888, Apr. 1972.

[146] N. N. Carlson, "A topological defect model of superfluid vortices," *Physica D: Nonlinear Phenomena*, vol. 98, p. 183–200, Nov. 1996.

[147] E. Estrecho, T. Gao, N. Bobrovska, D. Comber-Todd, M. D. Fraser, M. Steger, K. West, L. N. Pfeiffer, J. Levinsen, M. M. Parish, T. C. H. Liew, M. Matuszewski, D. W. Snoke, A. G. Truscott, and E. A. Ostrovskaya, "Direct measurement of polariton-polariton interaction strength in the Thomas-Fermi regime of exciton-polariton condensation," *Phys. Rev. B*, vol. 100, p. 035306, Jul 2019.

[148] M. Pieczarka, E. Estrecho, M. Boozarjmehr, O. Bleu, M. Steger, K. West, L. N. Pfeiffer, D. W. Snoke, J. Levinsen, M. M. Parish, A. G. Truscott, and E. A. Ostrovskaya, "Observation of quantum depletion in a non-equilibrium exciton–polariton condensate," *Nature Communications*, vol. 11, p. 429, Jan 2020.

[149] N. Bobrovska, E. A. Ostrovskaya, and M. Matuszewski, "Stability and spatial coherence of nonresonantly pumped exciton-polariton condensates," *Phys. Rev. B*, vol. 90, p. 205304, Nov 2014.

[150] G. Li, M. D. Fraser, A. Yakimenko, and E. A. Ostrovskaya, "Stability of persistent currents in open dissipative quantum fluids," *Physical Review B*, vol. 91, May 2015.

[151] Y. Castin, *Bose-Einstein Condensates in Atomic Gases: Simple Theoretical Results*, p. 1–136. Springer Berlin Heidelberg, 2001.

[152] M. Pieczarka, O. Bleu, E. Estrecho, M. Wurdack, M. Steger, D. W. Snoke, K. West, L. N. Pfeiffer, A. G. Truscott, E. A. Ostrovskaya, J. Levinsen, and M. M. Parish, "Bogoliubov excitations of a polariton condensate in dynamical equilibrium with an incoherent reservoir," *Physical Review B*, vol. 105, June 2022.

[153] R. Hanai, P. B. Littlewood, and Y. Ohashi, "Photoluminescence and gain/absorption spectra of a driven-dissipative electron-hole-photon condensate," *Physical Review B*, vol. 97, June 2018.

[154] P. G. Savvidis, C. Ciuti, J. J. Baumberg, D. M. Whittaker, M. S. Skolnick, and J. S. Roberts, "Off-branch polaritons and multiple scattering in semiconductor microcavities," *Phys. Rev. B*, vol. 64, p. 075311, Jul 2001.

[155] S. Utsunomiya, L. Tian, G. Roumpos, C. W. Lai, N. Kumada, T. Fujisawa, M. Kuwata-Gonokami, A. Löffler, S. Höfling, A. Forchel, and Y. Yamamoto, "Observation of Bogoliubov excitations in exciton-polariton condensates," *Nature Physics*, vol. 4, pp. 700–705, aug 2008.

[156] V. Kohnle, Y. Léger, M. Wouters, M. Richard, M. T. Portella-Oberli, and B. Deveaud-Plédran, "From single particle to superfluid excitations in a dissipative polariton gas," *Physical Review Letters*, vol. 106, p. 255302, jun 2011.

[157] J. M. Zajac and W. Langbein, "Parametric scattering of microcavity polaritons into ghost branches," *Phys. Rev. B*, vol. 92, p. 165305, Oct 2015.

[158] F. Tassone and Y. Yamamoto, "Exciton-exciton scattering dynamics in a semiconductor microcavity and stimulated scattering into polaritons," *Physical Review B*, vol. 59, p. 10830–10842, Apr. 1999.

[159] L. Ferrier, E. Wertz, R. Johne, D. D. Solnyshkov, P. Senellart, I. Sagnes, A. Lemaître, G. Malpuech, and J. Bloch, "Interactions in confined polariton condensates," *Phys. Rev. Lett.*, vol. 106, p. 126401, Mar 2011.

[160] Y. Sun, Y. Yoon, M. Steger, G. Liu, L. N. Pfeiffer, K. West, D. Snoke, and K. A. Nelson, "Direct measurement of polariton–polariton interaction strength," *Nature Physics*, vol. 13, pp. 870–875, Sep 2017.

[161] A. S. Brichkin, S. I. Novikov, A. V. Larionov, V. D. Kulakovskii, M. M. Glazov, C. Schneider, S. Höfling, M. Kamp, and A. Forchel, "Effect of coulomb interaction on exciton-polariton condensates in gaas pillar microcavities," *Phys. Rev. B*, vol. 84, p. 195301, Nov 2011.

[162] M. Pieczarka, M. Boozarjmehr, E. Estrecho, Y. Yoon, M. Steger, K. West, L. N. Pfeiffer, K. A. Nelson, D. W. Snoke, A. G. Truscott, and E. A. Ostrovskaya, "Effect of optically induced potential on the energy of trapped exciton-polaritons below the condensation threshold," *Physical Review B*, vol. 100, no. 8, p. 085301, 2019.

[163] A. Amo, J. Lefrère, S. Pigeon, C. Adrados, C. Ciuti, I. Carusotto, R. Houdré, E. Giacobino, and A. Bramati, "Superfluidity of polaritons in semiconductor microcavities," *Nature Physics*, vol. 5, p. 805–810, Sept. 2009.

[164] A. Tredicucci, Y. Chen, V. Pellegrini, M. Börger, and F. Bassani, "Optical bistability of semiconductor microcavities in the strong-coupling regime," *Physical Review A*, vol. 54, p. 3493–3498, Oct. 1996.

[165] A. Baas, J. P. Karr, H. Eleuch, and E. Giacobino, "Optical bistability in semiconductor microcavities," *Physical Review A*, vol. 69, Feb. 2004.

[166] P. G. Savvidis, J. J. Baumberg, R. M. Stevenson, M. S. Skolnick, D. M. Whittaker, and J. S. Roberts, "Angle-resonant stimulated polariton amplifier," *Physical Review Letters*, vol. 84, p. 1547–1550, Feb. 2000.

[167] I. Carusotto and C. Ciuti, "Probing microcavity polariton superfluidity through resonant rayleigh scattering," *Physical Review Letters*, vol. 93, Oct. 2004.

[168] A. Verger, C. Ciuti, and I. Carusotto, "Polariton quantum blockade in a photonic dot," *Phys. Rev. B*, vol. 73, p. 193306, May 2006.

[169] G. Li, M. M. Parish, and J. Levinsen, "Microscopic calculation of polariton scattering in semiconductor microcavities," *Physical Review B*, vol. 104, December 2021.

[170] H. Hu, H. Deng, and X.-J. Liu, "Polariton-polariton interaction beyond the born approximation: A toy model study," *Physical Review A*, vol. 102, December 2020.

[171] N. Prokof'ev, O. Ruebenacker, and B. Svistunov, "Critical point of a weakly interacting two-dimensional bose gas," *Physical Review Letters*, vol. 87, December 2001.

[172] N. Prokof'ev and B. Svistunov, "Two-dimensional weakly interacting bose gas in the fluctuation region," *Physical Review A*, vol. 66, October 2002.

[173] P. Le Jeune, X. Marie, T. Amand, F. Romstad, F. Perez, J. Barrau, and M. Brousseau, "Spin-dependent exciton-exciton interactions in quantum wells," *Physical Review B*, vol. 58, p. 4853–4859, August 1998.

[174] N. B. An, H. N. Cam, and N. T. Dan, "Spin-dependent exciton-exciton interaction potential in two- and three-dimensional semiconductors under excitation," *Journal of Physics: Condensed Matter*, vol. 3, p. 3317–3329, May 1991.

[175] M. Vladimirova, S. Cronenberger, D. Scalbert, K. V. Kavokin, A. Miard, A. Lemaître, J. Bloch, D. Solnyshkov, G. Malpuech, and A. V. Kavokin, "Polariton-polariton interaction constants in microcavities," *Phys. Rev. B*, vol. 82, p. 075301, Aug 2010.

[176] M. Vladimirova, S. Cronenberger, D. Scalbert, M. Nawrocki, A. V. Kavokin, A. Miard, A. Lemaître, and J. Bloch, "Polarization controlled nonlinear transmission of light through semiconductor microcavities," *Phys. Rev. B*, vol. 79, p. 115325, Mar 2009.

[177] I. A. Shelykh, Y. G. Rubo, G. Malpuech, D. D. Solnyshkov, and A. Kavokin, "Polarization and propagation of polariton condensates," *Phys. Rev. Lett.*, vol. 97, p. 066402, Aug 2006.

[178] I. A. Shelykh, G. Malpuech, and A. V. Kavokin, "Bogoliubov theory of bose-condensates of spinor exciton-polaritons," *physica status solidi (a)*, vol. 202, p. 2614–2620, Nov. 2005.

[179] P. Renucci, T. Amand, X. Marie, P. Senellart, J. Bloch, B. Sermage, and K. V. Kavokin, "Microcavity polariton spin quantum beats without a magnetic field: A manifestation of Coulomb exchange in dense and polarized polariton systems," *Phys. Rev. B*, vol. 72, p. 075317, Aug 2005.

[180] J. Kasprzak, R. André, L. S. Dang, I. A. Shelykh, A. V. Kavokin, Y. G. Rubo, K. V. Kavokin, and G. Malpuech, "Build up and pinning of linear polarization in the Bose condensates of exciton polaritons," *Phys. Rev. B*, vol. 75, p. 045326, Jan 2007.

[181] Z. Vörös, D. W. Snoke, L. Pfeiffer, and K. West, "Direct measurement of exciton-exciton interaction energy," *Physical Review Letters*, vol. 103, July 2009.

[182] M. M. Glazov, H. Ouerdane, L. Pilozzi, G. Malpuech, A. V. Kavokin, and A. D'Andrea, "Polariton-polariton scattering in microcavities: A microscopic theory," *Physical Review B*, vol. 80, Oct. 2009.

[183] S. Schumacher, N. H. Kwong, and R. Binder, "Influence of exciton-exciton correlations on the polarization characteristics of polariton amplification in semiconductor microcavities," *Physical Review B*, vol. 76, Dec. 2007.

[184] M. Combescot, O. Betbeder-Matibet, and R. Combescot, "Bose-einstein condensation in semiconductors: The key role of dark excitons," *Physical Review Letters*, vol. 99, Oct. 2007.

[185] O. Bleu, G. Li, J. Levinsen, and M. M. Parish, "Polariton interactions in microcavities with atomically thin semiconductor layers," *Phys. Rev. Research*, vol. 2, p. 043185, Nov 2020.

[186] M. Richard, J. Kasprzak, R. André, R. Romestain, L. S. Dang, G. Malpuech, and A. Kavokin, "Experimental evidence for nonequilibrium bose condensation of exciton polaritons," *Physical Review B*, vol. 72, Nov. 2005.

[187] A. V. Sekretenko, S. S. Gavrilov, and V. D. Kulakovskii, "Polariton-polariton interactions in microcavities under a resonant 10 to 100 picosecond pulse excitation," *Physical Review B*, vol. 88, no. 19, p. 195302, 2013.

[188] D. Sarchi and V. Savona, "Long-range order in the bose-einstein condensation of polaritons," *Physical Review B*, vol. 75, Mar. 2007.

[189] D. Caputo, D. Ballarini, G. Dagvadorj, C. Sánchez Muñoz, M. De Giorgi, L. Dominici, K. West, L. N. Pfeiffer, G. Gigli, F. P. Laussy, M. H. Szymańska, and D. Sanvitto, "Topological order and thermal equilibrium in polariton condensates," *Nature Materials*, vol. 17, p. 145–151, Dec. 2017.

[190] S. L. Harrison, H. Sigurdsson, and P. G. Lagoudakis, "Synchronization in optically trapped polariton stuart-landau networks," *Physical Review B*, vol. 101, Apr. 2020.

[191] J. D. Töpfer, H. Sigurdsson, L. Pickup, and P. G. Lagoudakis, "Time-delay polaritonics," *Communications Physics*, vol. 3, Jan. 2020.

[192] K. G. Lagoudakis, B. Pietka, M. Wouters, R. André, and B. Deveaud-Plédran, "Coherent oscillations in an exciton-polariton josephson junction," *Physical Review Letters*, vol. 105, Sept. 2010.

[193] R. Balili, V. Hartwell, D. Snoke, L. Pfeiffer, and K. West, "Bose-Einstein Condensation of Microcavity Polaritons in a Trap," *Science*, vol. 316, p. 1007, May 2007.

[194] E. A. Cerda-Méndez, D. Sarkar, D. N. Krizhanovskii, S. S. Gavrilov, K. Biermann, M. S. Skolnick, and P. V. Santos, "Exciton-polariton gap solitons in two-dimensional lattices," *Physical Review Letters*, vol. 111, Oct. 2013.

[195] M. D. Fraser, H. H. Tan, and C. Jagadish, "Selective confinement of macroscopic long-lifetime exciton and trion populations," *Physical Review B*, vol. 84, p. 245318, dec 2011.

[196] D. Press, S. Götzinger, S. Reitzenstein, C. Hofmann, A. Löffler, M. Kamp, A. Forchel, and Y. Yamamoto, "Photon Antibunching from a Single Quantum-Dot-Microcavity System in the Strong Coupling Regime," *Physical Review Letters*, vol. 98, p. 117402, mar 2007.

[197] S. Azzini, D. Gerace, M. Galli, I. Sagnes, R. Braive, A. Lemaître, J. Bloch, and D. Bajoni, "Ultra-low threshold polariton lasing in photonic crystal cavities," *Applied Physics Letters*, vol. 99, p. 111106, sep 2011.

[198] N. Y. Kim, K. Kusudo, C. Wu, N. Masumoto, A. Löffler, S. Höfling, N. Kumada, L. Worschech, A. Forchel, and Y. Yamamoto, "Dynamical d-wave condensation of exciton–polaritons in a two-dimensional square-lattice potential," *Nature Physics*, vol. 7, pp. 681–686, sep 2011.

[199] D. Tanese, H. Flayac, D. Solnyshkov, A. Amo, A. Lemaître, E. Galopin, R. Braive, P. Senellart, I. Sagnes, G. Malpuech, and J. Bloch, "Polariton condensation in solitonic gap states in a one-dimensional periodic potential," *Nature Communications*, vol. 4, p. 1749, Apr 2013.

[200] B. Besga, C. Vaneph, J. Reichel, J. Estève, A. Reinhard, J. Miguel-Sánchez, A. Imamoğlu, and T. Volz, "Polariton Boxes in a Tunable Fiber Cavity," *Physical Review Applied*, vol. 3, p. 014008, jan 2015.

[201] R. Panico, P. Comaron, M. Matuszewski, A. S. Lanotte, D. Trypogeorgos, G. Gigli, M. D. Giorgi, V. Ardizzone, D. Sanvitto, and D. Ballarini, "Onset of vortex clustering and inverse energy cascade in dissipative quantum fluids," *Nature Photonics*, vol. 17, p. 451–456, Mar. 2023.

[202] F. Dalfovo, S. Giorgini, L. P. Pitaevskii, and S. Stringari, "Theory of bose-einstein condensation in trapped gases," *Reviews of Modern Physics*, vol. 71, p. 463–512, Apr. 1999.

[203] E. Hecht, *Optics*. Pearson Education, Incorporated, 2017.

[204] K. Lagoudakis, "The physics of exciton-polariton condensates," Dec. 2013.

[205] F. E. Öztürk, T. Lappe, G. Hellmann, J. Schmitt, J. Klaers, F. Vewinger, J. Kroha, and M. Weitz, "Observation of a non-hermitian phase transition in an optical quantum gas," *Science*, vol. 372, p. 88–91, Apr. 2021.

[206] A. V. Nalitov, D. D. Solnyshkov, and G. Malpuech, "Polariton Z Topological Insulator," *Physical Review Letters*, vol. 114, p. 116401, mar 2015.

[207] J. E. Moore, "The birth of topological insulators," *Nature*, vol. 464, p. 194–198, Mar. 2010.

[208] C. Kane and J. Moore, "Topological insulators," *Physics World*, vol. 24, p. 32–36, Feb. 2011.

[209] F. D. M. Haldane, "Nobel lecture: Topological quantum matter," *Reviews of Modern Physics*, vol. 89, Oct. 2017.

[210] R. Moessner and J. E. Moore, *Topological Phases of Matter*. Cambridge University Press, Apr. 2021.

[211] A. T. Boothroyd, "Topological electronic bands in crystalline solids," *Contemporary Physics*, vol. 63, p. 305–327, Oct. 2022.

[212] T. Karzig, C.-E. Bardyn, N. H. Lindner, and G. Refael, "Topological polaritons," *Physical Review X*, vol. 5, July 2015.

[213] P. St-Jean, V. Goblot, E. Galopin, A. Lemaître, T. Ozawa, L. Le Gratiet, I. Sagnes, J. Bloch, and A. Amo, "Lasing in topological edge states of a one-dimensional lattice," *Nature Photonics*, vol. 11, p. 651–656, Sept. 2017.

[214] C. Li, F. Ye, X. Chen, Y. V. Kartashov, A. Ferrando, L. Torner, and D. V. Skryabin, "Lieb polariton topological insulators," *Physical Review B*, vol. 97, Feb. 2018.

[215] H. Sigurðsson and B. Piętka, "Versatile perovskites enable room-temperature topological polaritonics," *Nature Nanotechnology*, June 2024.

[216] D. D. Solnyshkov, G. Malpuech, P. St-Jean, S. Ravets, J. Bloch, and A. Amo, "Microcavity polaritons for topological photonics [invited]," *Optical Materials Express*, vol. 11, p. 1119, Mar. 2021.

[217] W. Liu, Z. Ji, Y. Wang, G. Modi, M. Hwang, B. Zheng, V. J. Sorger, A. Pan, and R. Agarwal, "Generation of helical topological exciton-polaritons," *Science*, vol. 370, p. 600–604, Oct. 2020.

[218] S. Mittal, S. Ganeshan, J. Fan, A. Vaezi, and M. Hafezi, "Measurement of topological invariants in a 2d photonic system," *Nature Photonics*, vol. 10, p. 180–183, Feb. 2016.

[219] Y. Hatsugai, "Chern number and edge states in the integer quantum hall effect," *Physical Review Letters*, vol. 71, p. 3697–3700, Nov. 1993.

[220] W. Hu, J. C. Pillay, K. Wu, M. Pasek, P. P. Shum, and Y. Chong, "Measurement of a topological edge invariant in a microwave network," *Physical Review X*, vol. 5, Feb. 2015.

[221] M. Aidelsburger, M. Lohse, C. Schweizer, M. Atala, J. T. Barreiro, S. Nascimbène, N. R. Cooper, I. Bloch, and N. Goldman, "Measuring the chern number of hofstadter bands with ultracold bosonic atoms," *Nature Physics*, vol. 11, p. 162–166, Dec. 2014.

[222] M. Atala, M. Aidelsburger, J. T. Barreiro, D. Abanin, T. Kitagawa, E. Demler, and I. Bloch, "Direct measurement of the zak phase in topological bloch bands," *Nature Physics*, vol. 9, p. 795–800, Nov. 2013.

[223] A. Ghatak, M. Brandenbourger, J. van Wezel, and C. Coulais, "Observation of non-hermitian topology and its bulk–edge correspondence in an active mechanical metamaterial," *Proceedings of the National Academy of Sciences*, vol. 117, p. 29561–29568, Nov. 2020.

[224] H. Zhou, C. Peng, Y. Yoon, C. W. Hsu, K. A. Nelson, L. Fu, J. D. Joannopoulos, M. Soljačić, and B. Zhen, "Observation of bulk fermi arc and polarization half charge from paired exceptional points," *Science*, vol. 359, p. 1009–1012, Mar. 2018.

[225] D. Z. Y. Ting and Y.-C. Chang, "Γ-X mixing in GaAs/$Al_xGa_{1-x}As$ and Al_xGa_{1-x} As/AlAs superlattices," *Physical Review B*, vol. 36, pp. 4359–4374, sep 1987.

[226] G. Ru, Z. B. Chen, X. Yu, F.-S. Choa, T. Worchesky, F. Liu, C. Lu, and J. B. Khurgin, "Gamma-x band mixing in gaas/alas superlattice," in *Applications of Photonic Technology 6* (R. A. Lessard and G. A. Lampropoulos, eds.), SPIE, Dec. 2003.

[227] P. Dawson, K. J. Moore, C. T. Foxon, G. W. 't Hooft, and R. P. M. van Hal, "Photoluminescence decay time studies of type II GaAs/AlAs quantum-well structures," *Journal of Applied Physics*, vol. 65, pp. 3606–3609, may 1989.

[228] J. Piprek, *Semiconductor optoelectronic devices*. Elsevier, 2003.

[229] B. Fluegel, K. Alberi, J. Reno, and A. Mascarenhas, "Spectroscopic determination of the bandgap crossover composition in mbe-grown alxga1-xas," *Japanese Journal of Applied Physics*, vol. 54, p. 042402, mar 2015.

[230] N. Chand, T. Henderson, J. Klem, W. T. Masselink, R. Fischer, Y.-C. Chang, and H. Morkoĉ, "Comprehensive analysis of si-doped $al_xga_{1-x}As$ ($x = 0$ to 1): Theory and experiments," *Phys. Rev. B*, vol. 30, pp. 4481–4492, Oct 1984.

[231] P. J. Pearah, W. T. Masselink, J. Klem, T. Henderson, H. Morkoç, C. W. Litton, and D. C. Reynolds, "Low-temperature optical absorption in AlxGa1-xAs grown by molecular-beam epitaxy," *Phys. Rev. B*, vol. 32, pp. 3857–3862, Sep 1985.

[232] M. Z. Baten, P. Bhattacharya, T. Frost, S. Deshpande, A. Das, D. Lubyshev, J. M. Fastenau, and A. W. K. Liu, "Gaas-based high temperature electrically pumped polariton laser," *Applied Physics Letters*, vol. 104, June 2014.

[233] Y. Balas, E. Sedov, G. Paschos, Z. Hatzopoulos, H. Ohadi, A. Kavokin, and P. Savvidis, "Stochastic single-shot polarization pinning of polariton condensate at high temperatures," *Physical Review Letters*, vol. 128, Mar. 2022.

[234] S. T. Lee, J. Haetty, A. Petrou, P. Hawrylak, M. Dutta, J. Pamulapati, P. G. Newman, and M. Taysing-Lara, "Interband transitions in $al_xga_{1-x}as$/alas quantum-well structures," *Phys. Rev. B*, vol. 53, pp. 12912–12916, May 1996.

[235] J. Ihm, "Effects of the layer thickness on the electronic character in GaAs-AlAs superlattices," *Applied Physics Letters*, vol. 50, pp. 1068–1070, apr 1987.

[236] E. O. Göbel and K. Ploog, "Fabrication and optical properties of semiconductor quantum wells and superlattices," *Progress in Quantum Electronics*, vol. 14, pp. 289–356, jan 1990.

[237] T. Tada, A. Yamaguchi, T. Ninomiya, H. Uchiki, T. Kobayashi, and T. Yao, "Tunneling process in AlAs/GaAs double quantum wells studied by photoluminescence," *Journal of Applied Physics*, vol. 63, pp. 5491–5494, jun 1988.

[238] J. Feldmann, M. Preis, E. Göbel, P. Dawson, C. Foxon, and I. Galbraith, "Γ-X-Γ electron transfer in mixed type I-type II GaAs/AlAs quantum well structures," *Solid State Communications*, vol. 83, pp. 245–248, jul 1992.

[239] H. W. van Kesteren, E. C. Cosman, P. Dawson, K. J. Moore, and C. T. Foxon, "Order of the X conduction-band valleys in type-II GaAs/AlAs quantum wells," *Physical Review B*, vol. 39, pp. 13426–13433, jun 1989.

[240] D. Birkedal, K. El Sayed, G. Sanders, C. Spiegelberg, V. Lyssenko, C. Stanton, J. Hvam, V. Timofeev, and M. Bayer, "Interwell excitons in GaAs superlattices," *Superlattices and Microstructures*, vol. 21, pp. 587–590, jun 1997.

[241] R. Cingolani, L. Baldassarre, M. Ferrara, M. Lugarà, and K. Ploog, "Type-I – type-II transition in ultra-short-period GaAs/AlAs superlattices," *Physical Review B*, vol. 40, pp. 6101–6107, sep 1989.

[242] H. Kato, Y. Okada, M. Nakayama, and Y. Watanabe, "Γ - X crossover in GaAs/AlAs superlattices," *Solid State Communications*, vol. 70, pp. 535–539, may 1989.

[243] M. W. Peterson, J. A. Turner, C. A. Parsons, A. J. Nozik, D. J. Arent, C. Van Hoof, G. Borghs, R. Houdré, and H. Morkoç, "Miniband dispersion in $GaAs/Al_xGa_{1-x}As$ superlattices with wide wells and very thin barriers," *Applied Physics Letters*, vol. 53, pp. 2666–2668, dec 1988.

[244] G. Danan, B. Etienne, F. Mollot, R. Planel, A. M. Jean-Louis, F. Alexandre, B. Jusserand, G. Le Roux, J. Y. Marzin, H. Savary, and B. Sermage, "Optical evidence of the direct-to-indirect-gap transition in GaAs-AlAs short-period superlattices," *Physical Review B*, vol. 35, pp. 6207–6212, apr 1987.

[245] K. Maezawa, T. Mizutani, and S. Yamada, "Effective mass and ground state of AlAs quantum wells studied by magnetoresistance measurements," *Journal of Applied Physics*, vol. 71, pp. 296–299, 01 1992.

[246] H. Im, P. C. Klipstein, R. Grey, and G. Hill, "Rotation of the conduction band valleys in alas due to X_X- X_Y mixing," *Phys. Rev. Lett.*, vol. 83, pp. 3693–3696, Nov 1999.

[247] J. F. Young, S. Charbonneau, and P. T. Coleridge, "Determination of x_z-x_x,y energy separation and intervalley relaxation times in type-ii $al_xga_{1-x}as$/alas multiple quantum wells," *Phys. Rev. B*, vol. 42, pp. 11434–11437, Dec 1990.

[248] S. Brem, A. Ekman, D. Christiansen, F. Katsch, M. Selig, C. Robert, X. Marie, B. Urbaszek, A. Knorr, and E. Malic, "Phonon-assisted photoluminescence from indirect excitons in monolayers of transition-metal dichalcogenides," *Nano Letters*, vol. 20, p. 2849–2856, Feb. 2020.

[249] Z. Huang, Y. Zhao, T. Bo, Y. Chu, J. Tian, L. Liu, Y. Yuan, F. Wu, J. Zhao, L. Xian, K. Watanabe, T. Taniguchi, R. Yang, D. Shi, L. Du, Z. Sun, S. Meng, W. Yang, and G. Zhang, "Spatially indirect intervalley excitons in bilayer Wse_2," *Physical Review B*, vol. 105, Jan. 2022.

[250] M. N. Brunetti, O. L. Berman, and R. Y. Kezerashvili, "Optical absorption by indirect excitons in a transition metal dichalcogenide/hexagonal boron nitride heterostructure," *Journal of Physics: Condensed Matter*, vol. 30, p. 225001, May 2018.

[251] E. V. Calman, L. H. Fowler-Gerace, D. J. Choksy, L. V. Butov, D. E. Nikonov, I. A. Young, S. Hu, A. Mishchenko, and A. K. Geim, "Indirect excitons and trions in mose2/wse2 van der waals heterostructures," *Nano Letters*, vol. 20, p. 1869–1875, Feb. 2020.

[252] J. Gu, L. Ma, S. Liu, K. Watanabe, T. Taniguchi, J. C. Hone, J. Shan, and K. F. Mak, "Dipolar excitonic insulator in a moiré lattice," *Nature Physics*, vol. 18, pp. 395–400, Apr 2022.

[253] M. M. Fogler, L. V. Butov, and K. S. Novoselov, "High-temperature superfluidity with indirect excitons in van der waals heterostructures," *Nature Communications*, vol. 5, p. 4555, Jul 2014.

[254] L. V. Butov, A. Zrenner, G. Abstreiter, G. Böhm, and G. Weimann, "Condensation of Indirect Excitons in Coupled AlAs/GaAs Quantum Wells," *Physical Review Letters*, vol. 73, pp. 304–307, jul 1994.

[255] L. V. Butov, C. W. Lai, A. L. Ivanov, A. C. Gossard, and D. S. Chemla, "Towards bose–einstein condensation of excitons in potential traps," *Nature*, vol. 417, pp. 47–52, May 2002.

[256] Z. Wang, D. A. Rhodes, K. Watanabe, T. Taniguchi, J. C. Hone, J. Shan, and K. F. Mak, "Evidence of high-temperature exciton condensation in two-dimensional atomic double layers," *Nature*, vol. 574, pp. 76–80, Oct 2019.

[257] L. H. Fowler-Gerace, Z. Zhou, E. A. Szwed, D. J. Choksy, and L. V. Butov, "Transport and localization of indirect excitons in a van der waals heterostructure," *Nature Photonics*, vol. 18, p. 823–828, June 2024.

[258] E. V. Calman, M. M. Fogler, L. V. Butov, S. Hu, A. Mishchenko, and A. K. Geim, "Indirect excitons in van der waals heterostructures at room temperature," *Nature Communications*, vol. 9, May 2018.

[259] A. Ciarrocchi, F. Tagarelli, A. Avsar, and A. Kis, "Excitonic devices with van der waals heterostructures: valleytronics meets twistronics," *Nature Reviews Materials*, vol. 7, pp. 449–464, Jun 2022.

[260] Y. Liu, Y. Zhu, Z. Yan, R. Bai, X. Zhang, Y. Ren, X. Cheng, H. Ma, and C. Jiang, "Excitonic devices based on two-dimensional transition metal dichalcogenides van der waals heterostructures," *Frontiers of Chemical Science and Engineering*, vol. 18, p. 16, 2 2024.

[261] O. Bleu, K. Choo, J. Levinsen, and M. M. Parish, "Dissipative light-matter coupling and anomalous dispersion in nonideal cavities," *Phys. Rev. A*, vol. 109, p. 023707, Feb 2024.

[262] E. Persson, I. Rotter, H.-J. Stöckmann, and M. Barth, "Observation of resonance trapping in an open microwave cavity," *Phys. Rev. Lett.*, vol. 85, pp. 2478–2481, Sep 2000.

[263] V. L. Grigoryan, K. Shen, and K. Xia, "Synchronized spin-photon coupling in a microwave cavity," *Phys. Rev. B*, vol. 98, p. 024406, Jul 2018.

[264] I. Boventer, C. Dörflinger, T. Wolz, R. Macêdo, R. Lebrun, M. Kläui, and M. Weides, "Control of the coupling strength and linewidth of a cavity magnon-polariton," *Phys. Rev. Res.*, vol. 2, p. 013154, Feb 2020.

[265] M. Harder, Y. Yang, B. M. Yao, C. H. Yu, J. W. Rao, Y. S. Gui, R. L. Stamps, and C.-M. Hu, "Level attraction due to dissipative magnon-photon coupling," *Phys. Rev. Lett.*, vol. 121, p. 137203, Sep 2018.

[266] M. Harder, B. M. Yao, Y. S. Gui, and C.-M. Hu, "Coherent and dissipative cavity magnonics," *Journal of Applied Physics*, vol. 129, p. 201101, 05 2021.

[267] Y.-P. Wang and C.-M. Hu, "Dissipative couplings in cavity magnonics," *Journal of Applied Physics*, vol. 127, p. 130901, 04 2020.

[268] F. Elste, S. M. Girvin, and A. A. Clerk, "Quantum noise interference and back-action cooling in cavity nanomechanics," *Phys. Rev. Lett.*, vol. 102, p. 207209, May 2009.

[269] T. Tawara, H. Kamada, T. Tanabe, T. Sogawa, H. Okamoto, P. Yao, P. K. Pathak, and S. Hughes, "Cavity-qed assisted attraction between a cavity mode and an exciton mode in a planar photonic-crystal cavity," *Opt. Express*, vol. 18, pp. 2719–2728, Feb 2010.

[270] C. Wang, Z. Fu, W. Mao, J. Qie, A. D. Stone, and L. Yang, "Non-hermitian optics and photonics: from classical to quantum," *Advances in Optics and Photonics*, vol. 15, p. 442, June 2023.

[271] W. Yu, J. Wang, H. Y. Yuan, and J. Xiao, "Prediction of attractive level crossing via a dissipative mode," *Phys. Rev. Lett.*, vol. 123, p. 227201, Nov 2019.

[272] S. Dhara, C. Chakraborty, K. M. Goodfellow, L. Qiu, T. A. O'Loughlin, G. W. Wicks, S. Bhattacharjee, and A. N. Vamivakas, "Anomalous dispersion of microcavity trion-polaritons," *Nature Physics*, vol. 14, pp. 130–133, Feb 2018.

[273] E. Y. Paik, L. Zhang, S. Hou, H. Zhao, Y. Chou, S. R. Forrest, and H. Deng, "High Quality Factor Microcavity for Van der Waals Semiconductor Polaritons Using a Transferrable Mirror," *Advanced Optical Materials*, vol. 11, p. 2201440, jan 2023.

[274] R. Binder, J. R. Schaibley, and N. H. Kwong, "Non-hermitian dispersion sign reversal of radiative resonances in two dimensions," *Phys. Rev. B*, vol. 109, p. 125301, Mar 2024.

[275] L. Pickup, H. Sigurdsson, J. Ruostekoski, and P. G. Lagoudakis, "Synthetic band-structure engineering in polariton crystals with non-hermitian topological phases," *Nature Communications*, vol. 11, p. 4431, Sep 2020.

[276] M. J. Jacquet, T. Boulier, F. Claude, A. Maître, E. Cancellieri, C. Adrados, A. Amo, S. Pigeon, Q. Glorieux, A. Bramati, and E. Giacobino, "Polariton fluids for analogue gravity physics," *Philosophical Transactions of the Royal Society A: Mathematical, Physical and Engineering Sciences*, vol. 378, p. 20190225, July 2020.

[277] P. St-Jean, A. Dauphin, P. Massignan, B. Real, O. Jamadi, M. Milicevic, A. Lemaître, A. Harouri, L. Le Gratiet, I. Sagnes, S. Ravets, J. Bloch, and A. Amo, "Measuring topological invariants in a polaritonic analog of graphene," *Phys. Rev. Lett.*, vol. 126, p. 127403, Mar 2021.

[278] P. Comaron, V. Shahnazaryan, W. Brzezicki, T. Hyart, and M. Matuszewski, "Non-hermitian topological end-mode lasing in polariton systems," *Physical Review Research*, vol. 2, June 2020.

[279] V. Ardizzone, F. Riminucci, S. Zanotti, A. Gianfrate, M. Efthymiou-Tsironi, D. G. Suàrez-Forero, F. Todisco, M. De Giorgi, D. Trypogeorgos, G. Gigli, K. Baldwin, L. Pfeiffer, D. Ballarini, H. S. Nguyen, D. Gerace, and D. Sanvitto, "Polariton bose–einstein condensate from a bound state in the continuum," *Nature*, vol. 605, pp. 447–452, May 2022.

[280] A. Rahmani, A. Opala, and M. Matuszewski, "Exceptional points and phase transitions in non-hermitian nonlinear binary systems," *Physical Review B*, vol. 109, Feb. 2024.

[281] A. Rahmani, M. Kędziora, A. Opala, and M. Matuszewski, "Non-hermitian synthetic lattices with light-matter coupling," *Physical Review B*, vol. 107, Apr. 2023.

[282] C. E. Whittaker, E. Cancellieri, P. M. Walker, D. R. Gulevich, H. Schomerus, D. Vaitiekus, B. Royall, D. M. Whittaker, E. Clarke, I. V. Iorsh, I. A. Shelykh, M. S. Skolnick, and D. N. Krizhanovskii, "Exciton polaritons in a two-dimensional lieb lattice with spin-orbit coupling," *Phys. Rev. Lett.*, vol. 120, p. 097401, Mar 2018.

[283] A. Gianfrate, H. Sigurðsson, V. Ardizzone, H. C. Nguyen, F. Riminucci, M. Efthymiou-Tsironi, K. W. Baldwin, L. N. Pfeiffer, D. Trypogeorgos, M. De Giorgi, D. Ballarini, H. S. Nguyen, and D. Sanvitto, "Reconfigurable quantum fluid molecules of bound states in the continuum," *Nature Physics*, vol. 20, p. 61–67, Jan. 2024.

[284] S. Alyatkin, H. Sigurdsson, A. Askitopoulos, J. D. Töpfer, and P. G. Lagoudakis, "Quantum fluids of light in all-optical scatterer lattices," *Nature Communications*, vol. 12, Sept. 2021.